

**PARAMETRIC STUDIES ON
FILM COOLING EFFECTIVENESS
AND HEAT TRANSFER COEFFICIENTS
OVER GAS TURBINE BLADE LEADING
EDGE SURFACES**

Thesis

Submitted in partial fulfillment of the requirement for the degree of

DOCTOR OF PHILOSOPHY

by

YEPURI GIRIDHARA BABU



DEPARTMENT OF MECHANICAL ENGINEERING
NATIONAL INSTITUTE OF TECHNOLOGY KARNATAKA
SURATHKAL, MANGALORE – 575025

SEPTEMBER, 2018

*Reserved copyrights with supervisor of this thesis, “**Parametric Studies on Film Cooling Effectiveness and Heat Transfer Coefficients over Gas Turbine Blade Leading Edge Surfaces**” N.I.T.K, Surathkal. No part of this thesis can be reproduced in any form or by any means without prior written permission of the Supervisor and N.I.T.K.*

DECLARATION

by the Ph.D. Research Scholar

I hereby *declare* that the Research Thesis entitled “**Parametric Studies on Film Cooling Effectiveness and Heat Transfer Coefficients over Gas Turbine Blade Leading Edge Surfaces**” which is being submitted to the **National Institute of Technology Karnataka, Surathkal** in partial fulfillment of the requirements for the award of the Degree of **Doctor of Philosophy** in Mechanical Engineering is a *bonafide report of the research work carried out by me*. The material contained in this Research Thesis has not been submitted to any University or Institution for the award of any degree.

Place : NITK, Surathkal

Yepuri Giridhara Babu

Date : 26th Sep 2018

Reg. No.: 121189ME12P07

Department of Mechanical Engineering

NITK, Surathkal, Mangalore - 575025

CERTIFICATE

This is to *certify* that the Research Thesis entitled “**Parametric Studies on Film Cooling Effectiveness and Heat Transfer Coefficients over Gas Turbine Blade Leading Edge Surfaces**” submitted by **Yepuri Giridhara Babu** (Register Number: 121189ME12P07) as the record of the research work carried out by him, is *accepted as the Research Thesis submission* in partial fulfillment of the requirements for the award of degree of Doctor of Philosophy.

Place : NITK, Surathkal

Date : 26th Sep 2018

Research Guide

Prof. T. P. Ashok Babu

Department of Mechanical Engineering

NITK, Surathkal, Mangalore - 575025

Place : NITK, Surathkal

Date : 26th Sep 2018

Chairman - DRPC

Department of Mechanical Engineering

NITK, Surathkal, Mangalore - 575025

ACKNOWLEDGMENTS

First and foremost, I express my sincere, heartfelt thanks and deepest gratitude to my research guide Dr. T.P. Ashok Babu, Professor, Former Dean (FW), Former Head of Mechanical Engineering Department, National Institute of Technology Karnataka, Surathkal for his valuable guidance, constant inspiration and support throughout my research work. I gratefully acknowledge his painstaking efforts in thoroughly going through and improving the manuscript without which this work would not have been completed.

I am thankful to Dr. Sastry V.R, Professor, Department of Mining Engineering and Dr. Kumar G.N, Professor, Department of Mechanical Engineering, NITK both members of Research Progress Assessment Committee for their valuable comments and critical suggestions to complete my research activities successfully.

It is my great pleasure in undertaking this research work at NITK, Surathkal, Mangalore and I sincerely express my gratitude to Director, NITK for providing this opportunity. I am also thankful to Dean (Academic) and Head, Department of Mechanical Engineering, NITK for providing all the facilities, help and an opportunity to carry out my research work.

I extend special gratitude to Director, CSIR-National Aerospace Laboratories (NAL), Bangalore for granting the permission to carry out my Ph. D work at NAL. I would like to thank Mr. Manjunath P., Head, Dr. Rajendran R., Ex. Jt. Head, Propulsion Division, and Dr. Venkateswarlu, Scientist-F, Material Science Division, CSIR-NAL for their great encouragement and advice to carry out my Ph.D. work at the NITK, Surathkal and NAL, Bangalore. I also wish to thank my heat transfer group colleagues at NAL (Mr. J. Felix, Mrs. Poornima, Mr. Maria Arockiam S., Mr. Sanmuganantham M. and Mr. Pradeep K. A.) for their constant support during all my Ph.D. activities at NAL.

Finally, I am very grateful to my wife Mrs. Bharathi and daughter Ms. Sravya for their constant help, continuous encouragement and support towards the completion of my research work effectively.

Yepuri Giridhara Babu

ABSTRACT

The effect of various geometrical and flow parameters on the adiabatic film cooling effectiveness and heat transfer coefficients over the gas turbine stator blade leading edge models was carried out for the optimization of the geometrical and flow parameters. In this study, the 4:1 scaled up adiabatic blade leading edge test models were used with a geometry similar to that of a typical gas turbine nozzle guide vane. The film cooling hole geometrical parameters on the blade leading edge region like film cooling hole orientation angle (15° , 30° and 45°), inclination angle (20° , 25° , 30° and 35°), spanwise pitch to diameter ratio (3 and 4) and variation of hole exit shape (Circular, Fan, and Laidback Fan shapes) effects have been studied.

Experiments were carried out using the Film Cooling Test Facility available at Heat Transfer Lab, Propulsion Division, CSIR - National Aerospace Laboratories, Bangalore. The experiments were conducted for adiabatic cooling effectiveness and heat transfer coefficients at a mainstream flow Reynolds number of 1×10^5 based on the leading edge diameter by varying the blowing ratios in the range of 1.0 to 2.5 at a density ratio of 1.3. The results were found for two pitch spanwise averaged values along the streamwise direction. A numerical study was also made for the same experimental cases to see the trends and deviations of the results and validation of the CFD. The numerical investigations were conducted with the help of ANSYS 14 Workbench, ICEM CFD meshing and FLUENT.

From both the experimental and numerical results, adiabatic film cooling effectiveness and heat transfer coefficient values over the blade leading edge region were found to increase with an increase in hole orientation location from the stagnation line, with the decrease in hole inclination angle, with the lower hole pitch and with the increase in hole exit area. The numerical results also showed the same trends as that of the experimental values with minor deviations at some locations, and the peaks in the numerical results indicated the hole locations. Among the considered blowing ratios, the blowing ratio 2.0 has shown the higher cooling effectiveness, and the heat transfer coefficient values were found to be increasing with the increase in blowing ratios on all considered models.

Key Words: Gas turbine blades, Blowing ratio, Density ratio, Effectiveness, Heat transfer coefficient, Inclination angle, Orientation angle, Pitch, Shape.

CONTENTS

	Page No.
ACKNOWLEDGMENTS	
ABSTRACT.....	i
CONTENTS.....	ii
LIST OF FIGURES	vii
LIST OF TABLES	xvii
NOMENCLATURE	xviii
1 INTRODUCTION.....	1
1.1 Need for Turbine Blade Cooling.....	4
1.2 Blade Cooling Classification	6
1.2.1 External cooling	8
1.2.1.1 Convection cooling.....	8
1.2.1.2 Transpiration cooling.....	9
1.2.1.3 Film cooling.....	9
1.2.2 Internal cooling	11
1.2.2.1 Impingement cooling.....	11
1.2.2.2 Pin-fin cooling	11
1.2.2.3 Rib Turbulated Cooling	12
1.3 Fundamentals of Film Cooling	12
1.3.1 Blowing Ratio (B.R)	14
1.3.2 Density Ratio (D.R).....	14
1.4 Heat Transfer Coefficients Concept.....	15
1.5 Introduction to CFD.....	16
1.5.1 How Does CFD Works	16

1.5.1.1	Pre-processor	16
1.5.1.2	Solver.....	16
1.5.1.3	Post Processing	17
1.5.2	Governing Equations of Fluid Flow and Heat Transfer.....	17
1.5.2.1	Mass Conservation Equation in Three Dimensions	17
1.5.2.2	Three dimensional Energy Equation	18
1.5.2.3	Navier- Stokes Equations for a Newtonian Fluid.....	19
1.5.2.4	Momentum Equation in Three Dimensions.....	19
1.5.3	Turbulence Models.....	20
1.6	Organization of the Thesis	21
2.	LITERATURE REVIEW AND OBJECTIVES OF THE WORK	22
2.1	Gas Turbine Blade Film Cooling Technology.....	22
2.2	Historical Background of Film Cooling	23
2.3	Expanded Exit Holes in Film Cooling	30
2.4	Computational Film Cooling Methods	30
2.5	Various Film Cooling Parameters.....	31
2.6	Research Gap	41
2.7	Scope and Objectives of the Work.....	42
2.7.1	The scope of the Work.....	42
2.7.2	Objectives of the Work	43
3	EXPERIMENTAL SETUP AND PROCEDURE.....	45
3.1	Test Models.....	45
3.1.1	Gas Turbine Blade Leading Edge Model Specifications	46
3.1.2	Test Model Details	46
3.1.3	Effect of Hole Orientation Angle (M1, M2, M3).....	47
3.1.4	Effect of Hole Inclination Angle (M4, M5, M6, M7)	48

3.1.5	Effect of Hole Pitch (M6 and M8)	49
3.1.6	Effect of Hole Exit Shape (M9, M10, M11)	50
3.1.7	Test Run Details	51
3.2	Fabricated Gas Turbine Leading Edge Models by RPT Method.....	52
3.3	Experimental Setup	53
3.4	Instrumentation systems used in the experiments.....	58
3.4.1	Pressure Measuring System	58
3.4.2	Temperature Measuring System	59
3.4.3	Mass Flow Measuring System	60
3.4.4	Specification of Instruments used	61
3.4.5	Experimental Uncertainty	62
3.5	Experimental Procedure	63
3.5.1	Film Effectiveness Measurement Experiments.....	64
3.5.2	Heat Transfer Coefficient Measurements	66
3.5.3	Study of Experimental Consistency	69
3.6	Validation of Experimental data	70
4	COMPUTATIONAL PROCEDURE.....	73
4.1	Model, Mesh Generation, and Boundary Conditions	73
4.2	Boundary Conditions for the Numerical Simulation	75
4.3	Grid Independency Test.....	77
5	RESULTS AND DISCUSSION	78
5.1	Effect of Hole Orientation Angle (HOA) along the streamwise direction (15°, 30° and 45° from stagnation line)	78
5.1.1	Experimental Adiabatic Film Effectiveness Measurements	78
5.1.2	Numerical Results of Adiabatic Film Cooling Effectiveness	84
5.1.3	Experimental and Numerical cooling effectiveness over the typical HOA model.....	93
5.2	Effect of Hole Inclination Angle (HIA) along the streamwise direction...	94

5.2.1	Experimental Adiabatic Film cooling effectiveness and HTC Results..	94
5.2.2	Numerical Adiabatic Film cooling effectiveness and HTC Results	104
5.2.3	Comparison of Experimental and CFD Results	115
5.3	Effect of Hole Pitch	121
5.3.1	Adiabatic Film Cooling Effectiveness Measurements	121
5.3.1.1	18 mm Spanwise Hole Pitch Model (M6) Cooling Effectiveness Results	121
5.3.1.2	22.4 mm Spanwise Hole Pitch Model (M8) Cooling Effectiveness Results	125
5.3.2	Heat Transfer Coefficient Measurements	129
5.3.2.1	18 mm Spanwise Hole Pitch Model (M6) HTC Results	130
5.3.2.2	22.4 mm Spanwise Hole Pitch Model (M8) HTC Results	134
5.3.3	Comparative Study of 18 mm and 22.4 mm Hole Pitch Models	137
5.3.3.1	Adiabatic Film Cooling Effectiveness Results Comparison	138
5.3.3.2	Heat Transfer Coefficients Comparative Results	141
5.4	Effect of Hole Shape	144
5.4.1	Experimental and Numerical Adiabatic Film Cooling Effectiveness Results	144
5.4.1.1	Circular Hole Model (M9-CHM)	144
5.4.1.2	Fan Shape Hole Model (M10-FSHM).....	148
5.4.1.3	Laid Back Fan Shape Hole Model (M11-LFSHM).....	151
5.4.2	Experimental and Numerical Heat Transfer Coefficient Results.....	154
5.4.2.1	Circular Hole Exit Shape Model HTC Results (M9-CHM).....	155
5.4.2.2	Fan Shape Hole Model HTC Results (M10-FSHM).....	158
5.4.2.3	Laidback Fan Shape Hole Model HTC Results (M11-LFSHM)..	161
5.4.3	Experimental and Numerical Comparative Study of shaped holes..	165
5.4.3.1	Experimental Comparative Study of Shaped hole models	165

5.4.3.2	Numerical Comparative Study of All Exit Hole Shapes	168
6	CONCLUSIONS	171
6.1	Future Scope of Work	174
	REFERENCES	175
	Appendix-I	184
I	MEASUREMENT OF MASS FLOW AND COEFFICIENT OF DISCHARGE	184
I.1	Coolant mass flow and Cd values	184
I.2	Mainstream mass flow measurements	201
	Appendix – II	202
II	CONDUCTION LOSS MEASUREMENTS	202
II.1	Voltage Versus Current Measurements	203
	Appendix-III	205
III	INFRA-RED THERMAL CAMERA CALIBRATION	205
	Appendix IV	210
IV	UNCERTAINTY MEASUREMENTS	210
IV.1	Uncertainty in Mass flow rate	212
IV.2	Uncertainty in Mainstream Reynolds Number	214
IV.3	Uncertainty in the Density ratio	216
IV.4	Uncertainty in the Blowing ratio	218
IV.5	Uncertainty in the Cooling Effectiveness	220
IV.6	Uncertainty in Heat transfer coefficient	222
IV.7	Uncertainty Summary	223
	BIODATA	224
	PUBLICATIONS	225

LIST OF FIGURES

Fig. 1.1 Simple open cycle gas turbine engine	2
Fig. 1.2 Simple closed cycle gas turbine engine.....	2
Fig. 1.3 P-V and T-S diagram of a simple gas turbine	3
Fig. 1.4 Typical turboprop gas turbine engine	3
Fig. 1.5 Effect of RIT on power output	5
Fig. 1.6 Variation of turbine entry temperature over the years.....	5
Fig. 1.7 Development of turbine inlet temperature.....	6
Fig. 1.8 Schematic of GT blade cooling (a) External (b) Internal	7
Fig. 1.9 Gas turbine blade external cooling region.....	7
Fig. 1.10 Schematic of different internal cooling regimes.....	8
Fig. 1.11 Transpiration cooling.....	9
Fig. 1.12 Film cooling.....	10
Fig. 1.13 Spanwise film cooling holes on leading edge	10
Fig. 1.14 Impingement cooling.....	11
Fig. 1.15 Pin-Fin cooling	12
Fig. 1.16 Film cooling concept	13
Fig. 3.1 Gas turbine blade cooling schematic	45
Fig. 3.2 M1_15° hole orientation angle	47
Fig. 3.3 M2_30° hole orientation angle	47
Fig. 3.4 M3_45° hole orientation angle	47
Fig. 3.5 M4_20° hole angle	48
Fig. 3.6 M5_25° hole angle	48
Fig. 3.7 M6_30° hole angle	48

Fig. 3.8 M7_35° hole angle	48
Fig. 3.9 Typical hole angle w.r.t. spanwise direction	48
Fig. 3.10 M8_30° Hole angle, 22.4 mm pitch	49
Fig. 3.11 M8_Geometrical details	49
Fig. 3.12 M9_Circular hole model.....	50
Fig. 3.13 M10_Fan shape hole model.....	50
Fig. 3.14 M11_Laidback fan shape hole model.....	50
Fig. 3.15 Hole Exit Shapes (a) M9 Circular shape (b) M10 Fan shape (c) M11 Laidback fan shape	50
Fig. 3.16 Fabricated leading edge model with S.S sheet and bus bars	52
Fig. 3.17 Test model with thermocouples and coolant chamber	52
Fig. 3.18 Schematic of film cooling test methodology	56
Fig. 3.19 Schematic view of the experimental test rig.....	56
Fig. 3.20 Schematic of the automated liquid nitrogen flow controller system	57
Fig. 3.21 Photographic view of the test rig with instrumentation.....	57
Fig. 3.22 Leading edge test model mounted in the test section	58
Fig. 3.23 Temperature DAQ system, pressure net scanner and IR instruments	59
Fig. 3.24 Infra Red Thermal Camera A 655sc.....	60
Fig. 3.25 Film cooling effectiveness data at two test runs.....	69
Fig. 3.26 Heat transfer coefficients data for two test runs	70
Fig. 3.27 Validation of CHM Experimental data at a blowing ratio of 1.5	71
Fig. 3.28 Validation of FSHM Experimental data at a blowing ratio of 1.5	72
Fig. 3.29 Validation of LFSHM Experimental data at a blowing ratio of 1.5	72
Fig. 4.1 LE model for the computation method.....	73
Fig. 4.2 Computational domain	73

Fig. 4.3 Solid and wire frame with mesh quality 0.55	74
Fig. 4.4 O-grid mesh for coolant holes.	74
Fig. 4.5 Comparison of different CFD models with experimental data.....	76
Fig. 4.6 Comparison of film cooling effectiveness for different mesh sizes.	77
Fig. 5.1 Typical thermal images of film cooling effectiveness at a B.R of 2.0	79
Fig. 5.2 Experimentally evaluated cooling effectiveness at a B.R of 1.25	80
Fig. 5.3 Experimentally evaluated cooling effectiveness at a B.R of 1.5	81
Fig. 5.4 Experimentally evaluated cooling effectiveness at a B.R of 1.75	81
Fig. 5.5 Experimentally evaluated cooling effectiveness at a B.R of 2.0	82
Fig. 5.6 Experimentally evaluated cooling effectiveness for 15° HOA model	83
Fig. 5.7 Experimentally evaluated cooling effectiveness for 30° HOA model	83
Fig. 5.8 Experimentally evaluated cooling effectiveness for 45° HOA model	84
Fig. 5.9 Temperature and velocity contours for 45° HOA model at a B.R of 1.5	85
Fig. 5.10 Velocity vectors for 30° HOA model at B.R of 1.5	85
Fig. 5.11 Numerically evaluated adiabatic cooling effectiveness at a B.R of 1.25	87
Fig. 5.12 Numerically evaluated adiabatic cooling effectiveness at a B.R of 1.5	87
Fig. 5.13 Numerically evaluated adiabatic cooling effectiveness at a B.R of 1.75	88
Fig. 5.14 Numerically evaluated adiabatic cooling effectiveness at a B.R of 2.0	88
Fig. 5.15 Numerically evaluated cooling effectiveness for 15° HOA model	89
Fig. 5.16 Numerically evaluated cooling effectiveness for 30° HOA model	89
Fig. 5.17 Numerically evaluated cooling effectiveness for 45° HOA model	90
Fig. 5.18 Numerically evaluated cooling effectiveness at a B.R of 1.25.....	90
Fig. 5.19 Numerically evaluated adiabatic cooling effectiveness at a B.R of 1.5	91
Fig. 5.20 Numerically evaluated adiabatic cooling effectiveness at a B.R of 1.75	91
Fig. 5.21 Numerically evaluated adiabatic cooling effectiveness at a B.R of 2.0	92

Fig. 5.22 Experimentally captured thermal image for a 30° HOA model at a B.R of 1.50.....	93
Fig. 5.23 CFD extracted temperature contour for a 30° HOA model at a B.R of 1.5093	
Fig. 5.24 Thermal images at different B.Rs of 20° HIA model.....	94
Fig. 5.25 Cooling effectiveness comparison of two test runs at a constant B.R.....	95
Fig. 5.26 Cooling effectiveness values for a 20° HIA model	96
Fig. 5.27 Heat transfer coefficient values for a 20° HIA model	97
Fig. 5.28 Cooling effectiveness values for a 25° HIA model	98
Fig. 5.29 Heat transfer coefficient values for a 25° HIA model	99
Fig. 5.30 Cooling effectiveness values for a 30° HIA model	100
Fig. 5.31 Heat transfer coefficient values for a 30° HIA model	100
Fig. 5.32 Cooling effectiveness values for a 35° HIA model	101
Fig. 5.33 Heat transfer coefficients values for a 35° HIA model	101
Fig. 5.34 Comparison of cooling effectiveness for all HIA models at a B.R of 1.0.	102
Fig. 5.35 Comparison of cooling effectiveness for all HIA models at a B.R of 1.5.	103
Fig. 5.36 Comparison of cooling effectiveness for all HIA models at a B.R of 2.0.	103
Fig. 5.37 Comparison of cooling effectiveness for all HIA models at a B.R of 2.5.	104
Fig. 5.38 Grid independency results for 25° HIA model at a B.R of 1.5	105
Fig. 5.39 Numerical Cooling effectiveness for a 20° HIA model	106
Fig. 5.40 Temperature contours of 20° HIA model at different B.Rs	107
Fig. 5.41 Numerical heat transfer coefficient values of a 20° HIA model	107
Fig. 5.42 Numerical cooling effectiveness of a 25° HIA model.....	108
Fig. 5.43 Numerical heat transfer coefficient values of a 25° HIA model	109
Fig. 5.44 Numerical cooling effectiveness of a 30° HIA model.....	110
Fig. 5.45 Numerical heat transfer coefficient values of a 30° HIA model	110

Fig. 5.46 Numerical cooling effectiveness of a 35° hole inclination angle model ...	111
Fig. 5.47 Numerical heat transfer coefficient for 35° hole inclination angle model	112
Fig. 5.48 Comparison of cooling effectiveness for all the models at a B.R of 1.0...	113
Fig. 5.49 Comparison cooling effectiveness for all the models at a B.R of 1.5	113
Fig. 5.50 Comparison of cooling effectiveness for HIA models at a B.R of 2.0.....	114
Fig. 5.51 Comparison of cooling effectiveness for HIA models at a B.R of 2.5.....	115
Fig. 5.52 Exp. Vs. CFD effectiveness results for a 25° HIA model at a B.R of 1.0.	116
Fig. 5.53 Exp. Vs. CFD effectiveness results for a 25° HIA model at a B.R of 1.5.	116
Fig. 5.54 Exp. Vs. CFD effectiveness results for a 25° HIA model at a B.R of 2.0.	117
Fig. 5.55 Exp. Vs. CFD effectiveness results for a 25° HIA model at a B.R of 2.5.	118
Fig. 5.56 Exp. Vs. CFD HTC results for a 25° HIA model at a B.R of 1.0.....	118
Fig. 5.57 Exp. Vs. CFD HTC results for a 25° HIA model at a B.R of 1.5.....	119
Fig. 5.58 Exp. Vs. CFD HTC Results for a 25° HIA model at a B.R of 2.0	119
Fig. 5.59 Exp. Vs. CFD HTC Results for a 25° HIA model at a B.R of 2.5	120
Fig. 5.60 Exp. and CFD temperature contours of effectiveness for 18 mm hole pitch model at a B.R of 2.0	122
Fig. 5.61 Exp. cooling effectiveness for 18 mm pitch model at B.Rs of 1.0 to 2.5..	123
Fig. 5.62 Numerical cooling effectiveness for 18 mm model at B.Rs of 1.0 to 2.5 .	123
Fig. 5.63 Exp. and Numerical cooling effectiveness for 18 mm model at a B.R of 1.5	124
Fig. 5.64 Exp. and Numerical cooling effectiveness at a B.R of 2.0.....	124
Fig. 5.65 Exp. and CFD temperature contours of effectiveness for a 22.4 mm hole pitch model at a B.R of 2.0	125
Fig. 5.66 Exp. cooling effectiveness for 22.4 mm pitch model at B.R of 1.0 to 2.5	126
Fig. 5.67 Numerical cooling effectiveness for a 22.4 mm model at B.R of 1.0 to 2.5	127

Fig. 5.68 Exp. Vs. Numerical cooling effectiveness for a 22.4 mm hole pitch model at a B.R of 1.5	128
Fig. 5.69 Exp. Vs. Numerical cooling effectiveness at a B.R of 2.0 for a 22.4 mm hole pitch model.....	128
Fig. 5.70 Exp. and CFD temperature contours of HTC for an 18 mm hole pitch model at a B.R of 2.5	130
Fig. 5.71 Exp. HTC results for an 18.4 mm hole pitch model at B.Rs of 1.0 to 2.5.	131
Fig. 5.72 Numerical HTC results for an 18.4 mm pitch model at B.Rs of 1.0 to 2.5	131
Fig. 5.73 Exp. Vs. Numerical HTC for an 18.4 mm hole pitch model at a B.R of 1.5	132
Fig. 5.74 Exp. Vs. Numerical HTC for an 18.4 mm hole pitch model at a B.R of 2.0	133
Fig. 5.75 Exp. and CFD temperature contours of HTC for a 22.4 mm hole pitch model at a B.R of 2.5	134
Fig. 5.76 Exp. HTC results for 22.4 mm hole pitch model at B.R of 1.0 to 2.5.....	135
Fig. 5.77 Numerical HTC results for a 22.4 mm hole pitch model at B.R of 1.0 to 2.5	135
Fig. 5.78 Exp. Vs. Numerical HTC for a 22.4 mm hole pitch model at a B.R of 1.5	136
Fig. 5.79 Exp. Vs. Numerical HTC for a 22.4 mm hole pitch model at a B.R of 2.0	137
Fig. 5.80 Exp. cooling effectiveness comparison for 18 and 22.4 mm hole pitch models at a B.R of 1.5.....	138
Fig. 5.81 Exp. cooling effectiveness comparison for 18 and 22.4 mm hole pitch models at a B.R of 2.0.....	138
Fig. 5.82 Numerical cooling effectiveness comparison for 18 and 22.4 mm Hole pitch models at a B.R of 1.5.....	139

Fig. 5.83 Numerical cooling effectiveness comparison for 18 and 22.4 mm Hole pitch models at a B.R of 2.0.....	140
Fig. 5.84 Exp. HTC comparison of 18 and 22.4 mm pitch models at a B.R of 1.5..	141
Fig. 5.85 Exp. HTC comparison of 18 and 22.4 mm pitch models at a B.R of 2.0..	141
Fig. 5.86 Numerical HTC comparison of 18 mm and 22.4 mm hole pitch models at a B.R of 1.5.....	142
Fig. 5.87 Numerical HTC comparison of 18 mm and 22.4 mm hole pitch models at a B.R of 2.0.....	143
Fig. 5.88 Exp. and Numerical temperature contours of effectiveness for CHM at a typical B.R of 2.0.....	145
Fig. 5.89 Exp. cooling effectiveness for CHM at the B.Rs of 1.0 to 2.5.....	146
Fig. 5.90 Numerical cooling effectiveness for CHM at the B.Rs of 1.0 to 2.5.....	147
Fig. 5.91 Exp. Vs. CFD cooling effectiveness comparison for CHM at the B.R of 2.0.....	147
Fig. 5.92 Exp. and Numerical temperature contours of effectiveness for FSHM at a typical B.R of 2.0.....	149
Fig. 5.93 Exp. cooling effectiveness for FSHM at the B.Rs of 1.0 to 2.5.....	149
Fig. 5.94 Numerical cooling effectiveness for FSHM at the B.Rs of 1.0 to 2.5.....	150
Fig. 5.95 Exp. Vs. Numerical effectiveness comparison for FSHM at the B.R of 2.0.....	150
Fig. 5.96 Exp. and Numerical temperature contours of effectiveness for LFSHM at a typical B.R of 2.0.....	151
Fig. 5.97 Exp. cooling effectiveness for LFSHM at the B.Rs of 1.0 to 2.5.....	152
Fig. 5.98 Numerical cooling effectiveness for LFSHM at the B.Rs of 1.0 to 2.5....	153
Fig. 5.99 Exp. Vs. Numerical cooling effectiveness for LFSHM at a B.R of 2.0....	154
Fig. 5.100 Exp. and Numerical temperature contours of HTC for CHM at a B.R of 2.0.....	155

Fig. 5.101 Exp. HTC values for a CHM model at the B.Rs of 1.0 to 2.5	156
Fig. 5.102 Numerical HTC values for a CHM model at the B.Rs of 1.0 to 2.5	157
Fig. 5.103 Exp. Vs. Numerical HTC Values for a CHM model at the B.R of 2.0 ...	158
Fig. 5.104 Exp. and Numerical temperature contours of HTC for FSHM models at a B.R of 2.0.....	159
Fig. 5.105 Exp. HTC values for an FSHM at the B.Rs of 1.0 to 2.5	159
Fig. 5.106 Numerical HTC values for an FSHM at the B.Rs of 1.0 to 2.5.....	160
Fig. 5.107 Exp. Vs. numerical HTC for FSHM at the B.R of 2.0	161
Fig. 5.108 Exp. and Numerical temperature contours of HTC for LFSHM at a B.R of 2.0.....	161
Fig. 5.109 Exp. HTC values for an LFSHM at the B.Rs of 1.0 to 2.5.....	163
Fig. 5.110 Numerical HTC values for an LFSHM at the B.Rs of 1.0 to 2.5	163
Fig. 5.111 Exp. Vs. Numerical HTC values for an LFSHM at the B.R of 2.0.....	164
Fig. 5.112 Exp. cooling effectiveness comparison of CHM, FSHM and LFSHM models at a B.R of 1.0.....	165
Fig. 5.113 Exp. cooling effectiveness comparison of CHM, FSHM and LFSHM models at a B.R of 1.5.....	166
Fig. 5.114 Exp. cooling effectiveness comparison of CHM, FSHM and LFSHM models at a B.R of 2.0.....	166
Fig. 5.115 Exp. cooling effectiveness comparison of CHM, FSHM and LFSHM models at a B.R of 2.5.....	167
Fig. 5.116 Numerical cooling effectiveness comparison of CHM, FSHM and LFSHM models at a B.R of 1.0.....	168
Fig. 5.117 Numerical cooling effectiveness comparison of CHM, FSHM and LFSHM models at a B.R of 1.5.....	168
Fig. 5.118 Numerical cooling effectiveness comparison of CHM, FSHM and LFSHM models at a B.R of 2.0.....	169

Fig. 5.119 Numerical cooling effectiveness comparison of CHM, FSHM and LFSHM models at a B.R of 2.5.....	169
Fig. I.1 Mass flow Vs. Coolant chamber pressure for a 20° hole Inclination angle model.....	186
Fig. I.2 Coolant Cd Vs. Coolant Reynolds number for a 20° hole Inclination angle model.....	187
Fig. I.3 Mass flow Vs. Coolant chamber pressure for a 25° hole Inclination angle model.....	188
Fig. I.4 Coolant Cd Vs. Coolant Reynolds number for a 20° hole Inclination angle model.....	189
Fig. I.5 Mass flow Vs. Coolant chamber pressure for a 30° hole Inclination angle model.....	190
Fig. I.6 Coolant Cd Vs. Coolant Reynolds number for a 30° hole Inclination angle model.....	191
Fig. I.7 Mass flow Vs. Coolant chamber pressure for a 35° hole Inclination angle model.....	192
Fig. I.8 Coolant Cd Vs. Coolant Reynolds number for a 35° hole Inclination angle model.....	193
Fig. I.9 Mass flow Vs. Coolant chamber pressure for Circular Hole model	194
Fig. I.10 Coolant Cd Vs. Coolant Reynolds number for Circular Hole Model	195
Fig. I.11 Mass flow Vs. Coolant chamber pressure for Fan Shaped Hole Model	196
Fig. I.12 Coolant Cd Vs. Coolant Reynolds number for Fan Shaped Hole Model ..	197
Fig. I.13 Mass flow Vs. Coolant chamber pressure for 0 and 45° Hole Orientation Angle model.....	198
Fig. I.14 Coolant Cd Vs. Coolant Reynolds number for 0 and 45° Hole Orientation Angle model.....	199

Fig. I.15 Mass flow Vs. Coolant chamber pressure for 15 and 30° hole Orientation angle model.....	200
Fig. I.16 Coolant Cd Vs. Coolant Reynolds number for 15 and 30° hole Orientation angle model.....	201
Fig. II.1 Heat Loss vs. Voltage for 30° HOA Model.....	202
Fig. II.2 Heat Loss Vs. Voltage for 45° HOA Model.....	203
Fig. II.3 Voltage Drop Vs. Current for 30° HOA Model.....	204
Fig. II.4 Voltage Drop Vs. Current for 45° HOA Model.....	204
Fig. III.1 Infra Red Thermal Camera A 655sc.....	206
Fig. III.2 Calibration curve to convert temperature to raw counts.....	208
Fig. III.3 Calibration curve to convert raw counts to temperature.....	209

LIST OF TABLES

Table 3.1 Blade LE model specifications	46
Table 3.2 Range, Resolution and Accuracy of instruments used	61
Table 3.3 Experimental test conditions for adiabatic film cooling effectiveness measurements.....	65
Table 3.4 Experimental test conditions for heat transfer coefficient measurements .	68
Table 4.1 Boundary conditions	75
Table 6.1 Brief conclusions	173
Table I.1 Coolant flow hole Cd for a 20° hole Inclination angle model.....	186
Table I.2 Coolant flow hole Cd for a 25° hole Inclination angle model.....	188
Table I.3 Coolant flow hole Cd for a 30° hole Inclination angle model.....	190
Table I.4 Coolant flow hole Cd for a 35° hole Inclination angle model.....	192
Table I.5 Coolant flow hole Cd for Circular Holes Model	194
Table I.6 Coolant flow hole Cd for Fan Shaped Holes Model	196
Table I.7 Coolant flow hole Cd for 0 and 45° Hole Orientation Angle Model	198
Table I.8 Coolant flow hole Cd for 15 and 30° Hole Orientation Angle Model	200
Table IV.1 Range, Resolution and Accuracy of instruments used	210

NOMENCLATURE

A	-	area (mm ²)
C	-	coefficient
D	-	leading edge diameter (mm)
d	-	hole diameter (mm)
E	-	voltage drop (volts)
h	-	heat transfer coefficient (W/m ² K)
I	-	current supplied (Amps)
K	-	thermal conductivity (W/mK)
L	-	length (mm)
M	-	total mass flow (kg/sec), Model
m	-	mass flow per unit area (kg/ m ² s)
P	-	pressure (kPa)
p	-	pitch (mm)
q	-	electrical heat input (Watt)
T	-	temperature (K)
V	-	Voltage
<i>v</i>	-	velocity (m/s)
W	-	width of stainless steel sheet (mm)
X	-	streamwise distance (mm)

Greek Symbols

ρ	-	density (kg/m ³)
η	-	film cooling effectiveness
μ	-	dynamic viscosity (Ns/m ²)
λ	-	wavelength (m)
Δ	-	differential
ω	-	uncertainty

Sub-Scripts

1, 2	-	inlet conditions, outlet conditions
c	-	coolant
d	-	discharge
m	-	mainstream
w	-	wall
up	-	upstream
down	-	downstream

Abbreviations

B.R	-	Blowing Ratio
CFD	-	Computational Fluid Dynamics
CHM	-	Circular Hole Model
DAQ	-	Data Acquisition System
Del.	-	Delta
D.R	-	Density Ratio
Exp.	-	Experimental
FSHM	-	Fan Shaped Hole Model
HIA	-	Hole Inclination Angle
HOA	-	Hole Orientation Angle
HP	-	Hole Pitch
HS	-	Hole Shape
HTC	-	Heat Transfer Coefficient
IR	-	Infra Red
LE	-	Leading Edge
LFSM	-	Laidback Fan Shaped Hole Model
NHFR	-	Net Heat Flux Ratio
Num.	-	Numerical
RIT	-	Rotor Inlet Temperature
RPT	-	Rapid Proto Typing
Temp.	-	Temperature

CHAPTER 1

INTRODUCTION

1 INTRODUCTION

Thermal efficiency and power output of the gas turbine engine increase with the increase in turbine inlet temperature (TIT). Increasing the turbine inlet temperature is one of the key technologies in raising gas turbine engine performance (Je-Chin 2012). As the turbine inlet temperature increases, the heat transfer to the turbine blades also increases. At the higher temperatures, blade materials may start to melt, or high thermal stresses may occur. Thus, to maintain an acceptable life and safety standards, the turbine blades need to be protected against the severe thermal environment. Hence, there is a critical need to cool the turbine blades and other turbine components for safe and reliable operation. The gas turbine blades need an optimized cooling by using the compressor bleed air without compromising on the overall engine efficiency. Gas turbine vanes and blades are cooled internally and externally to increase the thermal performance at higher power outputs. Internal cooling is achieved with the extraction of heat from outside of the blades by passing the coolant through several enhanced serpentine passages inside of the blades. Both jet impingement and pin-fin cooling are also used as a method of internal cooling. External cooling also called film cooling is achieved, with the internal coolant air is ejected out through discrete holes or slots to provide a coolant film to protect the outside surface of the blade from hot gases.

The gas turbine vane leading edges are the critical parts in the turbines as the hot gases directly hit them. Hence the optimized cooling of gas turbine blade leading edge surfaces is very important. Film cooling is one of the efficient cooling techniques to cool the hot section components of a gas turbine engines. Film cooling method of hot section components in the gas turbine engines is under continuous optimization for the enhanced cooling performance. Film cooling is typically applied on the leading edges of the turbine blades through showerhead holes. Optimized cooling of the leading edge region is essential due to the high thermal loads with the near stagnant mainstream conditions. The secondary air from the compressor is routed through the cooling holes in the turbine blades. It forms a protective layer on the blade to prevent the direct contact of hot air with the blade. The life of the blades and the efficiency of

the turbine increases with the increase of cooling effectiveness. Hence, Film cooling research of hot section components of gas turbine engines is under continuous optimization for the enhanced cooling performance.

Gas turbine engines mainly consist of three major components, i.e., compressor, the combustion chamber (or heat exchanger) and turbine. Generally, aero gas turbine engines usually operate on an open cycle like as shown in Fig. 1.1. Fresh air at ambient conditions is drawn into the compressor, where it is compressed to a pressure and temperature. The high pressure air proceeds into the combustion chamber, where the fuel is burned at constant pressure. The resulting high-temperature and high pressure gases enter the turbine, where they expand to the atmospheric pressure while producing power. The exhaust gases leaving the turbine are exhausted to the atmosphere, causing the cycle to be classified as an open cycle.

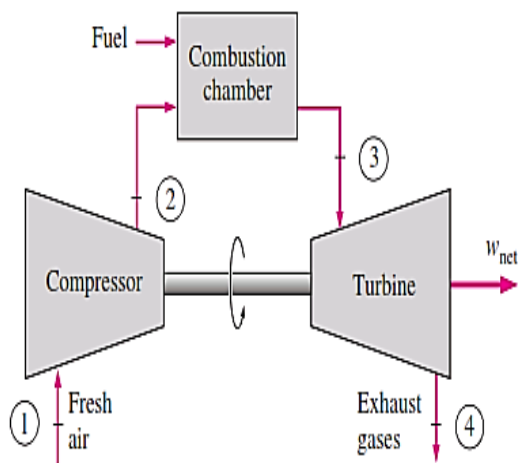


Fig. 1.1 Simple open cycle gas turbine engine

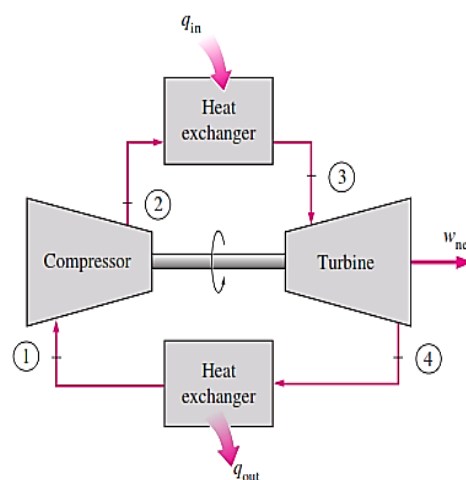


Fig. 1.2 Simple closed cycle gas turbine engine

Source: <http://sounak4u.weebly.com/gas-power-cycle.html>

The open cycle gas turbine engine described above can be modified as a closed cycle, as shown in Fig. 1.2 by utilizing the air-standard assumptions. Here the compression and expansion remain the same, but a constant pressure heat addition process replaces the combustion process from the external heat source, and the exhaust process is replaced by constant pressure heat rejection process to the ambient air. The ideal cycle

with the four internally reversible processes, where the working fluid changes this closed loop is the Brayton cycle. Fig. 1.3 shows the P-V and T-S plots of the Brayton cycle. The typical turboprop gas turbine engine with the details of major parts is shown in the Fig. 1.4.

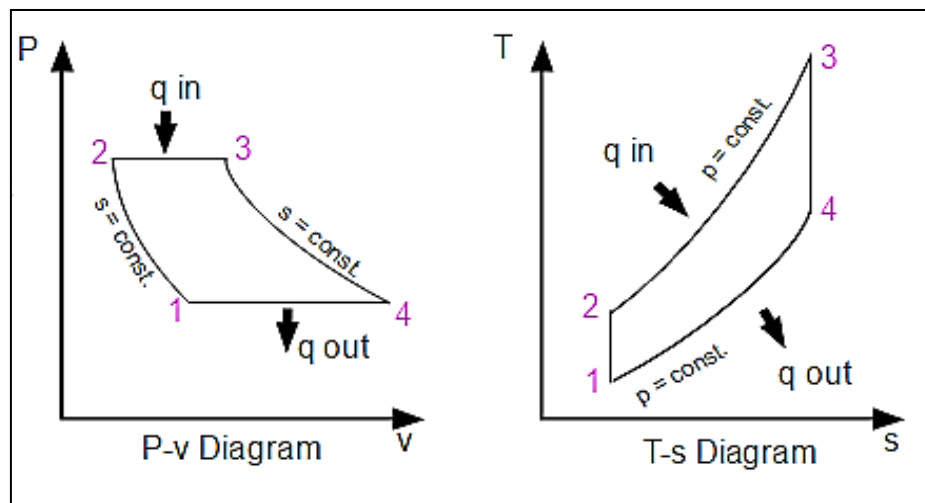


Fig. 1.3 P-V and T-S diagram of a simple gas turbine

Source: https://en.wikipedia.org/wiki/Brayton_cycle

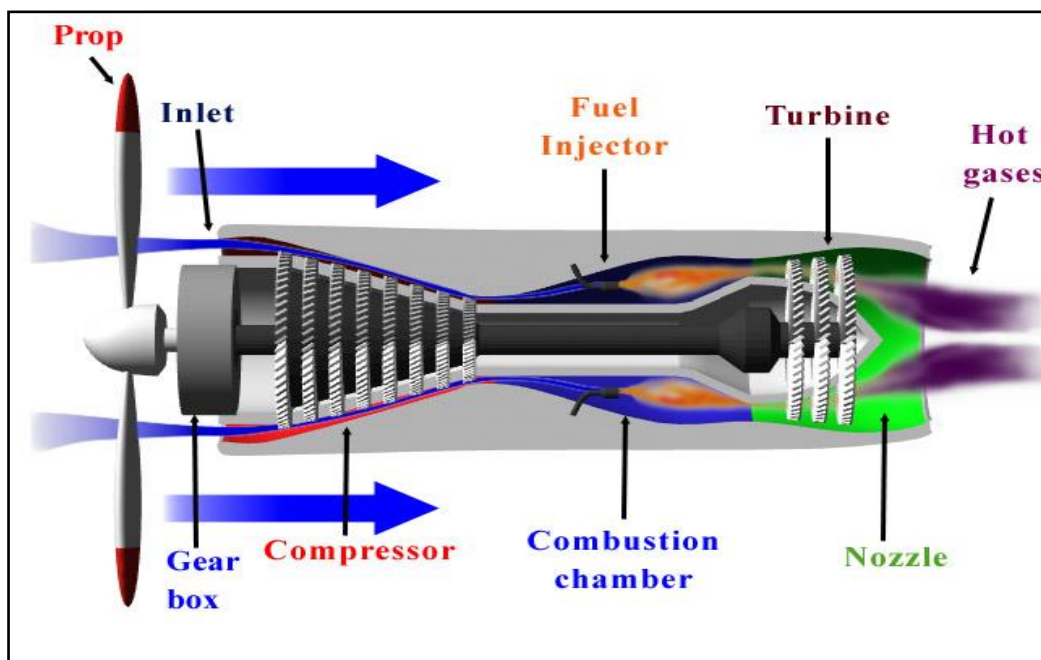


Fig. 1.4 Typical turboprop gas turbine engine

Source: <https://www.quora.com/Aerospace-and-Aeronautical-Engineering>

In the gas turbine engines, the turbine section produces the usable output shaft power to drive the propeller. The turbine also provides the additional power to drive the compressor and other engine accessories. This is done by expanding the high temperature and pressure gas by converting the gaseous thermal energy to mechanical shaft power. Turbine utilizes a large amount of air supplied by the compressor to produce the necessary power. The air supplied by the compressor, which draws the air from the atmosphere and supplies it to the combustion chamber and thereby to the turbine. The combustion takes place in the combustion chamber with the supplied air supplied by compressor and fuel spray and thereby this high pressure, and temperature air is expanded in the turbine. If the gas turbine engine is a perpetual machine, then all the air supplied by the compressor will be utilized by the turbine and the power developed by the turbine will be fully utilized by the compressor without any losses. However, there is always existence of the frictional and heat losses, which does not allow the system as perpetual. The additional energy is required to be added to the air to accommodate for these losses. The power output is the essential requirement from the engine (apart from simply driving the compressor); hence the more energy must be added to the air to produce this excess power. The energy addition is accomplished in the combustor to the system. The chemical energy from fuel is converted to heat energy by combustion in the form of high temperatures, and high pressure as the air passes through the combustor. The heat energy is converted back to mechanical energy in the turbine, providing power to drive the compressor and the output shaft.

1.1 Need for Turbine Blade Cooling

In today's modern world the gas turbine engines are operated with higher turbine inlet temperatures in the range of 1200-1800 °C in a different application like aircraft and land-based power plants. So, the materials used for gas turbine blades have to withstand these high temperatures without any thermal stresses and burnouts for the long life and safe operation. In another side, the efficiency and output power of gas turbine engines increase with the increasing turbine rotor entry temperatures as shown in Fig. 1.5. Gas turbine engine performance increases as the inlet temperature to the

turbine increases. Fig. 1.6 and Fig. 1.7 show the increase in rotor entry temperatures in advanced gas turbine engines with the various blade cooling techniques.

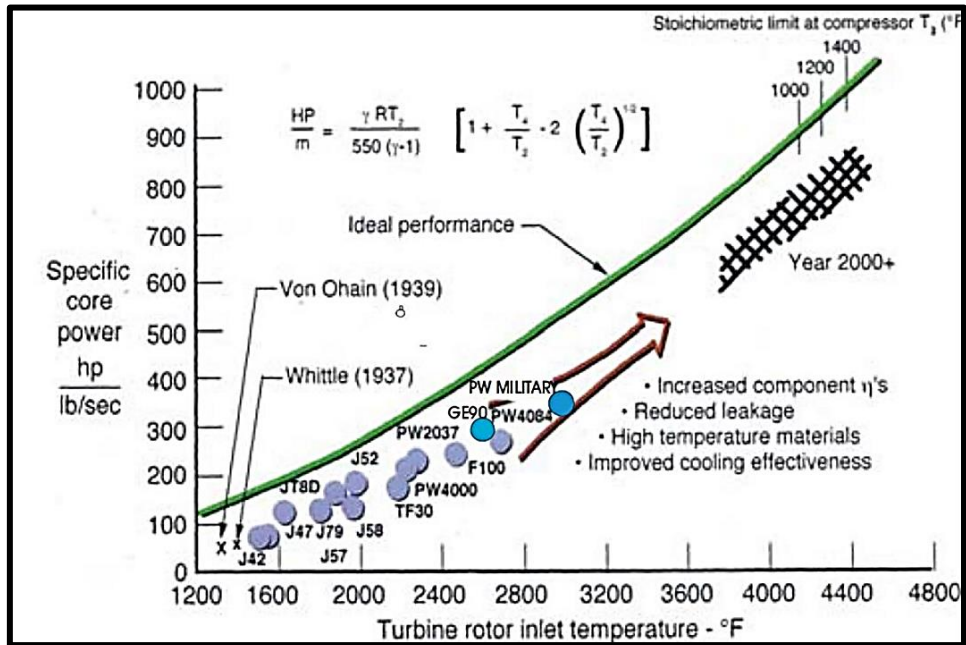


Fig. 1.5 Effect of RIT on power output

Source: (Je-Chin et al. 2012)

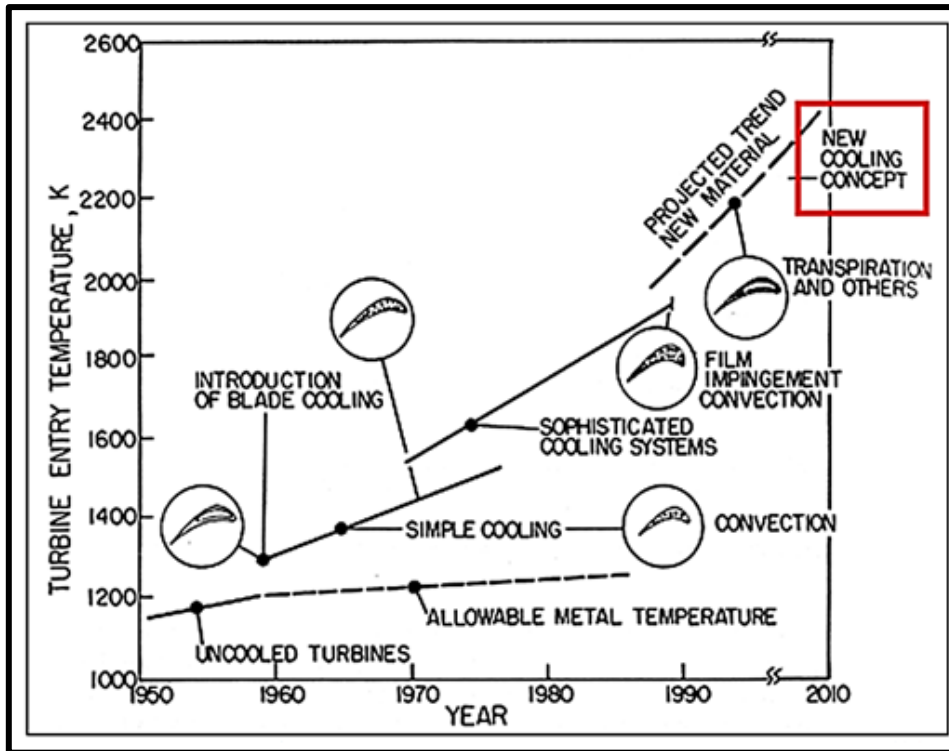


Fig. 1.6 Variation of turbine entry temperature over the years

Source: (Lakshminarayanan 1996)

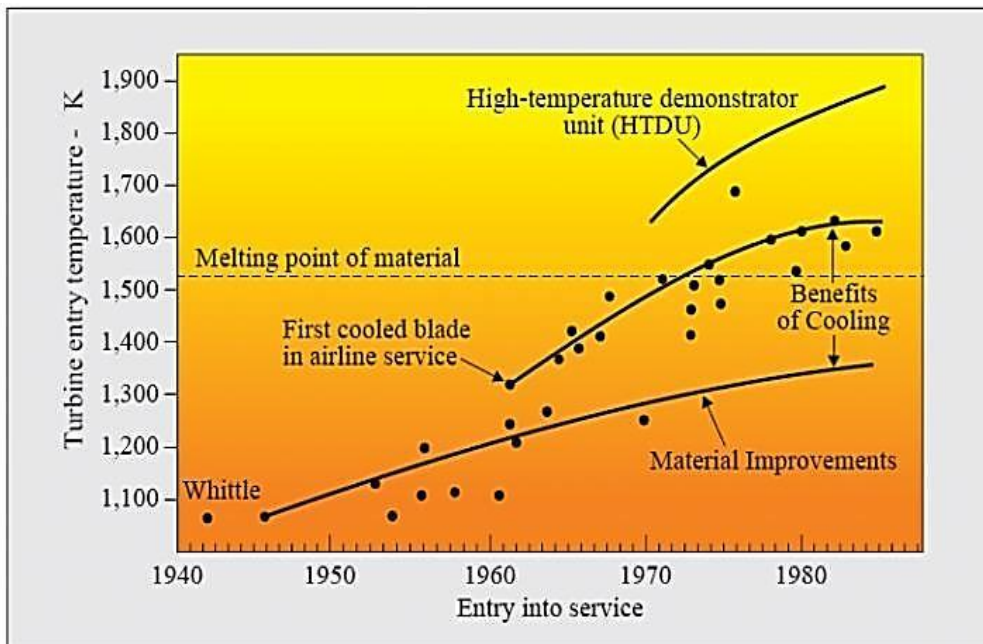


Fig. 1.7 Development of turbine inlet temperature

Source: (Yiping et al. 2007)

1.2 Blade Cooling Classification

Gas turbine blade cooling is classified as

1) External Cooling

- a) Convection Cooling
- b) Transpiration Cooling
- c) Film Cooling

2) Internal Cooling

- a) Impingement Cooling
- b) Pin-Fin Cooling
- c) Rib Turbulated Cooling

The various external and internal cooling techniques used in the gas turbine engine blades for achieving the higher thrust are shown in Fig. 1.8. the detailed external cooling and internal cooling regions are shown in the Fig. 1.9 and Fig. 1.10.

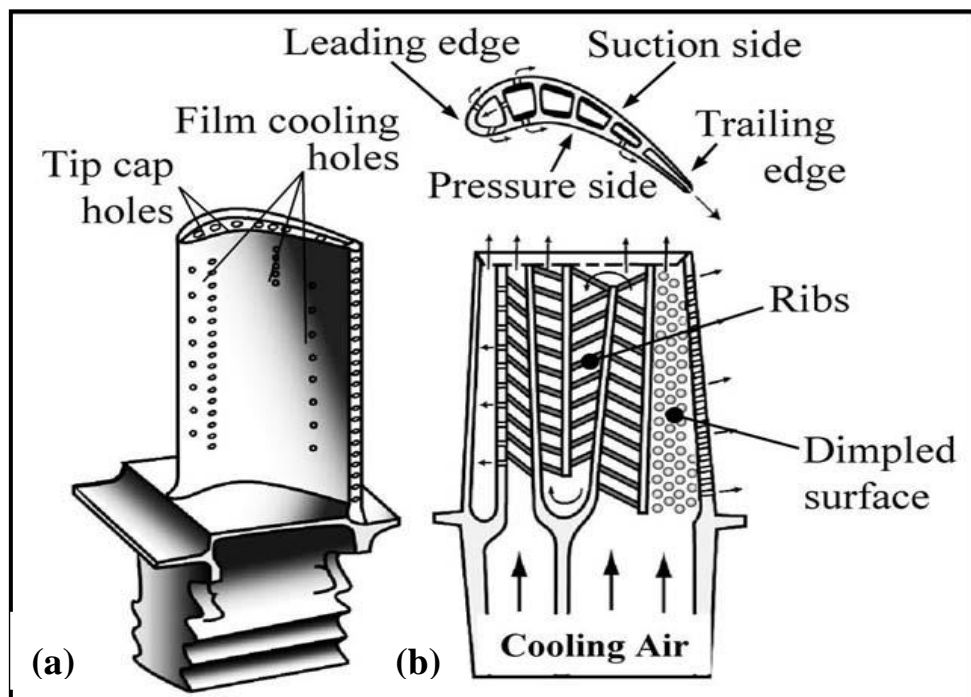


Fig. 1.8 Schematic of GT blade cooling (a) External (b) Internal

Source: (Robert et al. 2001)

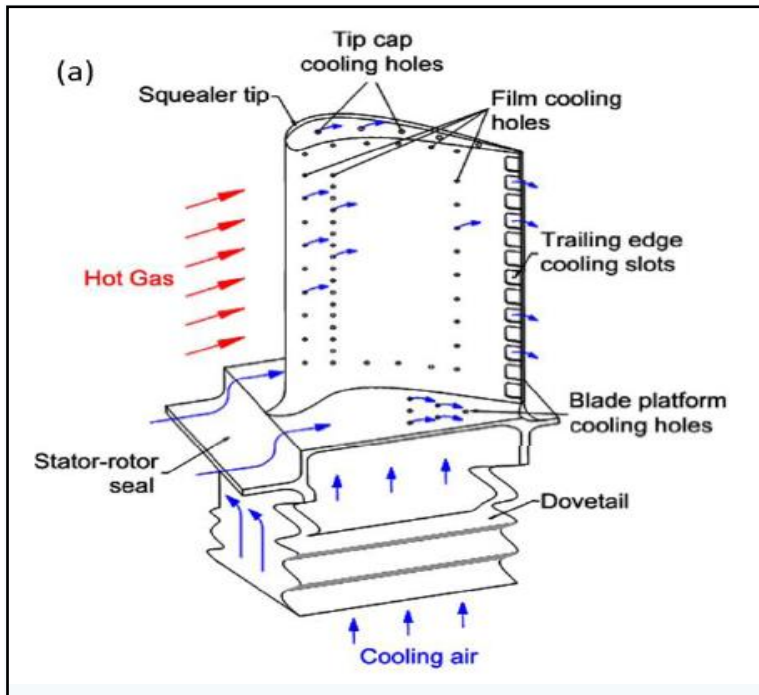


Fig. 1.9 Gas turbine blade external cooling region.

Source: (Je-Chin and Akhilesh 2010)

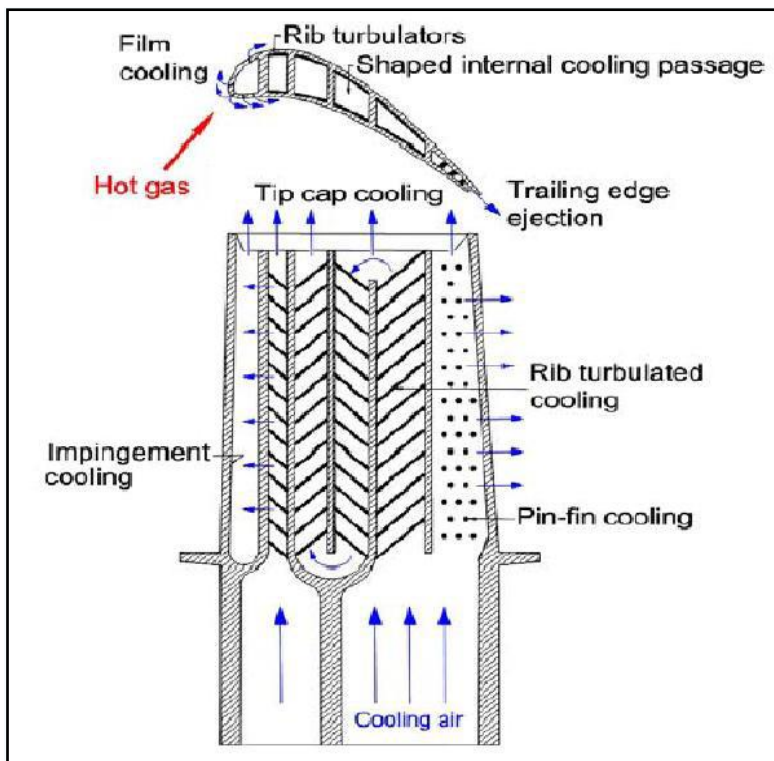


Fig. 1.10 Schematic of different internal cooling regimes.

Source: (Je-Chin and Akhilesh 2010)

1.2.1 External cooling

Ceramic Thermal Barrier Coating (TBC) is applied over the blade surfaces, which protects the external surfaces exposed to the hot gases along with the film of cold air. These are used when the stream temperature is above 1800 K along with the internal cooling. 1 to 3% of the compressed air is used for this purpose of cooling. Approximately around 200 – 300 K metal temperature can be reduced by using suitable blade material.

1.2.1.1 Convection cooling

It is the simplest and first turbine cooling method used. With convection cooling, the coolant (air) flows from the base of the turbine blade to the end through an internal passage within the blades. The effectiveness of cooling is limited by the size of the internal passage within the blade and restriction on the quantity of cooling air available.

Major disadvantages of this technique are,

- A large amount of cooling air required.
- This method failed to cool the thin trailing edge of the blade effectively. Since it is so thin, no cooling air passed through this portion of the blade.

1.2.1.2 Transpiration cooling

Transpiration cooling is the most efficient air cooling technique available this is sometimes referred to as full blade cooling. This method involves the use of a porous material through which the cooling air is forced into the boundary layer to form relatively cooling, insulation film or layer. The transpiration cooling technique is shown in the Fig. 1.11.

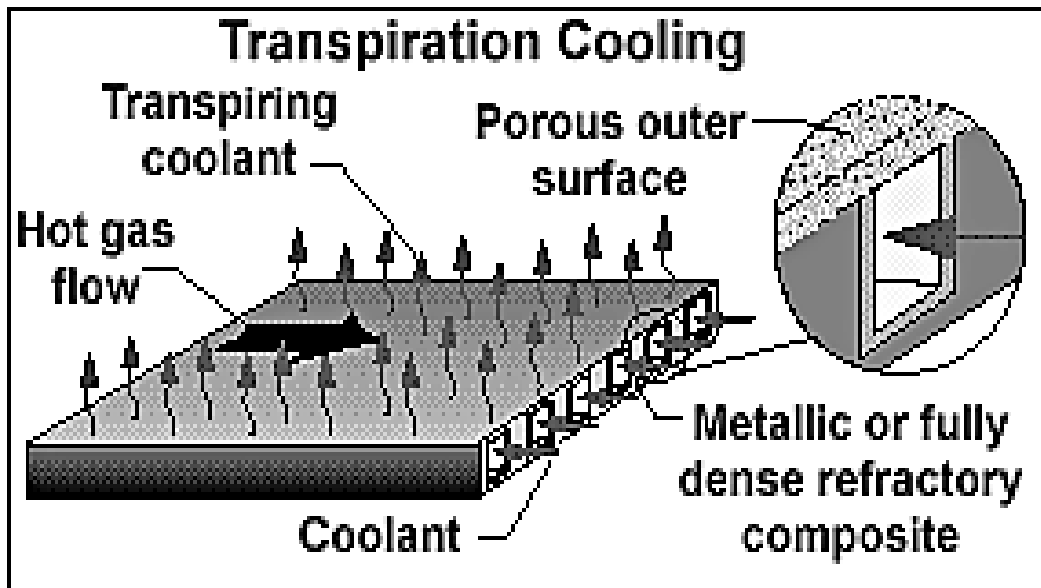


Fig. 1.11 Transpiration cooling

Source: <http://www.infrared-thermography.com/glossary2.htm>

1.2.1.3 Film cooling

Film cooling involves an injection of secondary air into the boundary layer of the primary fluid hot gas. This is an effective way to protect the surface from the hot gases by directing the cooling air into the boundary layer to provide protection, cold film along the surface. The cold air comes through the film holes and forms a protective layer over the downstream surface. This thin layer insulates the external surface of the blade from the hot air. The film cooling technique with cooling holes at the leading, mid-chord region and trailing edge is shown in Fig. 1.12.

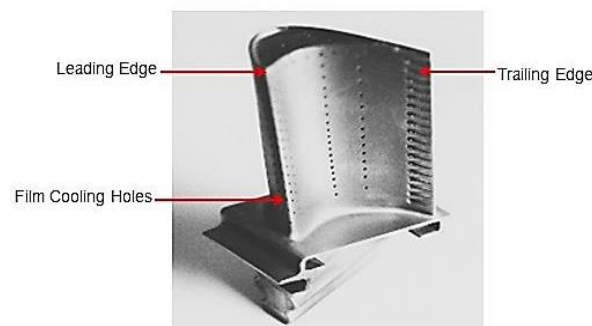


Fig. 1.12 Film cooling

Source: <http://www.me.umn.edu/labs/tcht/measurements/what.html>.

Film cooling is more efficient than normal convection cooling or impingement cooling. The cooling air absorbs energy as it passes inside the blades and through the holes, then further reduces the metal temperature by reducing the amount of energy transferred from the hot gases to blades.

At the leading edge region of the vanes, the mainstream flow strikes the vane with near stagnant flow conditions at the leading edge hub and the main flow will spread more towards the tip region. Due to this generally, the spanwise shaped holes are used on the leading edge region and the streamwise shaped holes are used on the pressure and suction sides of the vanes. This type of holes arrangement is seen in the published data and on the Pratt & Whitney cooling configurations. The typical arrangement of these holes can be seen in the Fig. 1.13.

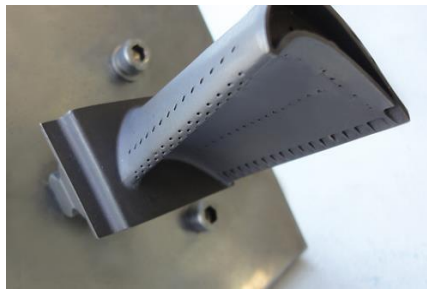


Fig. 1.13 Spanwise film cooling holes on leading edge

Source:http://d2n4wb9orp1vta.cloudfront.net/resources/images_RT_turbine-blade.jpg

1.2.2 Internal cooling

The outer surface is protected by the internal cooling channels located below the outer surface. This secondary air extracts the heat from the surface by acting as a heat sink. Whenever the temperature of the external stream is high (> 1800 K), internal cooling is employed.

1.2.2.1 Impingement cooling

This is a form of convection cooling which removes the heat by impinging the air on the inner surfaces of the aerofoil. The impingement cooling technique used in the turbine blade to cool the inner surface is shown in the Fig. 1.14.

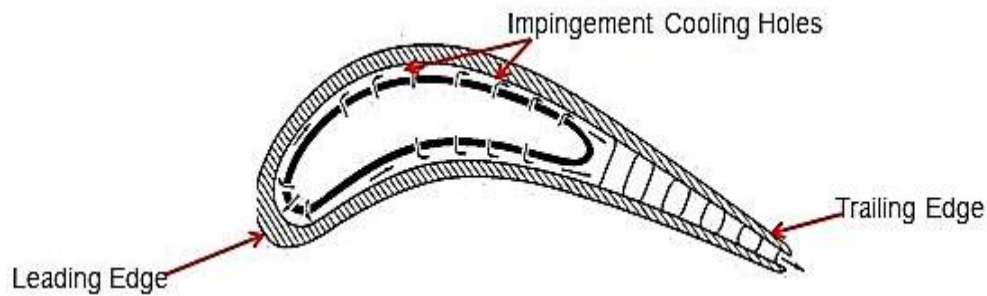


Fig. 1.14 Impingement cooling

Source: (Florschuetz et al. 1984)

1.2.2.2 Pin-fin cooling

The convective surface area is increased by using the short pin fins with a very high aspect ratio between 16:1 and 4:1. The convective surface promotes the higher heat transfer in the channels. The structural integrity of the inner surfaces will also be increased with the pin-fins along with the increase in cooling effectiveness. A typical pin-fin arrangement is shown in the Fig. 1.15. Pin-fin cooling is mostly used in the trailing edge regions of the gas turbine blades.

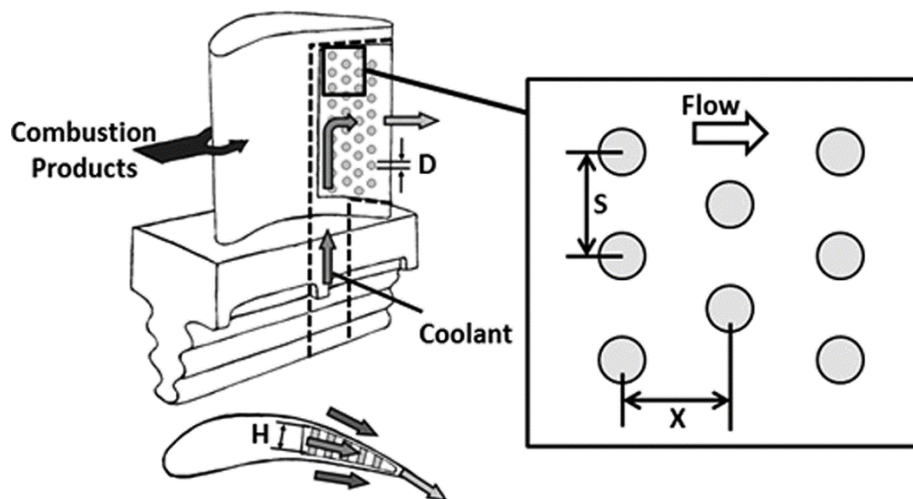


Fig. 1.15 Pin-Fin cooling

Source: (Jason 2014)

1.2.2.3 Rib Turbulated Cooling

To enhance the heat transfer in a modern gas turbine blades, the rib turbulators are cast on the opposite side walls of internal coolant passages. The blade internal coolant

passages are modeled as short, square or rectangular channels with various aspect ratios. The heat transfer augmentation in rectangular coolant passages with rib turbulators primarily depends on the rib turbulators geometry, such as rib size, shape, distribution, and flow attack angle, and the flow Reynolds number. Rib turbulators disturb only the near-wall flow for heat transfer enhancement.

1.3 Fundamentals of Film Cooling

Film cooling involves an injection of cold fluid into the boundary layer of the primary fluid hot gas. The airfoil surfaces are protected using the film cooling air which removes heat from the blade surface by convection. The thermal protection provides the reduced heat load to the airfoil surface. To estimate the heat loads on the surface, it is needed to know about the local wall temperature and the gas side heat transfer coefficients with the film injection.

The coolant to mainstream temperature and pressure ratios and the film cooling hole location, configuration, and distribution on a film cooled holes on airfoil are the important geometrical parameters, decides the film cooling effectiveness.

The coolant to mainstream temperature ratio can be related to the density ratio, and the pressure ratios can be related to the blowing ratios.

In a typical gas turbine airfoil, the temperature ratio varies from 0.5 to 0.85, corresponding density ratios approximately from 2.0 to 1.5 and the pressure ratios vary from 1.02 to 1.10, corresponding blowing ratios of approximately from 0.5 to 2.0 with the film cooling air. Fig. 1.16 shows the geometry of the film cooling and heat transfer model associated with it.

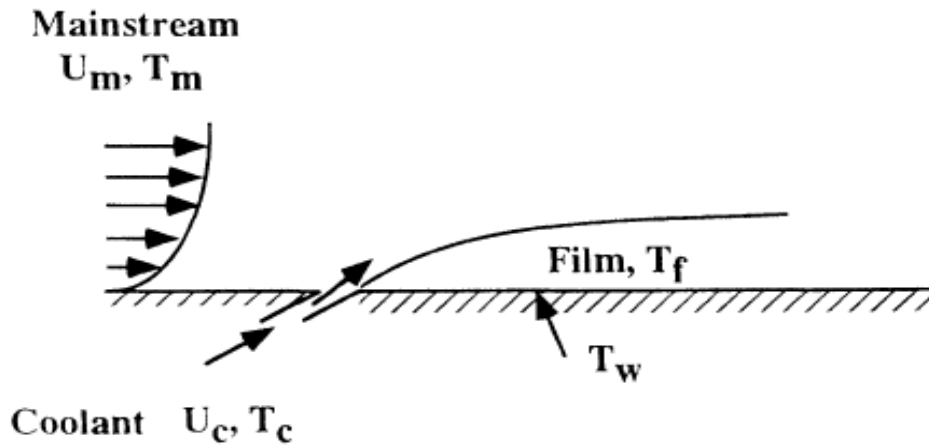


Fig. 1.16 Film cooling concept

Source: (Je-Chin and Srinath 2001)

Typically, the heat flux is represented as heat load to the surface without film cooling,

$$q = h_o(T_g - T_w) \quad (1.1)$$

Where,

h_o = surface heat transfer coefficient. $W/m^2 K$

T_g = gas temperature in K

T_w = wall temperature in K

The film temperature when is the combination of gas (T_g) and coolant temperature (T_c) which is the driving film temperature.

$$q = h(T_f - T_w) \quad (1.2)$$

Where,

$h = h_o$ is the heat transfer coefficient on the surface, $W/m^2 K$

T_f = film temperature in K

T_w = wall temperature in K

Adiabatic Film Cooling Effectiveness,

$$\eta = \frac{(T_g - T_f)}{(T_g - T_c)} \quad (1.3)$$

Where,

T_g = gas temperature in K

T_f = film temperature in K

T_c = coolant temperature in K

1.3.1 Blowing Ratio (B.R)

Blowing ratio is one of the most important parameters in film cooling, and it is defined as the ratio of coolant mass flux ratio to the mainstream mass flux ratio.

$$B. R = \frac{\rho_c V_c}{\rho_m V_m} \quad (1.4)$$

Where,

ρ_c = Coolant Density in kg/m^3

ρ_m = Mainstream Density in kg/m^3

v_c = Coolant Velocity in m/s

v_m = Mainstream Velocity in m/s

1.3.2 Density Ratio (D.R)

Density ratio is defined as it is the ratio of coolant density to mainstream density and it can be related to mainstream to coolant temperature ratio.

$$D. R = \frac{\rho_c}{\rho_m} = \frac{\left(\frac{p_c}{RT_c}\right)}{\left(\frac{p_m}{RT_m}\right)} = \frac{T_m}{T_c} \quad (1.5)$$

Where,

T_c = Coolant Temperature in K

T_m = Mainstream Temperature in K

p_c = Coolant Pressure in Pa

p_m = Mainstream Pressure in Pa

R = Characteristic Gas Constant in J/kg K

1.4 Heat Transfer Coefficients Concept

Heat transfer coefficient is calculated by using the following relation for all the models at the blowing ratios of 1.0, 1.50 and 2.0. Here, the heat transfer coefficient (h) is calculated from the net heat flux, $q = Q/A$, i.e., the net heat input per unit surface area of the plate.

Net Heat Input,

$$Q = hA\Delta T = Q_{gen} - Q_{loss} \quad (1.6)$$

Net Heat Flux,

$$q = \frac{Q}{A} = \frac{Q_{gen}}{A} - \frac{Q_{loss}}{A} \quad (1.7)$$

Heat transfer coefficient can be calculated as,

$$h = \frac{q}{(T_w - T_m)} = \frac{q_{gen} - q_{loss}}{(T_w - T_{aw})} \quad (1.8)$$

Where,

h - Heat transfer coefficient in $w/m^2 K$

q - Net local convective heat flux on the foil surface in w/m^2

q_{gen} - Surface generated heat flux from voltage-current measurement in w/m^2

q_{loss} - Local heat loss and is a function of the local wall temperature w/m^2

T_w - Local steady state foil temperature (local wall temperature) in K

T_{aw} - Local adiabatic wall temperature in K.

T_m - Mainstream temperature in K

1.5 Introduction to CFD

The partial differential equations govern the fluid (gas and liquid) flows in differential equations which represent conservation laws for the mass, momentum, and energy. Computational Fluid Dynamics (CFD) is the set of algebraic equations which can be solved using digital computers. This is very powerful and has a wide range of applications in almost all the fields.

1.5.1 How Does CFD Works

The fluid flow problems can be handled easily with the structured CFD codes. CFD packages include sophisticated user interfaces to input problem parameters and to examine the results. The CFD codes contain three main parts namely a pre-processor, a solver and a post-processor.

1.5.1.1 Pre-processor

Pre-processing consists of the input of a flow problem to a CFD program using an operator-friendly interface and the subsequent transformation of this input into a form suitable for use by the solver. The user activities at the pre-processing stage involve:

- Geometry Definition with the region of interest.
- Generation of Grid with the sub-division of the domain into some smaller elements or cells.
- Physical and chemical phenomena selection.
- Fluid properties definition.
- Boundary conditions specifications

1.5.1.2 Solver

Different solvers with the finite difference, finite element, and spectral methods can be used with three distinct streams of numerical solution techniques. The numerical methods of the solver perform the following steps:

- Unknown parameters approximation by using simple functions.
- Discretization of the problem using the governing flow equations and subsequent mathematical manipulations.
- Solving the algebraic equations for the results.

1.5.1.3 Post Processing

As in pre-processing a huge amount of development work has recently taken place in the post-processing field. Owing to the increased popularity of engineering

workstations, many of which have outstanding graphics capabilities, the leading CFD packages are now equipped with versatile data visualization tools. These include:

- Geometry domain geometry and Display of grid.
- Plotting of vectors.
- 2D and 3D surface plots.
- View generation and manipulation.
- Output values generation

1.5.2 Governing Equations of Fluid Flow and Heat Transfer

Various governing equations based fluid flows using the conservation laws are formed. These equations are used based on the following properties.

- The mass of fluid is conserved.
- The rate of change of momentum equals the sum of the forces on a fluid particle (Newton second law).
- The sum of the rate of heat addition to and the rate of work done on a fluid particle (First law of thermodynamics) is equal to the rate of change of energy.

1.5.2.1 Mass Conservation Equation in Three Dimensions

To write down a mass balance for the fluid element is the first step in deriving the equation of mass conservation equation.

The rate of increase of mass in fluid element = Net rate of work done on the fluid element + Net rate of flow of mass into the fluid element.

The rate of increase of mass inside the element is now equated to the net rate of flow of mass into the element across its faces. All terms of the resulting mass balance are arranged on the left-hand side of the equals sign, and the expression is divided by the element volume $\delta x \delta y \delta z$. These equations in the vector notation form are,

$$\frac{\partial \rho}{\partial t} + \text{div}(\rho u) = 0 \quad (1.9)$$

Above Equation is the unsteady, three-dimensional mass conservation or Continuity equation at a point in a compressible fluid. The first term on the left-hand side is the rate of change in time of the density (mass per unit volume). The Second term describes the net flow of mass out of the element across its boundaries and is called the convective term.

For incompressible fluids (i.e., a liquid) the density ρ is constant, and the equation becomes,

$$\text{div}(\rho u) = 0 \quad (1.10)$$

Or in longhand notation,

$$\frac{\partial u}{\partial x} + \frac{\partial v}{\partial y} + \frac{\partial w}{\partial z} = 0 \quad (1.11)$$

1.5.2.2 Three dimensional Energy Equation

The first law of thermodynamics states that the rate of change of energy of a fluid particle is equal to the rate of heat added to the fluid particle plus the rate of work done on the particle which is used in the derivation of the energy equation.

The rate of increase of fluid particle = Net rate of work does on fluid particle + Net rate of heat added to the fluid particle.

Energy equation is,

$$\begin{aligned}
\rho \frac{DE}{Dt} = & -div(\rho u) + \left[\frac{\partial(u\tau_{xx})}{\partial x} + \frac{\partial(u\tau_{yx})}{\partial y} + \frac{\partial(u\tau_{zx})}{\partial z} + \frac{\partial(v\tau_{xy})}{\partial x} \right. \\
& + \frac{\partial(v\tau_{yy})}{\partial y} + \frac{\partial(v\tau_{zy})}{\partial z} + \frac{\partial(w\tau_{xz})}{\partial x} + \frac{\partial(w\tau_{yz})}{\partial y} \\
& \left. + \frac{\partial(w\tau_{zz})}{\partial z} \right] + div(k grad T) + S_E
\end{aligned} \tag{1.12}$$

1.5.2.3 Navier- Stokes Equations for a Newtonian Fluid

In many fluid flows, the viscous stresses can be expressed as functions of the local deformation rate (or strain rate). In three-dimensional flows, the local rate of deformation is composed of the linear deformation rate and the volumetric deformation rate as explained in the following equations.

$$\rho \frac{Du}{Dt} = -\frac{\partial p}{\partial x} + div(\mu grad u) + S_{Mx} \tag{1.13}$$

$$\rho \frac{Dv}{Dt} = -\frac{\partial p}{\partial y} + div(\mu grad v) + S_{My} \tag{1.14}$$

$$\rho \frac{Dw}{Dt} = -\frac{\partial p}{\partial z} + div(\mu grad w) + S_{Mz} \tag{1.15}$$

1.5.2.4 Momentum Equation in Three Dimensions

Newton's second law states that the rate of change of momentum of a fluid particle equals to the sum of the forces acting on the particle,

$$\begin{aligned}
& \text{The rate of increase of mass in fluid particle} \\
& = \text{Sum of forces acting on the fluid particle}
\end{aligned}$$

We distinguish two types of forces on fluid particles as,

Surface forces - pressure forces and viscous forces.

Body forces - gravity force, centrifugal force, Coriolis force, etc.

X -Momentum sources,

$$\rho \frac{Du}{Dt} = \frac{\partial(-p + \tau_{xx})}{\partial x} + \frac{\partial\tau_{yx}}{\partial y} + \frac{\partial\tau_{zx}}{\partial z} + S_{Mx} \quad (1.16)$$

Y- Component,

$$\rho \frac{Dv}{Dt} = \frac{\partial\tau_{xy}}{\partial x} + \frac{\partial(-p + \tau_{yy})}{\partial y} + \frac{\partial\tau_{zy}}{\partial z} + S_{My} \quad (1.17)$$

Z- Component,

$$\rho \frac{Dw}{Dt} = \frac{\partial\tau_{xz}}{\partial x} + \frac{\partial\tau_{yz}}{\partial y} + \frac{\partial(-p + \tau_{zz})}{\partial z} + S_{Mz} \quad (1.18)$$

1.5.3 Turbulence Models

Fluctuating velocity fields characterize turbulent flows. The momentum, energy, species concentration equations causing the transported quantities will fluctuate as well as fluctuations mix. The fluctuations can be of small-scale and high frequency, even when they are too computationally expensive to simulate directly in practical engineering calculations.

The following different turbulence models are generally used to solve the flow field problems.

1. Turbulence
2. RANS based turbulence models
 - a. Linear eddy viscosity model
 - i. Algebraic models
 - ii. One equation models
 - iii. Two equation models
 1. k-epsilon models
 2. k-omega models
 3. Realisability issues
 - b. Nonlinear eddy viscosity models
 - c. Reynolds stress model (RSM)
3. Large eddy simulation (LES)
4. Detached eddy simulation (DES)

5. Direct numerical simulation (DNS)
6. Turbulence near-wall modeling
7. Turbulence free stream boundary conditions

After understanding the many aspects of a cooling system for the gas turbine engines, it is decided to study the critical flow and geometrical parameters for the enhancement of engine performance by going through the detailed literature survey. Enhancement of gas turbine engine power mainly depends upon the withstanding capacity of hot section components. Hence, the hot section components of the gas turbine engines need the efficient and optimized cooling methodology without compromising on the performance of other engine components. The optimization of cooling concepts is a continuous study with the better geometrical and flow parameters. Hence, this study has taken up in this work.

1.6 Organization of the Thesis

The present thesis is organized into six chapters. Chapter 1 provides the introduction to the film cooling and heat transfer coefficient measurements over the gas turbine blade leading edge along with the concepts of experimental and CFD activities. This chapter also presents the details of the various flow and geometrical parameters involved in the film cooling technology. Chapter 2 provides the detailed literature survey conducted for the present study. The published data is reviewed thoroughly underlying the physics and fundamental phenomenon involved in the film cooling technology. This chapter also presents the research gap, the objectives, and scope of the work.

Chapter 3 presents the experimental rig setup, test models selection and fabrication, instrumentation details, experimental methodology and the validation of experimental data. Chapter 4 presents the CFD methodology, mesh details, selection of turbulence model and grid independence study.

Chapter 5 presents the detailed experimental and numerical results along with the detailed discussions on the results and trends. Chapter 6 presents the conclusions of the present study and the recommendations for the future work.

CHAPTER 2

LITERATURE REVIEW

AND

OBJECTIVES OF THE WORK

2. LITERATURE REVIEW AND OBJECTIVES OF THE WORK

2.1 Gas Turbine Blade Film Cooling Technology

To increase the thermal efficiency of the gas turbine engines, the inlet temperature must be increased and to increase the life of the engine blades; they need to be cooled. The cooling of the hot section components will allow more fuel burn and is useful to enhance the engine power. The cooling of the hot section components like turbine vanes, blades and combustion chamber liners need the optimization with a lesser amount of compressor bleed air. Hence, the cooling optimization study is a continuous research activity for the optimization of coolant hole geometrical parameters. Film cooling technology is one of the widely used cooling technologies for the turbine blades cooling. Several experimental and numerical types of research have been made on gas turbine blade film cooling. In the development of film cooling technology, comparison of turbine vane effectiveness with and without film cooling has been made; the comparison indicated that film cooling had adverse effect near the suction surface trailing edge of the vanes. Film cooling was found to be beneficial to the cooling of the pressure surface of the vanes (Frederic et al. 1974).

The shaped injection holes were used for improving film cooling performance. They used the 10° spanwise diffused holes with a single row on flat plates. They found that the shaped hole provides better film cooling characteristics than the cylindrical hole because of the reduced momentum of the coolant jets attenuation and thus less penetration of the coolant into the mainstream (Goldstein et al. 1974).

To enhance the film cooling performance, multiple rows of holes are located at different angular locations from the stagnation line, and the hole in the rows was angled normal to the flow direction (Francis and Raymond 1983).

Surface flow visualizations show that the increase in the orientation angle results in better film coverage, especially in the spanwise direction, but produces more flow disturbances such as flow reversal and recirculation. A near-wall flow model for the velocity ratio of 2.0 has been proposed from the visualizations. The strength of the downstream secondary flow strongly depends on the velocity ratio (Woo et al. 1997).

Density ratio does not affect film cooling effectiveness for injection through the porous strip when the effectiveness is expressed as the distance parameter. And for injection through holes, the film cooling effectiveness is strongly dependent on density ratio, so that this dependence certainly has to be accounted for performance analysis of film cooling. Film cooling effectiveness is dependent on an involved interaction of separation and reattachment of jets of injected fluid on the lateral spreading and the energy transfer between the jet and main flow (Pedersen et al. 1977).

For low blowing rates with cooling jets remaining attached to the wall, centerline effectiveness (η_c) scales with mass flux ratio and at high blowing ratios detachment reattachment of cooling jets become important. Laterally averaged effectiveness is strongly depending on the lateral spreading of the cooling jets. Decreasing density ratio and increasing moment flux ratio was found to reduce lateral spreading of film cooling jets and thereby reduces laterally averaged effectiveness (Sinha et al. 1991).

2.2 Historical Background of Film Cooling

The comparison of the cooling effect of turbine vanes with and without film cooling was studied. The cooling effect of three film cooled vanes, each with different internal cooling configurations, was investigated; the cooling effectiveness of two film cooled vanes was compared to the cooling effectiveness of two non-film cooled vanes of similar internal geometry. The results of the comparison indicated that, for the vane configurations and test conditions examined, near the suction surface trailing edge of the vanes film cooling had shown the adverse effect. And, the film cooling was found beneficial for the cooling of the pressure surface of the vanes (Frederic et al. 1974).

With the data obtained from NASA, the comparison of predicted and experimental external heat transfers around a film cooled cylinder in cross flow was made (Francis and Raymond 1983). The injection was from single and multiple rows of holes located at the different angular location from the stagnation line. The hole in the rows was angled normal to the flow direction and at 25° angle to the cylinder wall. The initial calculation for injection from single rows of holes at 5° and 22.9° from the stagnation line showed that in the experiment the injected flow did not trigger the

boundary layer into the turbulent regime downstream of the rows. This is concluded because the assumption of laminar flow in calculations gave the best agreement with the experimental heat transfer data.

The effects of free stream turbulence and coolant density on film cooling effectiveness over a leading edge model with the three rows of holes at lower blowing ratios were studied (Ekkad et al. 1998). From these studies, it was revealed that with the increase in turbulence intensity, heat transfer coefficient is enhanced over a smooth surface (without film holes) whereas, it has shown a small effect on heat transfer coefficients at all blowing ratios for both the light and dense coolants on a cooling holes model. However, higher free-stream turbulence reduces film effectiveness significantly at lower blowing ratios and has a little effect on film effectiveness at higher blowing ratios. Increase in coolant density causes a decrease in heat transfer coefficients at all the blowing ratios. Lesser density coolant (air) provides better effectiveness at low blowing ratios, and higher density coolant (CO₂) provides the highest effectiveness at medium blowing ratios. However, at even higher blowing ratios, an increase in coolant density has little effect on film effectiveness distributions.

The detailed Nusselt number and film effectiveness distributions are carried out on a cylindrical leading edge model with film cooling. The higher coolant density and higher free stream turbulence effects were studied. The heat transfer coefficients over the smooth surface (without film holes) found enhanced with the increase in turbulence intensity. The increase in blowing ratio has shown the increase in Nusselt numbers downstream of injection. The increase in coolant density had shown the decrease in heat transfer coefficients at all blowing ratios. Better cooling effectiveness was observed with air at lower blowing ratios. At higher blowing ratios, an increase in coolant density has little effect on film effectiveness distributions. Higher free-stream turbulence has only a small effect on Nusselt numbers at all blowing ratios for both coolants. However, higher free-stream turbulence reduces film effectiveness significantly at lower blowing ratios for both coolants but has little effect on film effectiveness at a blowing ratio of 1.2.

Three types of hole geometries, i.e., a cylindrical hole, fan shaped hole and laid back fan shaped holes were studied (Shuye and Je-Chin 2001). They have studied for one row of film cooling holes, that expanded holes show significantly improved thermal protection of the surface downstream of the ejection location as compared to the cylindrical hole. The hole geometries used in this experiments have the film hole diameter of 1.905 mm and 10.16 mm apart from one another ($P/D=5.3$) have a radial angle of 90° and a tangential angle of 40° . For the fan shaped and laid back shaped hole, the calculation of the blowing ratio was based on the inlet cross-sectional area of these holes. In this study at the same blowing ratios, the shaped hole can be directly compared to those of the cylindrical hole, which makes it more convenient to evaluate the effect of hole shape. Experiments were performed at a cascade exit Reynolds no. of 5.3×10^3 . The corresponding flow velocity at the exit was 50 m/s, the air was used as a coolant and tested at blowing ratios of 0.4, 0.6, 0.8, 1.2 for the no rod and no wake cases and cases with the wake. This study was done only for single row holes not considering the entire leading edge region and at lower Reynolds number values.

The recent development in turbine blade film cooling, gas turbine blades are cooled internally and externally (Je-Chin and Ekkad 2001). A detailed film cooling and local heat transfer for the turbine region would be helpful to prevent blade failure due to local hot regions. The effective cooled blades are to be designed for advanced gas turbines, the flow visualization/measurements and the CFD simulation results would provide valuable estimates to enhance the engine performance.

The blade leading edge geometry consisting of one row of holes centered on the stagnation line and two additional rows located 3.5 hole diameters downstream on either side of the stagnation line is considered for the film cooling analysis. Here the short film hole diffuser section was conical in shape with a shallow half angle and was joined to a plenum by a cylindrical metering section (William and Leylek 2002). All holes are angled at 20 degrees with the leading edge surface. At a B.R=1.0 to 2.5, D.R= 1.8, the RANS Equation were solved with a pressure correction algorithm. The conical diffuser holes showed a 10 to 40% increase in laterally averaged effectiveness as a compared to the cylindrical holes over the complete leading edge, with the only exception being right at the location of the hole rows.

The film cooling performance of a flat plate in the presence of low and high free stream turbulence is investigated using liquid crystal thermography (James et al. 2003). This paper contributes high-resolution color images that clearly show how the free stream turbulence separate the cooling air around a larger area of the film cooled surface. Distribution of the adiabatic effectiveness is determined over the film cooled surface of the flat plate using hue method and image processing. At low blowing ratio, the increase in free stream turbulence reduces the coverage area of the cooling air due to increased mixing with the main flow. However, at high blowing ratio, when much of the jet has lifted off in the low turbulence case, high free stream turbulence turns its increased mixing into an asset, entraining some of the coolants that penetrate into the main flow and mixing it with the air near the surface.

The experimental investigations were performed to measure the detailed heat transfer coefficient and film cooling effectiveness on the squealer tip of a gas turbine blade in five-bladed linear cascades (Su and Je-Chin 2003). Hue detection based on transient liquid crystals technique was used to measure the heat transfer coefficient and film cooling effectiveness. All measurements were done for the three tip gap clearances of 1.0, 1.5, and 2.5% of the blade span at the two blowing ratios of 1.0 and 2.0. The Reynolds no based on cascade exit velocity and axial chord length was 1.1×10^6 and the total turning angle of the blade was 97.9 deg. The overall pressure ratio was 1.2, and the inlet exit Mach numbers were 0.25 and 0.59 respectively. The turbulence intensity level at the cascade inlet was 9.7%. The result showed that the overall heat transfer coefficient increased with increasing the tip gap clearance but decreased with increasing blowing ratio. Result also showed that overall film cooling effectiveness increased, but heat transfer coefficient decreased for squealer tip when compared to the plane tip at the same tip gap clearance and blowing ratio conditions.

The influence of shaped injection holes on turbine blade leading edge film cooling (Youn and Kim 2004) investigates the flow characteristic of the turbine blade leading edge film cooling using five different cylindrical body models with various injection holes, which are baseline cylindrical hole, two laid-back (span wise-diffused) holes and two teardrop-shaped (spanwise-and stream wise-diffused) holes respectively. Results show that the conventionally cylindrical holes have poor film cooling

performance compared to the shaped hole. The model consists of three staggered rows with a leading edge diameter of 80 mm and an injection angle of 30° relative to the spanwise direction. The shaped holes considered here had the exit opened by 10° in the spanwise direction. This analysis was done only for a single hole with different shapes at the lower Reynolds number of 7.1×10^4 , at a lower turbulence value of 0.2% and the lower density ratio of 1.0

The increasing adiabatic film cooling effectiveness by using an upstream ramp, instead of shaping the geometry of each hole; placing the tabs, struts, or vortex generators in each hole or creating the trench about a row of holes (Sangkwon and Tom 2007). Computationally they used, averaged Navier Stokes equations closed by the realizable $k-\epsilon$ turbulence model. The effect of the following parameters was investigated; angle of ramp $8.5, 10, \text{ and } 14^\circ$, the distance between the backward facing step and the row of film-cooling holes $0.5 D \text{ and } D$, blowing ratios at 0.36, 0.49, 0.56, and 0.98 and sharpness of the ramp at corners. Result obtained shows that an upstream ramp with a backward-facing step can greatly increase adiabatic surface effectiveness. The laterally averaged adiabatic effectiveness with a ramp can be two or more times higher than without the ramp by increasing upstream and lateral spreading of the coolant.

The numerical simulation of turbine blade film cooling at different blowing ratios and hole to hole space using $k-\epsilon$ turbulence model, the temperature field of different location hole rows on leading edge of turbine cascade is numerically simulated (Li et al. 2007). The cooling effectiveness over the blade suction surface is analyzed and compared at various blowing ratios, hole to hole spacing. The results showed that the cooling efficiency is proportional to the blowing ratios among 0.6 to 2.0. The cooling efficiency with the increase of the blowing ratio the former decline earlier and elevated afterward among 2.0 to 4.0, under different hole-to-hole distance conditions. And, the results also showed that the film cooling of hole-to-hole spacing at 4.0 D is superior to the distance of 3.0 D. Here, the area of film cooling of the smaller hole-to-hole space is better than, the bigger hole-to-hole space.

The effect of coolant-mainstream blowing ratio on leading edge film cooling flow and heat transfer-LES investigation is carried out over a cylindrical edge with flat after-body represents the blade leading edge, where the coolant is injected with a 30° compound angle (Ali and Danesh 2008). Three blowing ratios of 0.4, 0.8 and 1.2 are investigated. The increased mixing between coolant jet and mainstream resulted in a decrease of adiabatic effectiveness with an increase in blowing ratio. Increased heat transfer coefficient is obtained with the increase in turbulent intensities in the primary entrainment vortex.

The CFD predictions of pulsed film cooling heat flux on a turbine blade leading edge, a computational study was carried out to determine how leading edge film cooling performance is affected by pulsing the coolant flow (James et al. 2008). A cylindrical leading edge with a flat after the body is used to simulate the turbine blade leading edge region. A single coolant hole was located 21.5 degrees from the leading edge, angled 20 degrees to the surface and 90° from the streamwise direction. They used the computational model that was designed by Ekkad. A single coolant hole of dimension $D/d=18.07$ in the middle of the computational model has a length to diameter ratio of $L/d=11.69$, typical of an actual blade. The span leading edge is $209 d$, symmetry boundary condition is applied at the ends of the span. The computational domain extends the $146 d$ upstream of the leading edge and $146 d$ above the flat after body. The result shows that in case of 0.5 blowing ratios had slightly higher spanwise averaged adiabatic effectiveness than the case 0.25 Blowing ratio. Spatial and time-resolved adiabatic effectiveness and heat transfer coefficient data demonstrated that net heat flux is generally increased by pulsing the film coolant flow.

The experimental and numerical effects of hole exit shape and free stream turbulence on gas turbine blade leading edge film cooling were studied (Funazaki et al. 2012). The study made with several test cases with two blowing ratios, BR 1.0 and 2.0 and three mainstream turbulence intensities 1.0, 3.3, and 12.0% using two types of leading edge models with cylindrical holes and diffuser holes. Four rows of film cooling holes were considered in a staggered manner on the leading edge region at $\pm 25^\circ$ and $\pm 55^\circ$ orientations on either side of the stagnation line. Each row has five holes and has the hole inclination angle of 40° with the surface in a spanwise direction. Also, a detailed

investigation of the film cooling is carried out using CFD simulation. RANS approach using shear stress transport turbulence model and detached eddy simulation approach are employed to solve the flow field. In case of the diffuser hole, the effect of mainstream turbulence intensity appears significant, and its spanwise averaged film effectiveness is decreased.

The three-dimensional numerical investigations are carried out for the effect of film cooling on the thermal behavior of gas turbine blades, using a commercial computational fluid dynamics (CFD) code. Two film cooling configurations namely four rows film cooling with U-bend internal channel and eight rows film cooling with U-bend internal channel have been simulated to be transonic flow over a turbine blade with turbo-specific non-reflecting boundary conditions (Shaker et al. 2012). The results show that the heat transfer coefficient with film cooling is higher than that without film cooling. From the predicted temperature profile, it is observed that the blade with eight rows film cooling with U-bend internal channel shows better cooling performance than that with four rows. Further, increase leads to a reduction in temperature, and moreover, the lateral spreading facilitated the best coolant layer.

The effect of free stream turbulence on leading edge for the heat transfer coefficients and adiabatic film effectiveness is studied (Ken-ichi et al. 2012). The study examines several test cases with blowing ratio and three mainstream turbulence intensities using two types of leading edge models with cylindrical holes and diffuser holes. The result shows that in the case of the diffuser hole, the effect of mainstream turbulence intensity appears significantly, and spanwise averaged film effectiveness is decreased. The geometry of the test model used in these experiments is semicircular part of 80 mm in diameter (D), and flat plate part of 100 mm in length, and the height of the test model is 280 mm. The injection angles of 0, 25, 55 degrees in the spanwise direction are considered. In this study thermocouple rake having 13 K-type thermocouples was used to perform temperature measurement within planes normal to surface face. For numerical simulation, the commercial software ANSYS CFX 12 was used in this study. Time-averaged Reynolds-Averaged Navier-Stokes (RANS) approach using

Shear-Stress Transport (SST) two-equation model was employed to solve the flow field.

Different film cooling geometries of anti-vortex holes are analyzed for the adiabatic film cooling effectiveness by numerical analysis (Kyu et al. 2011). Better effectiveness is found with the anti-vortex holes in comparison to the baseline holes.

2.3 Expanded Exit Holes in Film Cooling

The film cooling effectiveness measurements for a cylindrical hole and two holes with a diffuser-shaped exit portion (i.e., a fan shaped and a laidback fan shaped hole) were presented (Gritsch et al. 1998). The laidback fan shaped hole provides a better lateral spreading of the ejected coolant than the fan-shaped hole, which leads to higher laterally averaged film-cooling effectiveness. Coolant passage crossflow Mach number and orientation strongly affect the flow field of the jet being ejected from the hole and, therefore, have an important impact on film cooling performance. This study was done on the flat plate with the single hole arrangement for finding out the effect of hole shape.

The highest effectiveness and best coverage of cooling are achieved by laterally diffused film holes. Film hole shaping can significantly affect the distribution of the exit plane variables, which determine downstream film cooling performance (Hams et al. 2000). It was found that holes with laid back type widened exits enhance the overall cooling performance of the showerhead, compared to classical cylindrical holes. This was primarily associated with the better lateral spread of the individual cooling jets, and with a considerably reduced tendency of jet detachment at higher blowing due to the diffuser effect. Laterally expanded holes performed better than cylindrical holes, but not as well as laid back shaped holes (Reiss and Bolcs 2000).

2.4 Computational Film Cooling Methods

In addition to experimental research, different computational methods are also tried to evaluate the film cooling performance and compared with the earlier experimental results. The 3D N-S code was compared with the experimentally obtained film cooled data. The comparison of surface heat transfers between a fully 3D Navier-Stokes code

with film injection and the experimental data obtained on a transonic rotating rotor blade with film cooling were studied (Vijay et al. 1997). The present approach was shown to provide a reasonably good prediction of the heat transfer at the leading edge and on the suction surface of a film-cooled rotor blade when compared to the experimental data, validating the code under blade rotation. On the pressure surface, the code under predicted the surface heat transfer. Reasons for differences on the pressure surface are cited; the most plausible one seems to be the presence of unsteady effects because of stator-rotor interaction in the experiments, which are neglected in the present computations. The Nusselt number on the blade surface is found as highly 3-D in the vicinity of holes and tends to become 2-D far downstream. At the hole exits, the coolant velocity and temperature distributions do not follow the power law profile. The counter-rotating secondary flow structure downstream of the jet exit is the most significant mechanism affecting the film-cooling performance in the streamwise injection cases (Vijay et al. 1998).

In computational film cooling analysis, the grid refinement is a very important parameter; the care should be given to the grid size, use of increased computational domain into plenum and hole side will give better results. Parametric variation studies have been performed to demonstrate the CFD validation with the experimental results, to use the CFD for the design of cooling hole geometries (Siddarth et al. 1999). Detailed distributions of coolant velocity, the temperature at the hole exits are also presented using computation method. Film-cooling performance of a streamwise injected case may be significantly improved by controlling the strength of the counter-rotating vortex pair. Methods may include: reducing or realigning the vorticity exiting the film hole; decreasing the vertical location of the streamwise vorticity pockets relative to the downstream wall and increasing the distance between the vorticity pockets to reduce their lift and convective strength (Walters and Leylek 2000).

Compounding improves the lateral uniformity of the adiabatic effectiveness. At high compound angles, the lateral distribution of hole is ruler-flat within only a few diameters downstream of the row of film holes, and the heat transfer coefficient was found to be augmented due to the compounding effects in all the cases studied however, there is net gain as the compound-angle injection is capable of providing a

highly sought-after feature in film cooling, namely, lateral spreading and uniformity (Mc Govern et al. 2000).

2.5 Various Film Cooling Parameters

The overall effect of an internal cross flow on film cooling performance strongly depends on hole geometry and blowing ratio. For the cylindrical hole, film-cooling performance is improved as compared to the plenum case. Jet detachment is delayed, and the jet is kept closer to the wall at elevated blowing ratios. Contrary to the cylindrical hole, film-cooling performance is reduced for both shaped holes with internal cross flow applied. The jet entering the diffuser section of the hole is highly disturbed causing poor performance of the diffuser and leading to a less uniform cooling film (Gritsch et al. 2003). The film-cooling performance is closely linked to whether the coolant jet has separated from the surface. For nominal conditions of a flat surface, low free stream turbulence and cylindrical holes, the film-cooling performance is reasonably predictable with empirical correlations. However, surface curvature, high free stream turbulence and shaping of the hole exit can greatly change film-cooling performance by significantly affecting the blowing ratio at which the coolant jet separates (Bogard and Thole 2006).

To compute the heat transfer coefficients on the blade, hub and shroud, a three-dimensional multi-block, Navier-Stokes code has been used for a rotating high-pressure turbine blade with eight rows of 172 film-cooling holes (Vijay et al. 1999). The adiabatic film cooling effectiveness and heat transfer coefficient distribution are computed for the adiabatic blade model using the k-w Wilcox's turbulence model. The effectiveness is found lower, and the heat transfer coefficient is found higher in the leading edge and tip regions with the given parameters.

The naphthalene sublimation technique and the heat/mass transfer analogy were used to measure the film cooling performance for one row of holes with 35° inclination angle (Goldstein et al. 1999). The mass transfer coefficient is measured using pure air film injection while the film cooling effectiveness is derived from a comparison of mass transfer coefficients obtained following injection of naphthalene-vapor-saturated air with that of pure air. It was concluded that the local and the laterally averaged film

cooling effectiveness generally agree with previous results at blowing ratios of 0.5 and 1.0. The relatively short injection hole configuration used provides effectiveness similar to that found with long injection holes at similar blowing rates. The local and the laterally averaged mass transfer coefficients obtained in the present study do not agree as well with previous heat transfer results perhaps due to conduction effects in the region of the large temperature gradient in the heat transfer measurements. The naphthalene sublimation technique and the heat/mass transfer analogy used in the present experiment can be used to obtain detailed local and averaged information on film cooling performance.

The three film-cooling hole geometries including a cylindrical hole and two holes with a diffuser shaped exit portion regarding local heat transfer coefficients as well as overall cooling performance in the vicinity of the injection location were studied (Gritsch et al. 2000). Tests were performed at an engine like coolant-to-main flow temperature ratio of 0.54 (DR.1.85) over a range of blowing ratios of 0.25 to 1.75. Additionally, the effect of internal coolant supply channel Mach number was investigated. The results revealed that holes with expanded exits have profoundly lower heat transfer coefficients at elevated blowing ratios as compared to a cylindrical hole. The laidback fan shaped hole provides better lateral spreading of the jet as compared to the fan shaped hole and, therefore, lower laterally averaged heat transfer coefficients; combining the effects of reduced heat transfer coefficients and increased film-cooling effectiveness, holes with expanded exits provide significantly improved overall film-cooling performance at elevated blowing ratios as compared to a cylindrical hole; Coolant crossflow Mach number has an impact on film-cooling performance in the near-hole region, particularly for the shaped holes. Therefore, crossflow at the hole entry side has to be taken into account when modeling film-cooling at engine representative conditions.

Some computational simulations are carried out for film cooling configurations involving cylindrical, forward diffused, laterally diffused, inlet shaped, and cusp-shaped film holes (Hyames and Leylek 2000). The key conclusions from this study are as follows: of the film holes tested in this work, the laterally diffused film hole provides the best coverage and highest effectiveness. The forward diffused film hole

performs well along the centreline but does not spread laterally. The cylindrical and inlet-shaped film hole performs poorly at both blowing ratios; the coolant lifts off from the test surface in these cases. Film hole shaping can significantly affect the distribution of the exit plane variables, which determine downstream film cooling performance. Crossflow and streamwise effects were studied. The CFD can be used to sort the relative performance of shaped film cooling configurations and provide logic for determining the reasons for increases or decreases in film cooling performance.

The two film-cooling configurations are investigated at the different flow and geometric parameters typically seen in modern gas turbine engines (Brittighams and Lylek 2000). The superposition of effects for compound-angle cylindrical holes and streamwise shaped holes need not necessarily apply to compound angle shaped holes, are important conclusions can be drawn from this work.

The study has been conducted to acquire discharge coefficients of cylindrical holes and expanded hole exits with different coolant cross flow orientation (Gritsch et al. 2000). The hole inlet cross flow Mach numbers, pressure ratios and hole exit cross flow Mach numbers across the hole have been varied with different engine-like conditions.

Boundary layer temperature distribution and adiabatic film cooling effectiveness were experimentally studied to find the effects of orientation angles and velocity ratios (Sung et al. 2000). Hole orientation angles of 0, 30, 60, and 90 degrees are investigated at the velocity ratios in the range of 0.5 to 2.0. Thermochromic liquid crystal technology is used to find the film cooling effectiveness.

Flat plate specimens are studied with double walled film cooled design for the overall cooling performance using the infrared camera (Sweeney and Rhodes 2000). 30° hole angle has shown the good spanwise-averaged effectiveness of the normal hole by approximately 10 percent.

One row of the cylindrical holes model was investigated using the local adiabatic film cooling effectiveness at typical high-density ratio conditions were carried (Baldauf et al. 2001). High-resolution thermography system is used for the detailed 2D surface

temperature investigations. Optimum overall cooling conditions are arrived using both the heat transfer and local effectiveness data. The computational data is validated with the experimental data and used for the refinement of the turbulence model.

An investigation has been carried out for the impact of various hole geometrical parameters on the discharge coefficient and film-cooling effectiveness of fan-shaped film-cooling holes (Gritsch et al. 2005). The pressure losses are not affected much by the geometry of the fan-shaped hole. All the hole geometry parameters only have a weak impact on laterally averaged film cooling effectiveness, within the range investigated. The hole length to diameter ratio effect was found very small. The pitch to diameter ratio effect is as expected large as it determines the amount of coolant spent per unit span. The effect of coverage ratio and area ratio is negligible. Putting a compound angle has some detrimental effect at high blowing ratios which can be overcome by using non-symmetric diffusion. Since many of the parameters investigated do only have a small impact on film cooling effectiveness the cooling designer may be more tolerant on the hole shape if requirements from manufacturing process necessitate doing so.

Shaped hole film-cooling technology has become the standard in today's highly cooled gas turbine airfoils (Ronald 2005). The review was done with the origins of shaped film cooling and summarized the current state of knowledge concerning this technology, including the flow field, heat transfer coefficients, and adiabatic film effectiveness. The benefits of shaped film holes using expanded exits of the fan and laidback geometries, summarized as, Higher centreline and laterally averaged adiabatic film effectiveness, in some cases approaching that of two-dimensional slot film. The shaped holes with the sufficient length of transition and exit diffusion area will provide the better overall cooling effectiveness over cylindrical holes. The diffusion areas depend upon the geometry of the surface and are not the same for all the surfaces. However, the manufacturing technology has to be improved to fabricate different hole exit shapes.

A detailed study (Yiping et al. 2007) was made with hole shape and hole angles with three rows of holes at a lower Reynolds number of 19,500 based on the leading edge

diameter using an ABS plastic material using the transient method. The leading edge test surface has the three rows of six film cooling holes each and all film holes inclined at 30° to the test surface in the spanwise direction and 90° to the flow direction. The different film cooling hole angles are studied in the range of 30 to 45° inclined with the test surface. The addition of the compound angle to the baseline holes increased the effectiveness, whereas the heat transfer coefficient is affected nominally. Shaping the compound angle further improved the effectiveness, whereas the heat transfer coefficients are slightly affected. Hence it is shown that complex hole exits shown better effectiveness over the baseline hole geometries.

Two showerhead film cooling designs, a heavily film cooled model with seven rows of film holes and each design, four different film-hole configurations were studied (Zhihong and Je-Chin 2009). Pressure Sensitive Paint experiments were performed to measure the film cooling effectiveness on the leading edge models. With the heavily distributed film holes, PSP method is very convenient for the film cooling effectiveness measurements. The effectiveness of the 3-row design has shown the lower values in comparison to the 7-row design at the same blowing ratio. These results may not be as accurate as thermographic results.

Film cooling effectiveness is measured by purging the coolant flow through the wheel space cavity on the first stage of the rotating platform of three stage turbine facility (Suryanarayanan et al. 2009). The film cooling data is found on a rotating platform with the purge flow through the disk cavity. This is the first available film cooling data with the rotating conditions.

The experimental investigation is carried out to find out the film cooling effectiveness on the pressure side of the high pressure contour of the blade surface (Giovanna et al. 2010). The contour surface causes for the stagnation region with the jet lift-off condition, and the accurate data on this surface is very useful. The cylindrical and shaped holes are studied at the pressure side of the vane by varying the different mass flow ratios in the range of 0 to 1.5% , and the detailed results are presented in this paper.

Numerical film cooling effectiveness analysis is carried out over a fan-shaped hole model for the optimization of turbulence models (Lee and Kim 2010). SST type

model for the averaged and local film-cooling effectiveness is validated with the experimental results. The geometrical parameters of injection hole angle, lateral expansion angle, length to diameter ratio effects have been studied. At a blowing ratio of 0.5 the optimum injection angle is found as 40.34° , a lateral expansion angle of 21.83° and length-to-diameter ratio as 7.45. For the better-performing film-cooling holes, the surrogate design approach can safely be used with the reduced computational time.

Influence of coolant density on turbine blade film cooling using pressure sensitive paint has been carried out for the different density ratios at 1.0, 1.5 and 2.5. Three foreign gases of N_2 for the low density, CO_2 for medium density and the mixture of SF_6 and argon for the high density are used as coolant gases during the experiments. The coolants to the mainstream air blowing ratios of 1.2 to 2.2 are used for the cooling effectiveness analysis at all the three density ratios. The showerhead holes are inclined 30° from the spanwise direction, whereas the pressure side and the suction side holes bear a streamwise injection angle of 45° with the surface and an additional 45° in the lateral direction. The cooling effectiveness increase is found with the increase in blowing ratio up to 1.7 on the pressure side and up to 1.4 on the suction side of the vane. No major improvement is seen after that and found a drop in cooling effectiveness at the downstream side of the suction side. The increase in the coolant density has shown the improvement in cooling effectiveness everywhere on the surface except for the small region on the suction side (Diganta et al. 2012).

The film cooling effectiveness measurements were carried out at three exit Reynolds numbers by varying the blowing ratios in the range of 1.0 to 2.0 at a free stream turbulence intensity of 12% (Xue et al. 2013). On both the pressure and suction side of the vane, shaped holes are added downstream of the leading edge region. The addition of the shaped holes improved the effectiveness at all the blowing ratios over the baseline holes. The Nusselt number values have shown higher with the increase in exit Mach numbers, whereas the cooling effectiveness is decreased.

Surface temperature measurements downstream of a row of film cooling holes on the suction side of scaled up, simulated adiabatic, and conducting gas turbine vanes are carried out (Jason et al. 2013). Parallel measurements are made on adiabatic and

conducting vanes with the same test geometries and test conditions for the adiabatic and overall effectiveness measurements. The overall effectiveness measurements with and without film cooling compared, allowing the contribution of film cooling to the overall cooling to be separated with the internal convective cooling. An additional film cooling caused a decrease in vane surface temperature for all conditions. The research was carried out to provide the validation of computational conjugate heat transfer codes using experimental results. Previous experimental studies of conjugate heat transfer available in the open literature are limited in the scope of the data or were conducted on less realistic test models. The presented data in this paper represents a significant improvement in the experimental conjugate heat transfer and can be used for the benchmarking of computational codes.

An experimental and computational study is carried out on a typical gas turbine NGV leading edge. The effect of Reynolds number and blowing ratio was studied by considering two materials with different thermal conductivities of 0.2 W/m K (material A) and 14.9 W/m K (material B) for the overall cooling effectiveness and heat transfer distributions. The path lines, no dimensional temperature contours and Nusselt number distributions describing the mainstream coolant interaction at the exit of film holes were made. The computational results of static pressure and overall effectiveness distribution on the NGV surface are validated with the experimental data, which had shown the closer expected values. The overall effectiveness of material 'B' is higher than material 'A.' And the distribution in streamwise and spanwise directions is more uniform compared to material 'A' owing to the higher thermal conductivity. The sudden peaks in the effectiveness distribution of material A, disappear in the case of material B, owing to the lateral diffusion within the plate. The effect of blowing ratio is different for the pressure side and suction side of the stagnation line. The coolant tends to distribute more towards the pressure surface as the blowing ratio increases. Hence, the effectiveness increased with increase in blowing ratio, on the pressure side and decreased on the suction side. The effectiveness is higher on the pressure side at $M = 2$ and on the suction side at $M = 1$, for material A. When considering the whole blade, a more uniform distribution of overall effectiveness between pressure and suction side was noticed at $M = 1$,

resulting in less thermal gradient whereas the averaged overall effectiveness value is higher at $M = 1.5$. For material B, the overall effectiveness value is higher at $M = 1.5$ throughout the leading edge. For both Materials A and B, when blowing ratio was increased from 1 to 2, the region with higher effectiveness was seen getting shifted from hub to tip. An increase in Reynolds number has showed an increase in heat transfer on both the external and internal sides of the leading edge even though external heat transfer is more dominant (Chandran and Prasad 2015).

The experiments using the TLC thermography and the numerical simulations with DES are carried out for the film cooling effectiveness over a wide range of blowing ratios on straight and curved shape holes (Jun and Shun 2013). The curved injection has shown a higher heat transfer coefficient with the improvement in the net heat flux ratio.

Adiabatic and conjugate film cooling and heat transfer computational studies have been performed on the convex surface. The results have shown the temperature level for the adiabatic state is higher than the conjugate state for both one layer and multi-layers. In the case of the multi-layer state, the outer surface temperature is lower than that of the one-layer state which consequently shows higher centerline and lateral film cooling effectiveness. (Yusop et al. 2013).

An experimental investigation is carried out for the smooth expansion holes placed over the gas turbine vane leading edge (Tarek et al. 2013). 2 d and 4 d expansion holes have been studied with the standard cylindrical holes at an inclination angle of 60 and 90 degrees. Smooth expansion holes have shown higher effectiveness over the standard cylindrical exit holes with the same flow conditions. The pressure side has shown the higher effectiveness compared to the suction side due to the jet lift-off condition over the suction side. However, the smooth expansions improved the coolant uniformity over the surfaces and improved the effectiveness.

The numerical simulation data is validated with experimental data for the film cooling effectiveness with a backward injection. From the results, the backward injection showed the improvement in the film cooling performance on a flat surface at both laboratory and gas turbine operating conditions. The coolant jet interaction with main flow in case of backward injection makes the cooling in the spanwise direction much

higher and uniform in comparison to the forward injection. For the cooling with a curved surface, the performance of film cooling with backward injection decreases along centreline on both concave and convex surfaces, especially in the region close to the cooling hole. However, the spanwise distribution becomes more uniform due to the backward jet, and on the pressure side, some higher improvement is seen. When the blowing ratio varies, the advantage of backward injection stays the same. Results from cases with different blowing angles also suggest that film cooling with forward injection shown poor performance than the backward injection. (Li et al. 2013).

Evolution of the blades and advanced technologies which could be applied in the future of typical air-cooled turbine blades produced by Rolls-Royce are reviewed and results described. Over a long term, the gas turbine TET keeps increasing. Turbine blades are highly dependent on development in material science and blade cooling technology. Thermal barrier coating as an economical and effective way to protect the turbine blade attracts more attention than ever. Moreover, the CMCs are to be considered as future blade material, although many challenges need to be overcome. Blade cooling technology has been developed from single-pass convection cooling to sophisticated multi-pass serpentine cooling coupled with film cooling. Advanced cooling schemes such as dual wall cooling will be the future direction and Blade tip design to minimize over-tip leakage and improve turbine efficiency needs to be further developed (Xu et al. 2014).

Adiabatic film cooling effectiveness measurements were carried out over a shower head region of C3X turbine vane (Marc et al. 2014). The adiabatic effectiveness improved with the increase in the mass flux ration in the tested range of values. Here the overall cooling effectiveness and the impingement effects have been studied over the stator vane. Overall cooling effectiveness values have shown higher than the adiabatic values due to the impingement. The hotspots are reduced by incorporating the staggered manner cooling holes.

Contoured crater design with a V-shaped protrusion is numerically investigated for film cooling performance using LES and compared with a baseline no-crater configuration (Prasad and Sumanta 2015). The validity of the numerical simulations is established through the excellent agreement between the baseline case simulations

and the published experimental data. Three crater depths in the range of 0.2 to 0.75 D are studied. Craters for all the depth under consideration in showed the significant improvements in cooling performance. The laterally averaged cooling performance increased with crater depth with a near eight-fold improvement in the laterally averaged cooling effectiveness immediately downstream of the hole. At higher blowing ratios baseline hole suffers a complete loss of cooling performance, while crater retains the film cooling effectiveness. The corresponding performance gains are even greater when compared to the reported gains for trenched holes.

The uncertainty analysis of the experimental data is performed based on the uncertainty levels of the instruments used in the experiments (Holman 2012). The procedure used in the experimental methods for engineers is considered for the experimental uncertainty calculations in the present study.

From the above-detailed literature survey, it is found that the optimization of turbine blade leading edge region cooling is a continuous process for the increase of gas turbine engine power with the improvement of specific fuel consumption. The film cooling requires the investigation of various geometrical parameters like hole shape, hole location, the diameter of the hole, hole angle concerning leading edge surface and the flow parameters like coolant to mainstream blowing ratio (B.R) and density ratio (D.R). Amongst them blowing ratio has a significant effect on the film cooling effectiveness and heat transfer coefficient in controlling the bleed air from the compressor. Based on the literature review (Yiping et al. 2007, Funazaki et al. 2012 and Diganta et al. 2012), it is observed that the spanwise inclined holes are used on the leading edge region. Hence, the spanwise inclined holes are used in the present study over the leading edge surfaces. Based on the literature review (William and Leyelek 2002, Su and Je-Chin 2003, Funazaki et al. 2012, Xue et al. 2013, and Chandran and Prasad 2015), it is observed that the effect of coolant flow is very less on the leading edge region for the blowing ratios below 1.0, Hence, the blowing ratios above 1.0 are considered for the present study to find the optimized blowing ratio which gives the highest cooling effectiveness for the planned test models.

2.6 Research Gap

It is very important to understand the heat transfer aspects on turbine components under actual engine conditions for the better performance of engines. Turbine nozzle guide vane leading edges are one of the critical components facing the highest heat loads with almost stagnant pressure conditions. Typical measurements on a turbine nozzle guide vane under engine conditions will provide the good heat transfer information on gas path components. Instrumentation and experimentation on actual turbine stages under engine conditions are very rare. The lack of accurate high-temperature measurement tools and difficulty in instrumentation of the turbine stage with temperature and pressure measuring devices are some of the reasons for the few attempts to study turbine heat transfer on an actual stage under actual engine conditions (Je-Chin et al. 2012).

The single row of holes on the flat plate and leading edge model provides only the limited information of film cooling effectiveness and heat transfer coefficient values along the downstream of holes, and the cumulative effect of downstream rows of holes are not available. In the proposed work, a scaled up gas turbine vane leading edge region with all the film cooling hole rows is considered for the analysis of cooling effectiveness and heat transfer coefficients. The non-dimensional flow parameters of Reynolds number, Blowing Ratio, and Density Ratios are considered with the actual vane leading edge configuration with engine similar conditions for the cooling effectiveness studies. It is expected that the present results are scalable with the engine conditions.

The proposed work is taken up with the following research gaps of available open literature

1. There is no previous work on full leading edge model with a full number of film cooling shaped holes with different rows in a staggered manner arrangement. Most of the shaped holes film cooling data available in the literature are only on the flat plates with the single row or single hole arrangement.
2. There is no data available in the open literature for the comparison of different hole inclination angles in a staggered manner arrangement of rows of holes on the complete leading edge.

3. There is not much data available in the open literature on hole orientation angle effects, hole pitch and hole diameter effects for the complete leading edge shower head region.
4. There is not much CFD data available on the complete blade leading edge model with the film cooling hole configurations.

2.7 Scope and Objectives of the Work

2.7.1 The scope of the Work

The cooling performance of the film cooling configuration is influenced by the combined effects of film cooling effectiveness and surface heat transfer coefficients. Some studies have been considered over leading edge film cooling performance using configurations of circular holes and shaped holes. But all the published literature has the limited data with single hole data, or with a single row of holes and on the flat plates. There is not a much data on the complete leading edge with the multiple rows in a staggered manner. With the facility availability at CSIR- National Aerospace Laboratories, the study of various geometric parameters is taken up with holes in a staggered manner on the turbine blade complete leading edge region.

2.7.2 Objectives of the Work

- To find the adiabatic film cooling effectiveness (non-conductive models) over the gas turbine blade leading edge configurations.
- To find the heat transfer coefficients over the gas turbine blade leading edge configurations.
- Mass flow and coefficient of discharge values for all the considered hole configurations over the gas turbine blade leading edge configurations.
- CFD modeling to find out the flow field velocity vectors, adiabatic film cooling effectiveness and heat transfer coefficients over the gas turbine blade leading edge models and validation with the experiments.

The following parameters are considered to find the adiabatic film cooling effectiveness and heat transfer coefficients over the gas turbine blade leading edge configurations.

- ❑ The effect of hole orientation angle along a streamwise direction (15°, 30° and 45° from the stagnation line).
- ❑ The effect of hole inclination angle in a spanwise direction (20°, 25°, 30° and 35° with wall surface).
- ❑ The effects of hole pitch 18 and 22.4 mm in spanwise direction (p/d ratios of 3.2 and 4).
- ❑ The effect of hole exit shape with the change in area ratio (Circular, Fan-shaped, Laidback Fan shaped holes with the area ratios of 1.0, 3.0 and 7.0)

To carry out the above studies, the following low thermal conductivity adiabatic test models are fabricated using the Selective Laser Sintering (SLS) method of Rapid Prototyping (RPT) technology.

1). **Three scaled up to test models** with each having the one row of film cooling holes at 15°, 30°, and 45° hole orientation angles respectively from stagnation line in a streamwise direction to bring out the effect of **hole orientation angle**. Each row has the five holes with the hole diameter of 3.2 mm, pitch of 20 mm and has the hole inclination angle of 20° in spanwise direction.

2). **Four scaled up to test models** with each having the five rows of film cooling holes with the hole angles at 20°, 25°, 30° and 35° respectively in a spanwise direction to bring out the effect of **hole inclination angle**. One row of holes on stagnation line and two rows of holes on either side of the stagnation line at 30° and 60° orientations respectively. Each row had the five holes with the hole diameter of 5.6 mm, the pitch of 20 mm and arranged in a staggered manner.

3). **One test model is** having the five rows of film cooling holes with the hole pitch of 22.4 mm to bring out the **effect of hole pitch**. One row of holes on stagnation line and two rows of holes on either side of the stagnation line are placed at 30° and 60° orientations respectively. Each row has the five holes arranged in a staggered manner. The model is made to compare its test data with the base model having the hole inclination angles 30° having the hole pitch of 18 mm. (5.6 mm hole dia., 30° hole injection angle).

4). **Three test models** with each having the five rows of film cooling holes with the hole shape of circular, fan shape and laid back fan shapes to bring out the **effect of hole shape**. One row of holes on stagnation line and two rows of holes on either side of the stagnation line are placed at 30° and 60° orientations respectively. Each row has the five holes arranged in a staggered manner with the hole injection angle of 30 degrees with the spanwise. (4 mm hole dia., 21 mm hole pitch).

The hole configurations and flow parameters are made based on the literature survey and based on the actual engine configurations to find the cooling effectiveness at the mid-span location of the blade leading edge regions.

Experiments are carried out using the Film cooling test facility available at Heat Transfer Lab, CSIR-National Aerospace Laboratories, Bangalore. The experiments are conducted at a nominal flow Reynolds number of 1×10^5 based on the leading edge diameter by varying the blowing ratios in the range of 1.0 to 2.5 at a density ratio of 1.30. The mainstream flow Reynolds number is maintained as per the real engine NGV configuration, and it is 1×10^5 based on the leading edge diameter and 3×10^5 based on the Hydraulic diameter (The hydraulic diameter of the main channel is 0.2676 m).

CHAPTER 3

EXPERIMENTAL SETUP AND PROCEDURE

3 EXPERIMENTAL SETUP AND PROCEDURE

The experimental activities are carried out at CSIR-National Aerospace Laboratories, Bengaluru. The Film cooling test rig available at Propulsion Division, NAL is used for this experimental work. The schematic view of the gas turbine blade with the external film cooling holes and internal ribs is shown in the Fig. 3.1. The Fig. 3.1 also clearly shows leading edge, pressure and suction sides along with the cooling holes arrangement.

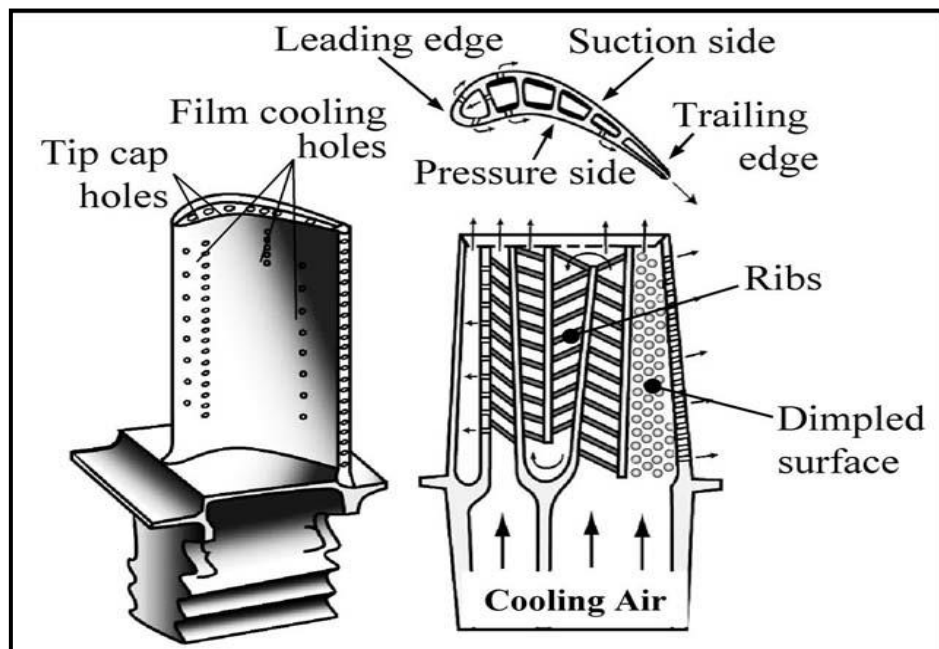


Fig. 3.1 Gas turbine blade cooling schematic

Source: (Robert Kim et al. 2001)

3.1 Test Models

The test models are generated using solid works software having a semicircular cross-section with an outer diameter of 90 mm and the inner diameter of 70 mm, with the film holes at different hole orientation angles, hole inclination angles, hole pitches and hole exit shapes. In total, eleven test models are prepared to bring out the effects of hole orientation angle, inclination angle, pitch, and hole exit shape.

3.1.1 Gas Turbine Blade Leading Edge Model Specifications

Table 3.1 Blade LE model specifications

Sl. No.	Model Description	Dimensions
1	Leading Edge Outer Diameter	90 mm
2	Leading Edge Inner Diameter	70 mm
3	Film Cooling Hole Diameter	3.2 mm (Hole Orientation effect) 5.6 mm (Hole Inclination and Pitch effect) 4.0 mm (Hole exit shape effect)
4	Film Cooling Hole Pitch	18 and 22.4 mm
5	Leading Edge Model Height	210 mm
6	No. Holes / Row	5
7	No. of Rows	5 (One row of holes on stagnation line and Two rows of holes on either side of stagnation line placed at 30 and 60 Degrees orientation)

The detailed geometrical specifications of the test models considered in this film cooling work are shown in Table 3.1.

3.1.2 Test Model Details

- ❑ Effect of Hole Orientation Angle (03 Models-15°, 30°, 45° Hole Orientations Angles): M1, M2, M3 [d=3.2 mm, p=20 mm, $\alpha = 20^\circ$.]
- ❑ Effect of Hole Inclination Angle (04 Models - 20°, 25°, 30° and 35° Hole Inclination Angles): M4, M5, M6, M7 [d=5.6 mm, p=18 mm]
- ❑ Effect of hole pitch (01 Model – 30° Hole Inclination, 22.4 mm pitch): M8 [d=5.6 mm, p=22.4 mm, $\alpha=30^\circ$]
- ❑ Effect of Hole Shape (03 Models - Circular, Fan Shaped, Laid Back Fan Shaped Models): M9, M10, M11 [d=4 mm, p=21 mm, $\alpha=30^\circ$]

Total No. of test models = 03+04+01+03 = 11 models

3.1.3 Effect of Hole Orientation Angle (M1, M2, M3)

(M1, M2, M3_3.2 mm Hole Diameter, 20 mm Pitch)

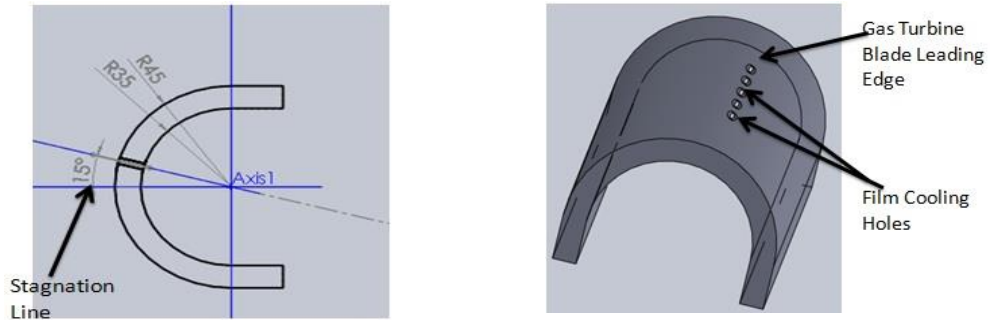


Fig. 3.2 M1_15° hole orientation angle

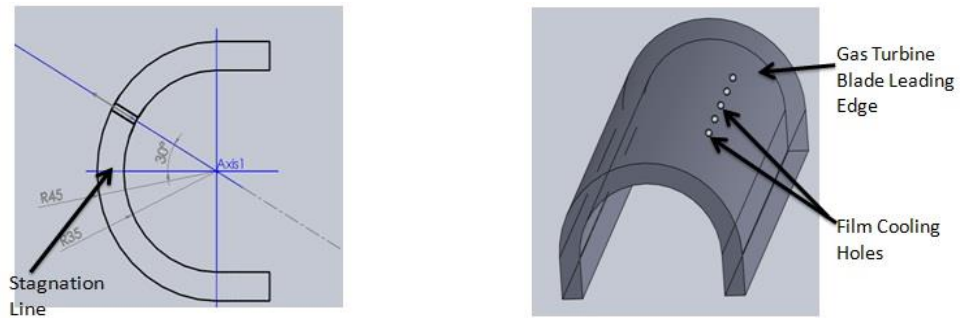


Fig. 3.3 M2_30° hole orientation angle

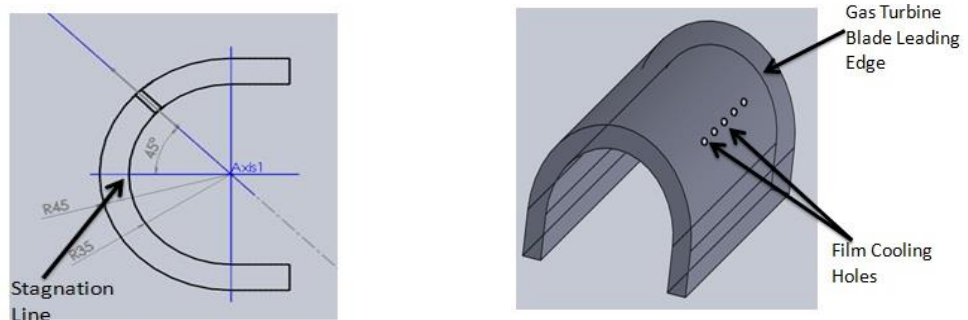


Fig. 3.4 M3_45° hole orientation angle

M1, M2, M3: Gas turbine blade leading edge models with the row of five film cooling holes at 15°, 30°, and 45° orientations in the streamwise direction from stagnation line respectively. The geometrical details of these models are shown in the Fig. 3.2 to Fig. 3.4. These models are generated using the solid works drawing software.

3.1.4 Effect of Hole Inclination Angle (M4, M5, M6, M7)

(M4, M5, M6, M7_5.6 mm Hole Diameter, 18 mm Pitch)

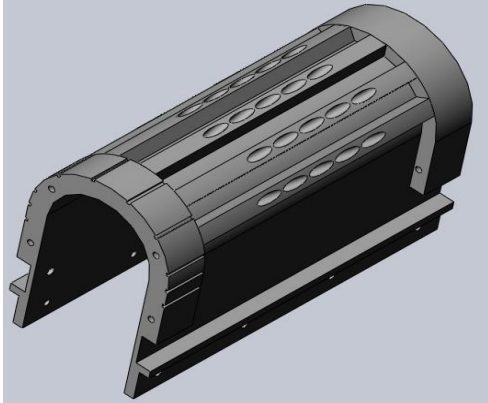


Fig. 3.5 M4_20° hole angle

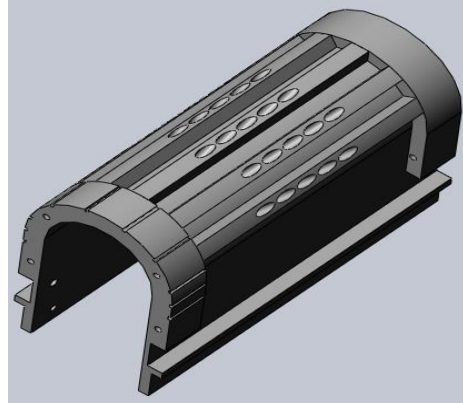


Fig. 3.6 M5_25° hole angle

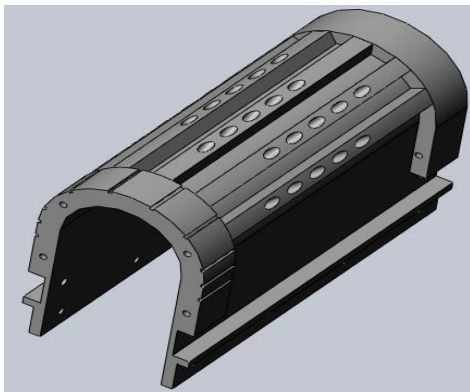


Fig. 3.7 M6_30° hole angle

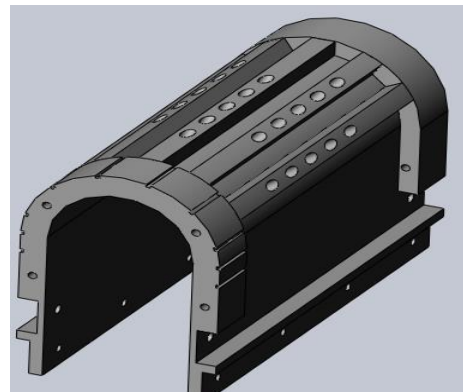


Fig. 3.8 M7_35° hole angle

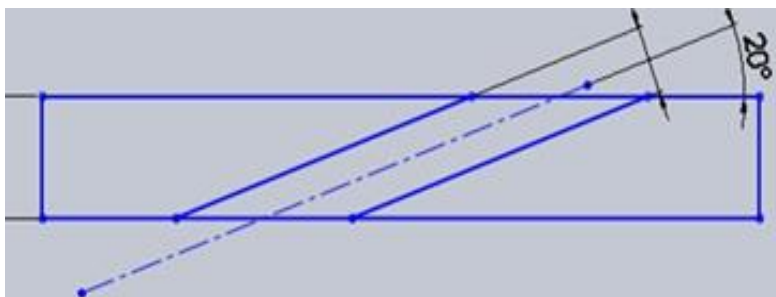


Fig. 3.9 Typical hole angle w.r.t. spanwise direction

M4, M5, M6, M7: Gas turbine blade leading edge models with film cooling holes at 20°, 25°, 30° and 35° hole inclination angles with spanwise direction having the five rows as one row of holes on stagnation line and two rows of holes on either side of

stagnation line at 30° and 60° orientation respectively. The geometrical details of these models are shown in the Fig. 3.5 to Fig. 3.9.

3.1.5 Effect of Hole Pitch (M6 and M8)

(M6_5.6 mm Hole Diameter, 18 mm Pitch and
M8_5.6 mm Hole Diameter, 22.4 mm Pitch)

18 mm pitch has p/d of 3.2 and 22.4 mm pitch has a p/d of 4

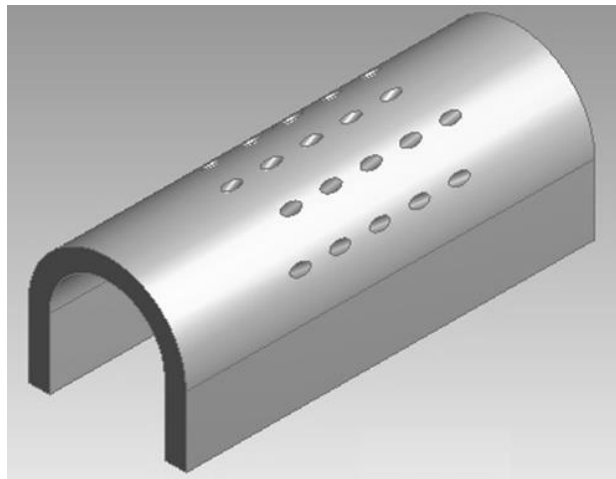


Fig. 3.10 M8_30° Hole angle, 22.4 mm pitch

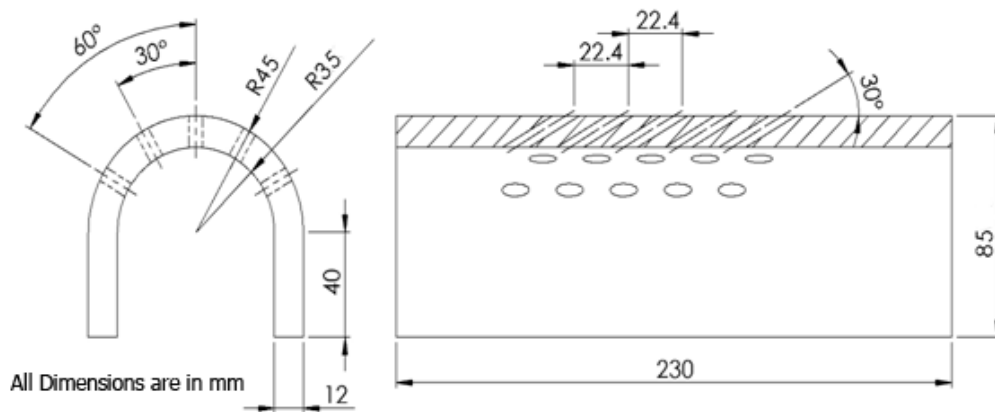


Fig. 3.11 M8_Geometrical details

M8: Gas turbine blade is leading edge model with film cooling holes at 30° hole inclination angle with the spanwise direction having the five rows as one row of holes on stagnation line and two rows of holes on either side of stagnation line at 30 and 60 degrees orientation respectively. The geometrical details of this model are shown in the Fig. 3.10 and Fig. 3.11.

3.1.6 Effect of Hole Exit Shape (M9, M10, M11)

(M9, M10, M11_4 mm Hole Diameter, 21 mm Pitch)

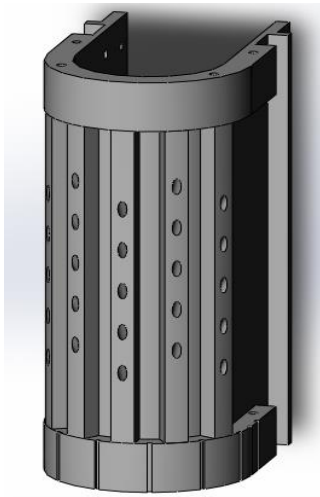


Fig. 3.12 M9_Circular hole model

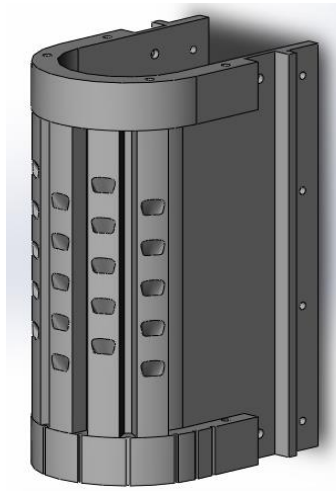


Fig. 3.13 M10_Fan shape hole model



Fig. 3.14 M11_Laidback fan shape hole model

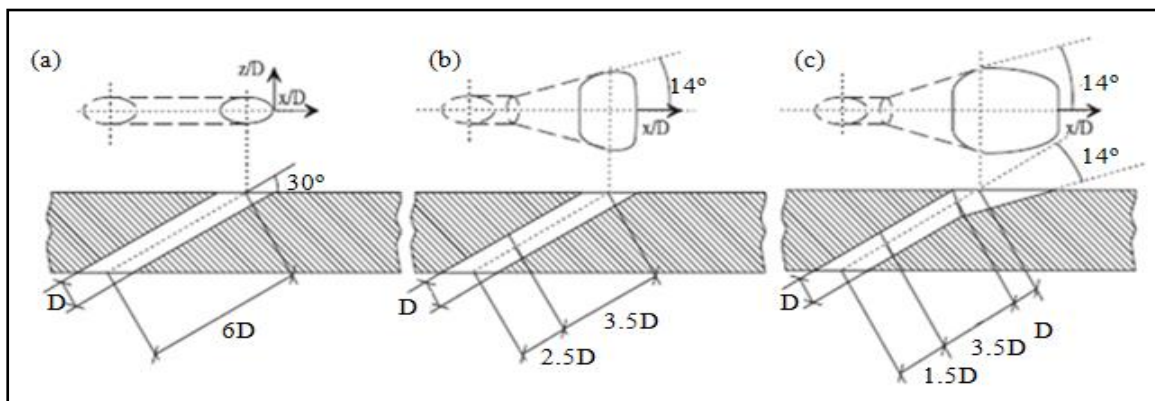


Fig. 3.15 Hole Exit Shapes (a) M9 Circular shape (b) M10 Fan shape (c) M11 Laidback fan shape

M9, M10, M11: Gas turbine blade leading edge models having the circular, fan shaped and laidback fan shaped holes at 30° hole inclination angle with spanwise direction having the five rows as one row of holes on stagnation line and two rows of holes on either side of stagnation line at 30° and 60° orientation respectively. 5:1 scaled up inlet hole diameter of 4 mm is considered for these shaped hole models. The geometrical details and the hole angles of these models for the different shapes are shown in the Fig. 3.12 to Fig. 3.15.

Based on the detailed literature survey and with the current work experience in cooling effectiveness measurements, the shaped holes over the leading edge test models are taken up for the analysis of better cooling effectiveness.

Gritsch et al. (1998) used one hole to find out the adiabatic wall effectiveness measurements of film-cooling holes with expanded exits. Gritsch et al. (2000) used one hole to find out the near hole heat transfer coefficients with the expanded exits. Gritsch et al. (2005) used one row of holes to find out the effect of hole geometry on the thermal performance of fan-shaped film cooling holes. These considered expanded hole geometries showed the better cooling effectiveness over the simple cylindrical hole geometries. Hence, these similar expanded holes are considered for the complete leading edge region with the actual scaled up geometry with the realistic non-dimensional flow parameters in the proposed study to know the cumulative effect of rows on cooling effectiveness and heat transfer coefficients.

The coolant jet spreads more laterally, and velocity of the coolant at the exit of the shaped holes is lower than the cylindrical holes with the lower lift-off due to the increase in the area at the exit of the shaped holes. Hence, the drag effect is lower on the mainstream in the case of shaped holes as compared to the drag effect of circular holes. This is an added advantage in the aerodynamics point of view along with the higher cooling effectiveness. Hence the introduction of shaped holes is more beneficial than the regular cylindrical holes in aerodynamics point of view over the blade passage area.

3.1.7 Test Run Details

Sl. No.	Test Model Geometry Details	No. of Models	No. of Test Runs
1	Hole Orientation Angle models	03	24 Runs
2	Hole Inclination Angle models	04	32 Runs
3	Hole Pitch variation models	01	08 Runs
4	Hole Shape variation models	03	24 Runs

Total number of test rig runs including repeat runs = 88 + 88 = 176 Runs.

3.2 Fabricated Gas Turbine Leading Edge Models by RPT Method

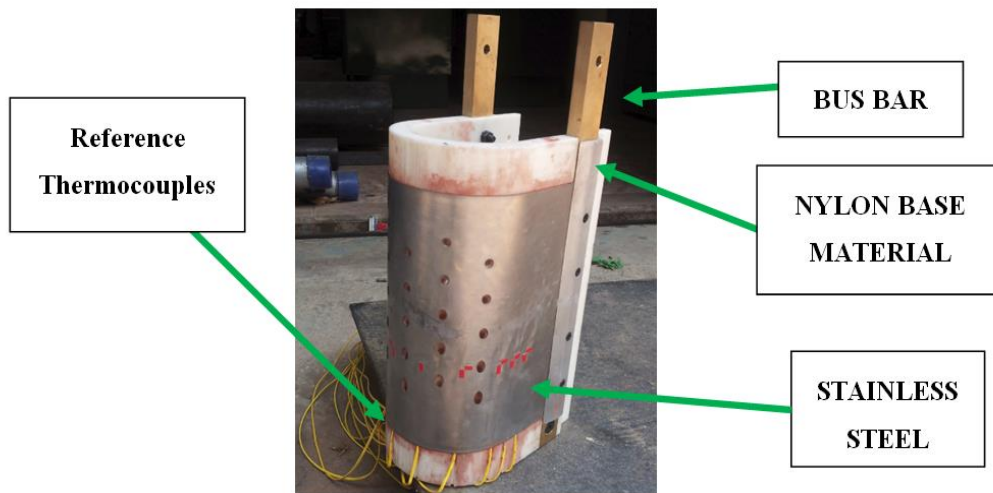


Fig. 3.16 Fabricated leading edge model with S.S sheet and bus bars

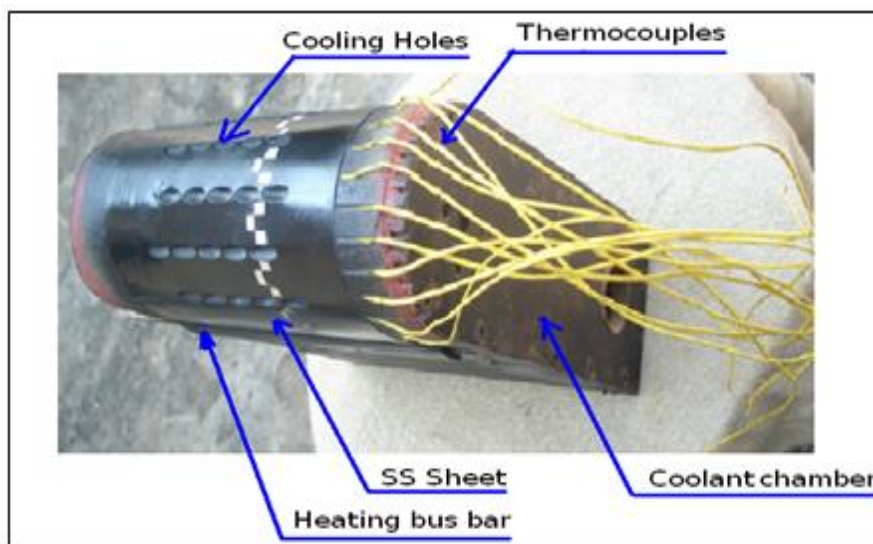


Fig. 3.17 Test model with thermocouples and coolant chamber

Semicircular leading edge models are made with the low thermal conductivity nylon based material to avoid heat losses from the gas path noncontact side of the model. These models are prepared by Rapid Proto Typing (RPT) method with Selective Laser Sintering (SLS) process. The material used for the model is nylon, having a low thermal conductivity 0.3 W/mK , which can withstand up to $140 \text{ }^\circ\text{C}$. Hard foam is filled in the model slots to have the further low thermal conductivity. The test models are prepared half-cylindrical with flat downstream surfaces by attaching the coolant chamber. Models are prepared with an outer diameter of 90 mm , and the inner

diameter of 70 mm and the model height is considered as 210 mm. The test models are with the rows of film cooling holes with the various film cooling hole geometries. The test models are prepared to bring out the effect of hole geometrical and location parameters. The Fig. 3.16 shows a fabricated model of turbine blade leading edge scaled up configuration. The stainless steel sheet having a thickness of 0.15 mm with a required film cooling hole geometry, machined by water jet cutting is wound over the model. During the heat transfer coefficient measurement experiments, this stainless steel sheet with an area of 210 x 160 mm is connected in series by brass bus bars to supply the high current at low voltage to have the constant heat flux condition over the model for heat transfer coefficient experiments. The reference thermocouples are soldered underside of the s.s sheet for applying the correction factor to the thermogram data in both the film cooling effectiveness and heat transfer coefficient experiments data analysis. These thermocouples mounted on the model are routed through the model slots as shown in the Fig. 3.17. The fabricated test model is black painted to have the uniform emissivity for the capture of accurate infrared thermal images. The markers are placed on the test model, to identify the thermocouple locations on the IR thermal image. Fig. 3.17 shows the black painted leading edge test model with the coolant chamber, prepared for placing in the test section.

3.3 Experimental Setup

Experimental work is carried out in open type subsonic film cooling test rig available at Heat Transfer Laboratory, Propulsion Division, CSIR-National Aerospace Laboratories, Bengaluru. The schematic view of the film cooling methodology is shown in Fig. 3.18 and the schematic view of the experimental test rig is shown in Fig. 3.19. The schematic of the coolant air supply line with automatic liquid nitrogen supply heat exchanger bath is shown in the Fig. 3.20. The photographic view of the complete test rig with instrumentation is shown in Fig. 3.21. For the experiments, the mainstream air is drawn from the centralized compressed air facility. The compressed air is passed through the settling chamber for having the uniform flow and then passed into the test section having the size of 320 x 230 x 700 mm where it flows over a leading edge test surface as shown in Fig. 3.22. The required mainstream air velocity at the inlet to the test section is maintained by controlling the air through the pressure

control valve placed much ahead of the test section in the main flow line. The experimental test rig is also having the 150 kW electrical heater in the main streamline, for heating the mainstream air for the higher density experiments. The maximum air temperature of 150 °C can be achieved for the main flow. Settling tank with honeycomb meshes is placed in the main flow line ahead of the test section to have the uniform flow into the test section. From the main supply of compressed air, a by-pass is provided to the coolant line settling tank for the coolant supply to the coolant chamber of the test model through the liquid nitrogen heat exchanger bath. The coolant air mass flow is controlled using the pressure regulator placed in the coolant line. The coolant air is passed through a liquid nitrogen heat exchanger bath and to the coolant chamber of the test model. The heat exchanger consists of a copper coil with some turns covered inside an insulating chamber. The coolant air temperature is maintained at 231 K by maintaining the level of liquid nitrogen in the heat exchanger to have the required density ratio of 1.30. An automated liquid nitrogen flow controller is used to maintain the level of liquid nitrogen in the heat exchanger as per the coolant temperature requirement. The schematic of the automated liquid nitrogen flow control system is shown in the Fig. 3.20. Both the mainstream flow and coolant flow parameters are maintained accurately to have the required blowing and density ratios. Initially, around 20 minutes is required for achieving the steady state flow conditions of both the mainstream and coolant flows. In the subsequent flow settings for other blowing ratios, around 10 minutes is required for achieving the steady state coolant flow conditions. The coolant flow temperature is maintained by controlling the liquid nitrogen flow in coolant line heat exchanger bath. After achieving the steady state flow conditions of both the main and coolant flow conditions, the thermal images of the test surface are captured using an IR thermal camera.

The temperature acquired by the IR camera is not the real wall temperature hence the thermal images data is corrected by using the pre-calibrated equations. The detailed camera calibration methodology and the calibration equations are shown in an appendix -III. To perform in-situ calibration, K-type thermocouples are mounted over the test surface at various locations for exact surface temperature measurement.

Visible markers of aluminum are attached to the surface near thermocouples, to recognize the thermocouple location when viewing through the IR camera. Temperatures indicated by these thermocouples are used to correct the thermal images. Apart from this, two K-type thermocouples are placed in the mainstream duct and coolant chamber to measure mainstream and coolant flow temperature. All these thermocouples are connected through a connector to a FLUKE 2680A data acquisition system temperature scanner. The scanner, in turn, is connected to a computer, in which the temperatures are displayed with the help of FLUKE DAQ software. Static and differential pressures in the mainstream and coolant air flow are measured by connecting the pressure ports (near the inlet to the mainstream duct and coolant chamber) to the Pressure Net Scanner. Pressure Net Scanner is connected to a computer, which displays and records the pressures at required locations. A pitot tube and thermocouples are located upstream of the leading edge model at a distance of 150 mm to measure the flow velocity and total temperature. Total and static pressure taps of the pitot tube are located at two positions centrally on top and bottom of the test section duct at 150 mm ahead inlet to the leading edge model. Similarly, thermocouples are placed at two positions centrally on sidewalls of the test section duct at 150 mm ahead inlet to the leading edge model. The location of the thermocouples in both the mainstream and coolant air lines and the pressure sensor locations are shown in the Fig. 3.19, i.e., the schematic of the experimental test set up.

Using the pressure regulator, the coolant air pressure is maintained in the coolant chamber as per the required blowing ratios, and the respective coolant mass flow is measured using the orifice meter in the coolant line.

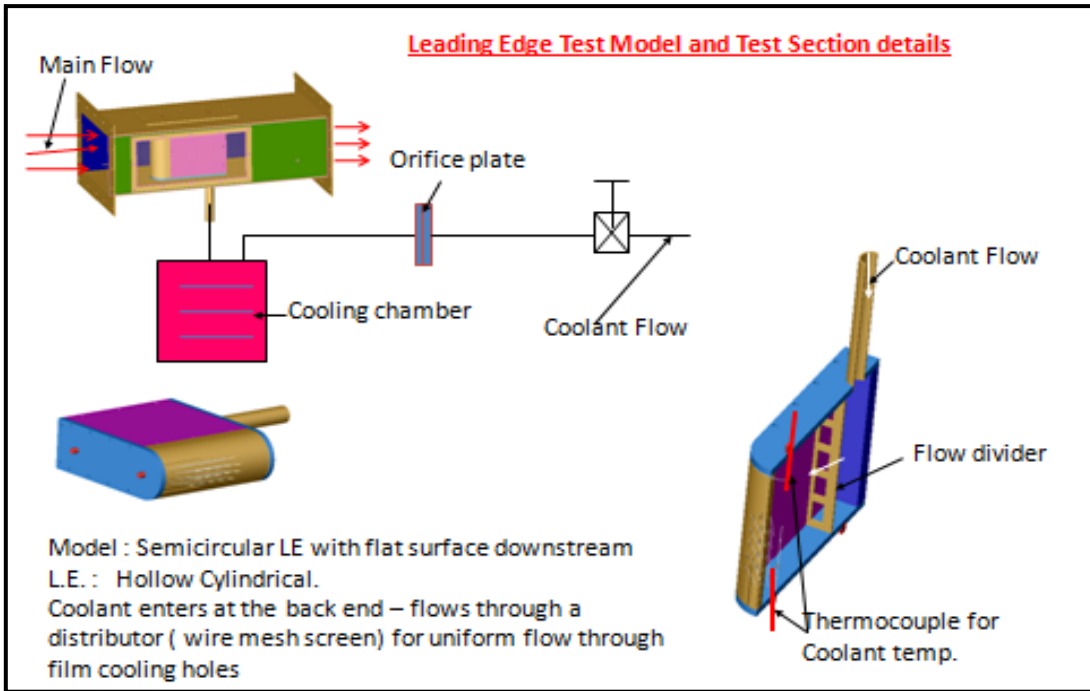


Fig. 3.18 Schematic of film cooling test methodology

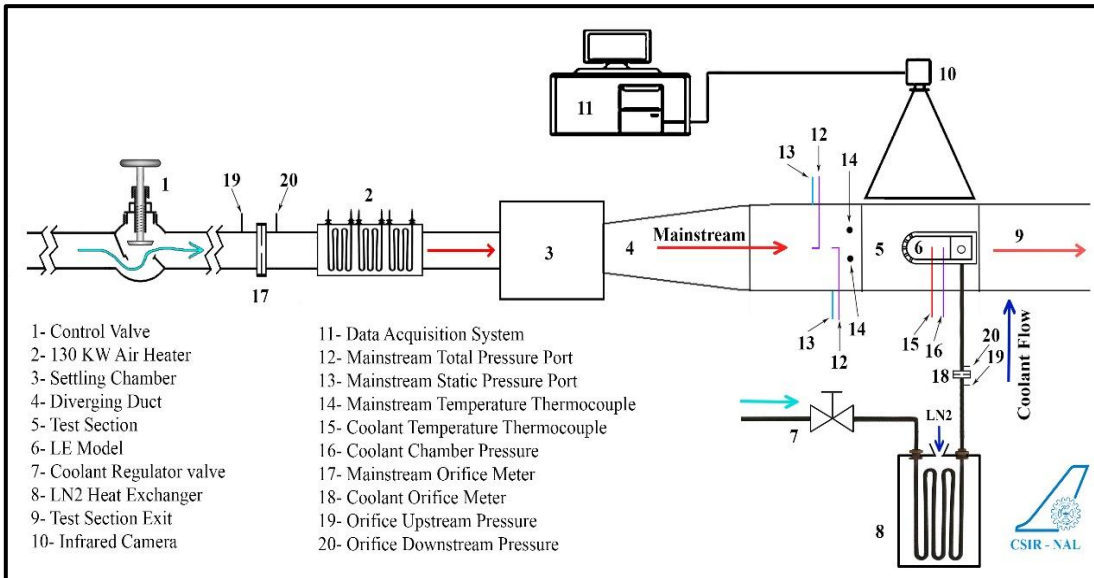


Fig. 3.19 Schematic view of the experimental test rig

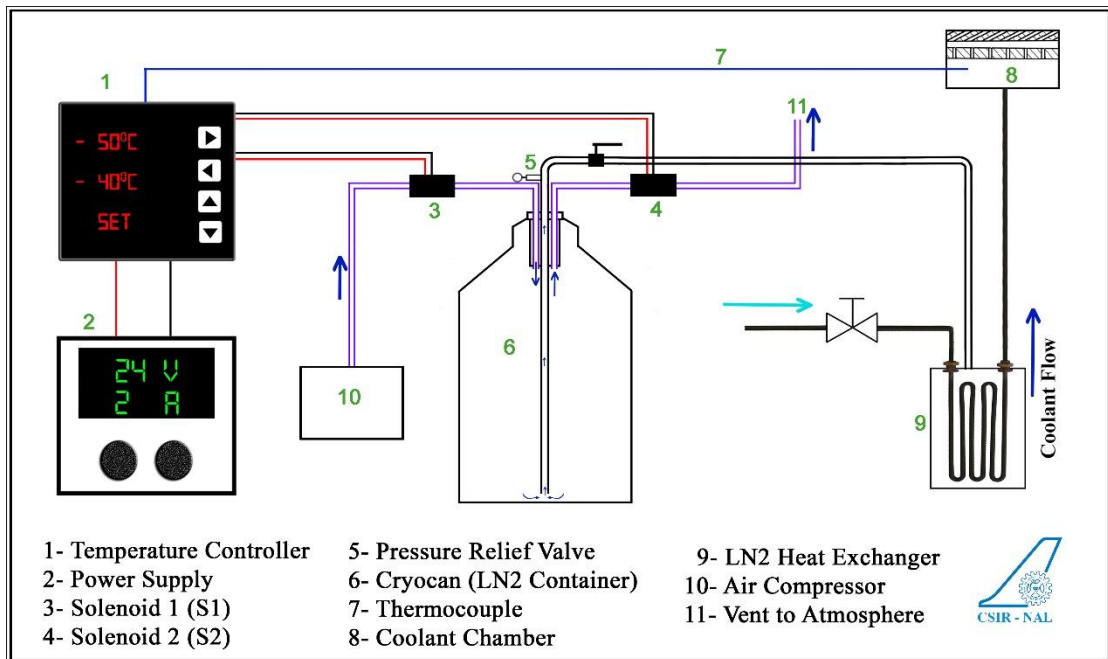


Fig. 3.20 Schematic of the automated liquid nitrogen flow controller system

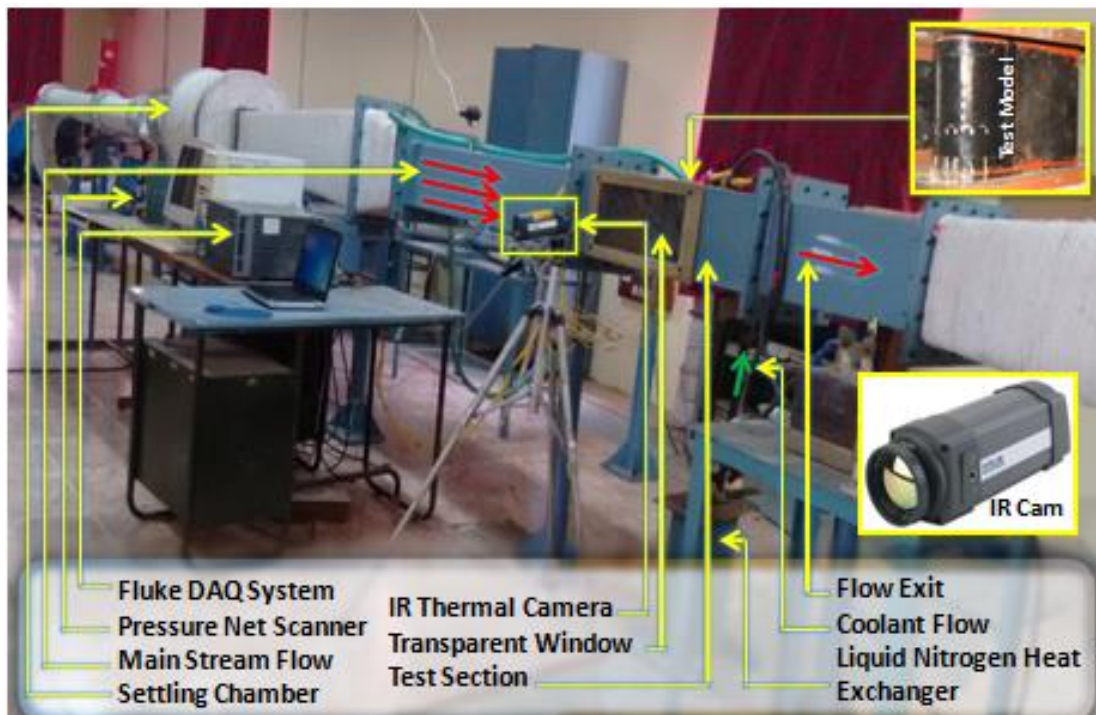


Fig. 3.21 Photographic view of the test rig with instrumentation

(Source: CSIR-National Aerospace Laboratories, Bengaluru)

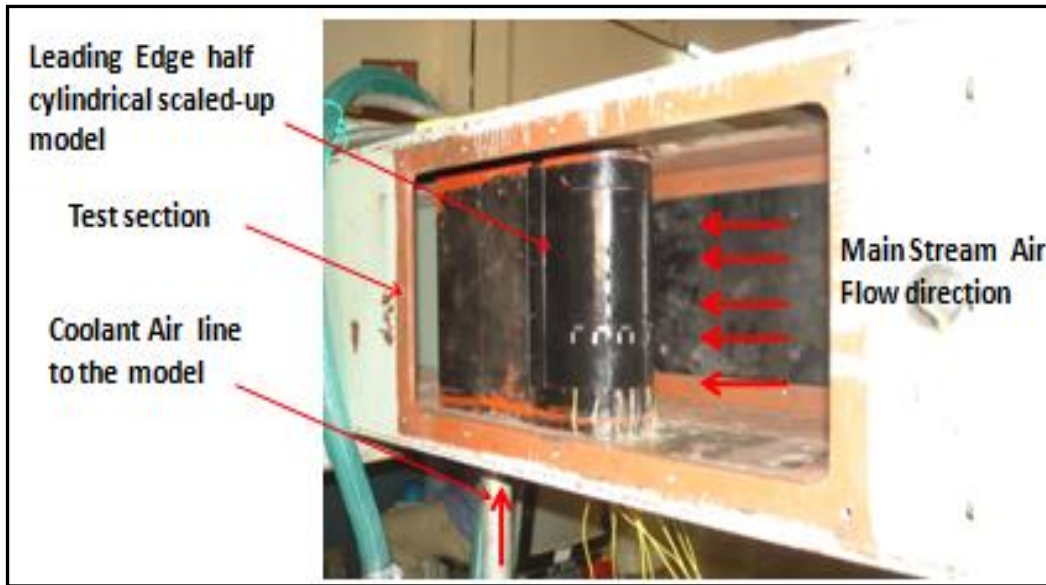


Fig. 3.22 Leading edge test model mounted in the test section

3.4 Instrumentation systems used in the experiments

The instruments used in the experiments are explained below in detail along with their specifications and ranges

3.4.1 Pressure Measuring System

Fig. 3.23 shows the instruments connected to the test rig. Pressure net scanner is used for measuring the pressure through the pressure ports. Pressure measurements are carried out using the Pressure Net Scanner (Model 9116 Pneumatic Intelligent Pressure Scanner) by providing static pressure ports and pitot tubes at the mainstream, at orifice meter and coolant chamber with a maximum uncertainty of 150 Pa (level of confidence of approximately 95%). The pressure measurements are made at the inlet and outlet of the test section, coolant orifice, and mainstream orifice respectively. At the inlet to the test section, static pressure is measured, and the pitot tubes are placed for total pressure measurement. By maintaining the required pressure difference total and static pressures, the mainstream velocity is being maintained. The location of the pressure ports in both the mainstream and coolant air lines are shown in the Fig. 3.19, i.e., the schematic of the experimental test set up. Pressure Net scanner used for the pressure data acquisition during experiments is shown in Fig. 3.23.

3.4.2 Temperature Measuring System

To monitor the mainstream temperature, thermocouples are connected at the inlet of the test section duct at two locations. On the test model, the thermocouples are soldered underneath of the surface S.S sheet at different spacing locations to measure the surface temperature during the experiments to implement the correction factor for IR thermal images. In total, sixteen K-type thermocouples (calibrated accuracy of ± 0.36 °C) are used in the experiments, two in the mainstream, two in the coolant chamber, twelve on the test surface as a reference for correcting the thermal images and one for the atmospheric temperature measurement.

Since the thermocouples are used in both hot and cold environments, the k-type are used for the better suitability. K-type thermocouples can be used from -270 to 1260 °C and has a standard accuracy of $\pm 0.75\%$ over a full scale. K- type thermocouples (Chromel / Alumel) are inexpensive, corrosion resistant and has the lower oxidation properties. These thermocouples are calibrated over a range of -50 to 150 °C and have an accuracy of ± 0.36 °C. The locations 14 and 15 indicate the mainstream and coolant air temperature measurement thermocouple locations in the schematic view of the experimental test set up, i.e., Fig. 3.19.

A fluke made data acquisition system is used to record the thermocouples temperature data during experiments is shown in Fig. 3.23. All these thermocouples are connected to the 80 channel FLUKE 2680A temperature scanner data acquisition system.



Fig. 3.23 Temperature DAQ system, pressure net scanner and IR instruments

The infrared radiations emitted by the test surface are captured using FLIR A655sc long wave infrared camera, which operates in a range of 7.5 to 14.0 μm . The camera has different ranges to measure the surface temperature in the range of $-40\text{ }^{\circ}\text{C}$ to $2000\text{ }^{\circ}\text{C}$. The camera was set at a range 1 of $-40\text{ }^{\circ}\text{C}$ to $150\text{ }^{\circ}\text{C}$ with the accuracy of $\pm 2\text{ }^{\circ}\text{C}$ over the full-scale measurement. The camera captures high-quality thermal images of 640×480 pixels resolution. The images captured by IR camera are recorded and saved to a computer using FLIR Research IR software. The transparent window was so selected that it allows the infrared radiation in the spectral band of the IR camera. The test surface is viewed using an IR camera, through this transparent window of thin polyurethane sheet of thickness at five μm and it has a very little effect on IR transmissivity. The photographic view of the Infrared camera is shown in the Fig. 3.24.



Fig. 3.24 Infra Red Thermal Camera A 655sc

3.4.3 Mass Flow Measuring System

The coolant and mainstream mass flow rates were measured by orifice meters. The orifice diameter of 20.13 mm is used in the coolant flow line, and 119.78 mm is used in the mainstream flow line. The upstream and downstream static pressure ports to the orifice plate are made at D , and $D/2$ locations as per the BIS standards reference IS15675:2006 for the mass flow measurements. The mass flow measurement equations are made and used as per the BIS standards. The detailed mass flow measurement methodology and the acquired mass flow data and coefficient of discharge values of cooling holes are shown in an appendix -I.

3.4.4 Specification of Instruments used

The instruments used in the experiments for the data acquisition and monitoring of the flow parameters are shown in Table 3.2. The details of specifications, range, accuracy, and resolution values are shown in the table for all the instruments. All the instruments are calibrated using the standard calibration of primary and secondary sources before using in the experiments.

Table 3.2 Range, Resolution and Accuracy of instruments used

Sl. No.	Name of Instrument	Specifications & Range	Accuracy & Resolution	Nos. Used
1	Intelligent Pressure Scanner (Model: 9116, Pressure System)	Measurement Range: 10 Inches of Water Column to 10 PSI. (Differential Pressures) No. of Channels: 16 Operating temperature: 0 to 50 °C	Accuracy: $\pm 0.05\%$ of FS Resolution: 0.01 Inch of the water column	01 No.
2	Fluke Temp. Data Acquisition System (Model No: 2680 A)	No. of Channels: 80 Channels	Accuracy: ± 0.75 °C Resolution: 0.01 °C	01 No.
3	FLIR Make A655sc InfraRed Camera	Measurement Temperature range: -40 to 2000 °C (In Four Ranges)	Accuracy: ± 2 °C Resolution: 0.001 °C	01 No.
4	K – Type Thermocouples	Omega Make, -200 to 1260 °C (Calibrated over a range of -50 to 150 °C and have an accuracy of ± 0.36 °C)	Accuracy: ± 0.36 °C Resolution: 0.01 °C	12 Nos.
5	Pressure Gauges	Omega make, 0-14 Bar	Accuracy: ± 0.2 Bar Resolution: 0.02 Bar	04 Nos.

3.4.5 Experimental Uncertainty

Uncertainty estimates are determined using the methodology proposed by J. P. Holman (2012) in the book “Experimental Methods for Engineers”. Uncertainty in the calculation comes from the measurement of mainstream and coolant pressures, temperatures, and test surface infra-red wall temperatures measurements. The calibrated pressure sensors and thermocouples are used for maintaining the flow parameters as per the requirement. The temperatures are measured using type K thermocouples with the uncertainty of ± 0.36 °C. The measurement system (FLUKE 2680A data acquisition system temperature scanner) has an overall absolute accuracy of ± 0.75 °C. Hence, the overall uncertainty on the temperature measurement is approximately 1.1 °C. This uncertainty is dependent upon the thermocouple calibration procedure. Uncertainty in the test surface wall temperature measured by the IR camera is ± 2 °C. Some uncertainty also gets involved during calibration of thermal images. This happens due to uncertainty in determining the exact locations of thermocouples concerning pixel values used for calibration. Pressure Net scanner uncertainty is $\pm 0.05\%$ of the measured pressure, and this uncertainty is dependent upon the pressure transducer calibration procedure. All the instruments used in the experiments are calibrated with the standard calibrating of primary and secondary sources. Orifice mass flow meters are used for coolant and mainstream mass flow data acquisition.

Cooling effectiveness is found for the film cooling configurations by varying the flow parameters at different geometrical parameters of cooling holes. The flow parameters varied are density ratio (Coolant and mainstream temperatures variation), blowing ratio (coolant and mainstream pressures variation) and Reynolds number (coolant and mainstream pressures variation). Hence, the uncertainty in the pressure and the temperature measurements has a strong impact on the cooling effectiveness accuracy. The uncertainties in the blowing ratios, density ratios, Reynolds numbers and thereby the uncertainties of cooling effectiveness and heat transfer coefficients are calculated. The typically calculated uncertainties of measured and calculated parameters with the detailed analysis are shown in an appendix-IV.

The error estimate is carried out based on the accuracy deviations in the measurements of pressure, temperature and mass flows. By using these deviations, an error estimate is made for the Reynolds number; mass flows, density ratio, blowing ratio, cooling effectiveness and heat transfer coefficient values for the accuracy of results. Based on the calculations, the % error in the flow parameters and the derived results are found as follows. These values need to be considered for the accuracy of results.

- Reynolds numbers are 0.49% (at a Reynolds number of 3×10^5 based on the hydraulic diameter of the duct, the uncertainty is ± 1505 , and at a Reynolds number of 1×10^5 based on the test model leading edge diameter, the uncertainty is ± 500).
- Coolant mass flow is 0.06% (at a mass flow of 35.5 Kg/hr, the uncertainty is ± 0.021 Kg/hr) and 0.005% (at a mass flow of 140.6 Kg/hr, the uncertainty is ± 0.0076 Kg/hr).
- Mainstream mass flow is 0.007% (at a mass flow of 4877.5 Kg/hr, the uncertainty is ± 0.3242 Kg/hr).
- Density ratio of 1.24 is 0.58% (± 0.072).
- Blowing ratios is 0.51% (at a blowing ratio of 2.5, the uncertainty is ± 0.013 , and at a blowing ratio of 1.1, the uncertainty is ± 0.006).
- Cooling effectiveness at 0.85 is 3% (the uncertainty is ± 0.025) and 0.3 is 8.09% (the uncertainty is ± 0.024).
- Heat transfer coefficient at $71 \text{ W/m}^2\text{K}$ is 6.99% (the uncertainty is $\pm 5 \text{ W/m}^2\text{K}$)

3.5 Experimental Procedure

Form the adiabatic wall effectiveness approach, the adiabatic film cooling effectiveness is determined at a density ratio of 1.30 by varying the blowing ratios. The mainstream air is passed at the room temperature, and the coolant air is maintained at a temperature of 231 K to have the density ratio of 1.30. The coolant air is passed the liquid nitrogen heat exchanger bath, and the level of liquid nitrogen is controlled to maintain the coolant temperature. Heat transfer coefficients are measured by maintaining the constant heat flux conditions over the test surface at a

density ratio of 1.0. The turbulence intensity has been measured at 90 mm (One leading edge diameter) upstream the leading edge of the vane, using the hotwire anemometer with M/s Dantec make velocity probes, and it was found to be 8.0%. Both the cooling effectiveness and heat transfer coefficient experiments were performed at a mainstream Reynolds number of 1×10^5 based on the leading edge diameter.

Mainstream Reynolds number is maintained based on the leading edge diameter of the test model placed centrally at the mid-span of the test section. Here the leading edge diameter is 90 mm, and the test section is having the size of 320 x 230 x 700 mm. The Reynolds number is maintained as per the real engine NGV configuration, and it is 1×10^5 based on the leading edge diameter and 3×10^5 based on the Hydraulic diameter (The hydraulic diameter of the mainstream flow channel is 0.2676 m).

3.5.1 Film Effectiveness Measurement Experiments

In film cooling experiments, the mainstream air at room temperature is allowed to flow over the test surface, and the coolant air is passed through the liquid nitrogen heat exchanger bath, which ejects through the film cooling holes. The required coolant flow is maintained to have the blowing ratios in the range of 1.0 to 2.5. The coolant temperature is maintained at 231 K by controlling the liquid nitrogen flow to the heat exchanger to have the required density ratio of 1.30. The mainstream air at ambient temperature coming from the centralized compressor facility is maintained at a total to the static differential pressure of 15.76 mm of H₂O to have the Reynolds number of 1×10^5 based on the leading edge diameter and 3×10^5 based on the hydraulic diameter of the mainstream flow channel. Initially, around 20 minutes is required for achieving the steady state flow conditions of both the mainstream and coolant flow in the film cooling effectiveness experiments. In the subsequent flow settings of other blowing ratios, around 10 minutes is required for achieving the steady state flow conditions.

After achieving the steady state flow conditions of both the mainstream and coolant flows, the wall temperature of the test model surface is captured using the non-contact type infrared camera as a thermographic image. The acquired thermal images raw data is converted into the wall temperature data by applying the correction factors.

The mainstream temperature data is acquired using the calibrated thermocouples at the inlet of the test model. The film effectiveness measurements are made with the mainstream at ambient temperature, coolant temp at 231 K and with the wall temperature measured as adiabatic wall temperature, as the surface is unheated and well insulated. The local wall temperature is a mixture temperature of the coolant and the mainstream.

Thus, the film effectiveness is found using the following relation

$$\eta = \frac{(T_m - T_w)}{(T_m - T_c)} \quad (3.1)$$

Where,

T_m = Mainstream temperature in K

T_w = Local measured steady state wall temperature in K

T_c = Coolant temperature before injection in K

The planned test condition parameters for the film cooling effectiveness are shown in Table 3.3.

Table 3.3 Experimental test conditions for adiabatic film cooling effectiveness measurements

Adiabatic Film Cooling Effectiveness										
Main Stream Conditions (27 °C)						Coolant Conditions (-42 °C)				
B.R	Temp	Density	Velocity	Mainstream (ΔP)		Temp	Density	Velocity	Coolant Chamber Pressure	
Const.	K	Kg/m ³	m/s	N/m ²	mm of H ₂ O	K	Kg/m ³	m/s	N/m ²	mm of H ₂ O
1.00	300	1.051	17.15	154.56	15.76	231	1.364	13.21	119.09	12.14
1.25	300	1.051	17.15	154.56	15.76	231	1.364	16.52	186.08	18.98
1.50	300	1.051	17.15	154.56	15.76	231	1.364	19.82	267.96	27.32
1.75	300	1.051	17.15	154.56	15.76	231	1.364	23.13	364.72	37.19
2.00	300	1.051	17.15	154.56	15.76	231	1.364	26.43	476.38	48.58
2.50	300	1.051	17.15	154.56	15.76	231	1.364	33.04	744.34	75.90

Note: Density of Air at 27 °C and 920 m sea level of Bengaluru is 1.051 kg/m³

and at -42 °C is 1.364 Kg/m³

B.R = ($\rho_c v_c$) / ($\rho_{ms} v_{ms}$)	D.R = ρ_c / ρ_{ms}	D.R = T_{ms} / T_c	Abs. Viscosity	MS Reynolds Number	Main Stream Mass Flow		
					kg/s)	(kg/min)	(Kg/hr)
1.00	1.30	1.30	1.6E-05	100012	1.33	79.60	4775.81
1.25	1.30	1.30	1.6E-05	100012	1.33	79.60	4775.81
1.50	1.30	1.30	1.6E-05	100012	1.33	79.60	4775.81
1.75	1.30	1.30	1.6E-05	100012	1.33	79.60	4775.81
2.00	1.30	1.30	1.6E-05	100012	1.33	79.60	4775.81
2.50	1.30	1.30	1.6E-05	100012	1.33	79.60	4775.81

Note: Absolute Viscosity at Room Temperature is 1.6×10^{-5} N-s/m²

3.5.2 Heat Transfer Coefficient Measurements

The heat transfer coefficients are measured with mainstream and coolant air supply at the room temperature and by maintaining the test surface at a constant heat flux. The test model is made of a low conducting material to avoid heat losses from the gas path noncontact side of the model. During the heat transfer coefficient measurement experiments, the thin stainless steel sheet with the hole geometries wound on the test model surface, is heated with the constant heat flux conditions by connecting the brass bus bars in series to supply the high current at a low voltage over the model. The stainless steel sheet is having an area of 210 x 160 mm with the thickness of 0.15 mm, is fabricated with a required film cooling hole geometry, using water jet cutting is wound over the test surface. The reference thermocouples are soldered underside of the stainless steel sheet for applying the correction factor to the thermogram data during both the film cooling effectiveness and heat transfer coefficient experiments data analysis. The test surface heated, serves as a constant heat flux surface for the heat transfer tests. Since a very thin stainless steel sheet with the thickness of 0.15 mm is used for heating by wounding over the surface with thermal insulating, the non-uniformity of heat flux is not found much over the surface. It is being checked before performing the actual experiments. The conduction loss data is estimated by the conduction loss experiments separately by varying the current and voltage

conditions. The details of conduction loss experiments and estimates are shown in an appendix-II. The total input electrical power is calculated by measuring the supplied voltage and current values to the test surface. The net heat input to the test surface is calculated by subtracting the conduction losses from the input electrical power. Here, the input electrical power and the conduction losses are calculated per unit surface area of the test plate. Hence, the calculated net heat flux, q is the net heat input per unit surface area of the test plate. The net heat transfer surface area is calculated by subtracting the film cooling holes surface area from the total test plate surface area. The heated surface exposed to the mainstream and coolant flows at the required blowing ratio settings. During the heat transfer coefficient experiments, initially it takes around 20 minutes for the first blowing ratio and constant heat flux settings and after that, around 15 minutes is required for the subsequent conditions to reach the steady state requirements. After achieving the steady state conditions of flow conditions at the required blowing ratios, the surface temperature data of the test model is captured by the infrared camera as thermographic images. The wall temperature is extracted from the thermographic image data by incorporating the correction factors, and the mainstream temperature is measured by thermocouples. The planned test condition flow parameters for the heat transfer coefficient experiments are shown in Table 3.4.

Here in the heat transfer coefficient measurement experiments, the test surface is maintained at a constant heat flux condition, the mainstream and coolant flows are allowed to flow over the test surface at the same temperature at the required blowing ratio flow conditions. Here both the mainstream and coolant air are passed at room temperature, and the mainstream flow is kept constant. The coolant flow is varied to have the different blowing ratios, and the heat transfer coefficients are calculated accordingly. The heat over the test surface is carried out by the mainstream and coolant flows at a rate as per the hole geometric and flow conditions. The effect of film cooling hole geometrical parameters on the heat transfer coefficients is studied in these experiments.

The overall cooling effectiveness estimate will be made by the designers based on these combined effects of adiabatic film cooling effectiveness and the heat transfer coefficients. The adiabatic film cooling effectiveness and the heat transfer coefficients

will provide the better insight for the optimization of hole geometries with the proper trends. Heat transfer coefficients are calculated by using the following relation for all the models at the blowing ratios of 1.0, 1.5, 2.0 and 2.5. Here, the heat transfer coefficient (h) is calculated from the net heat flux, $q = Q/A$, i.e., the net heat per unit over the test model surface area.

Net Heat Input,

$$Q = h A \Delta T = Q_{\text{gen}} - Q_{\text{loss}} \quad (3.2)$$

Net Heat Flux,

$$q = \frac{Q}{A} = \frac{Q_{\text{gen}}}{A} - \frac{Q_{\text{loss}}}{A} \quad (3.3)$$

Heat Transfer Coefficient,

$$h = \frac{q}{(T_w - T_m)} = \frac{q_{\text{gen}} - q_{\text{loss}}}{(T_w - T_m)} \quad (3.4)$$

Where,

- Q = Net input heat, Watts
- Q_{gen} = Total input heat, Watts
- Q_{loss} = Conduction heat loss, Watts
- A = Net heating surface area, m^2
- q = Net input heat flux, Watts/m^2
- q_{gen} = Total input heat flux, Watts/m^2
- q_{loss} = Conduction heat flux loss, Watts/m^2
- T_w = wall temperature of test model surface, K
- T_m = Mainstream flow temperature, K

Table 3.4 Experimental test conditions for heat transfer coefficient measurements

Heat Transfer Coefficient										
Main Stream Conditions (27 °C)						Coolant Conditions (27 °C)				
B.R	Temp	Density	Velocity	Mainstream (ΔP)		Temp	Density	Velocity	Chamber Pressure	
<i>Const.</i>	<i>K</i>	<i>Kg/m³</i>	<i>m/s</i>	<i>N/m²</i>	<i>mm of H₂O</i>	<i>K</i>	<i>Kg/m³</i>	<i>m/s</i>	<i>N/m²</i>	<i>mm of H₂O</i>
1.00	300	1.051	17.15	154.56	15.76	300	1.051	17.15	154.56	15.76
1.25	300	1.051	17.15	154.56	15.76	300	1.051	21.44	241.50	24.63
1.50	300	1.051	17.15	154.56	15.76	300	1.051	25.73	347.76	35.46

1.75	300	1.051	17.15	154.56	15.76	300	1.051	30.01	473.34	48.27
2.00	300	1.051	17.15	154.56	15.76	300	1.051	34.30	618.25	63.04
2.50	300	1.051	17.15	154.56	15.76	300	1.051	42.88	966.01	98.51
Note: Density of Air at 27 °C and 920 m sea level of Bengaluru is 1.051 kg/m ³										
B.R = $(\rho_c v_c) /$ $(\rho_{ms} v_{ms})$	D.R = ρ_c / ρ_{ms}	D.R = T_{ms} / T	Abs. Viscosity	MS Reynolds Number	Main Stream Mass Flow					
					(kg/s)	(kg/min))	(Kg/hr)			
1.00	1.00	1.00	1.6E-05	100012						
1.25	1.00	1.00	1.6E-05	100012	1.33	79.60	4775.81			
1.50	1.00	1.00	1.6E-05	100012	1.33	79.60	4775.81			
1.75	1.00	1.00	1.6E-05	100012	1.33	79.60	4775.81			
2.00	1.00	1.00	1.6E-05	100012	1.33	79.60	4775.81			
2.50	1.00	1.00	1.6E-05	100012	1.33	79.60	4775.81			
Note: Absolute Viscosity at Room Temperature is 1.6 x10 ⁻⁵ N-s/m ²										

3.5.3 Study of Experimental Consistency

To get experimental consistencies, two test runs are conducted at same blowing ratio during both film cooling effectiveness and heat transfer coefficients measurement experiments for all the considered models. The Fig. 3.25 shows the variation of average film cooling effectiveness along the downstream from the stagnation line for circular hole shape model at B.R 2.5. The Fig. 3.26 shows the variation of average heat transfer coefficient value along the downstream from stagnation line for fan shape model at B.R 2.5. From the experimental consistency between run-1 and run-2 for same blowing ratios, it is found that difference in film cooling effectiveness and heat transfer coefficient values between two test runs are negligible and thus experimental consistency is achieved.

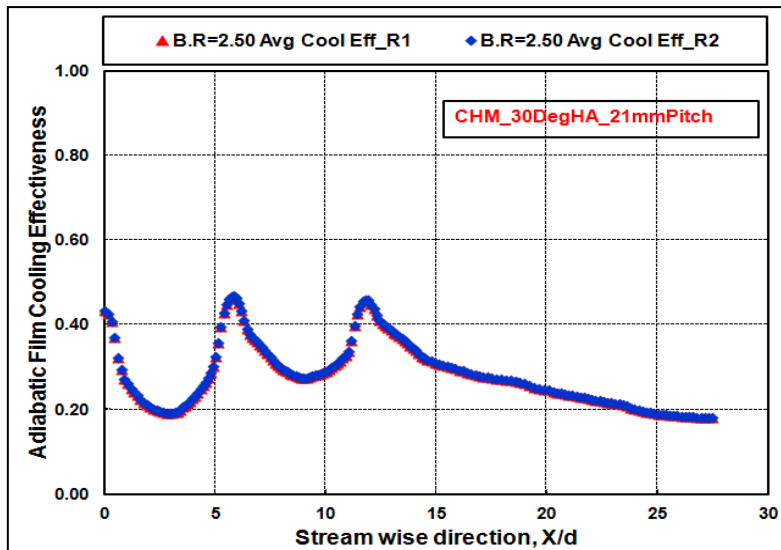


Fig. 3.25 Film cooling effectiveness data at two test runs

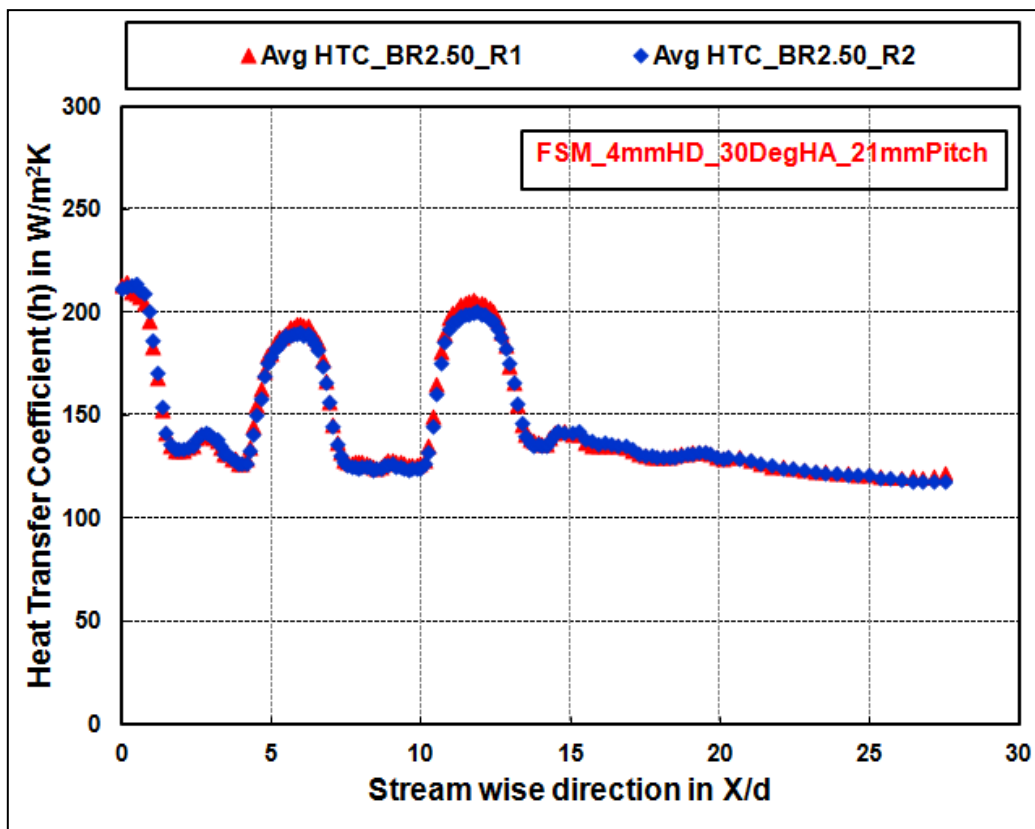


Fig. 3.26 Heat transfer coefficients data for two test runs

3.6 Validation of Experimental data

The film cooling effectiveness measurements for cylindrical hole and diffuser -shaped exits (i.e., a fan shaped and a laidback fan shaped holes) were presented in the open

literature over a flat plate (Gritsch et al. 1998). Since the similar hole configurations are used in the present study, experimental validation is made using the available data from Gritsch et al. (1998). The density ratio of 1.85 is maintained by Gritsch et al. in their study, and since the density ratio of 1.85 could not be maintained with the available test facility, the maximum possible density ratio of 1.60 is maintained in the present validation study. Because of this difference in the density ratio, the effectiveness results from Gritsch et al. is little higher than the present results. The similar test models are generated for the validation study with the hole inclination angle of 30° for all the models. Comparative plots are made at the blowing ratio of 1.5, and the comparative results are shown in the Fig. 3.27 to Fig. 3.29. Fig. 3.27 shows the centreline adiabatic film cooling effectiveness comparison with Gritsch et al. results for a circular hole model.

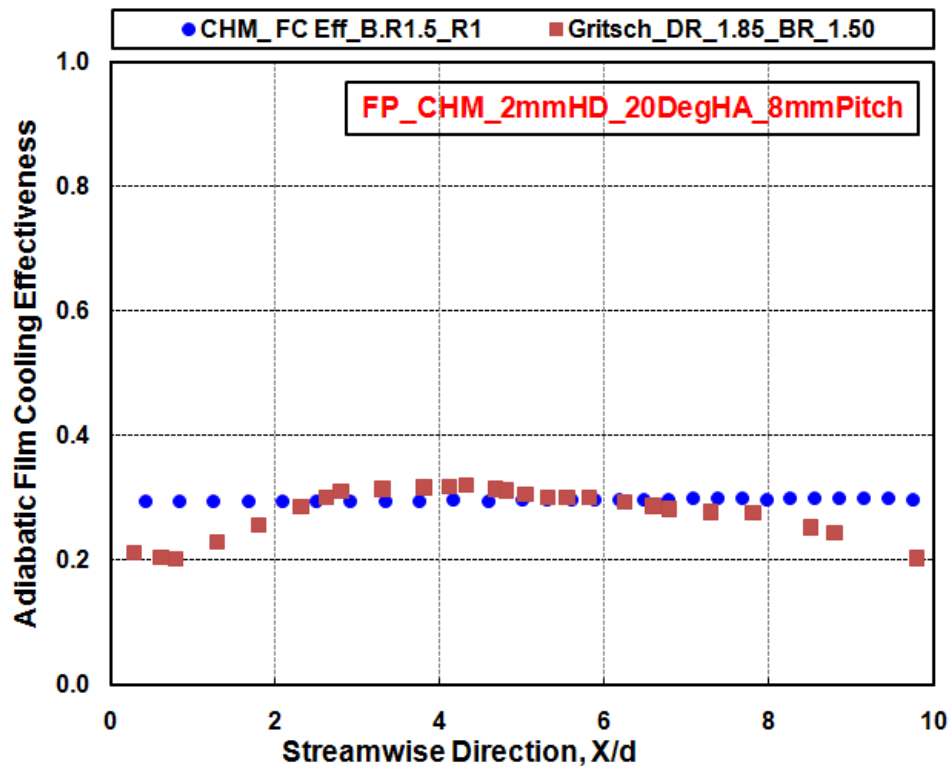


Fig. 3.27 Validation of CHM Experimental data at a blowing ratio of 1.5

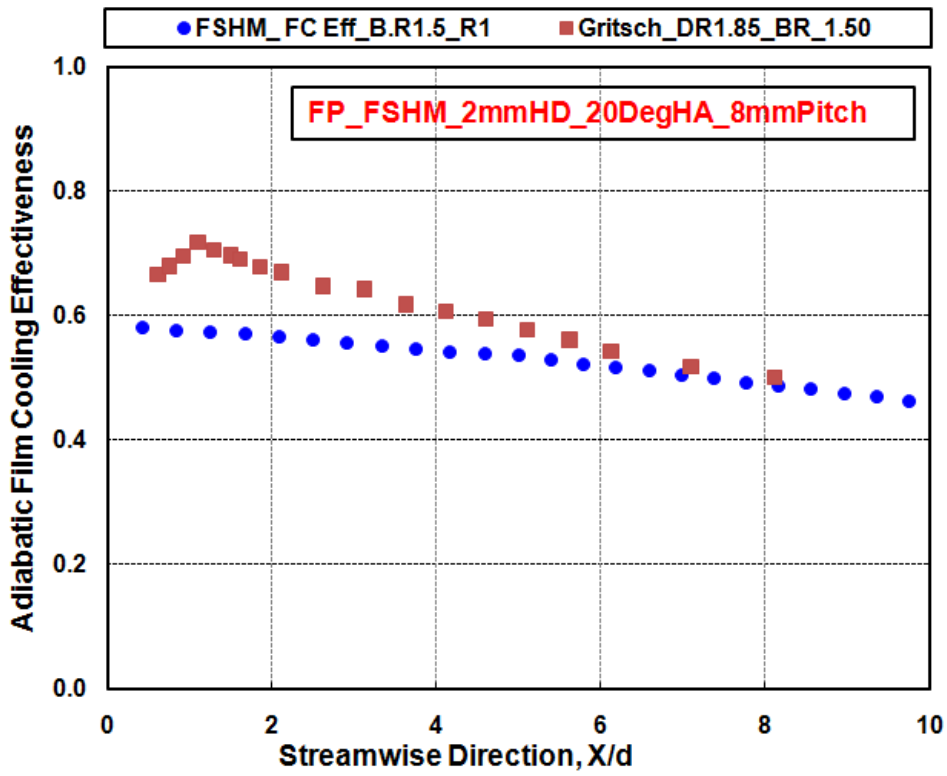


Fig. 3.28 Validation of FSHM Experimental data at a blowing ratio of 1.5

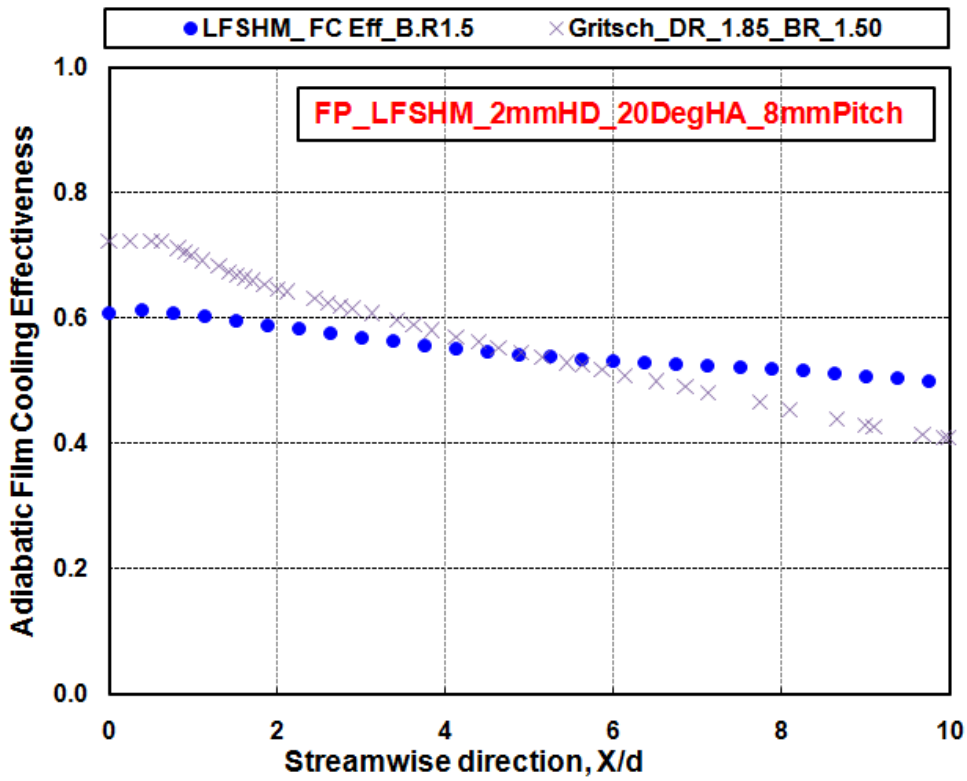


Fig. 3.29 Validation of LFSHM Experimental data at a blowing ratio of 1.5

Fig. 3.28 and Fig. 3.29 shows the comparison of the fan shaped and laidback fan shaped hole models effectiveness with that of the published data. The validation plots have shown that the present study cooling effectiveness results are same as observed by Gritsch et al. with minor deviation due to the lower density ratio in the present study.

The similar geometries considered in the published data are generated for the validation purpose with the flat plate cases. There is no work done by others with these geometries on the gas turbine blade leading edge regions (curved surfaces). With the confidence of these validated results on the flat plates, the leading edge surfaces are generated with these geometries in the present study.

CHAPTER 4

COMPUTATIONAL PROCEDURE

4 COMPUTATIONAL PROCEDURE

4.1 Model, Mesh Generation, and Boundary Conditions

Adiabatic film cooling effectiveness and heat transfer coefficients data is made numerically for different blowing ratios in the range of 1.0 to 2.5 for all the test models having the different geometric conditions to bring out the effects of hole orientation angle, hole inclination angle, hole pitch and hole shape on the gas turbine blade leading edge surface. The leading edge models are generated using solid works modeling software, meshing is done in ICEM CFD, and the computational domain is solved in ANSYS Fluent solver.

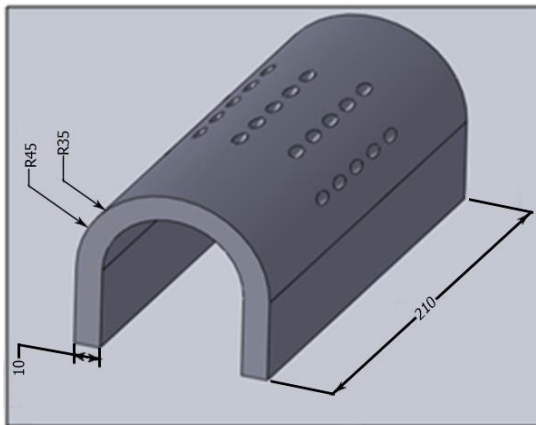


Fig. 4.1 LE model for the computation method

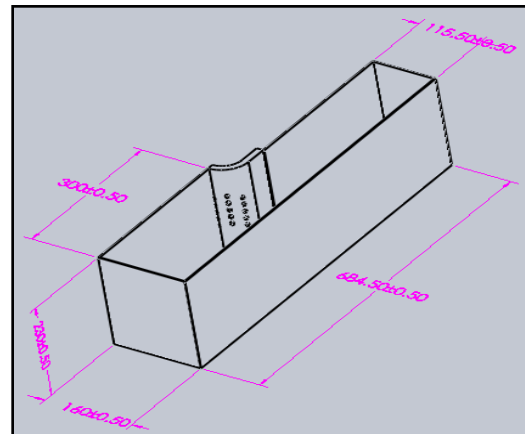


Fig. 4.2 Computational domain

The model consists of leading edge of a gas turbine blade with the symmetrical computational domain. Computational domain with the size of 684.5 x 210 x 160 mm with leading edge outer diameter of 89 mm and the inner diameter of 65 mm, having five rows of film cooling holes with the required hole diameters and pitch. A typical leading model used for computational method validity is shown in Fig. 4.1. The computational domain is taken as per leading edge film cooling experimental test section and is shown in the Fig. 4.2. Assuming symmetrical flow over the leading edge model considered half of the test section for the analysis to avoid some element cells and analysis running time. The same experimental test matrix is used in the computational analysis.

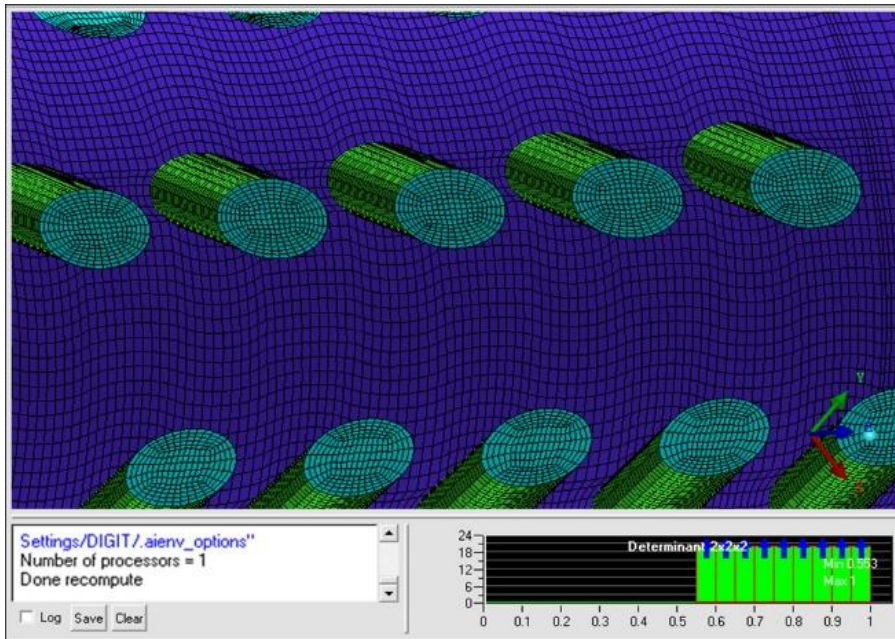


Fig. 4.3 Solid and wire frame with mesh quality 0.55

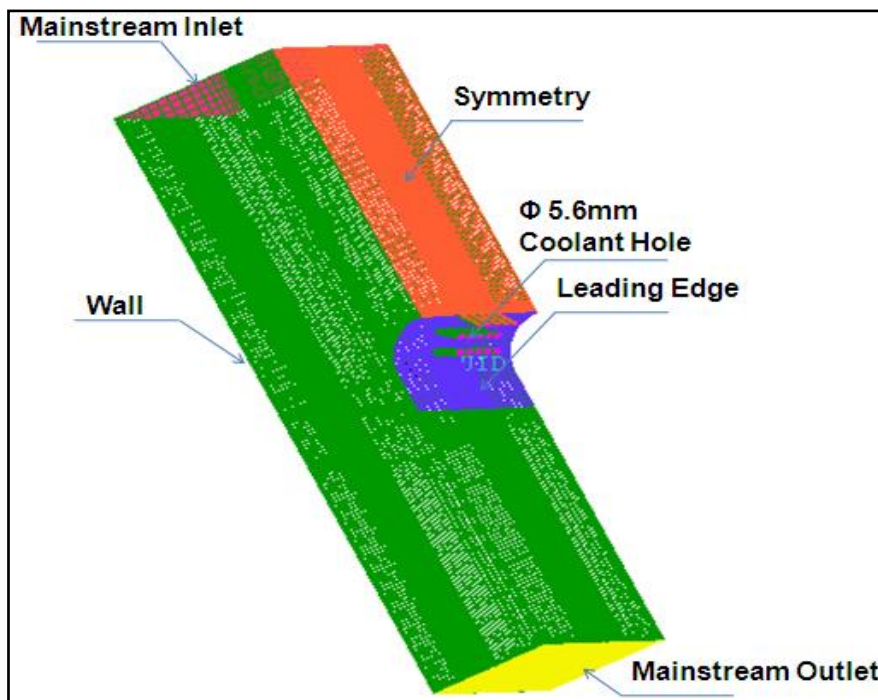


Fig. 4.4 O-grid mesh for coolant holes.

The pre-processor, solver and Postprocessor modules are employed by ANSYS 14 Fluent. The output mesh file obtained is in ‘. mesh’ format, which is used to run in fluent. Hexa type mesh is used for mainstream till leading edge of the fluid region to obtain the highest accuracy, and O grid mesh is used for the coolant flow. The mesh

quality having above 0.55 is shown in the Fig. 4.3 and. Initially by assuming $y^+ = 30$ thickness of the first layer of the grid over the leading edge surface is calculated, as per the calculation obtained first layer thickness is $\delta y = 0.161$. A total of 688228 hexahedral cells have obtained for the entire computational domain. Coolant holes are attached to the blade leading edge model with mesh connectivity by using splitting technique near the hole with fine mesh. The coolant hole with the coolant flow meshed with O grid is shown in the Fig. 4.4.

In the process of finding the solution for film cooling effectiveness and heat transfer coefficients, a k- ϵ realizable turbulence model is used to solve the computation domain and k- ϵ turbulence model is two-equation turbulence models. To choose better turbulence model suitable for this computation domain, literature survey has done, and it is found that the two-equation turbulence models are a good performer for considered flow field. Hence, the k- ϵ realizable turbulence model is used for all the blowing ratios for the CFD simulation. The coolant temperature of 231 K is applied during the film cooling experiments, and constant heat flux of experimental value is applied during heat transfer coefficients simulation to the leading edge surface to have the similar conditions as that of experiments.

4.2 Boundary Conditions for the Numerical Simulation

Table 4.1 Boundary conditions

Sl. No.	Boundary Name	Boundary Conditions
1	Mainstream inlet	Pressure inlet
2	Mainstream outlet	Pressure outlet
3	Coolant inlet	Pressure inlet
4	Coolant outlet	Interior
5	Leading edge	Adiabatic wall
6	Sidewalls	Wall
7	Symmetry	Symmetry

In the process of finding the solution for film cooling effectiveness and heat transfer coefficient, the k- ϵ realizable turbulence model is used for all the blowing ratios for the CFD simulation. The type of boundary conditions applied in the computational model shown in the Table 4.1, are applicable for the considered model configurations.

The boundary condition values are used same as per experimental test conditions which were obtained during experiments for both film cooling and heat transfer coefficient experiments. Based on the turbulence model study, it is to capture the flow phenomenon surface of the plate, or away from the boundary layer, then the k- ϵ realizable turbulence model will be used.

Initially, the three turbulence models, i.e., k-w-sst, k- ϵ standard and k- ϵ realizable turbulence models are tried to get the solution with the compound angled model, among which the k- ϵ realizable turbulence model gives the better solution, which is nearer to the experimental values as shown in Fig. 4.5. The lateral conduction is more predominant for this selected model, and due to the presence of this lateral conduction in the experiments, the effectiveness is found little higher than the CFD results.

Hence, the k- ϵ realizable turbulence model is used for the considered models for the CFD simulation. The applied mainstream and coolant boundary conditions for all the computational models are shown in Table 4.1. The boundary condition values are used the same as that of experimental test values for calculating the adiabatic film effectiveness and heat transfer coefficient respectively.

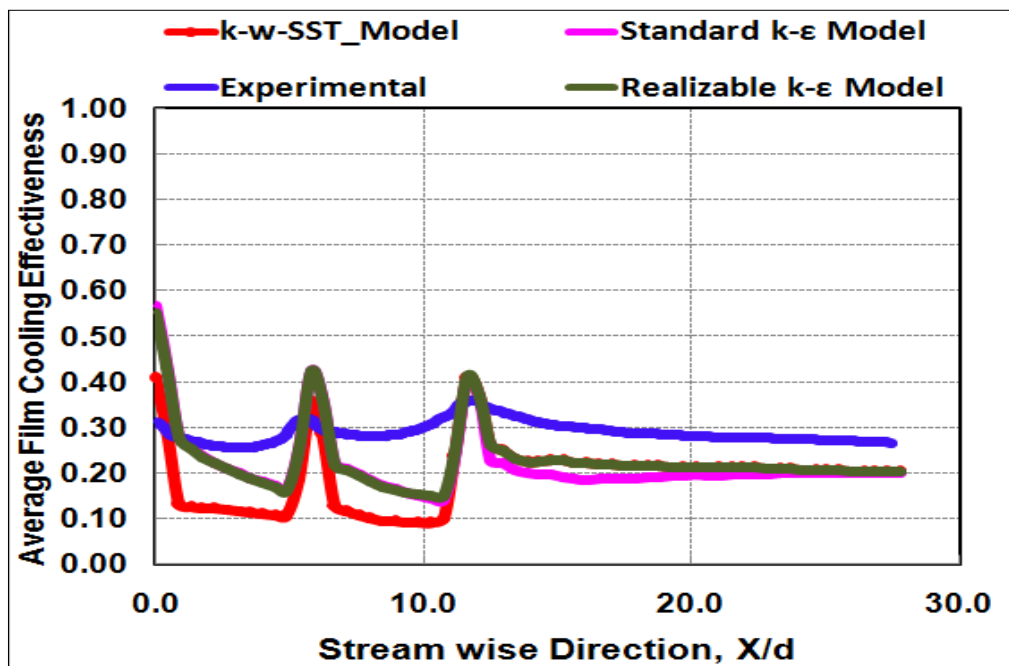


Fig. 4.5 Comparison of different CFD models with experimental data

The realizable k- ϵ model is a relatively recent development and differs from the standard k- ϵ model in two important ways,

- The realizable k- ϵ model contains a new formulation for the turbulent viscosity.
- A new transport equation for the dissipation rate, ϵ , has been derived from an exact equation for the transport of the mean-square vorticity fluctuation.

4.3 Grid Independency Test

The grid independency study was performed for different mesh size, i.e., for different element numbers. The averaged mesh quality of all these meshes considered is higher than 90%. The figure shows four different meshes with element numbers of 436198, 661084, 1137648 and 1435231. The grid dependency is plotted for all these considered mesh sizes and is as shown in Fig. 4.6. For the consider element numbers, the mesh with 436198 elements and higher showed same results and hence the lowest of them i.e., 436198 elements are considered suitable for all the further studies, the 661084 mesh size was considered in order to reduce running time and the results were nearer to the experimental values also showed the consistency and the flow patterns were also same as experimental results.

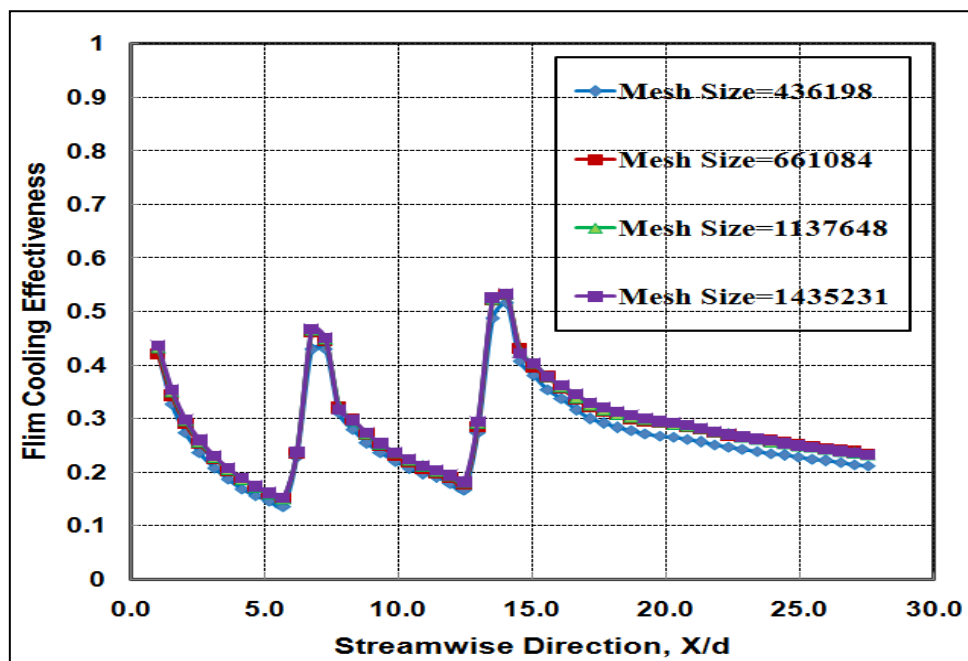


Fig. 4.6 Comparison of film cooling effectiveness for different mesh sizes.

CHAPTER 5

RESULTS AND DISCUSSION

5 RESULTS AND DISCUSSION

For the calibration of the experimental setup and for finding the correction constants some pre experiments like mass flow rate, heat conduction loss and the voltage drop across the test models are done before doing adiabatic film cooling effectiveness and heat transfer coefficients experiments to have the accurate results.

The semicircular leading edge NGV test models are considered for the cooling effectiveness and heat transfer measurements. The test models are symmetrical with the cooling holes on either side from the leading edge stagnation line. The cooling effectiveness data is captured over the test surface on one side from the leading edge stagnation line. The two pitch region cooling effectiveness and heat transfer coefficient data along the spanwise is averaged and plotted along the streamwise direction to know the effect of different hole geometrical parameters along the lateral surface of the test model. Here the different test models are considered to bring out the effect of geometrical parameters over the cooling effectiveness for which, the averaged cooling effectiveness will provide the better idea than the local cooling values.

5.1 Effect of Hole Orientation Angle (HOA) along the streamwise direction (15° , 30° and 45° from stagnation line)

To bring out the effect of hole orientation angle, three test models are considered (M1, M2, and M3) with the row of 5 holes at 15° , 30° , 45° hole orientation angles respectively from the stagnation line. The hole inclination angle of 20° is considered for all these hole orientation models.

5.1.1 Experimental Adiabatic Film Effectiveness Measurements

Thermal images are taken by the non-contact type infrared thermal camera during the experiments after achieving steady state conditions of both mainstream and coolant flows. Fig 5.1 shows the typical thermal images for the three test models with 15° , 30° , 45° hole orientation angles respectively from the stagnation line. These models are having one row of holes on either side of stagnation line with five holes, and these holes are made with 20° hole inclination angle with the surface. All the three test models have the cooling hole rows symmetrically along the stagnation line about the

flow direction of the test model. The units of scale on thermal images of Fig. 5.1 are the thermal radiation count captured by the infra-red camera. These count values are converted to the temperature using the in-situ calibration with the thermocouples placed on the test plate. And the correction factor is applied to the thermal image temperatures using the pre-calibrated IR camera equation. Using the corrected thermocouple temperature values, the cooling effectiveness and heat transfer coefficient values are calculated. The diffused temperature contour reflects in the adiabatic film cooling effectiveness plots since it is a translation based on mainstream and coolant steady state temperature values. These images show the cooling hole locations at different hole orientation angles from the blade leading edge stagnation line. The coolant air is seen coming through the holes against the mainstream flow. The hole orientation models are having only one row of holes with five holes, and these holes are made with 20° hole inclination angle with the surface. The effect of the mainstream is more on the 15° hole orientation angle model whereas the effect of the mainstream is lower on other models. Due to this the coolant effect is seen more on the 30° and 45° hole orientation angle models showing the spanwise tilt of coolant.

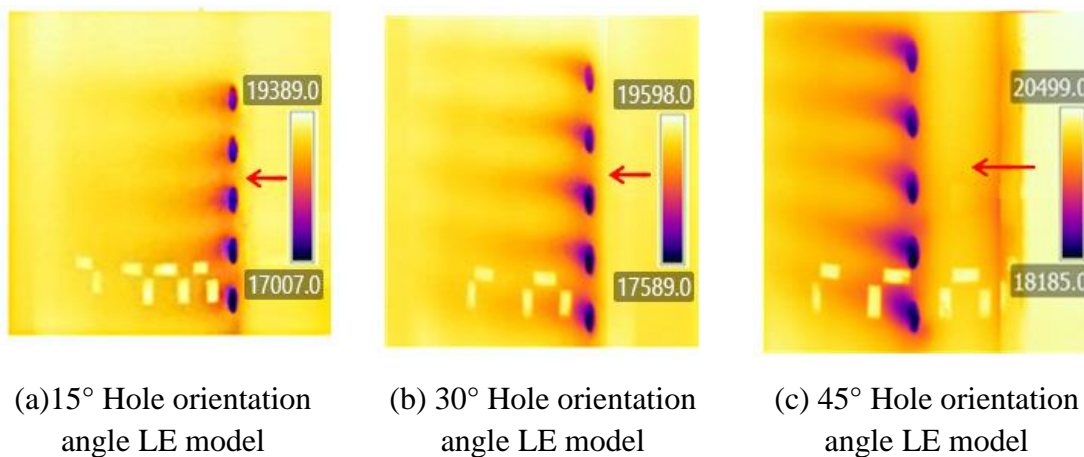


Fig. 5.1 Typical thermal images of film cooling effectiveness at a B.R of 2.0

Adiabatic film cooling effectiveness is calculated experimentally for three gas turbine vane leading edge models with 15° , 30° and 45° respective orientation rows of coolant holes from the stagnation line. The extracted data is processed, and adiabatic cooling effectiveness is found along the streamwise direction. The two pitch region

spanwise averaged cooling effectiveness results are plotted along the streamwise direction. The cooling effectiveness results are plotted from the downstream of cooling holes row along the streamwise direction. The detailed experimental results are shown in the following figures. The coolant hole coefficient of discharge values is also found for these hole orientation models; the Cd values are found to be increasing with the increase in hole orientation angle. The detailed mass flow and Cd calculations and values are given in an appendix-I.

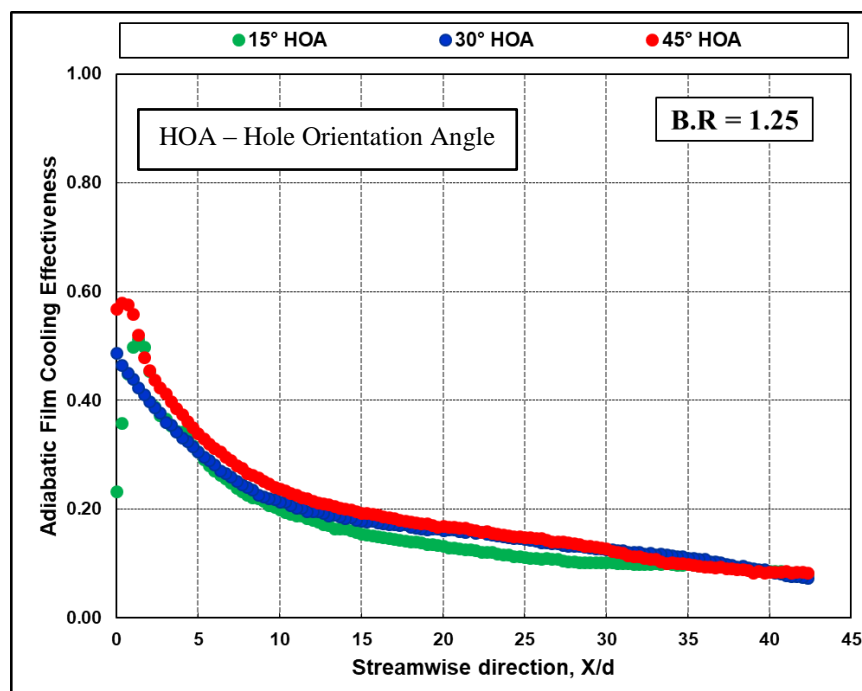


Fig. 5.2 Experimentally evaluated cooling effectiveness at a B.R of 1.25

At the blowing ratios of below 1.0, the effect of coolant flow is very less on the leading edge region. The same has been observed in the literature survey also (William and Leyelek 2002, Su and Je-Chin 2003, Funazaki et al. 2012, Xue et al. 2013, and Chandran and Prasad 2015). Hence, the blowing ratios above 1.0 are considered, and experiments are carried out to find the optimized blowing ratio which gives the highest cooling effectiveness. Fig. 5.2 and Fig. 5.3 shows that adiabatic film cooling effectiveness at a B.R of 1.25 and 1.5 for the hole orientation angle models. Adiabatic film cooling effectiveness is found to be increasing with the increase in hole orientation angle from the stagnation line.

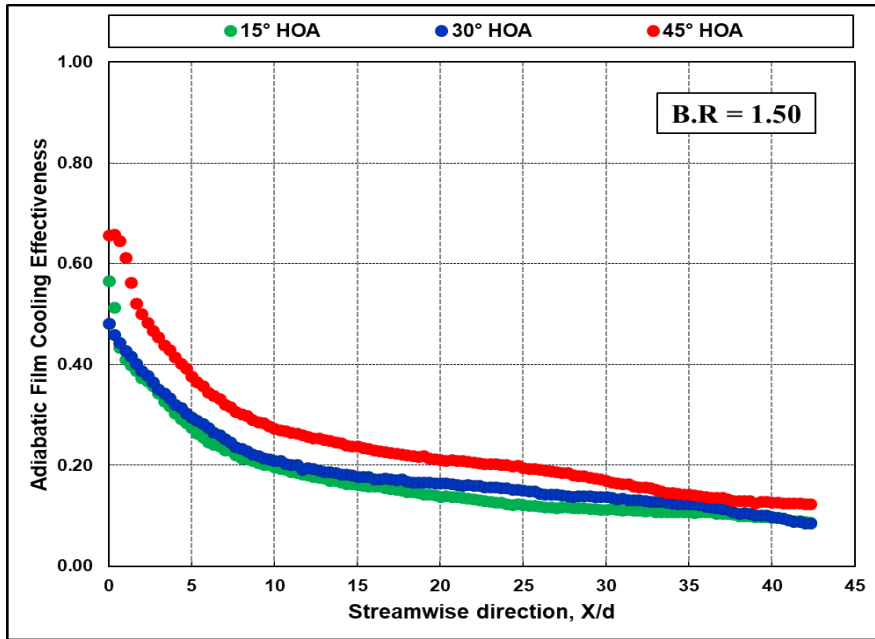


Fig. 5.3 Experimentally evaluated cooling effectiveness at a B.R of 1.5

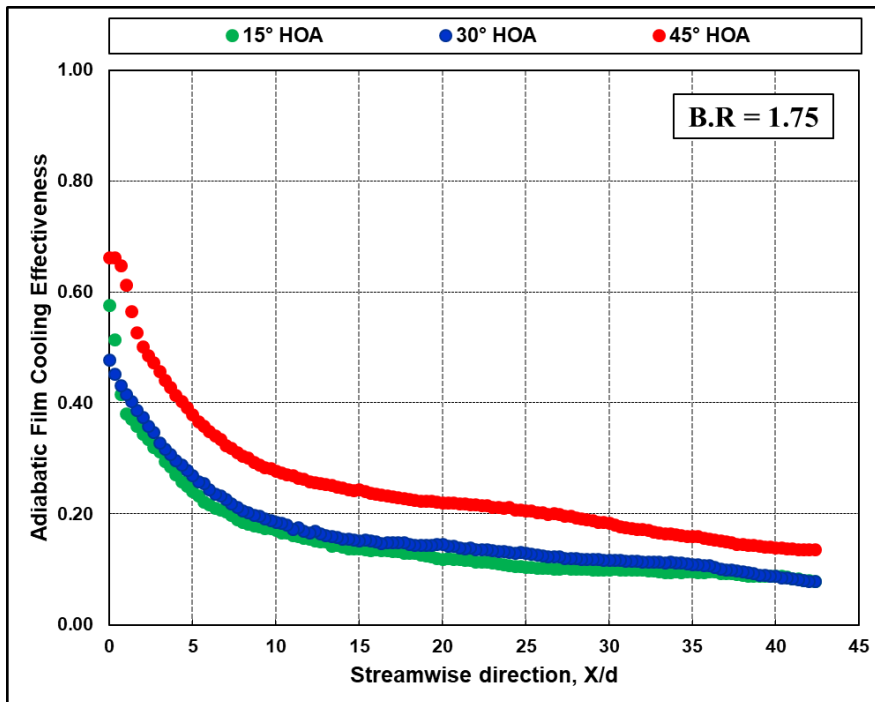


Fig. 5.4 Experimentally evaluated cooling effectiveness at a B.R of 1.75

At a B.R of 1.25, the 45° hole model shows little higher cooling effectiveness than the 15° and 30° hole models whereas the 15° and 30° hole models show almost the same cooling effectiveness. But at a B.R of 1.5, the 45° model shows around 20% higher cooling effectiveness than the 30° model and 30° model shows little higher cooling

effectiveness than the 15° hole orientation angle model. Fig. 5.2 to Fig. 5.5 show the cooling effectiveness plots at the downstream of a single row of holes for the respective blowing ratios of 1.25, 1.5, 1.75 and 2.0.

The Fig. 5.4 and Fig. 5.5 show the adiabatic film cooling effectiveness at a B.R of 1.75 and 2.0 for the 15°, 30° and 45° models. At a B.R of 1.75 and 2.0, the 45° model shows the significant increase in cooling effectiveness when compared to other 15° and 30° hole models. Here, 45° model shows around 20% higher cooling effectiveness than the 30° model and 30° model shows little higher cooling effectiveness than the 15° hole orientation angle model.

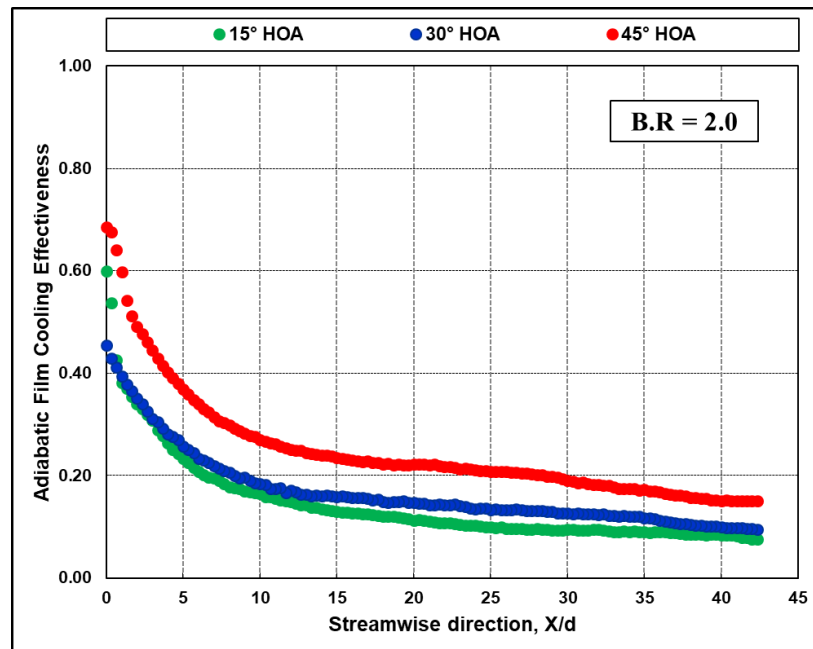


Fig. 5.5 Experimentally evaluated cooling effectiveness at a B.R of 2.0

In the 45° hole orientation angle model, the film cooling holes are away from the stagnation line compared to the other two models. The coolant flow comes out with the lower velocity with the same mass flow hence, has the higher force than the flow through the 15°, and 30° hole orientation flows. The coolant flow through these holes has a less resistance from the main flow due to the distributed main low at the downstream regions from the stagnation line of the test model. For these reasons, the 45° hole orientation angle model showed the higher cooling effectiveness than the other two models.

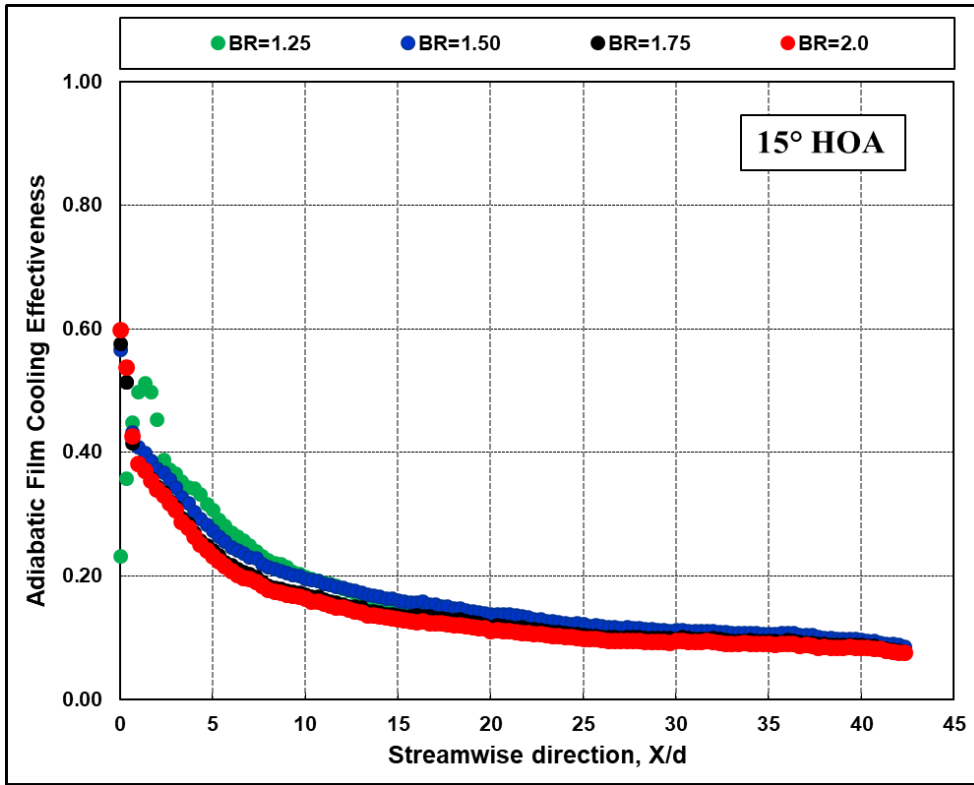


Fig. 5.6 Experimentally evaluated cooling effectiveness for 15° HOA model

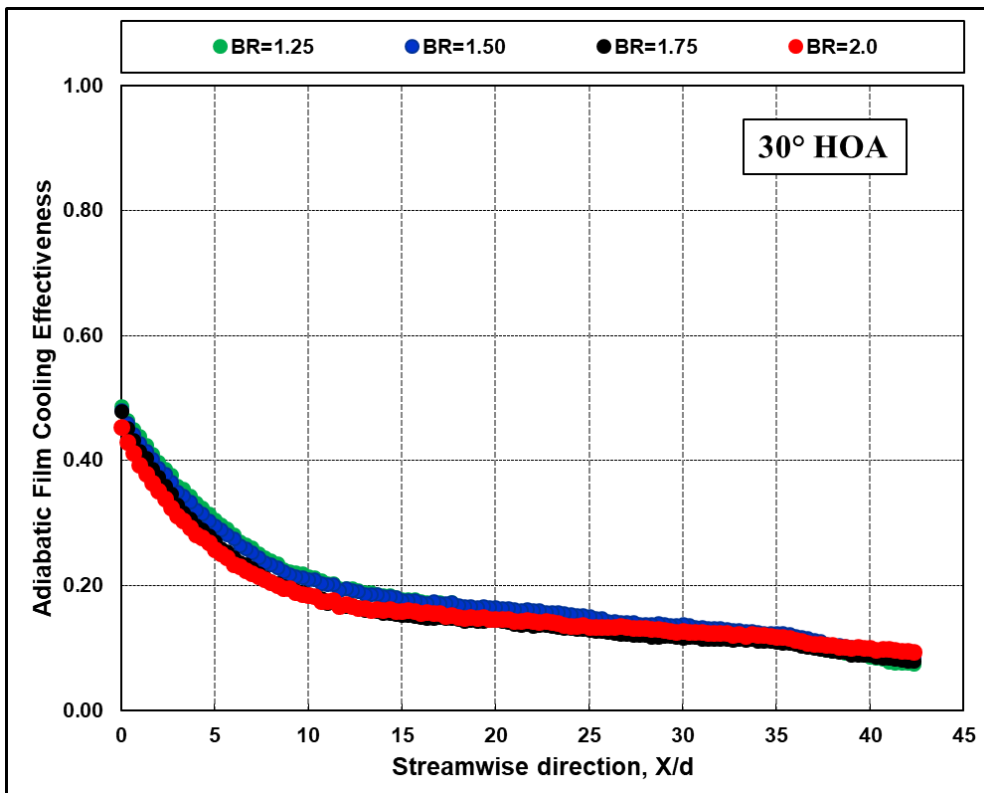


Fig. 5.7 Experimentally evaluated cooling effectiveness for 30° HOA model

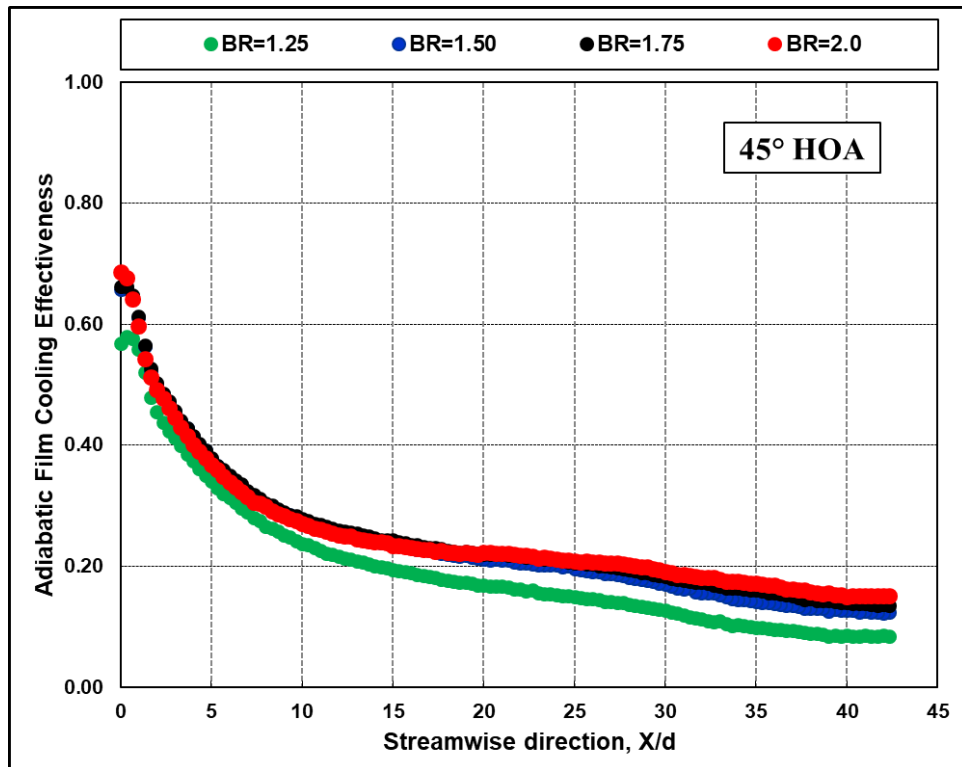


Fig. 5.8 Experimentally evaluated cooling effectiveness for 45° HOA model

The Fig. 5.6, Fig. 5.7 and Fig. 5.8 show the effect of blowing ratio on the 15°, 30°, and 45° models respectively. From the Fig. 5.6 and Fig. 5.7, the 15° and 30° hole orientation models show an increase in adiabatic film effectiveness up to blowing ratio of 1.5, and after that, it decreases. Hence, the 15° and 30° hole models show the highest cooling effectiveness at an optimized blowing ratio of 1.5. Whereas the 45° hole model, shows the increase in adiabatic film cooling effectiveness with the increase in blowing ratio up to the blowing ratio of 1.5 and after that not shown any much increase in cooling effectiveness as shown in the Fig. 5.8. Hence, for all these 15°, 30°, and 45° hole orientation models, the blowing ratio 1.5 can be considered as an optimized blowing ratio with the higher cooling effectiveness.

5.1.2 Numerical Results of Adiabatic Film Cooling Effectiveness

The temperature and velocity contours are extracted numerically from the CFD for the 15°, 30°, and 45° hole orientation angle models at the considered blowing ratios, and the extracted results are used for the cooling effectiveness analysis. Fig. 5.9 shows the typical temperature and velocity contours extracted from CFD at a blowing ratio of

1.5 for the 45° hole orientation angle model. The units of scale on temperature contour are the temperature in Kelvin and units of scale on velocity contour are the velocity values in meter per second. The temperature and velocity contours are shown the meaningful results in the form of temperatures and flow patterns over the test model surface. From the temperature contours, it can be observed the reduction in temperature values concerning the increase in hole orientation angle, this relates to the increase in adiabatic cooling effectiveness from 15° to 45° hole orientation.

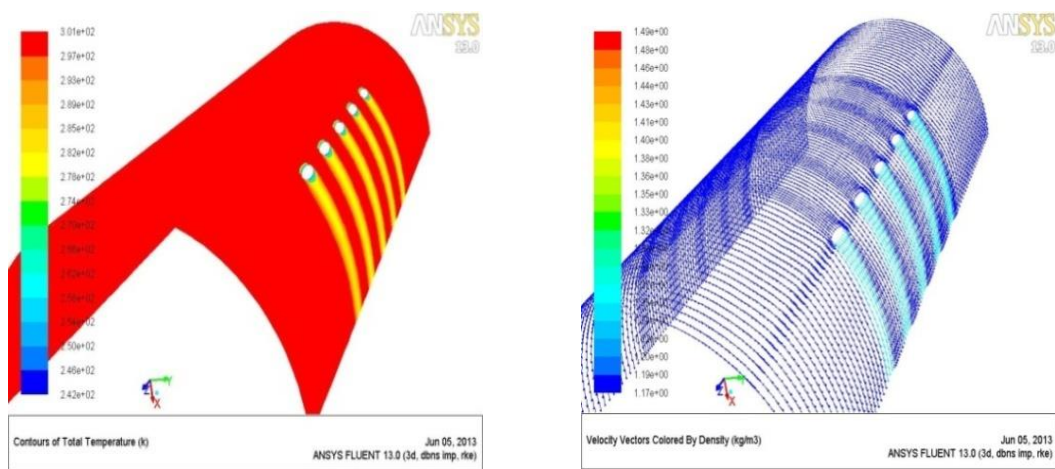


Fig. 5.9 Temperature and velocity contours for 45° HOA model at a B.R of 1.5

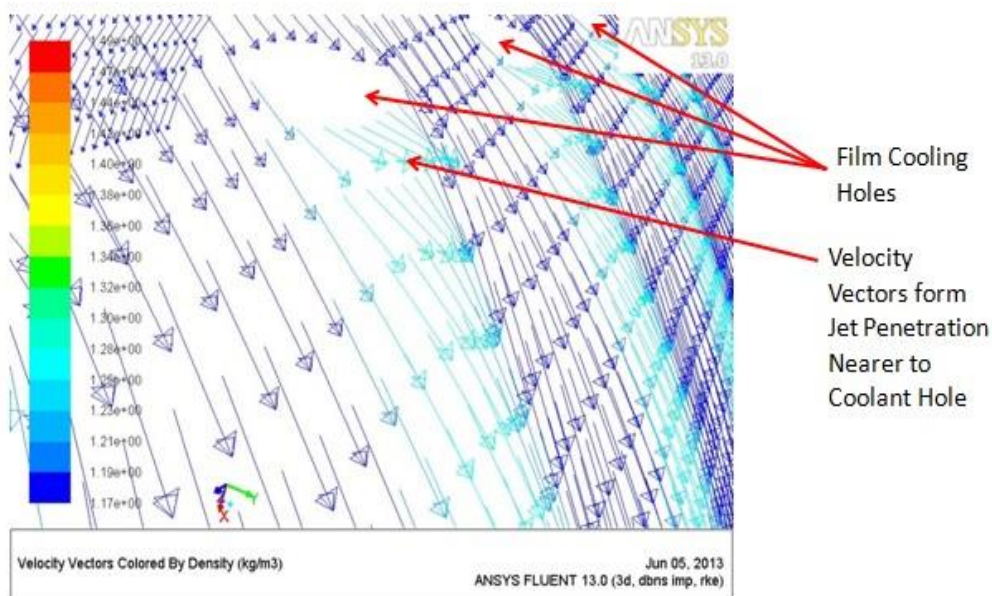


Fig. 5.10 Velocity vectors for 30° HOA model at B.R of 1.5

The Fig. 5.10 shows the typical flow field velocity vectors extracted from CFD for a 30° hole orientation model at a blowing ratio of 1.5, and it clearly shows that the coolant flow created a film over the leading edge surface. From the figure, it can be observed that near the cooling hole, velocity vectors forms jet penetration and coolant flow is mixed with mainstream flow. In the downstream region, the coolant flow creates a film over the gas turbine leading edge surface, and it protects the surface from the mainstream flow.

The adiabatic film cooling effectiveness is found numerically for blowing ratios 1.25, 1.5, 1.75 and 2.0 at a density ratio of 1.30 for three models, i.e., 15°, 30° and 45° hole orientation angle models. The effectiveness is calculated using the temperature contours extracted from fluent results. The numerical spanwise averaged cooling effectiveness is found along the streamwise direction of downstream of the row of cooling holes similarly that of experimental cooling effectiveness results.

The Fig. 5.11 to Fig. 5.14 shows the numerically extracted adiabatic film cooling effectiveness at a blowing ratio of 1.25, 1.5, 1.75 and 2.0 for the 15°, 30° and 45° hole orientation angle models respectively. From these graphs, it can be observed that the 45° holes model gives the higher cooling effectiveness compared to the 15° and 30° hole models. But among 15° and 30° hole models, the effect of blowing ratio found not much significant among the considered blowing ratios.

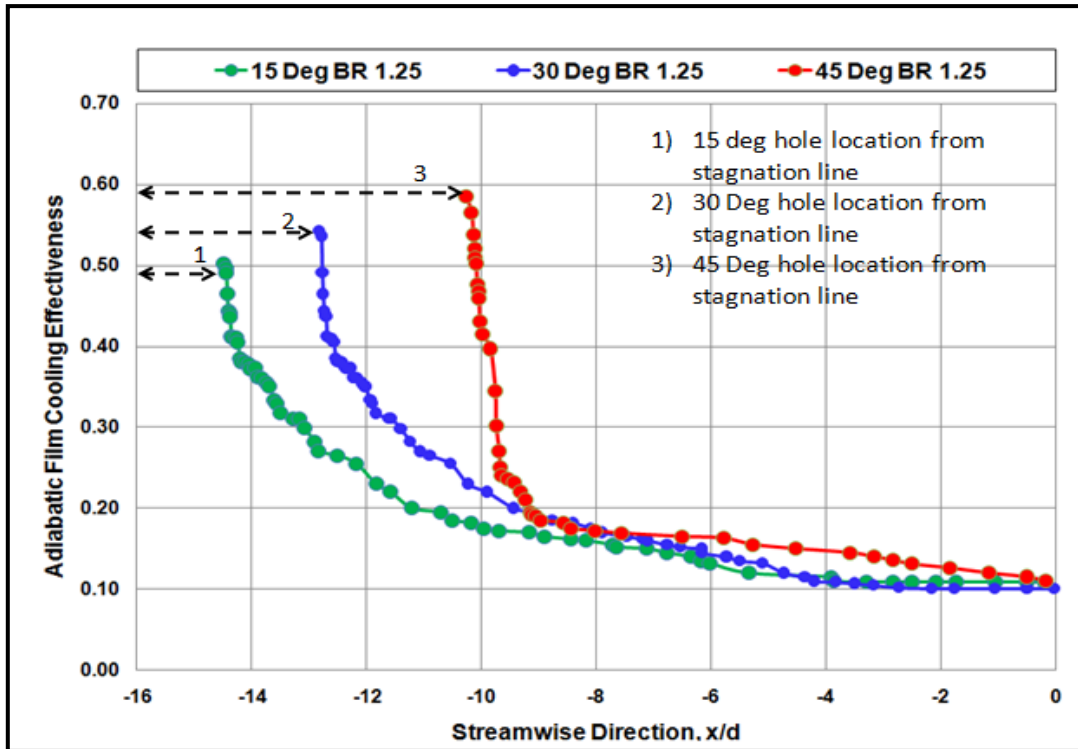


Fig. 5.11 Numerically evaluated adiabatic cooling effectiveness at a B.R of 1.25

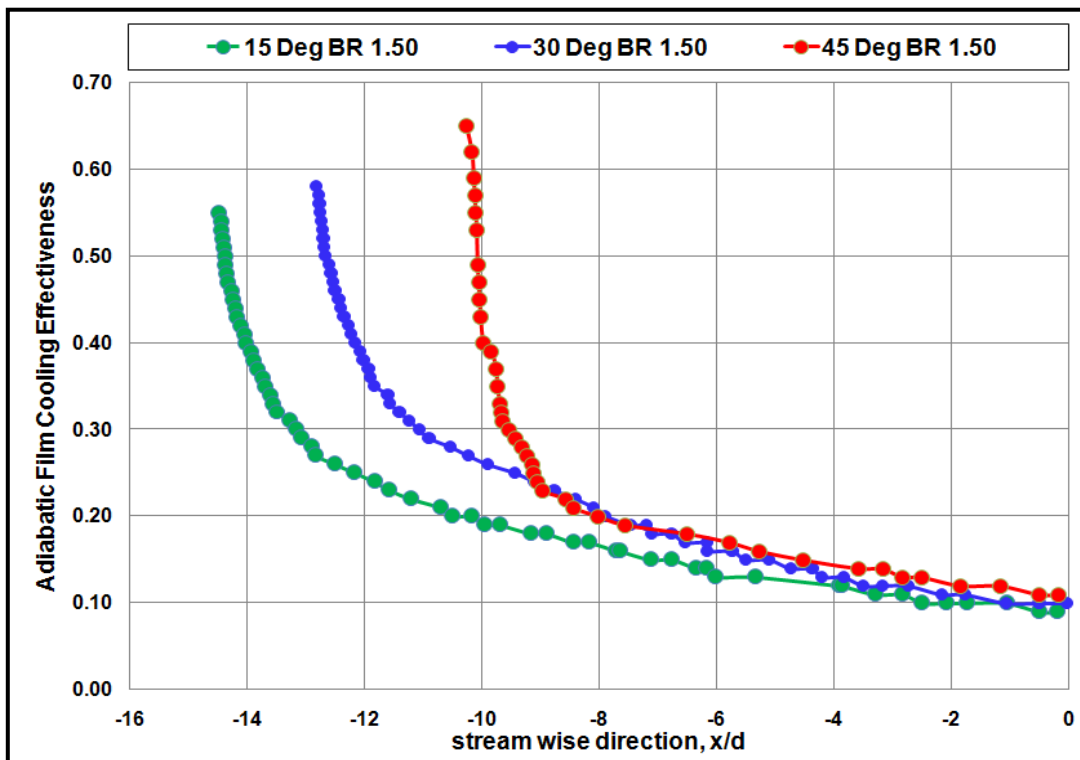


Fig. 5.12 Numerically evaluated adiabatic cooling effectiveness at a B.R of 1.5

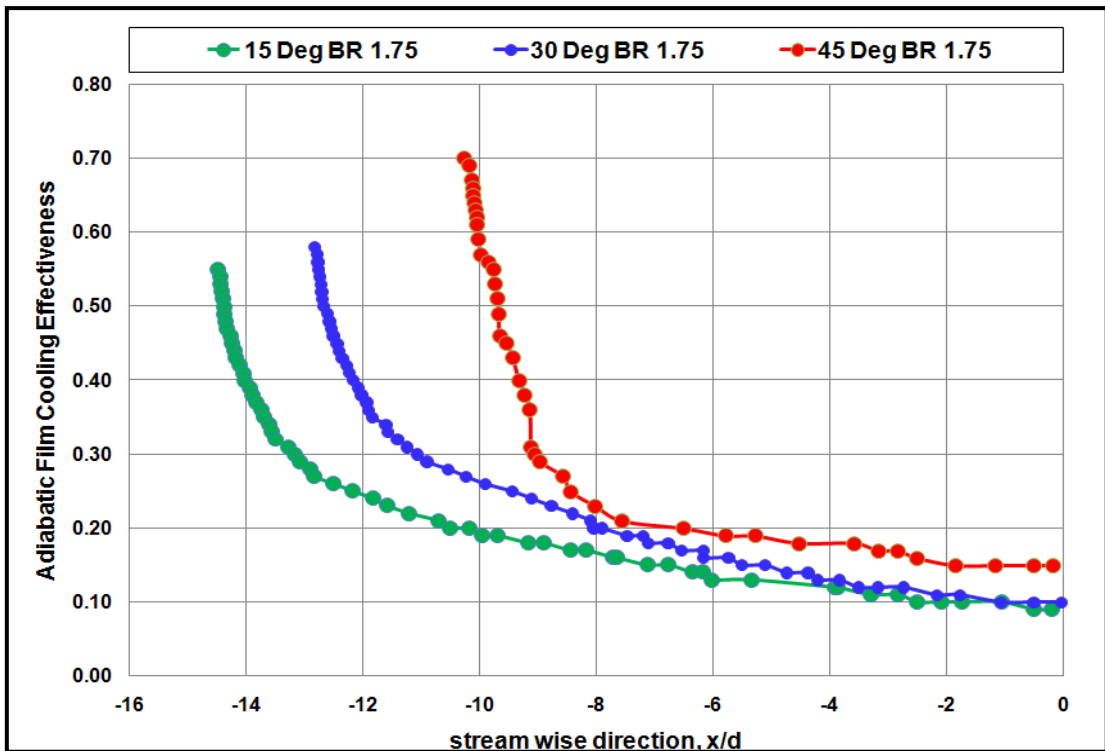


Fig. 5.13 Numerically evaluated adiabatic cooling effectiveness at a B.R of 1.75

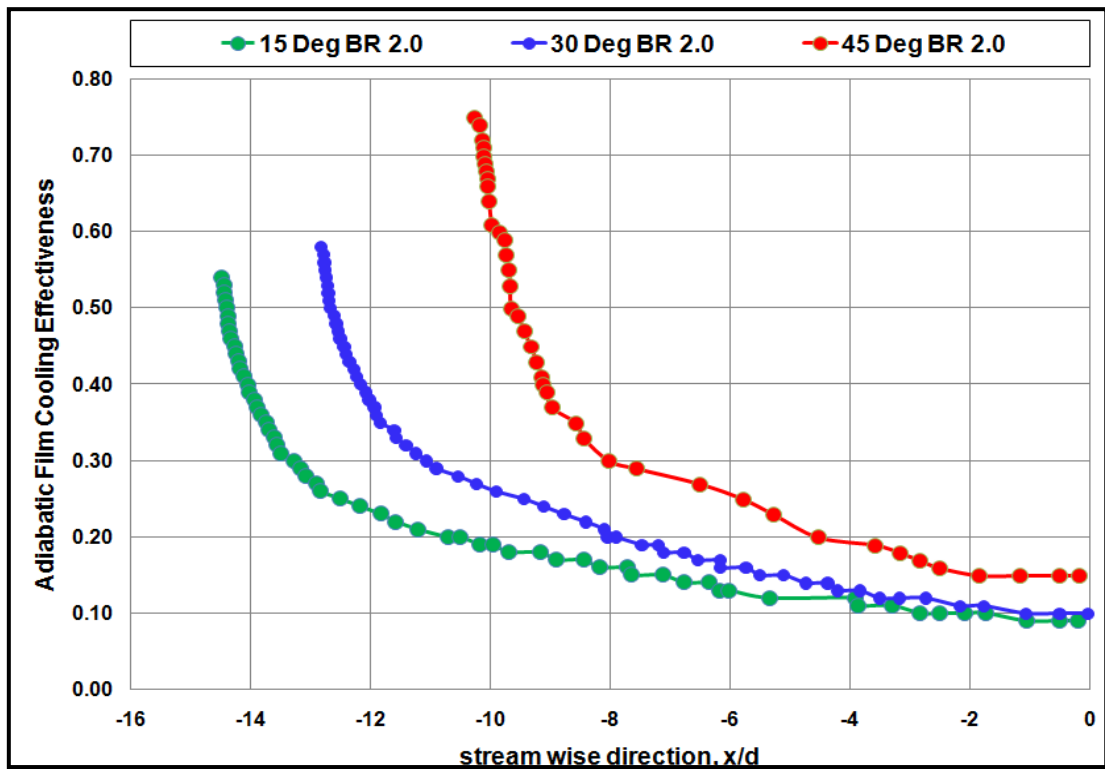


Fig. 5.14 Numerically evaluated adiabatic cooling effectiveness at a B.R of 2.0

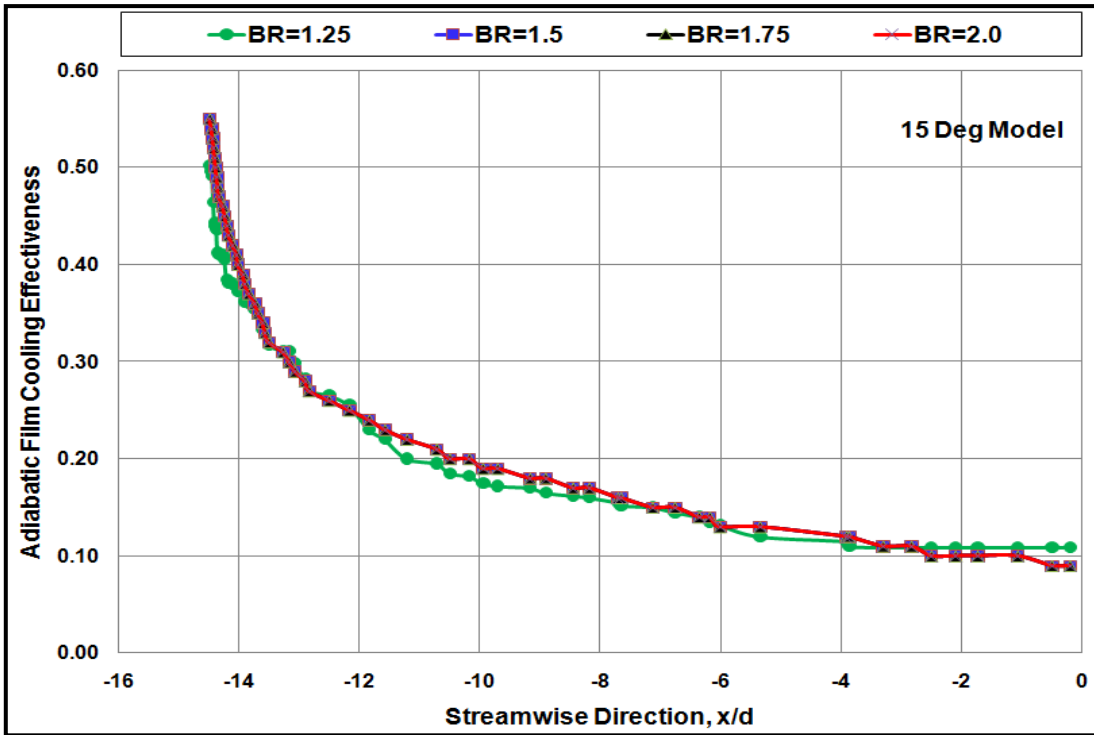


Fig. 5.15 Numerically evaluated cooling effectiveness for 15° HOA model

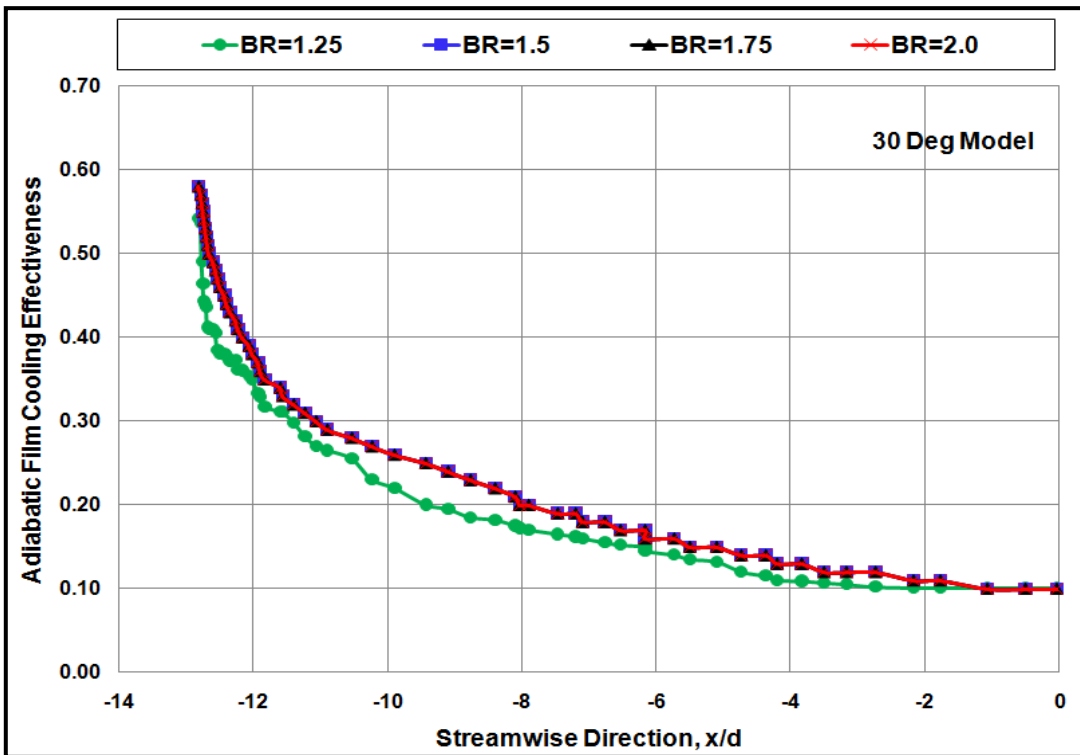


Fig. 5.16 Numerically evaluated cooling effectiveness for 30° HOA model

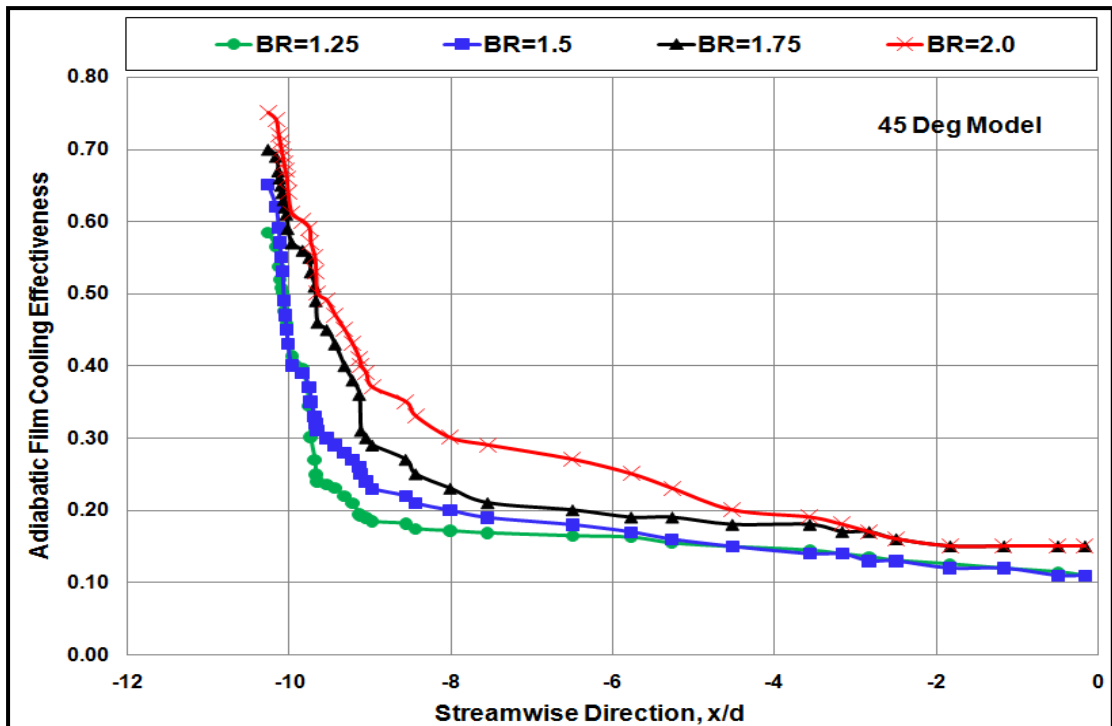


Fig. 5.17 Numerically evaluated cooling effectiveness for 45° HOA model

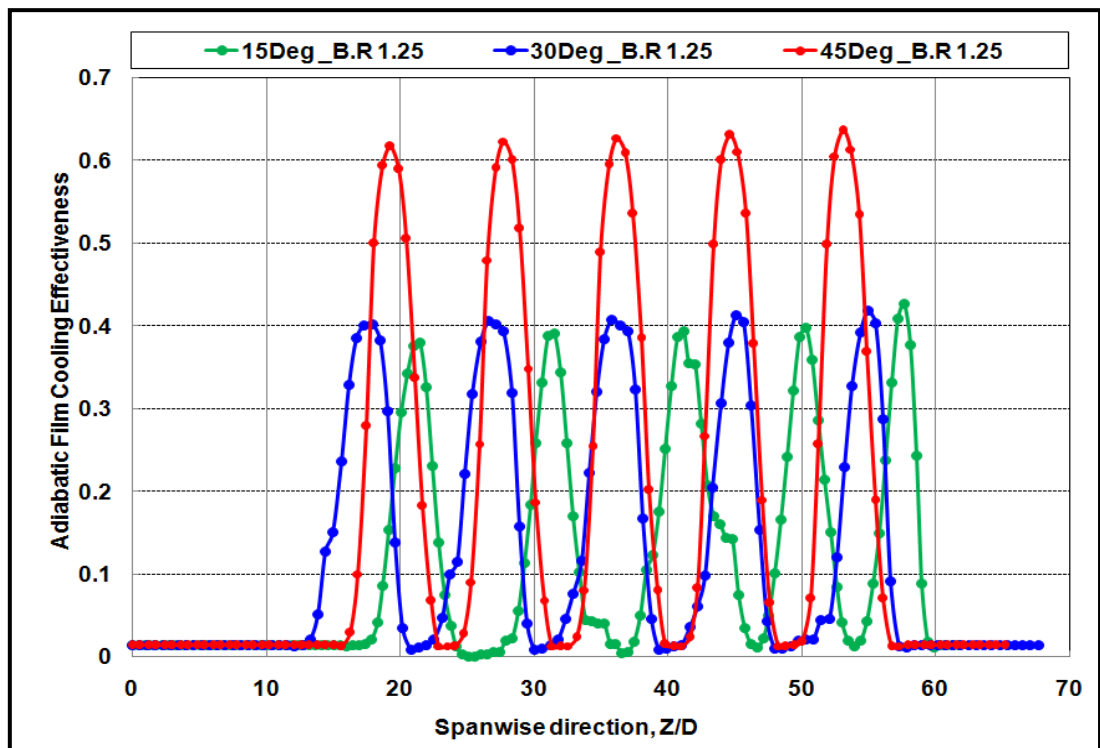


Fig. 5.18 Numerically evaluated cooling effectiveness at a B.R of 1.25

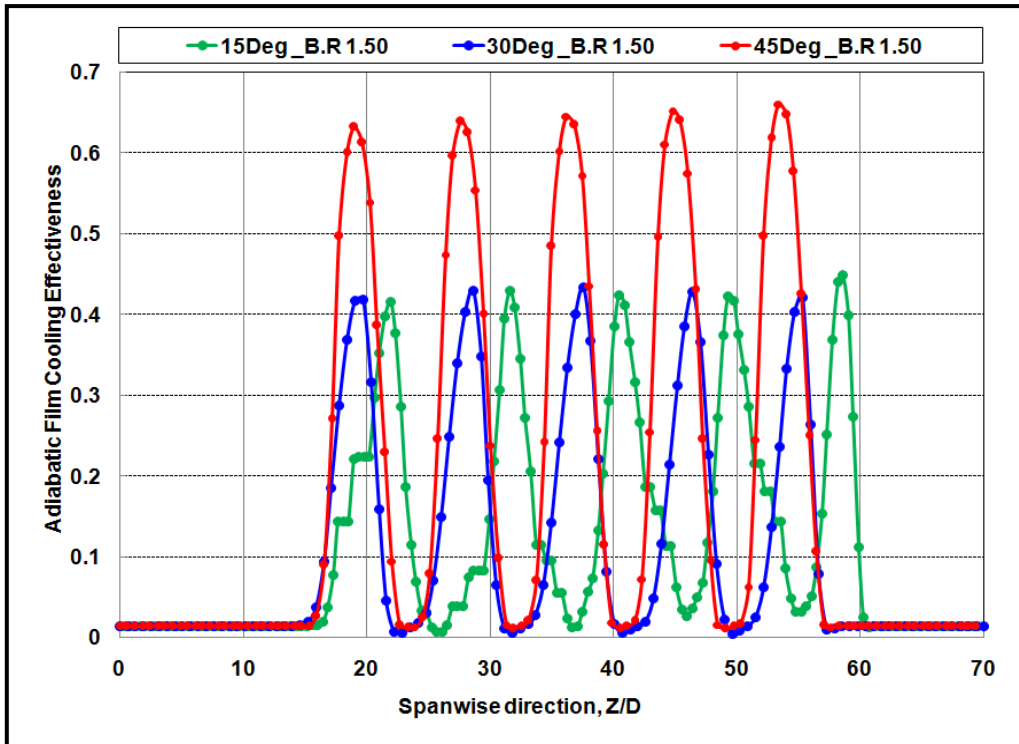


Fig. 5.19 Numerically evaluated adiabatic cooling effectiveness at a B.R of 1.5

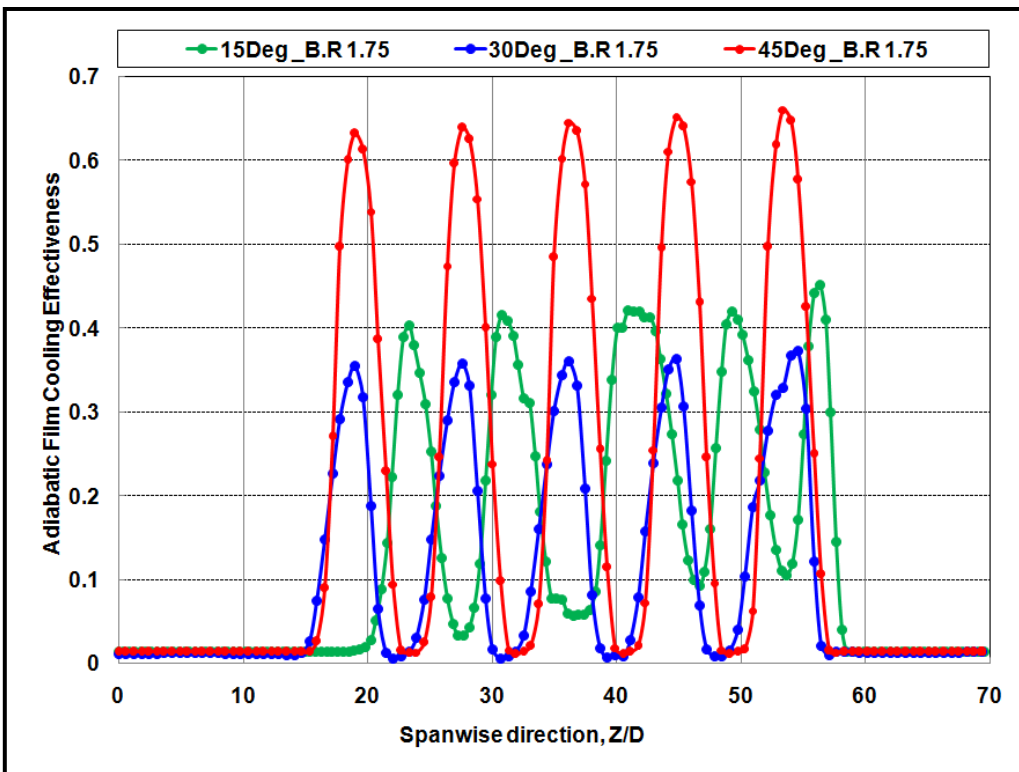


Fig. 5.20 Numerically evaluated adiabatic cooling effectiveness at a B.R of 1.75

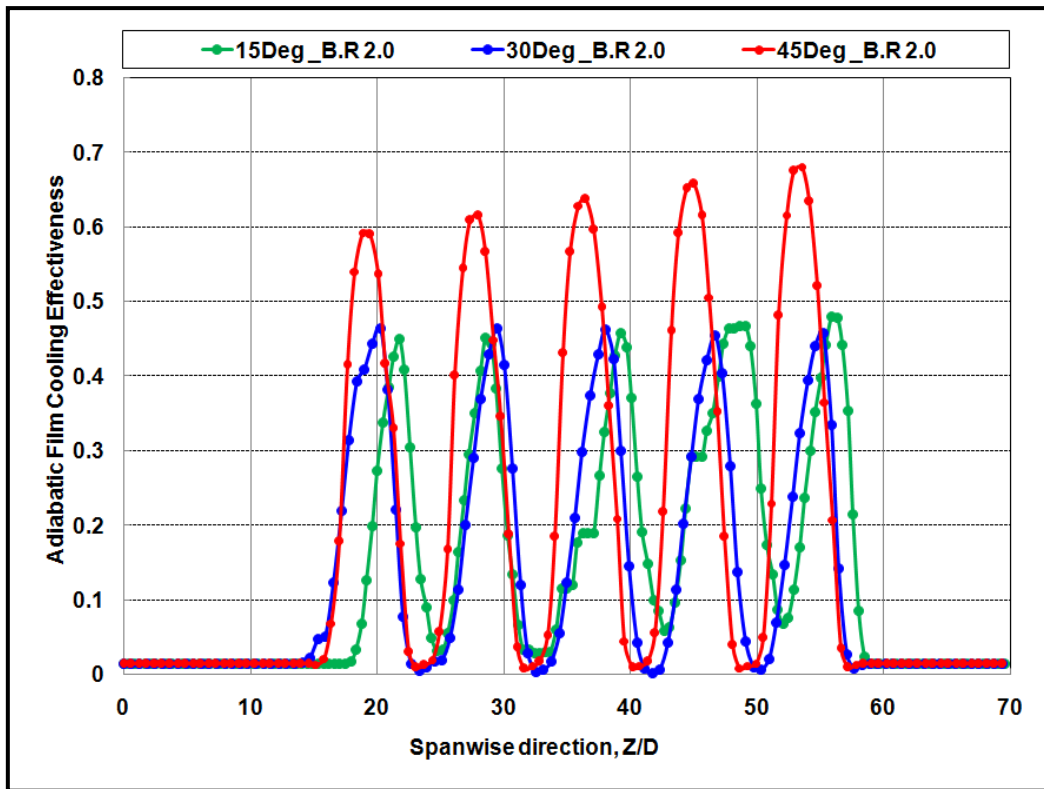


Fig. 5.21 Numerically evaluated adiabatic cooling effectiveness at a B.R of 2.0

The numerically extracted adiabatic film cooling effectiveness for the 15°, 30°, and 45° hole orientation models at a blowing ratio of 1.25, 1.5, 1.75 and 2.0 respectively shown in the Fig. 5.15 to Fig. 5.17. The comparative adiabatic film cooling effectiveness results for the 15°, 30° and 45° hole models at individual blowing ratios of 1.25, 1.5, 1.75 and 2.0 are shown in the Fig. 5.18 to Fig. 5.21. The adiabatic film cooling effectiveness for the 15° and 30° hole models will increase up to the blowing ratio of 1.5 after that there is not shown any improvement for blowing ratios of 1.75 and 2.0. Hence, it indicates that 15° and 30° hole models show the optimized cooling effectiveness at the blowing ratio of 1.5. Whereas the 45° hole model, shows the increase in adiabatic film cooling effectiveness with the increase in blowing ratio up to the blowing ratio of 2.0 among the considered range and the increase from blowing ratio of 1.5 to 2.0 is very marginal. Hence for the 45° hole model also the blowing ratio of 1.5 can also be considered as an optimized blowing ratio.

5.1.3 Experimental and Numerical cooling effectiveness over the typical HOA model

The Fig. 5.22 and Fig. 5.23 shows the typical experimental and numerical cooling effectiveness temperature contours of 30° hole orientation angle model at a blowing ratio of 1.5. When the secondary air is injected through a coolant hole, the film is creating over the gas turbine blade leading edge and provides the surface thermal protection from hot gases. The units of scale on a thermal image of Fig. 5.22 are the thermal radiation count captured by the infra-red camera and the units of scale on a thermal image of Fig. 5.23 are the temperature values in Kelvin extracted from CFD analysis.

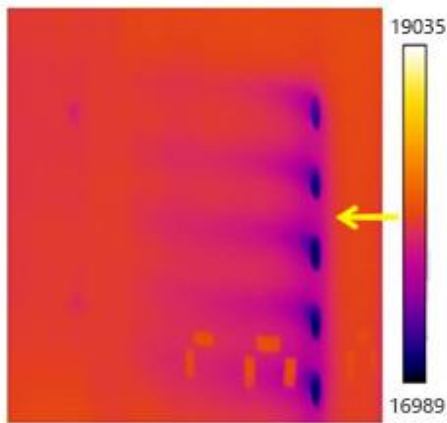


Fig. 5.22 Experimentally captured thermal image for a 30° HOA model at a B.R of 1.50

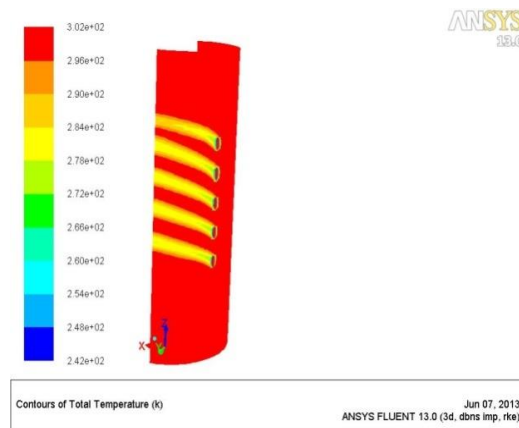


Fig. 5.23 CFD extracted temperature contour for a 30° HOA model at a B.R of 1.50

The CFD extracted results have shown the same trends as that of the experimental cooling effectiveness values. However, the CFD results are overpredicted than that of experimental values. The frictional and mixing phenomenon losses are unable to consider by the CFD. Hence, the CFD has shown the overpredicted results especially at the immediate downstream of holes. The experimental and numerical cooling effectiveness differences are observed more due to the generation of test models with multiple rows of holes and blocking of holes for the individual hole row effects in case of experiments. Whereas, in the numerical analysis the test models are considered with the specific hole rows to bring out the hole geometrical parameters.

5.2 Effect of Hole Inclination Angle (HIA) along the streamwise direction

To bring out the effect of hole inclination angle, four test models are considered (M4, M5, M6 and M7) with one row of holes on stagnation line and two rows of holes on either side of stagnation line at 30° and 60° with the hole inclination angle of 20°, 25°, 30° and 35° respectively.

5.2.1 Experimental Adiabatic Film cooling effectiveness and HTC Results

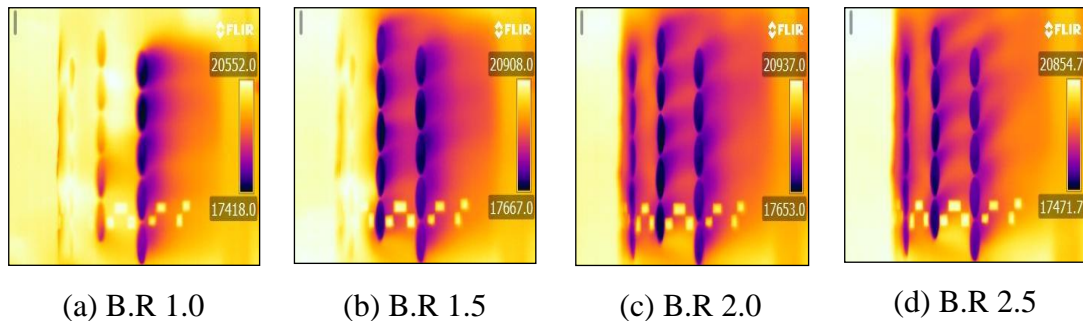


Fig. 5.24 Thermal images at different B.Rs of 20° HIA model

The mass flow measurements and coefficient of discharge values are found for all the four test models individually by varying the coolant chamber pressure. The average coefficient of discharge for the hole inclination angle models was found to be increasing marginally with the increase in angle. The approximate average coefficient of discharge for these models is found as 0.68. The detailed mass flow and Cd calculations and values are given in an appendix-I.

Heat transfer coefficient and Film cooling effectiveness values are evaluated experimentally for all the four leading edge models with 20°, 25°, 30° and 35° hole inclination angles. The typical infrared camera captured thermal images of adiabatic film cooling effectiveness at different blowing ratios for a 20° hole inclination angle model are shown in the Fig. 5.24. The units of scale on thermal images of Fig. 5.24 are the thermal radiation count captured by the infra-red camera.

To get experimental consistency, two test runs are conducted at same blowing ratio during both film cooling effectiveness and heat transfer coefficients measurement experiments. Fig. 5.25 shows the variation of effectiveness along the downstream from the stagnation line for 20° hole inclination angle model to show experimental consistency between run-1 and run-2 at a blowing ratio of 2.5. From the Fig. 5.25, it is found that the difference in film cooling effectiveness between two test runs is negligible and proved the best experimental repeatability.

Adiabatic film cooling effectiveness is found by averaging in spanwise and plotted along the streamwise direction including the film cooling hole regions. The peaks in the Fig. 5.25 show the highest effectiveness due to the presence of coolant air at the hole exit regions. At the blowing ratios of 1.0 and 1.5, the coolant flow is not much established at the leading edge stagnation region with lower coolant flow whereas at the blowing ratio of 2.0 and above the coolant flow is established better at the leading edge region to overcome over the mainstream flow pressure.

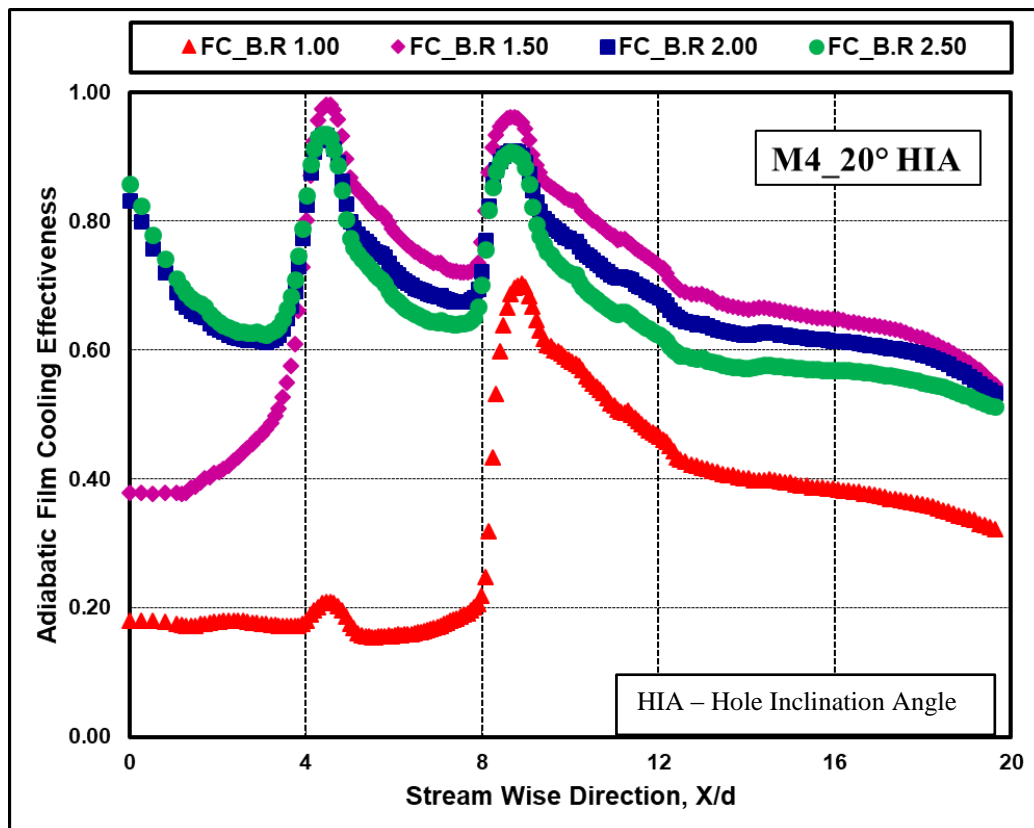


Fig. 5.25 Cooling effectiveness comparison of two test runs at a constant B.R

The mainstream flow at the leading edge stagnation region is a complex with direct hitting over the surface and flow distribution variations over to the pressure and suction sides of the vane. At the lower blowing ratios, with the lower coolant pressure values and with the complex distribution of mainstream flow at the leading edge region, the cooling effectiveness is lower at the leading edge region up to an x/d of 4. Whereas after the x/d of 4, the cooling effectiveness is shown higher even at a lower blowing ratio of 1.5 along the downstream of streamwise direction. By comparing the cooling effectiveness results, on an overall average, the blowing ratio 1.5 is shown the higher cooling effectiveness. Hence, the blowing ratio of 1.5 is considered as the optimized blowing ratio for this geometry.

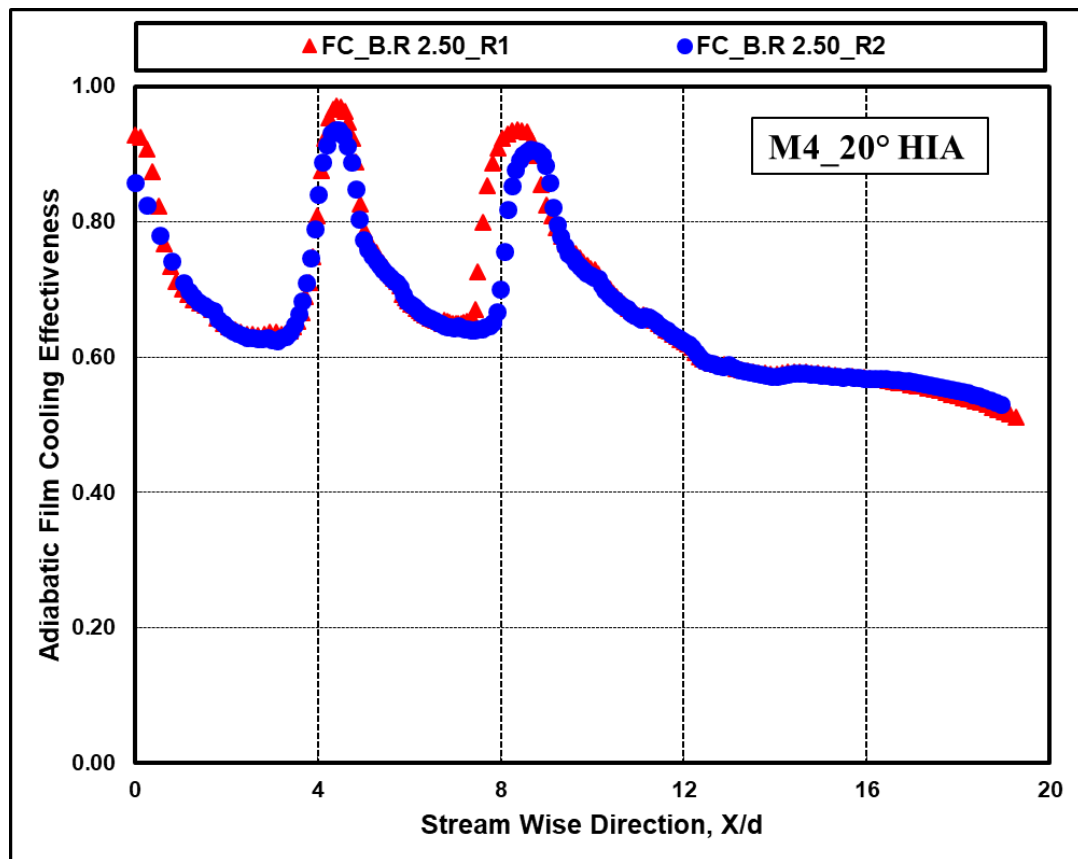


Fig. 5.26 Cooling effectiveness values for a 20° HIA model

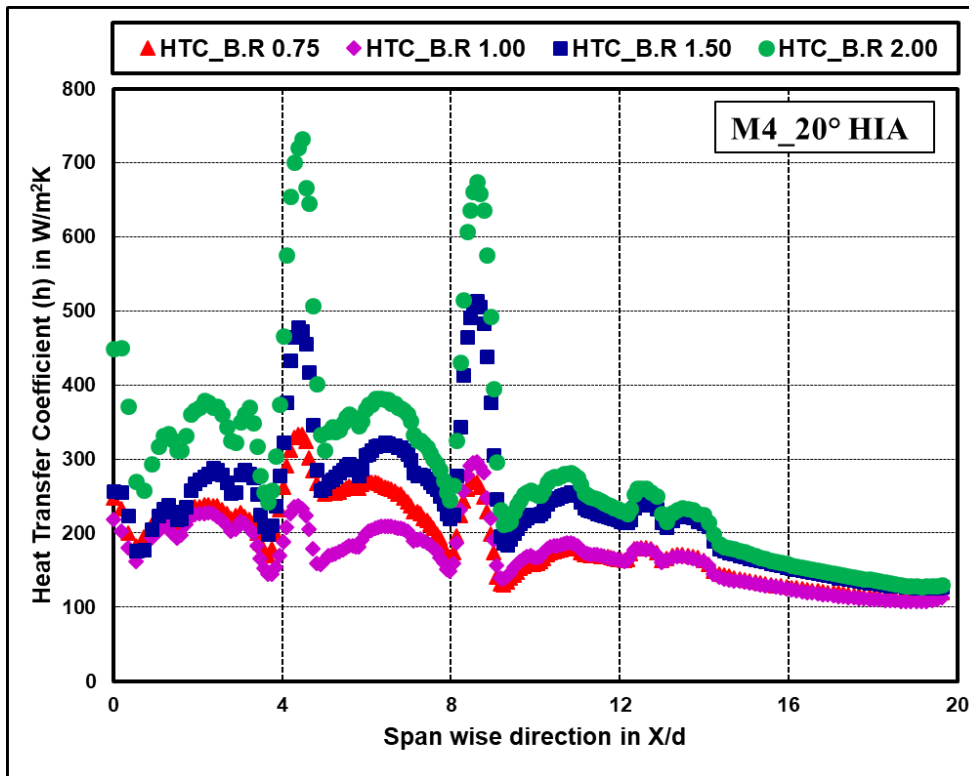


Fig. 5.27 Heat transfer coefficient values for a 20° HIA model

Fig. 5.26 and Fig. 5.27 shows the variation of adiabatic film cooling effectiveness and heat transfer coefficients respectively for 20° hole inclination angle model. Effectiveness increased with increase in blowing ratio from 1.0 to 1.5, but the effectiveness is lower at the stagnation region because of coolant flow restricted by the mainstream due to mainstream higher pressure over the stagnation. With the further increase in blowing ratio over 1.5, the effectiveness is decreased continuously at the downstream of holes except at the stagnation hole region. Effectiveness is found to be increased with increase in blowing ratio up to 2.5 at the stagnation hole region due to the higher coolant pressures with increasing in blowing ratio. The cooling effectiveness is plotted for the spanwise two pitch average values along the streamwise direction considering the hole region values. The two peaks of cooling effectiveness in the plots indicate the highest effectiveness due to the direct exit of coolant air at the hole exit regions.

The effect of blowing ratio depends upon three major factors of coolant flow or film formation over the test surface they are attachment-detachment and reattachment.

Attachment is higher at the lower blowing ratio, as the blowing ratio increases detachment and reattachment of coolant flow over the test surface come into the picture. Among all the four blowing ratios considered, the B.R 1.5 is showing higher film cooling effectiveness except stagnation region. Considering overall film cooling, B.R 1.5 is considered as optimized blowing ratio for 20° hole inclination angle model. From the heat transfer coefficient measurement experiments, it is found that the heat transfer coefficients are increased with increase in blowing ratio up to 2.0.

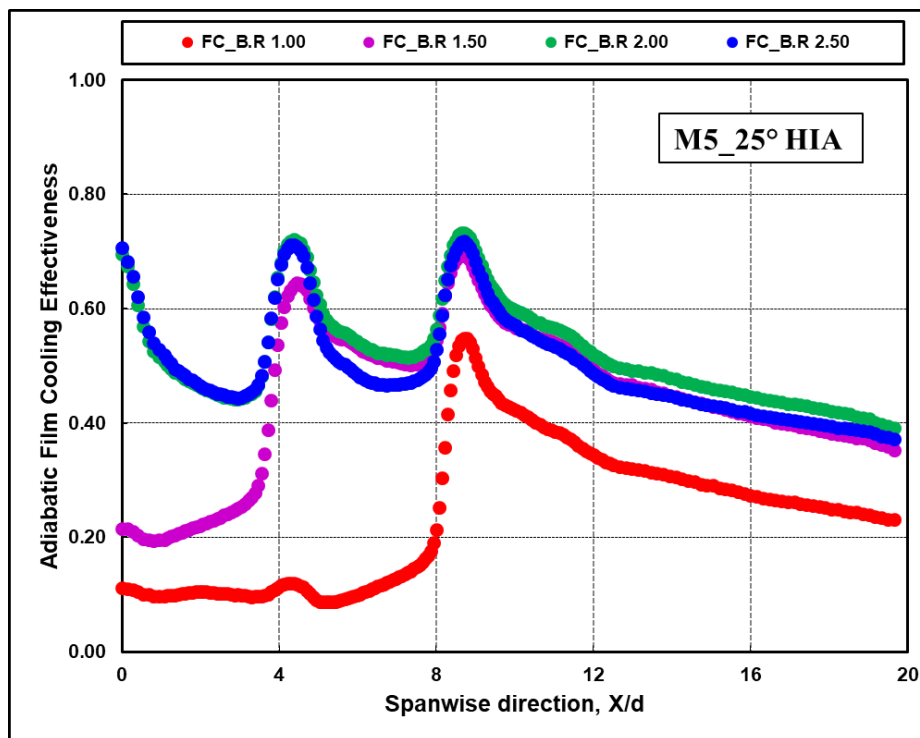


Fig. 5.28 Cooling effectiveness values for a 25° HIA model

Fig. 5.28 shows the variation of adiabatic film cooling effectiveness for 25° hole inclination angle model; the adiabatic film cooling effectiveness is increased with increase in blowing ratio up to 2.0. Further increase in blowing ratio to 2.5 the effectiveness is reduced as shown in Fig. 5.28.

The increase in effectiveness between the blowing ratio of 1.5 to 2.0 is small so that the blowing ratio 1.5 can be considered as optimized blowing ratio for 25° hole inclination angle model. For 25° hole inclination angle model also there is no flow of coolant through the stagnation row holes and some small flow of coolant at the lower

blowing ratio 1.0 due to higher pressure gradients on stagnation. As the flow passes towards downstream the pressure reduces continuously and increases the velocity of the flowing fluid attains the highest coolant flow through the last row of coolant holes. Fig. 5.29 shows the heat transfer coefficients distribution for 25° hole inclination angle model. Heat transfer coefficients are increased with increase in blowing ratio up to 2.5. Heat transfer coefficients values are found highest in the hole region because of higher mass flows at this region.

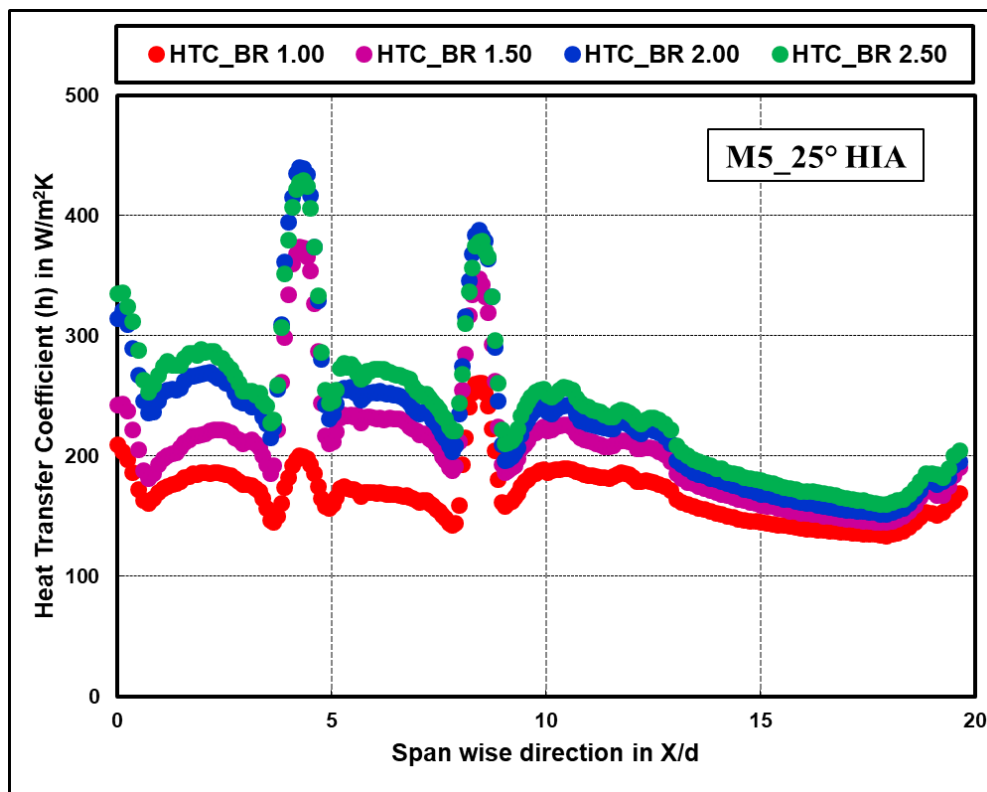


Fig. 5.29 Heat transfer coefficient values for a 25° HIA model

Adiabatic film cooling effectiveness and heat transfer coefficients distribution in streamwise for 30° hole inclination angle mode are shown in the Fig. 5.30 and Fig. 5.31 respectively. Film cooling effectiveness is increased to a maximum level with increasing blowing ratio of 1.0 to 1.5, except stagnation region. Further, increase in blowing ratio of 1.5 to 2.0 and 2.0 to 2.5 the effectiveness is reduced. Hence in 30° hole inclination angle model case also blowing ratio 1.5 is considered as optimized blowing ratio. The heat transfer coefficients results are increasing with increasing blowing ratio up to 2.5.

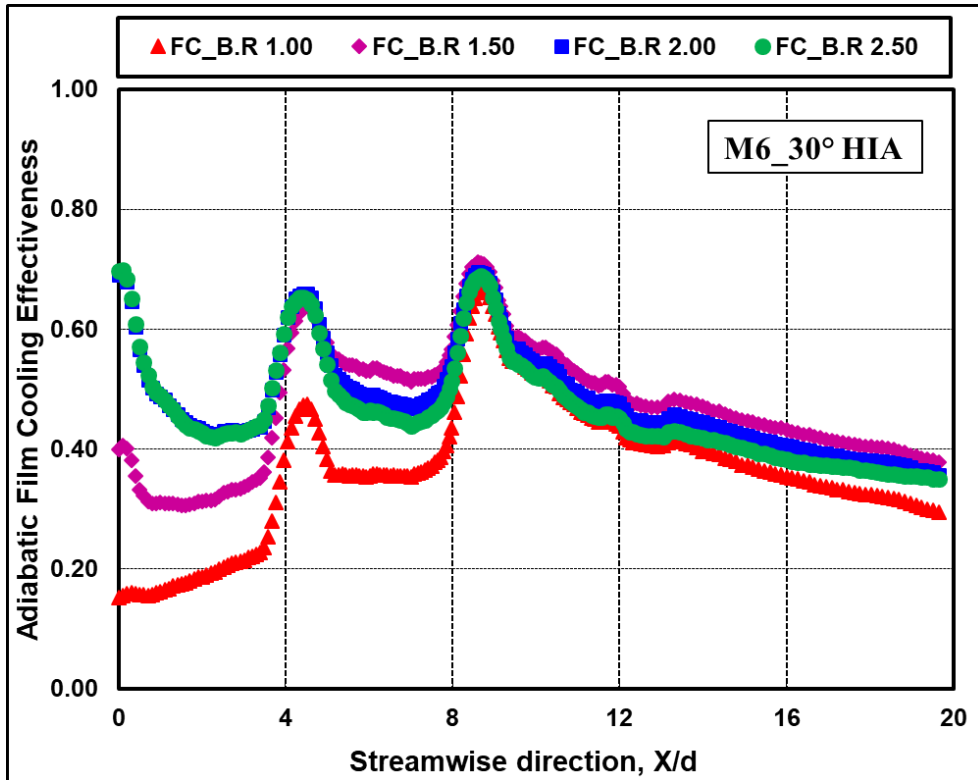


Fig. 5.30 Cooling effectiveness values for a 30° HIA model

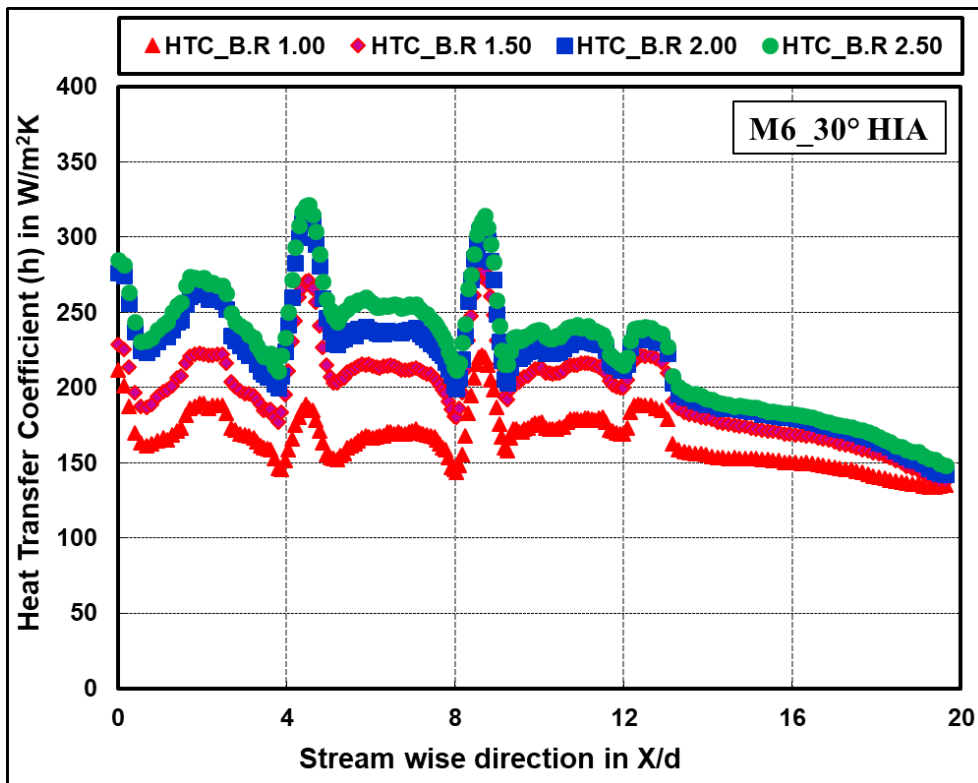


Fig. 5.31 Heat transfer coefficient values for a 30° HIA model

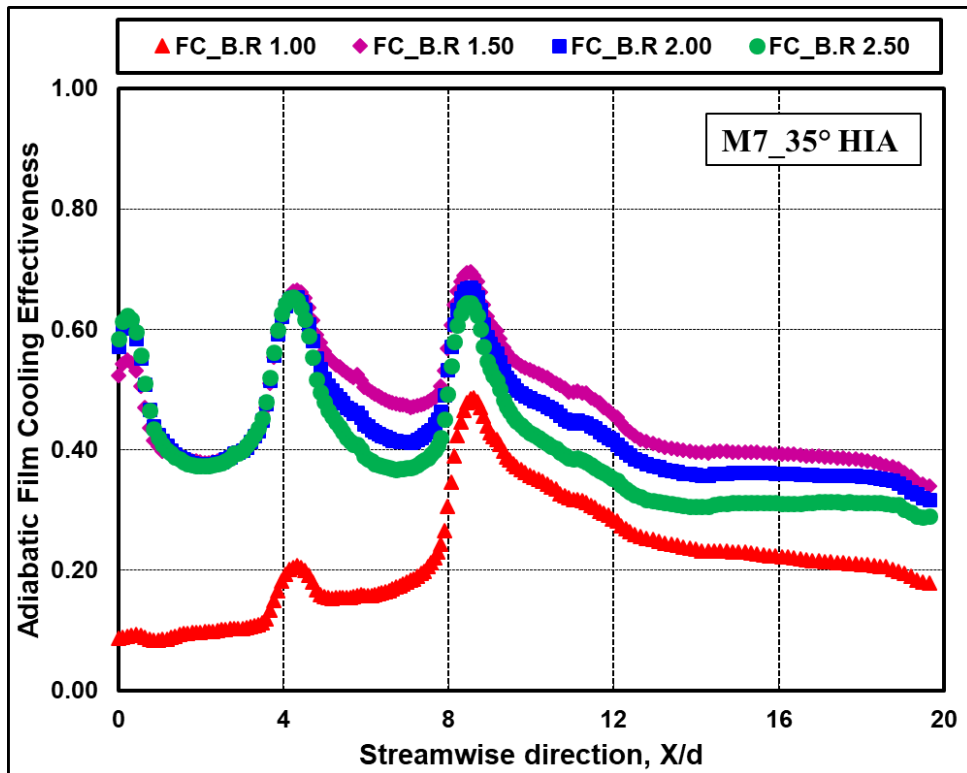


Fig. 5.32 Cooling effectiveness values for a 35° HIA model

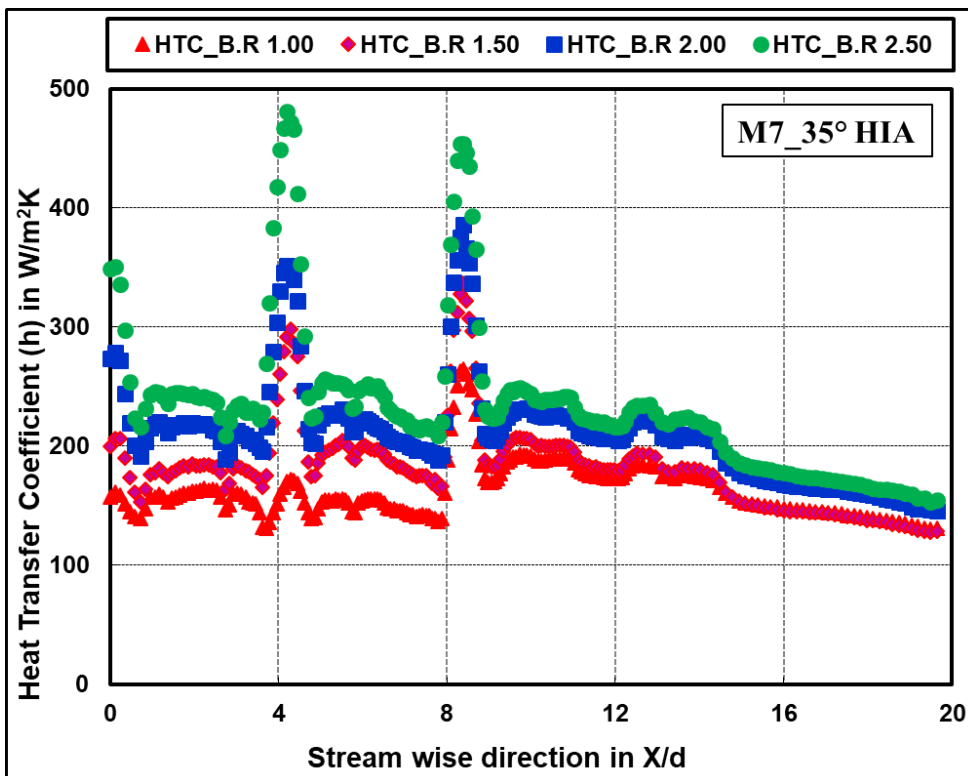


Fig. 5.33 Heat transfer coefficients values for a 35° HIA model

Adiabatic film cooling effectiveness variation and heat transfer coefficients distribution over 35° hole inclination angle model are shown in Fig. 5.32 and Fig. 5.33 respectively. Film cooling effectiveness has shown the highest at blowing ratio of 1.5 and found lowest at lower blowing ratio of 1.0. Further increasing blowing ratio from 1.5 to 2.0 and 2.5 the film cooling effectiveness is reduced continuously. Heat transfer coefficients are increases with increasing in blowing ratio.

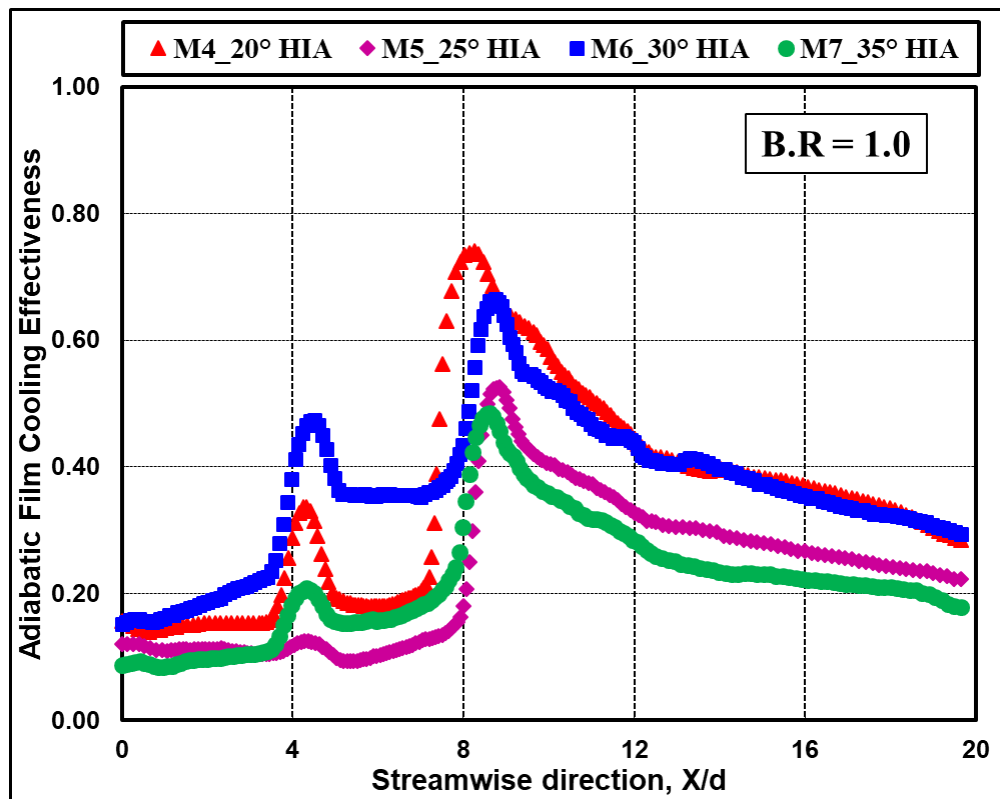


Fig. 5.34 Comparison of cooling effectiveness for all HIA models at a B.R of 1.0

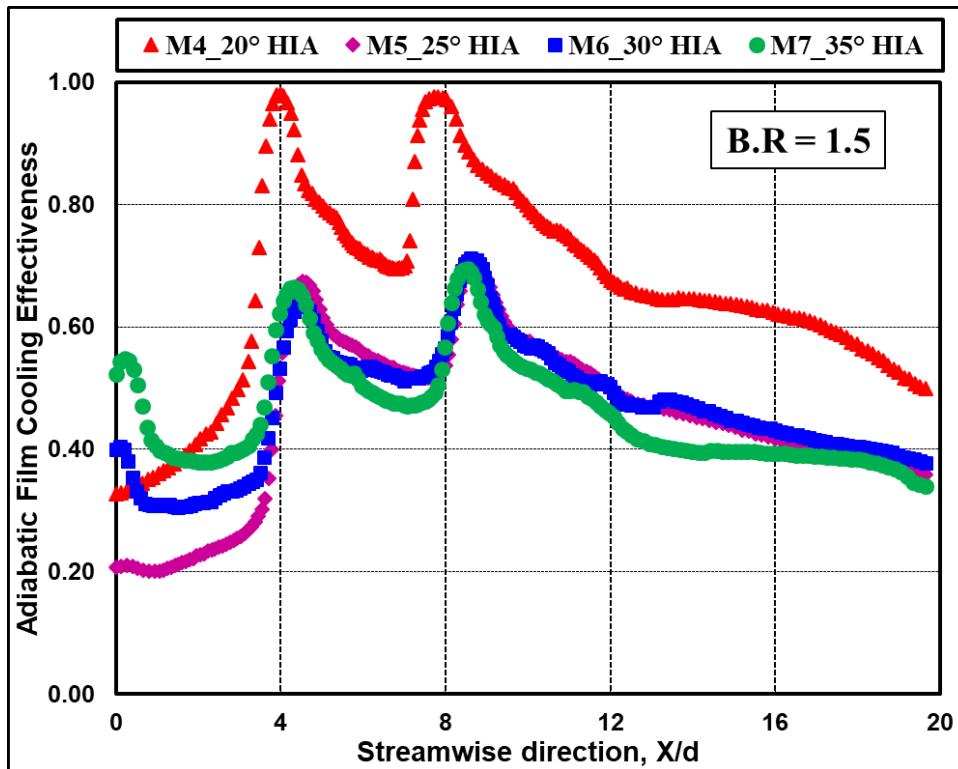


Fig. 5.35 Comparison of cooling effectiveness for all HIA models at a B.R of 1.5

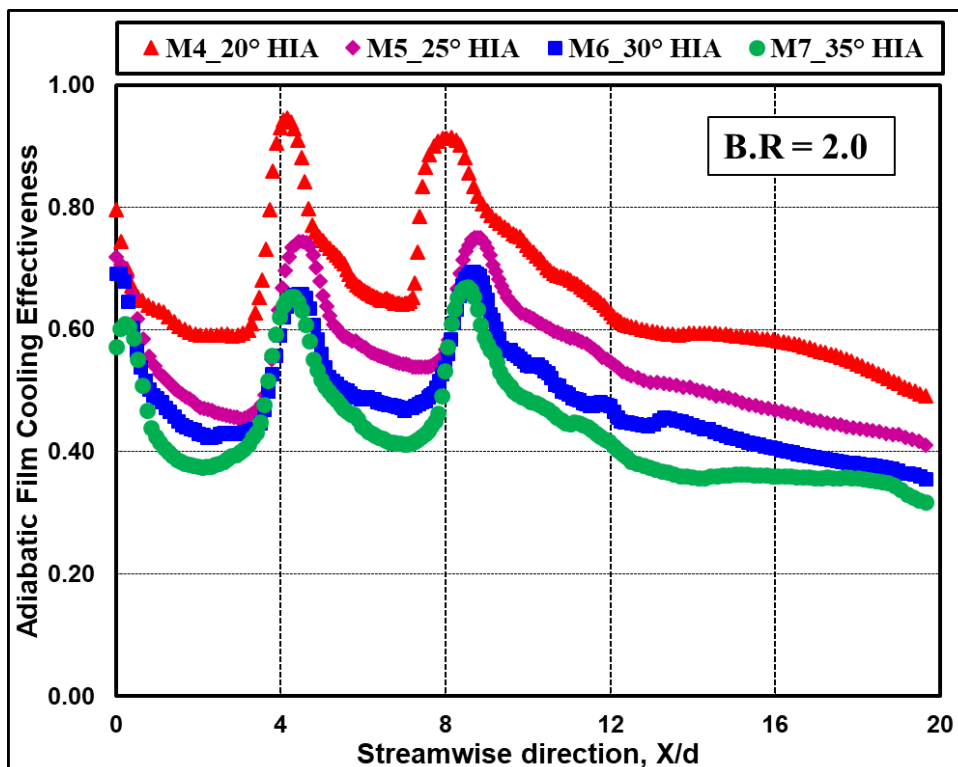


Fig. 5.36 Comparison of cooling effectiveness for all HIA models at a B.R of 2.0

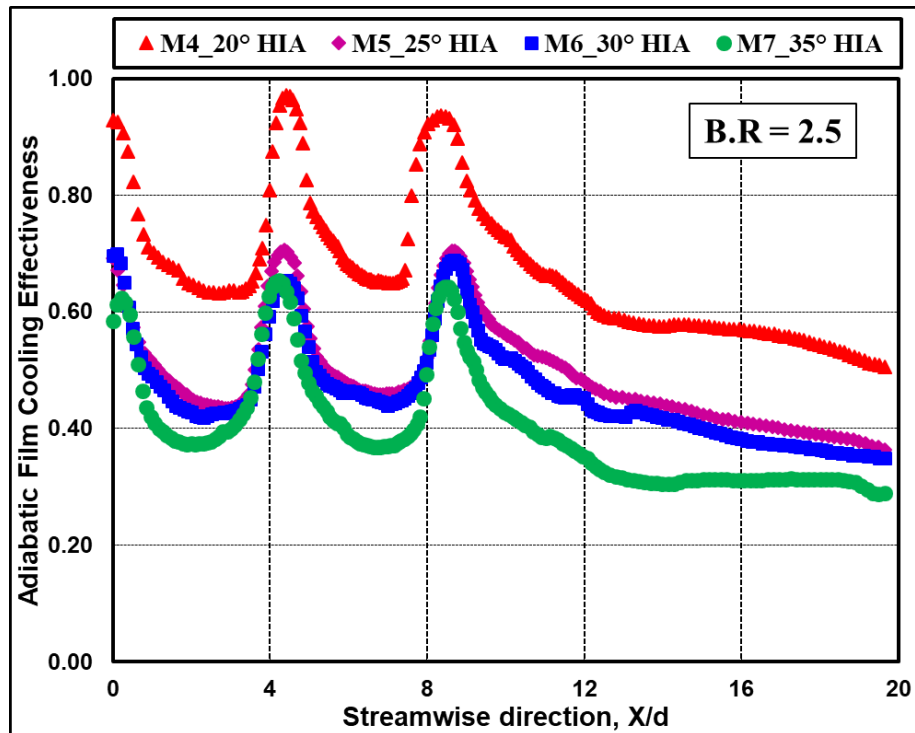


Fig. 5.37 Comparison of cooling effectiveness for all HIA models at a B.R of 2.5

Fig. 5.34 to Fig. 5.37 shows the comparison of adiabatic film cooling effectiveness for all the four considered models at blowing ratio of 1.0, 1.5, 2.0 and 2.5 respectively. The comparison is made by keeping blowing ratio constant and varying hole inclination angle, from the comparison it is found that at higher blowing ratios as the increase in hole inclination angle the film cooling effectiveness is decreased gradually. At lower blowing ratio 1.0, the 30° hole inclination angle model is showing good results compared to the other three models. At the blowing ratio of 1.5, 2.0 and 2.5, 20° hole inclination angle model is showing higher film cooling effectiveness than the 25°, 30°, and 35° hole inclination angle models. This is due to the higher lateral distribution of film and more attachment of coolant on the leading edge surface.

5.2.2 Numerical Adiabatic Film cooling effectiveness and HTC Results

Fig. 5.38 shows grid independency results at a blowing ratio of 1.5 for 25° hole inclination angle. Initially, 454470 element size is considered and is increased to 688228, and found that there is a small change in film cooling effectiveness with

mesh change. After that, the mesh size is increased to 803325 and found there is no change in the results of film cooling effectiveness. Hence, 688228 grid size is used for all the three considered models of CFD simulation. Adiabatic Film cooling effectiveness and heat transfer coefficients values are evaluated numerically for all the four leading edge models with 20°, 25°, 30° and 35° hole inclination angles.

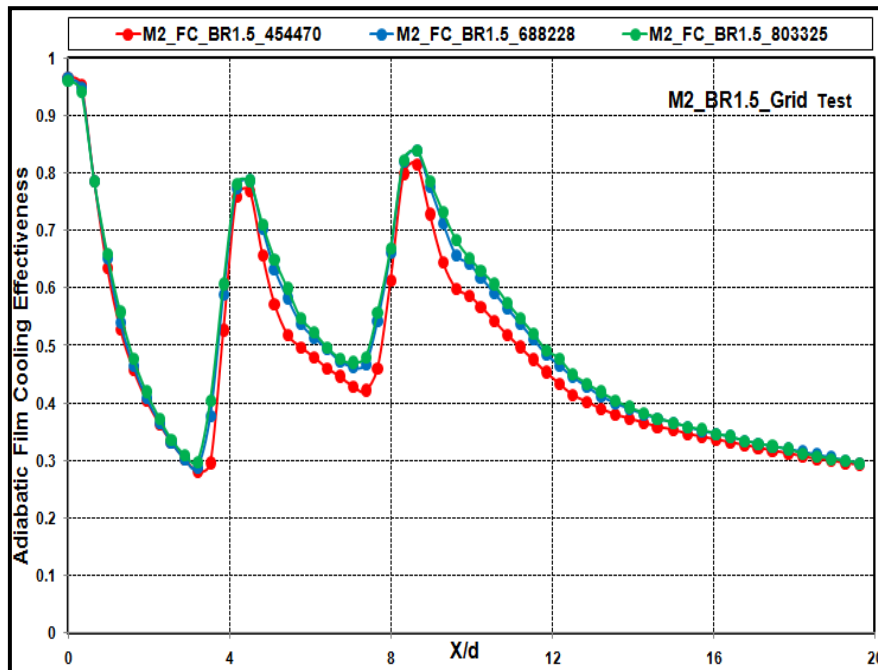


Fig. 5.38 Grid independency results for 25° HIA model at a B.R of 1.5

Fig. 5.39 shows the variation of adiabatic film cooling effectiveness for 20° hole inclination angled model. From the figure it is found that effectiveness is increased with increase in blowing ratio from 1.0 to 1.5, For blowing ratio 1.0 effectiveness is lower at the stagnation region because of coolant flow is restricted by the mainstream due to higher pressure at the stagnation and the downstream, it is found higher.

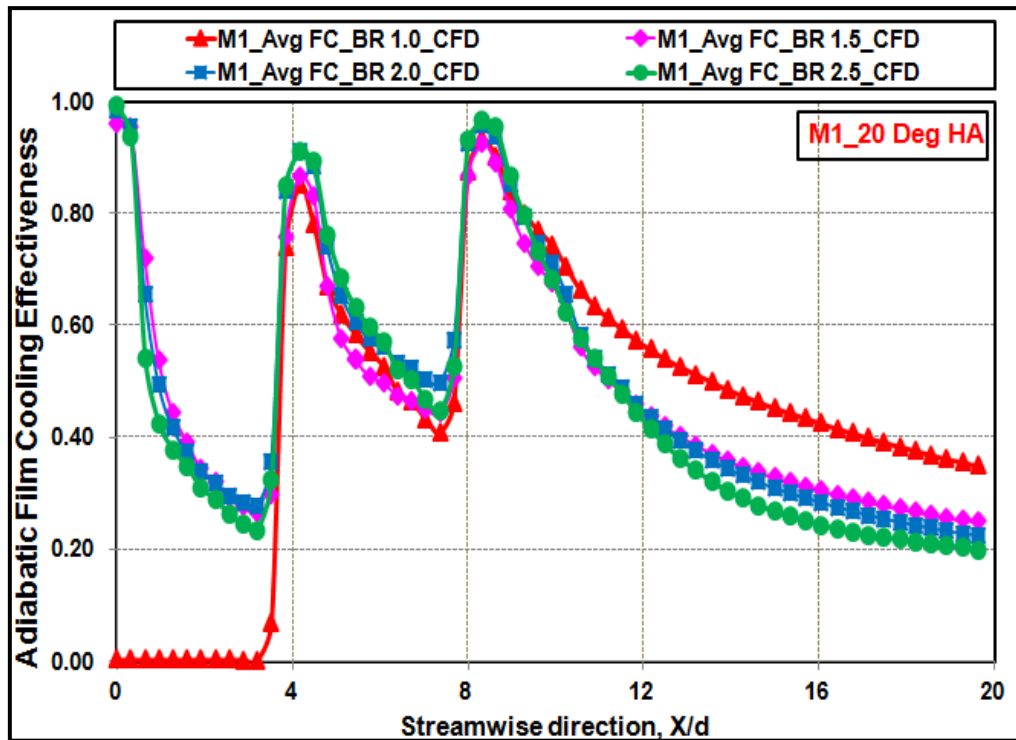


Fig. 5.39 Numerical Cooling effectiveness for a 20° HIA model

Further increase in blowing ratio from 1.5 to 2.5 the effectiveness is decreased continuously at the downstream of holes except for stagnation hole region. Effectiveness is found to be unchanged with increasing in blowing ratio up to 2.5 at the stagnation hole region because of the flow restrictions are reduced due to coolant pressure increases. Among all the four blowing ratios considered, the BR 1.5 is showing higher film cooling effectiveness. Considering overall flow film cooling area, BR 1.5 is considered as optimized blowing ratio for 20° hole injection angle model. The effect of blowing ratio depends upon three major factors of coolant flow or film formation over the test surface: they are attachment, detachment, and reattachment. Attachment is higher at the lower blowing ratio, as the blowing ratio increases detachment and reattachment of coolant flow over the test surface come into the picture. Typical temperature contours of all the four blowing ratios for 20° hole inclination angle model is shown in Fig. 5.40. From the temperature contours the major film cooling phenomenon attachment, detachment and reattachment are easily understandable. The units of scale on the temperature contours of Fig. 5.40 are the numerically extracted temperature values in Kelvin.

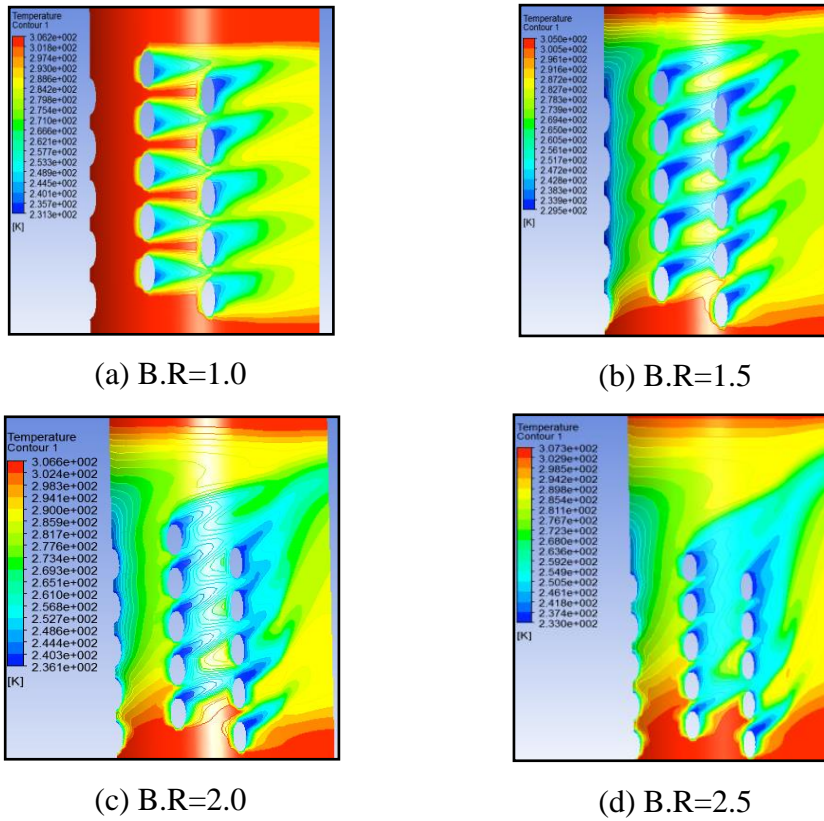


Fig. 5.40 Temperature contours of 20° HIA model at different B.Rs

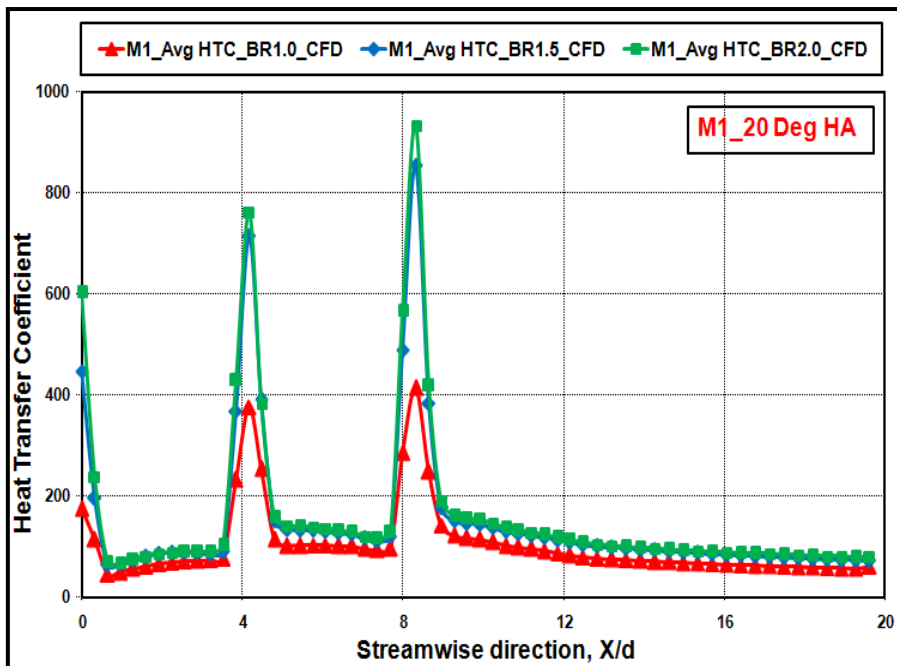


Fig. 5.41 Numerical heat transfer coefficient values of a 20° HIA model

An attempt is made to evaluate heat transfer coefficients results numerically with the same experimental geometrical and flow parameters. Experimentally available constant heat flux is applied on the leading edge surface to evaluate heat transfer coefficients. Fig. 5.41 shows the results of numerically evaluated heat transfer coefficients for 20° hole inclination angle model, from the figure the heat transfer coefficients results in increases with increase in blowing ratio.

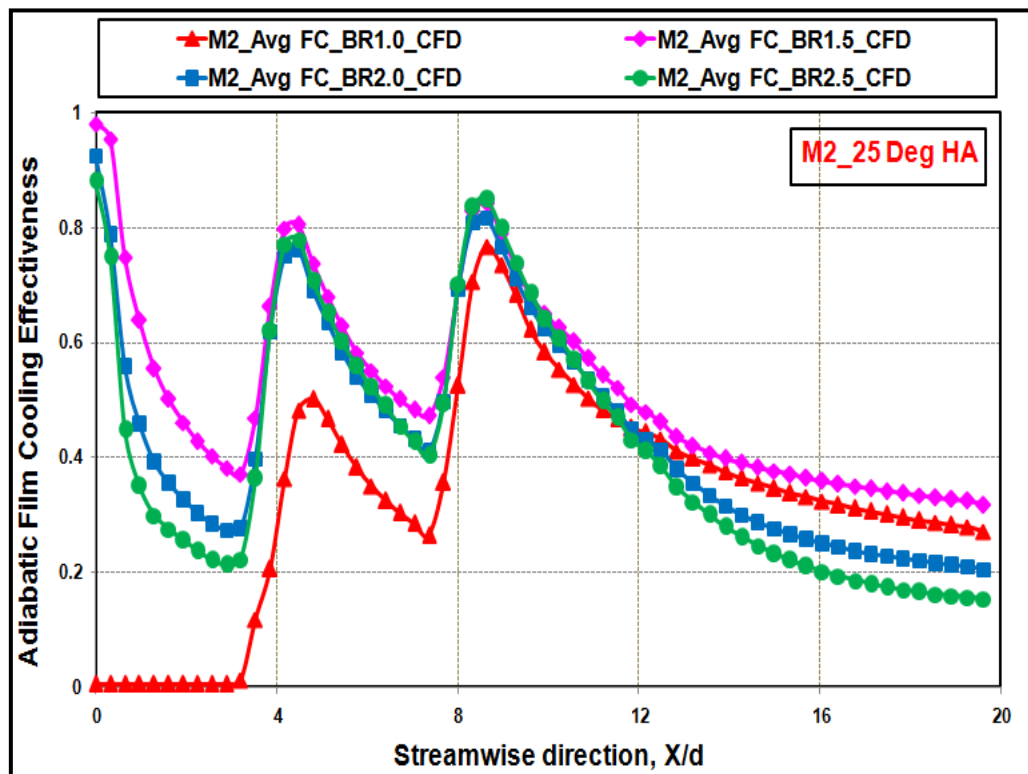


Fig. 5.42 Numerical cooling effectiveness of a 25° HIA model

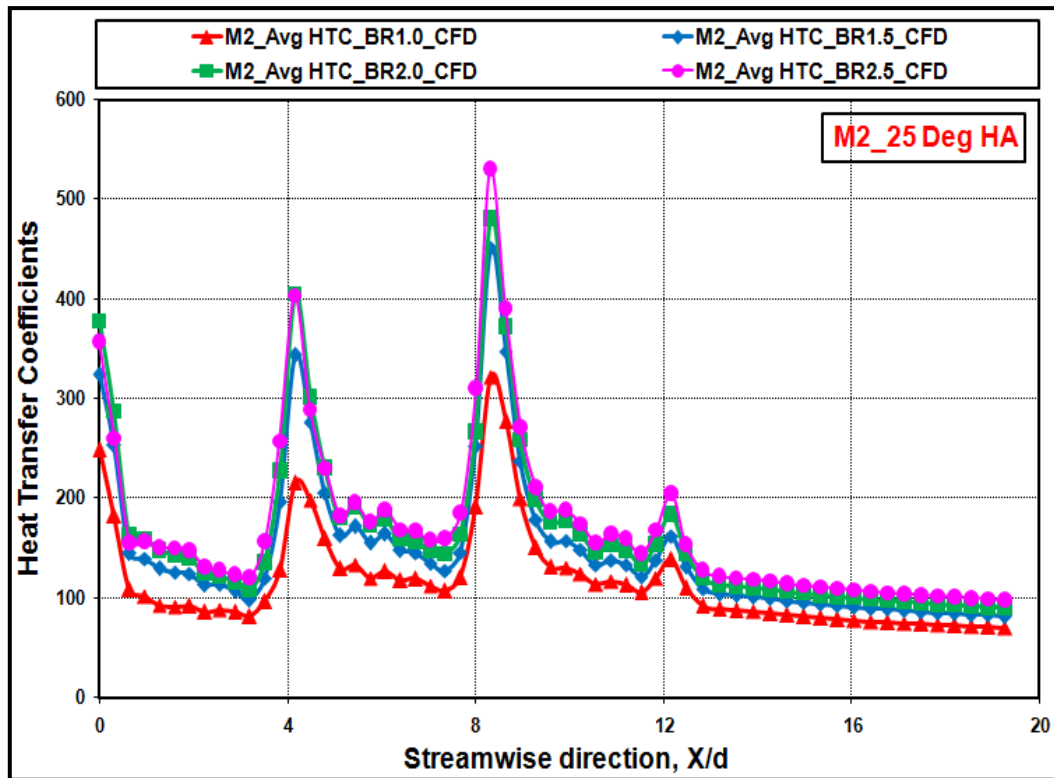


Fig. 5.43 Numerical heat transfer coefficient values of a 25° HIA model

Fig. 5.42 and Fig. 5.43 shows the numerically evaluated results of adiabatic film cooling effectiveness and heat transfer coefficients in W/m^2K for 25° hole inclination angle model. For 25° hole inclination angle model, film cooling effectiveness increase with an increase in blowing ratio of 1.0 to 1.5. Since there is no improvement in adiabatic film cooling effectiveness from a blowing ratio of 1.5 to 2.0 so, the blowing ratio 1.5 can be considered as optimized blowing ratio for 25° hole inclination angle model. As the blowing ratio increases, the heat transfer coefficients values are found to be increased.

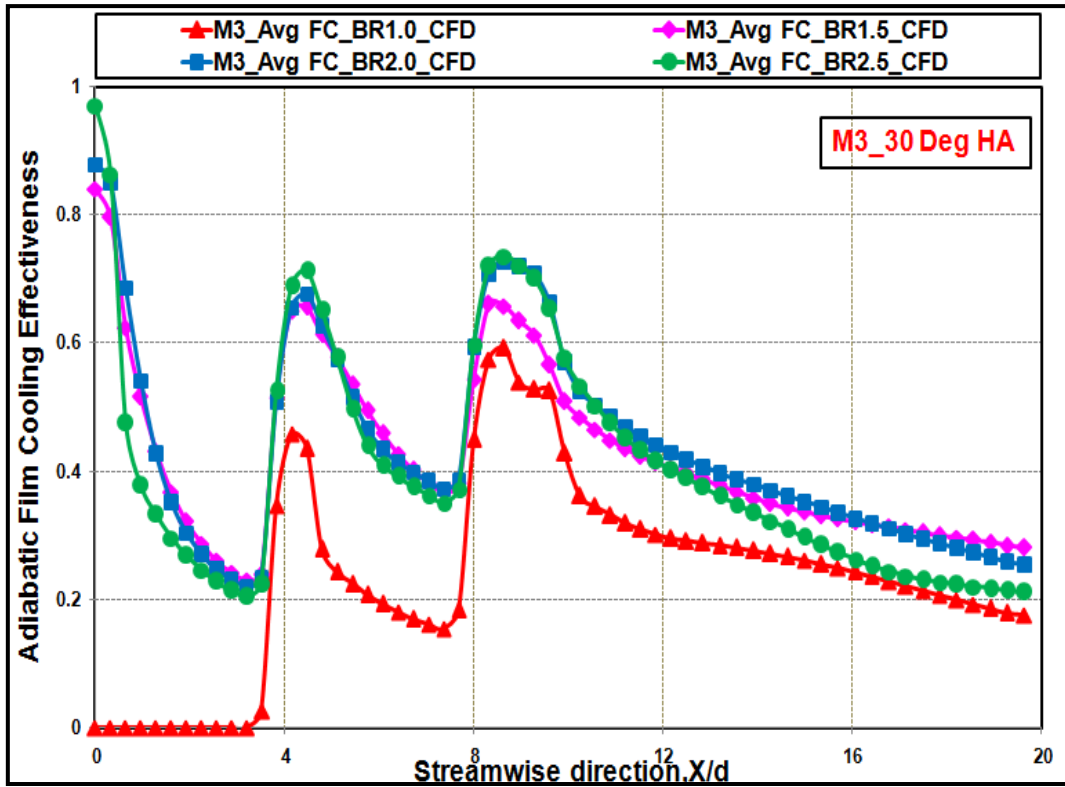


Fig. 5.44 Numerical cooling effectiveness of a 30° HIA model

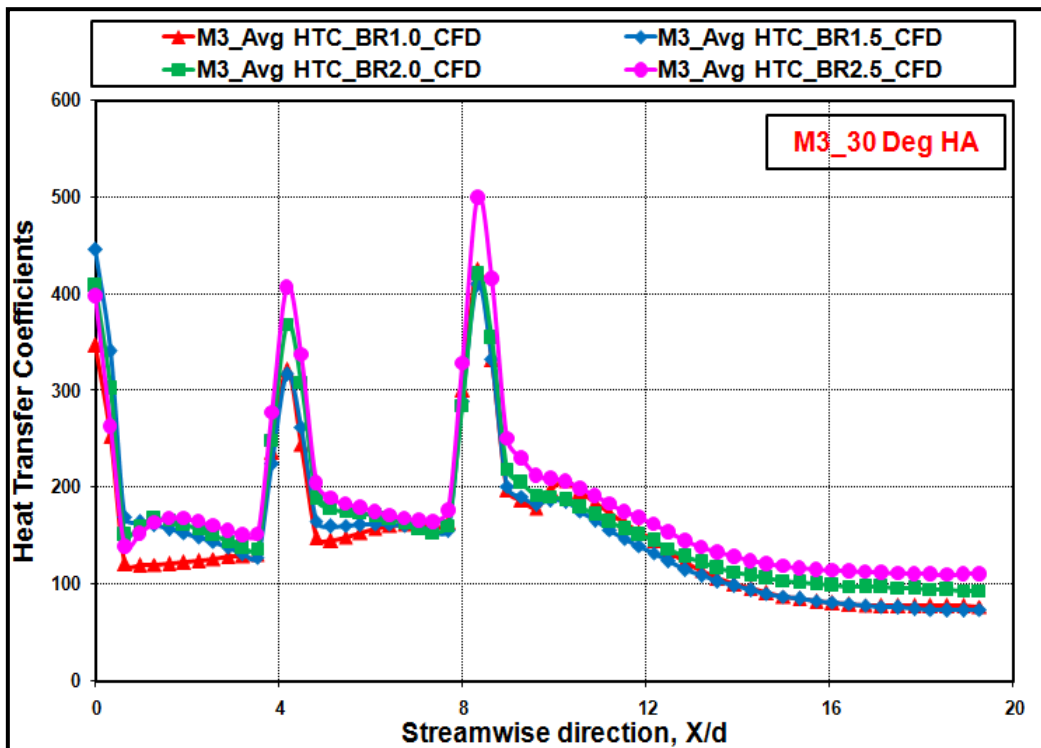


Fig. 5.45 Numerical heat transfer coefficient values of a 30° HIA model

Adiabatic film cooling effectiveness distribution in streamwise for 30° hole inclination angle model is shown in the Fig. 5.44. Effectiveness is increased to a maximum level with increasing blowing ratio from 1.0 to 2.0, further increase in blowing ratio of 2.0 to 2.5 the effectiveness is reduced. But the improvements in adiabatic film cooling effectiveness between the increase in blowing ratio of 1.5 to 2.0 not much higher. Hence in 30° hole inclination angle model case also blowing ratio 1.5 is considered as optimized blowing ratio. Fig. 5.45 shows the numerically evaluated heat transfer coefficients in W/m^2K for 30° hole inclination angle model, from the figure heat transfer coefficients, increase with an increase in blowing ratio.

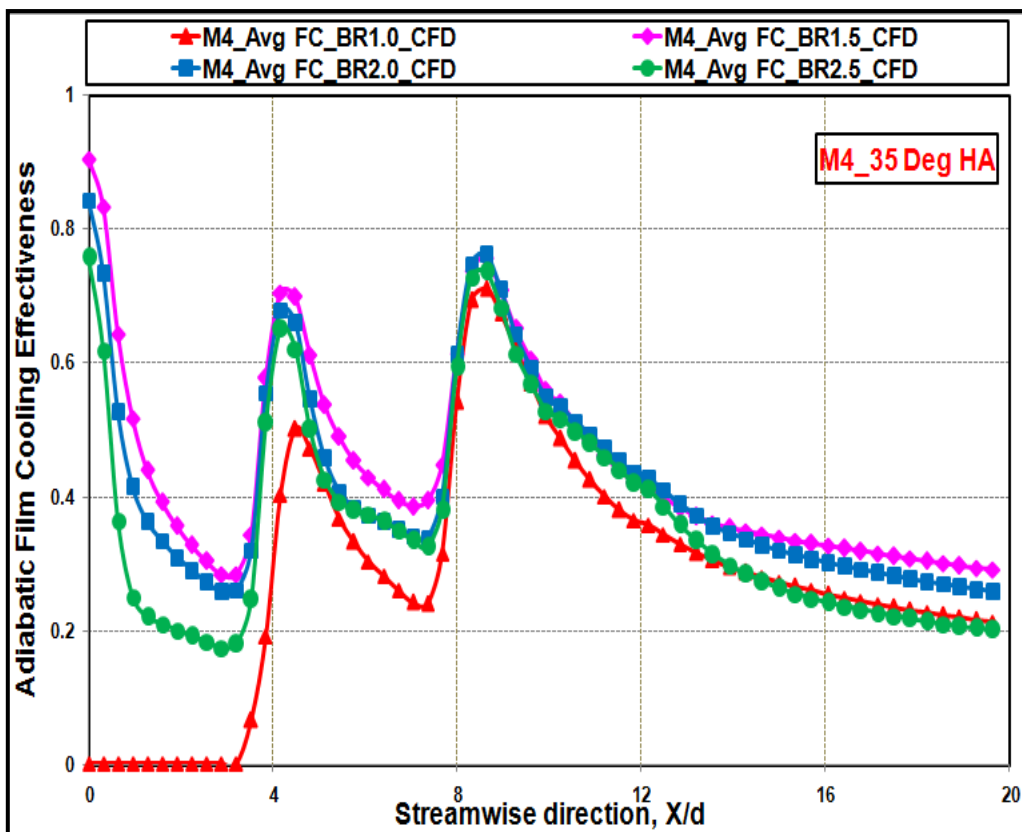


Fig. 5.46 Numerical cooling effectiveness of a 35° hole inclination angle model

CFD results of adiabatic film cooling effectiveness for 35° model is shown in Fig. 5.46. From the Fig. 5.46, for 35° hole inclination angle model, the film cooling effectiveness is higher at a blowing ratio of 1.5 and lower at blowing ratio 1.0 as found in all other models. It is found that there is no use for increasing the blowing ratio beyond 1.5 because the film cooling effectiveness is reduced with a further

increase in blowing ratio from 1.5 to 2.5. From the comparison, by keeping hole inclination angle constant and varying the blowing ratio, it is found that blowing ratio 1.5 is optimized and blowing ratio 1.0, 2.0 and 2.5 are showing poor performance than blowing ratio 1.5

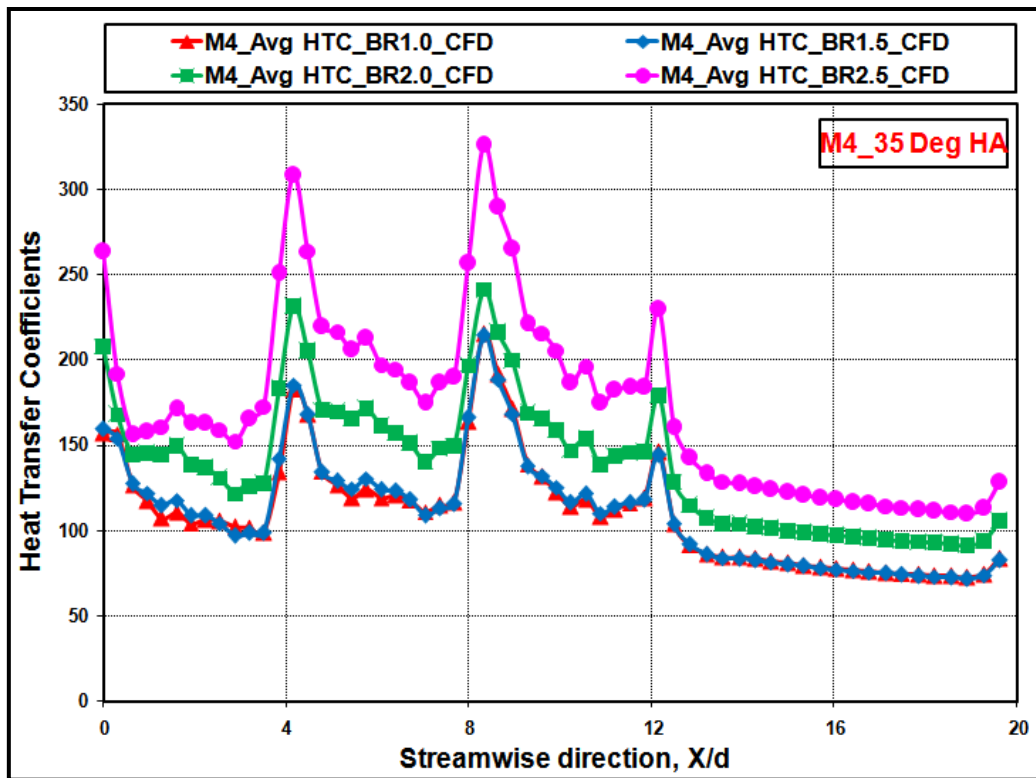


Fig. 5.47 Numerical heat transfer coefficient for 35° hole inclination angle model

For 35° hole inclination angle model both the experiment and the numerically calculated heat transfer coefficient values have shown similar results. Heat transfer coefficient is found to be increasing with the increase in blowing ratio as shown in Fig. 5.47.

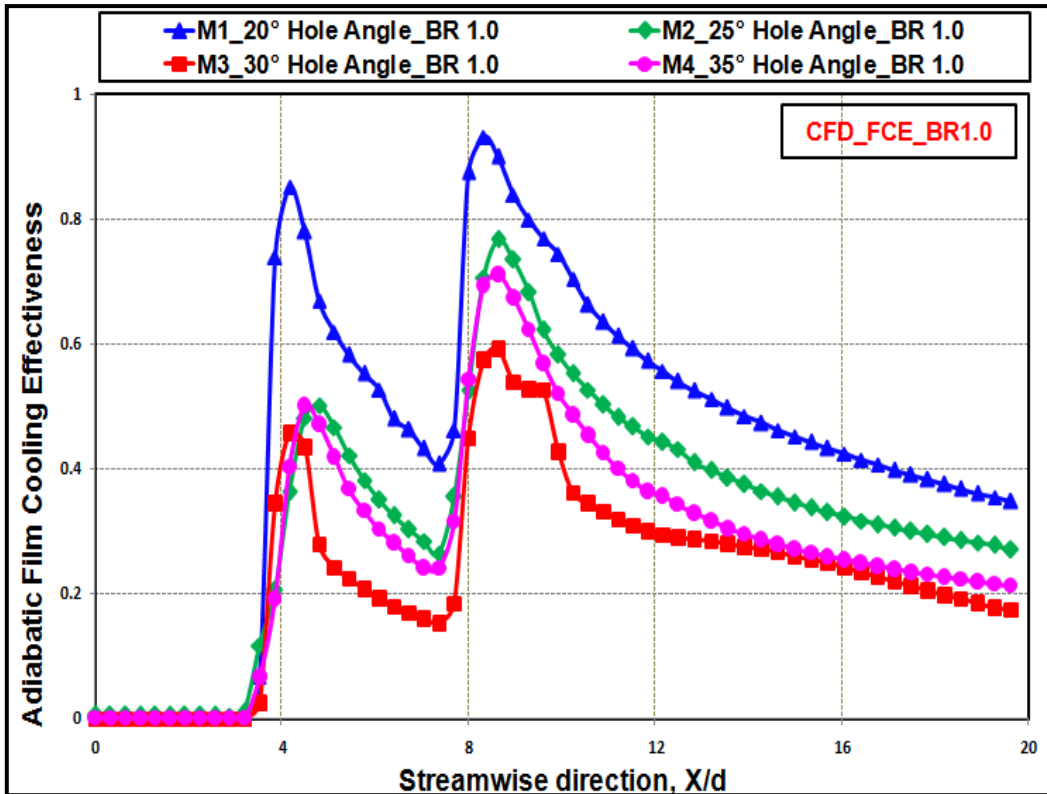


Fig. 5.48 Comparison of cooling effectiveness for all the models at a B.R of 1.0

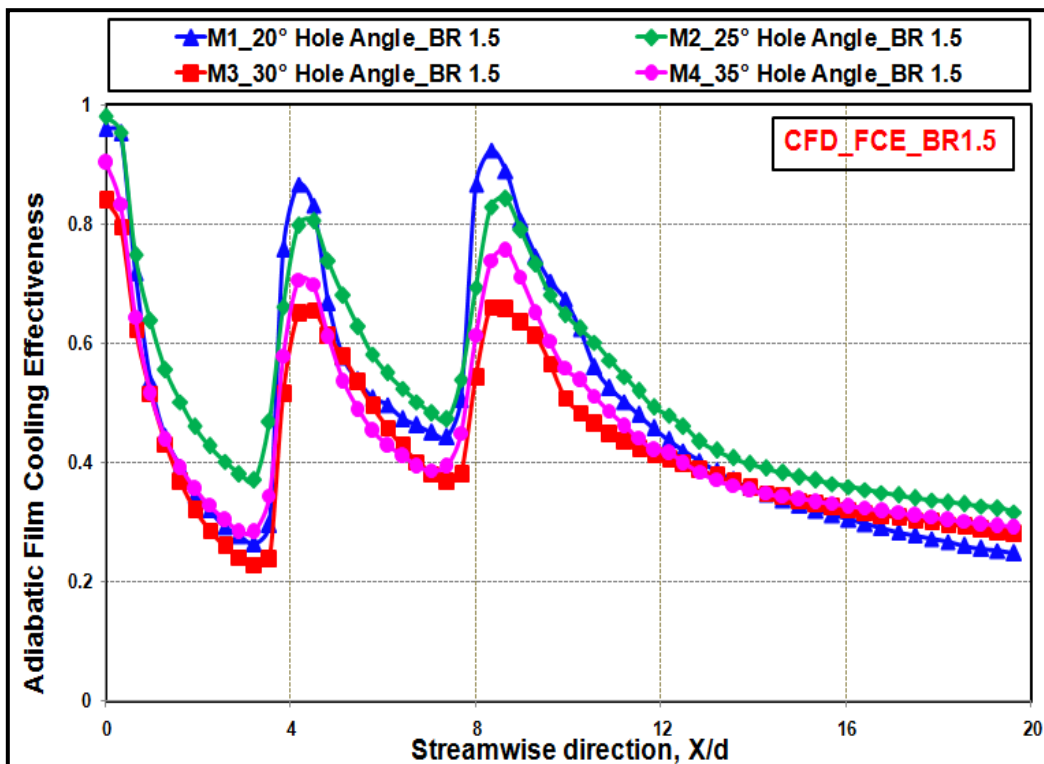


Fig. 5.49 Comparison cooling effectiveness for all the models at a B.R of 1.5

Fig. 5.48, Fig. 5.49, Fig. 5.50 and Fig. 5.51 shows the comparison of numerically calculated adiabatic film cooling effectiveness for all the four considered models at blowing ratios of 1.0, 1.5, 2.0 and 2.5 respectively. Similar to the experimental case, the comparison is made by keeping blowing ratio constant and varying hole inclination angle.

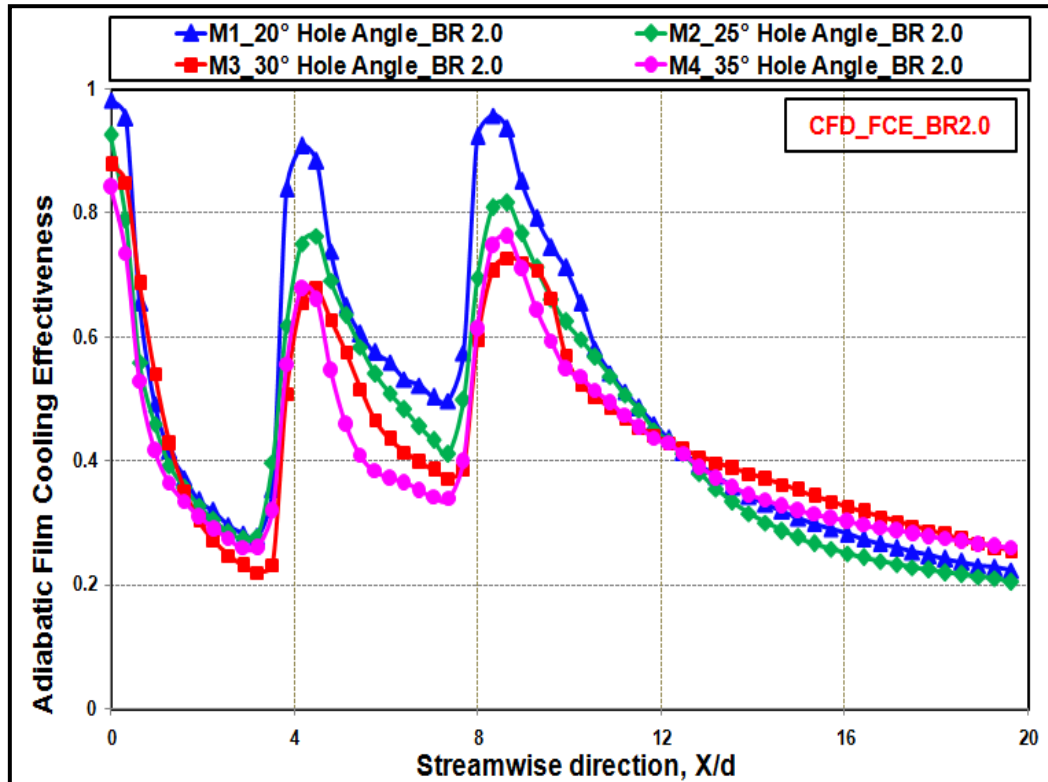


Fig. 5.50 Comparison of cooling effectiveness for HIA models at a B.R of 2.0

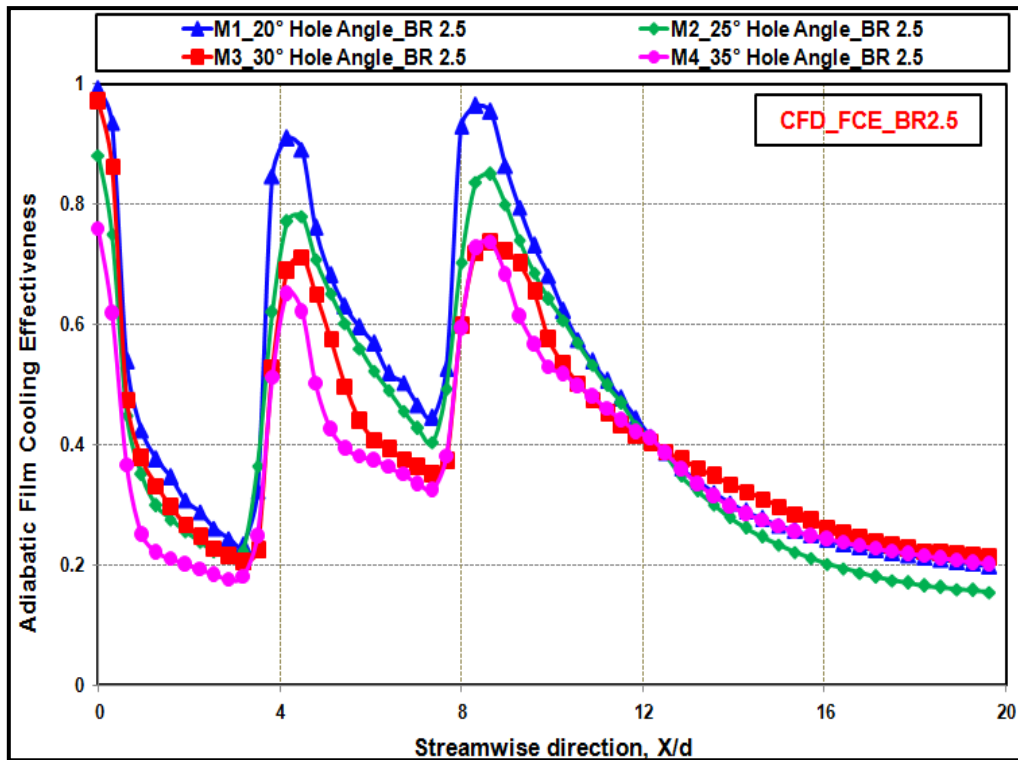


Fig. 5.51 Comparison of cooling effectiveness for HIA models at a B.R of 2.5

From the comparison, it is found that at all the blowing ratios the film cooling effectiveness increases as the hole inclination angle decreases. Among the 20°, 25°, 30°, and 35° hole inclination angle models, the marginal difference in the cooling effectiveness is seen between the 30° and 35° models whereas the 20° hole inclination angle model has shown the significant improvement in the cooling effectiveness. This may be because of higher lateral distribution of film and more attachment of coolant on the leading edge surface.

5.2.3 Comparison of Experimental and CFD Results

CFD simulation results are compared with experimental results to validate the CFD results. From CFD simulation the adiabatic film cooling effectiveness values give similar to experimental values. The adiabatic film cooling effectiveness is calculated along the streamwise direction for the blowing ratios in the range of 1.0 to 2.5. The peaks in the plots indicate the adiabatic film cooling effectiveness values near the holes regions and CFD contours have shown the meaningful results with experimental contours.

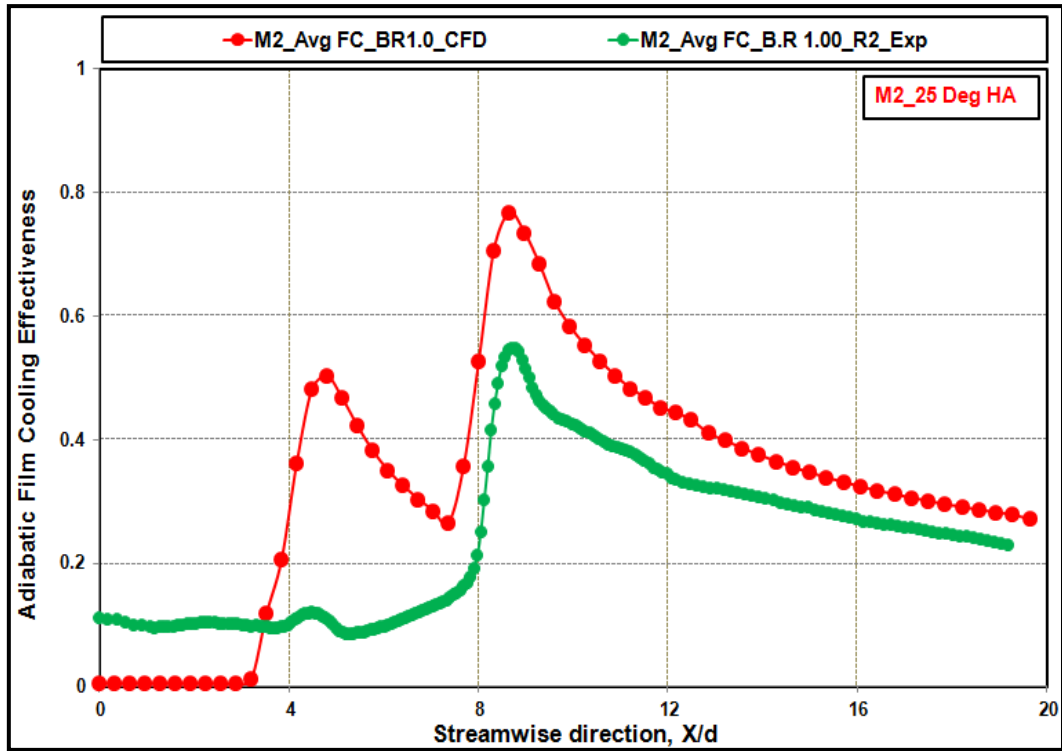


Fig. 5.52 Exp. Vs. CFD effectiveness results for a 25° HIA model at a B.R of 1.0

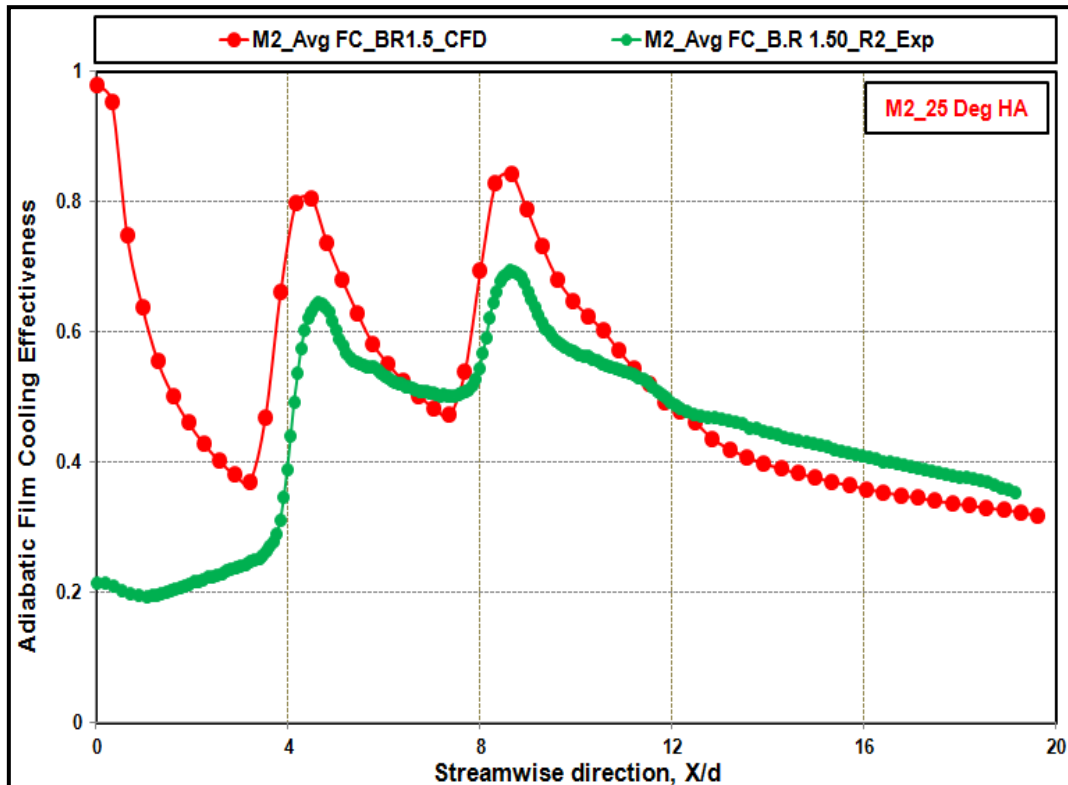


Fig. 5.53 Exp. Vs. CFD effectiveness results for a 25° HIA model at a B.R of 1.5

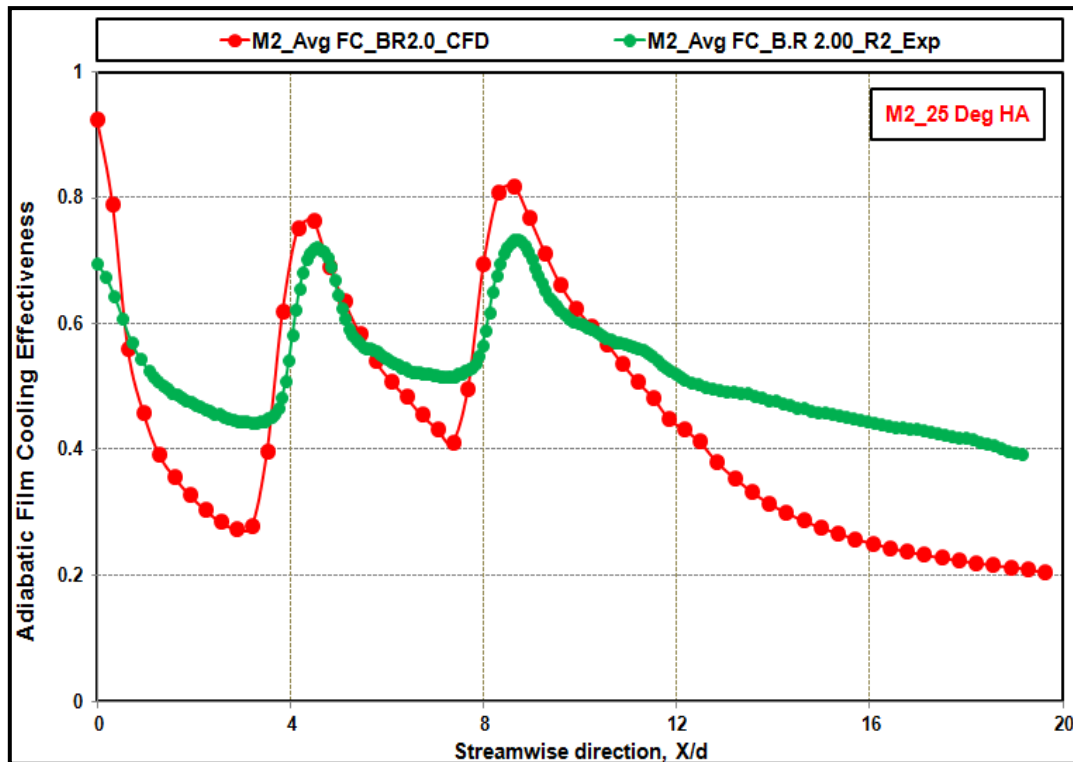


Fig. 5.54 Exp. Vs. CFD effectiveness results for a 25° HIA model at a B.R of 2.0

Fig. 5.52 shows the comparison of CFD results with experimental results at a blowing ratio of 1.0 for 25° hole inclination angle model, here CFD results show little higher values than the experimental results. At stagnation hole region experimental results showed higher cooling effectiveness values due to conduction cooling effect.

Experimental and CFD film cooling effectiveness results at a blowing ratio of 1.5 and 2.0 for 25° model is shown in Fig. 5.53 and Fig. 5.54 respectively. CFD results shown higher deviations at the hole region and little deviation at downstream region of holes. CFD results of film cooling effectiveness have shown the good trends and a better match with the experimental results.

At higher blowing ratios, CFD results have good matching with the experimental results, a comparison of experimental results with CFD results for 25° model is shown in Fig. 5.55 at a blowing ratio of 2.5. There is slight variation in numerically calculated film cooling effectiveness compared with experimental results at the lower blowing ratios.

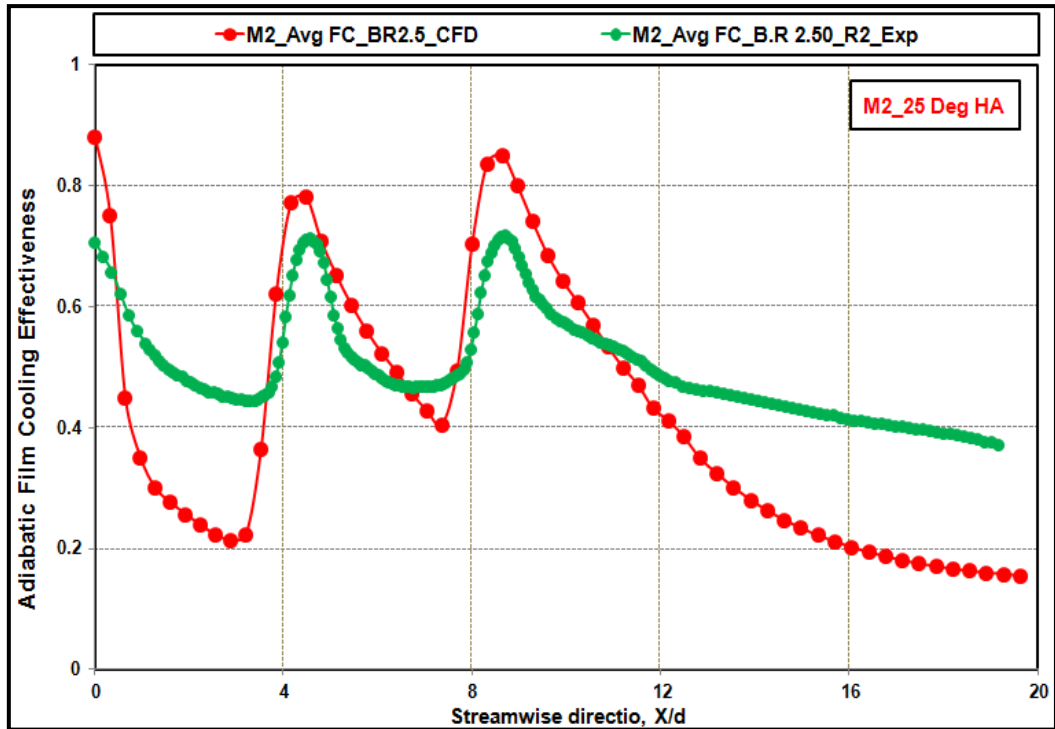


Fig. 5.55 Exp. Vs. CFD effectiveness results for a 25° HIA model at a B.R of 2.5

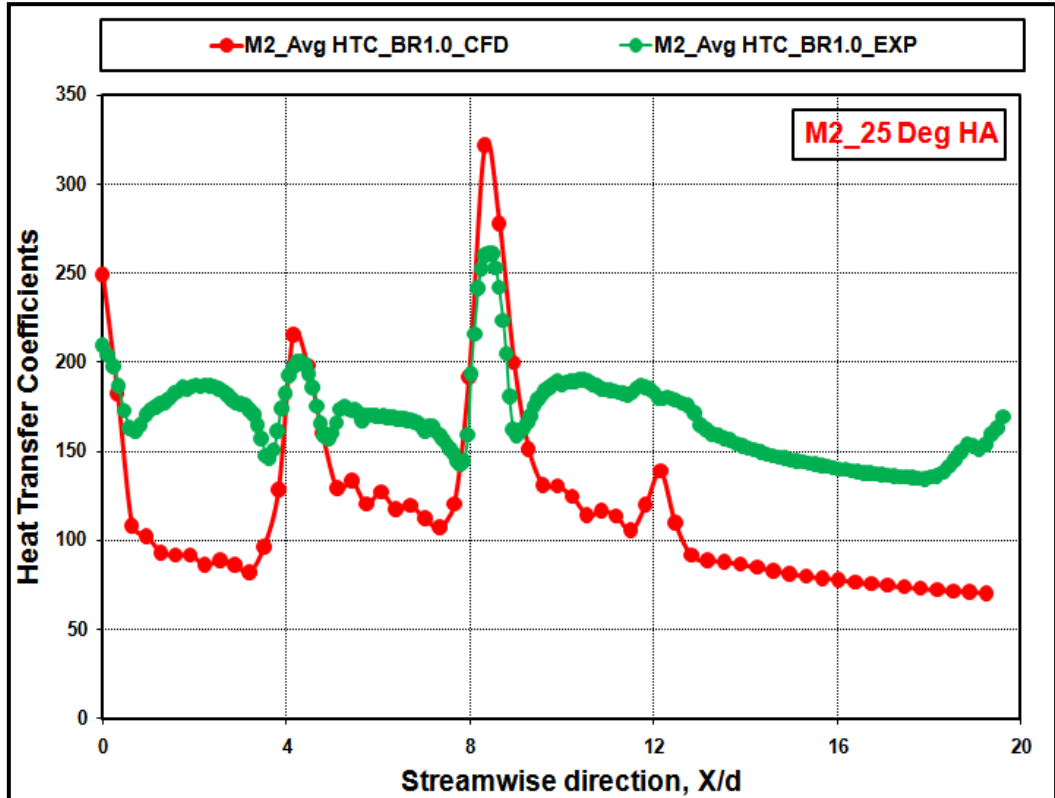


Fig. 5.56 Exp. Vs. CFD HTC results for a 25° HIA model at a B.R of 1.0

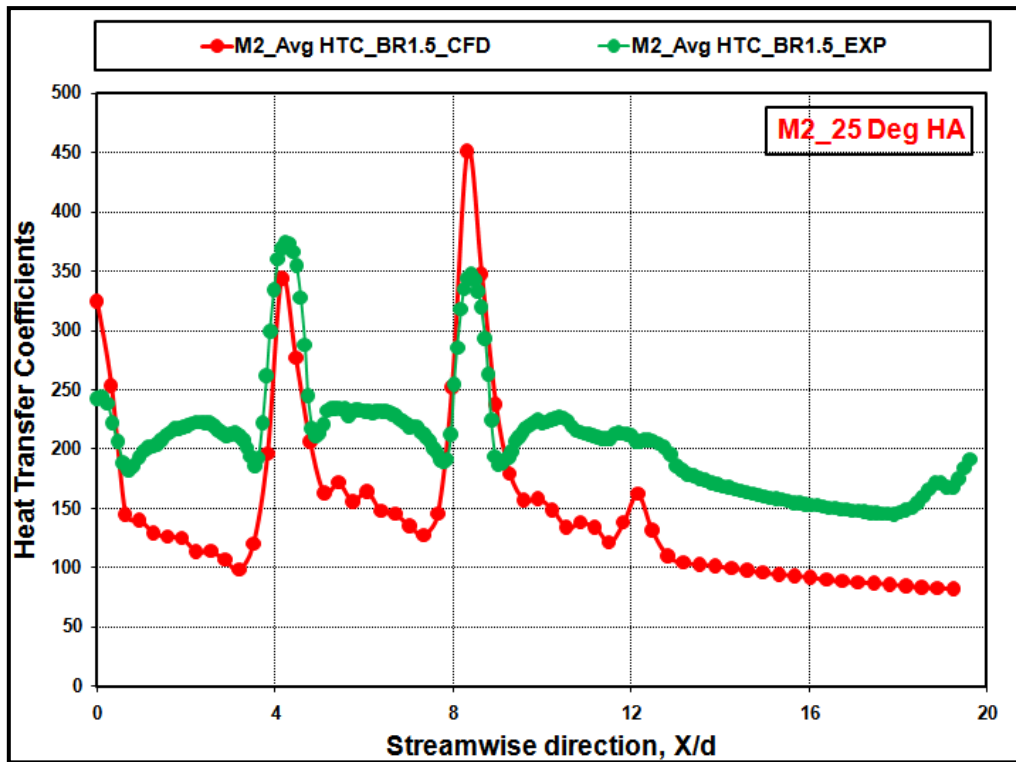


Fig. 5.57 Exp. Vs. CFD HTC results for a 25° HIA model at a B.R of 1.5

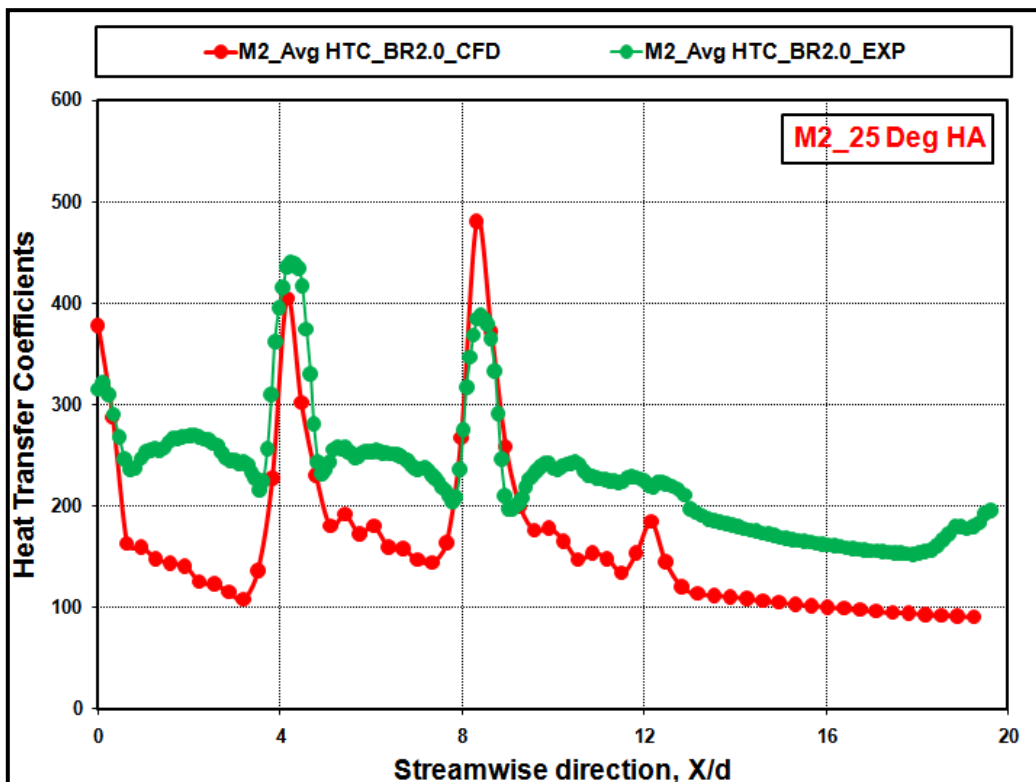


Fig. 5.58 Exp. Vs. CFD HTC Results for a 25° HIA model at a B.R of 2.0

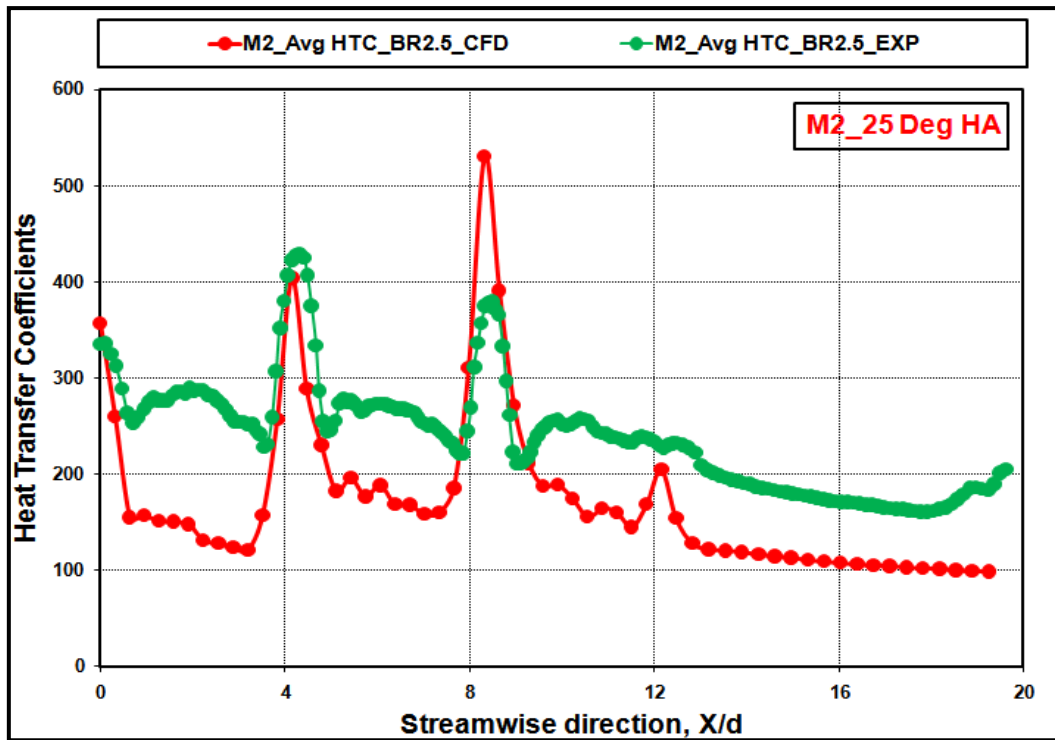


Fig. 5.59 Exp. Vs. CFD HTC Results for a 25° HIA model at a B.R of 2.5

Comparison of heat transfer coefficients in W/m^2K between experimental results and CFD results for 25° model at blowing ratio 1.0, 1.5, 2.0 and 2.5 is shown in the Fig. 5.56 to Fig. 5.59 respectively. From the comparison, it is found that experimentally evaluated heat transfer coefficient results have shown higher than the CFD simulated results, but the results are in similar trends.

The numerically obtained results have shown the similar trends of experimental cooling effectiveness values. However, the numerical results have shown the overprediction than that of experimental values. And in the case of heat transfer coefficients, the numerical studies have shown the lesser predicted results than the experimental values with the similar trends. Numerically obtained results are useful in choosing the better geometry based on the trends of results even though the results are not accurate as that of the experimental values. The deviations in the heat transfer coefficients among the experimental and CFD are observed more, mainly due to the non-consideration of near stagnant conditions of mainstream flow, complex mixing phenomenon and frictional losses, and the presence of lateral conduction in the experiments.

5.3 Effect of Hole Pitch

To bring out the effect of hole pitch (HP), two test models (M6 and M8) are considered with one row of holes on stagnation line and two rows of holes on either side of stagnation line at 30° and 60° with the hole inclination angle of 30° having the hole pitches of 18 and 22.4 mm respectively. Both these test models have the hole diameter of 5.6 mm with p/d values of 3.2 and 4 respectively for the hole pitches of 18 and 22.4 mm.

5.3.1 Adiabatic Film Cooling Effectiveness Measurements

Adiabatic film cooling effectiveness measurements are carried out both experimentally and numerically over the leading edge test surfaces at different flow conditions, by varying the blowing ratios in the range of 1.0 to 2.5 at a density ratio of 1.3. Temperature distribution over test surface under these flow conditions is obtained and used for adiabatic film cooling effectiveness calculations. Results are plotted regarding laterally averaged adiabatic film cooling effectiveness along the streamwise direction.

5.3.1.1 18 mm Spanwise Hole Pitch Model (M6) Cooling Effectiveness Results

The typical experimental thermal images and the temperature contours obtained in numerical simulations of cooling effectiveness measurements at a blowing ratio of 2.0 for the 18 mm hole pitch model are shown in the Fig. 5.60. These images are processed to find temperature values and used in the cooling effectiveness calculations. From Fig. 5.60, it can be seen that flow patterns are almost the same in both experiments and numerical simulations. Flow distribution over the test surface is little different in numerical simulations compared to experiments. At stagnation holes region, there is not a much coolant flow through the holes in numerical simulation at blowing ratio of 1.0, since the coolant pressure is lower than mainstream, but there is little coolant flow at stagnation holes in the experiment. At blowing ratios of 1.5 and above, the more coolant flow is observed at the stagnation holes region in numerical simulations than in experiments.

The units of scale on a thermal image of Fig. 5.60 are the thermal radiation count captured by the infra-red camera and the units of scale on the numerical thermal image of Fig. 5.60 are the temperature values in Kelvin extracted from CFD analysis.

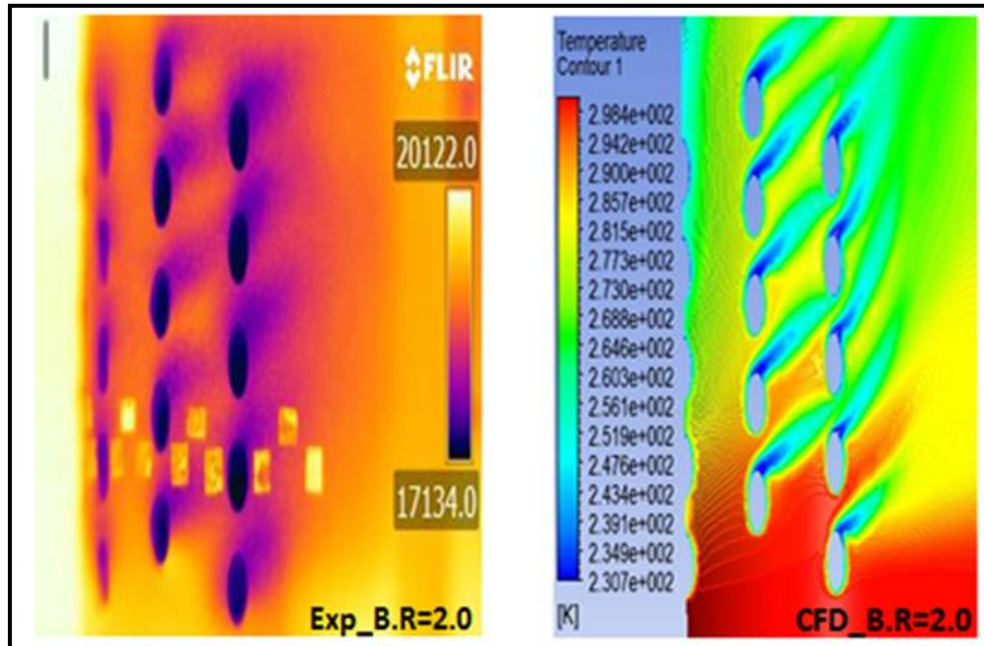


Fig. 5.60 Exp. and CFD temperature contours of effectiveness for 18 mm hole pitch model at a B.R of 2.0

Fig. 5.61 and Fig. 5.62 shows experimental and numerical laterally averaged adiabatic film cooling effectiveness results plotted along the streamwise direction for model 6 at blowing ratios in the range of 1.0 to 2.5. Experimental results are showing an increase in effectiveness with an increase in blowing ratio up to blowing ratio of 2.0 considerably. From blowing ratio of 2.0 to 2.5, there is only a marginal increase in averaged effectiveness is observed and this amount of increase is not a consideration with the quantum of increase in coolant mass flow supply. Hence, a blowing ratio of 2.0 is considered as optimized blowing ratio for this geometry. Numerical results are showing similar trends as experimental results at all the considered blowing ratios. Peaks in the plots are indicating hole locations, and they are in good agreement in both experimental and numerical results.

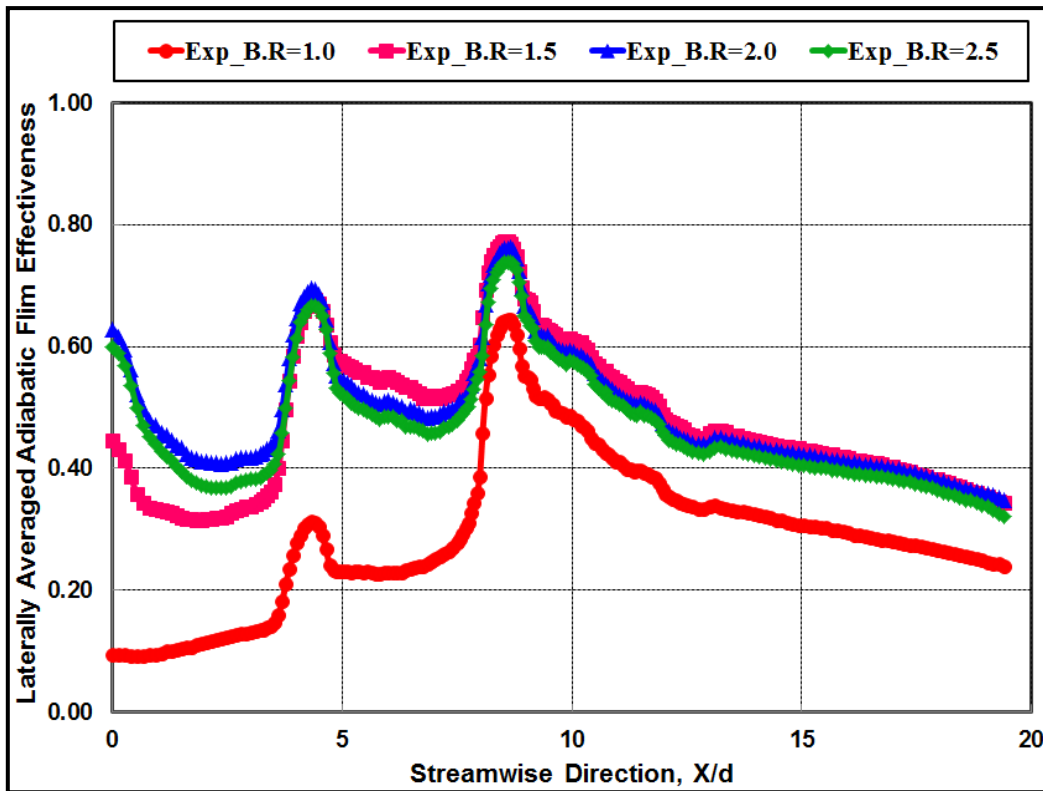


Fig. 5.61 Exp. cooling effectiveness for 18 mm pitch model at B.Rs of 1.0 to 2.5

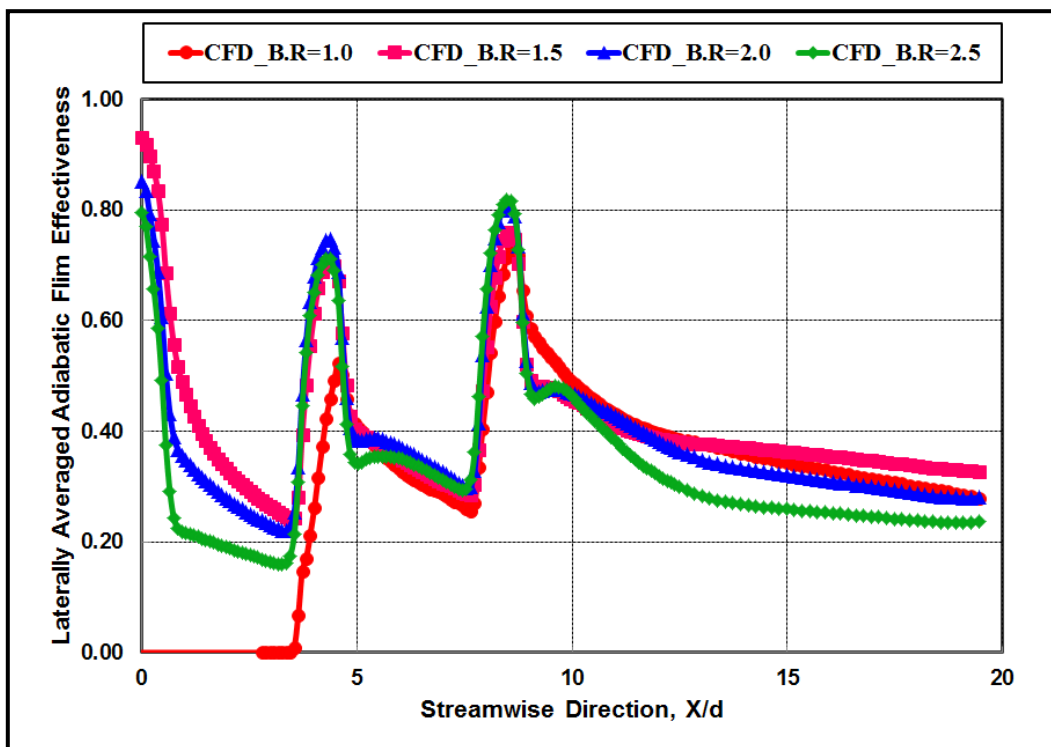


Fig. 5.62 Numerical cooling effectiveness for 18 mm model at B.Rs of 1.0 to 2.5

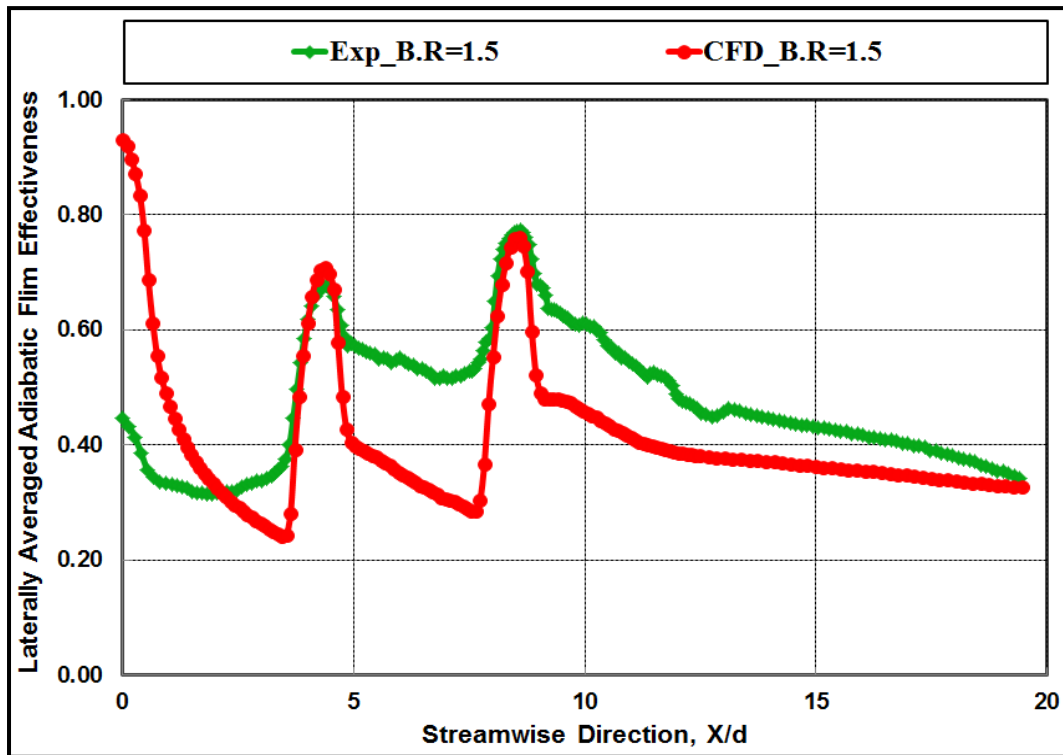


Fig. 5.63 Exp. and Numerical cooling effectiveness for 18 mm model at a B.R of 1.5

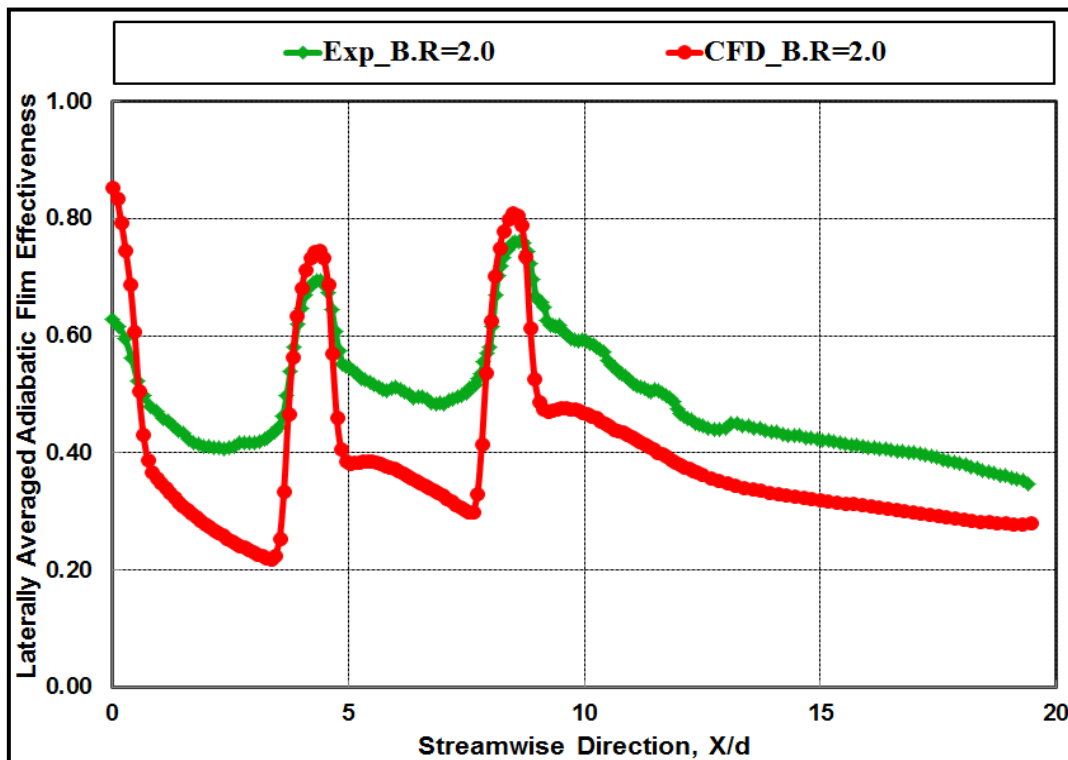


Fig. 5.64 Exp. and Numerical cooling effectiveness at a B.R of 2.0

Fig. 5.63 and Fig. 5.64 shows the experimental and numerical averaged effectiveness results compared individually for blowing ratios of 1.5 and 2.0. In both the blowing ratio cases, the numerical results are showing similar trends as in experimental results. Peaks are indicating the location of hole rows where both experimental and numerical averaged effectiveness results are matching except at stagnation hole regions. At downstream regions numerically averaged results are showing lesser values than experimental results because of difference in flow distribution and film coverage over the test surface. Similar trends and peak matchings are observed at other considered blowing ratios. Numerical averaged effectiveness results are showing 0.1 to 0.25 lesser averaged effectiveness values at downstream holes region than in experimental results at all the considered blowing ratios.

Here, the CFD extracted results have shown little lower predicted cooling effectiveness results than that of experimental values but, able to capture the same experimental trends. This numerical analysis is helpful for choosing the better geometry based on the trends of results even thou the results are not accurate as that of the experimental values. The deviation of CFD results from experimental values is caused due to the non-consideration of frictional and mixing phenomenon losses in the numerical analysis.

5.3.1.2 22.4 mm Spanwise Hole Pitch Model (M8) Cooling Effectiveness Results

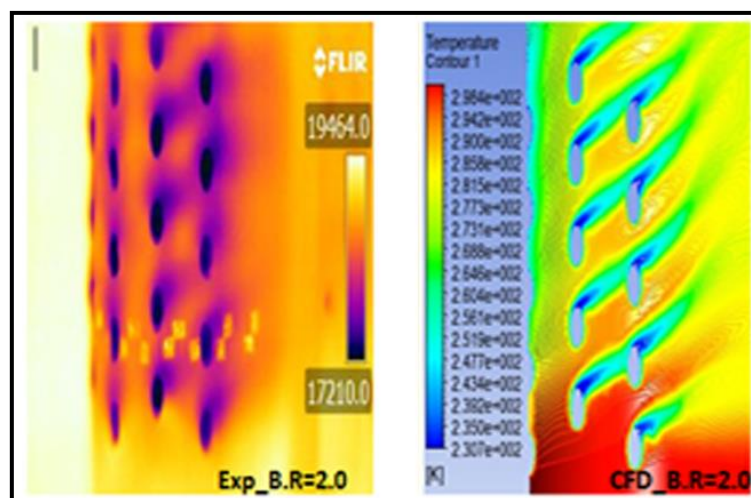


Fig. 5.65 Exp. and CFD temperature contours of effectiveness for a 22.4 mm hole pitch model at a B.R of 2.0

The typical experimental thermal images and the temperature contours obtained in numerical simulations of cooling effectiveness measurements at the blowing ratio of 2.0 for a 22.4 mm hole pitch model are shown in the Fig. 5.65. These images are processed to find temperature values and used in the cooling effectiveness calculations. From Fig. 5.65, it is seen that flow patterns are almost the same in both experiments and numerical simulations. At stagnation holes region, the coolant flow is not observed through the holes in numerical simulation at a blowing ratio of 1.0. This is due to the dominating mainstream flow than the coolant flow at lower blowing ratios, whereas the little coolant flow is observed at stagnation holes during the experiments. At a blowing ratio of 1.5 and above, the more coolant flow is observed at the stagnation holes region in both the experimental and numerical simulations.

The units of scale on a thermal image of Fig. 5.65 are the thermal radiation count captured by the infra-red camera and the units of scale on the numerical thermal image of Fig. 5.65 are the temperature values in Kelvin extracted from CFD analysis.

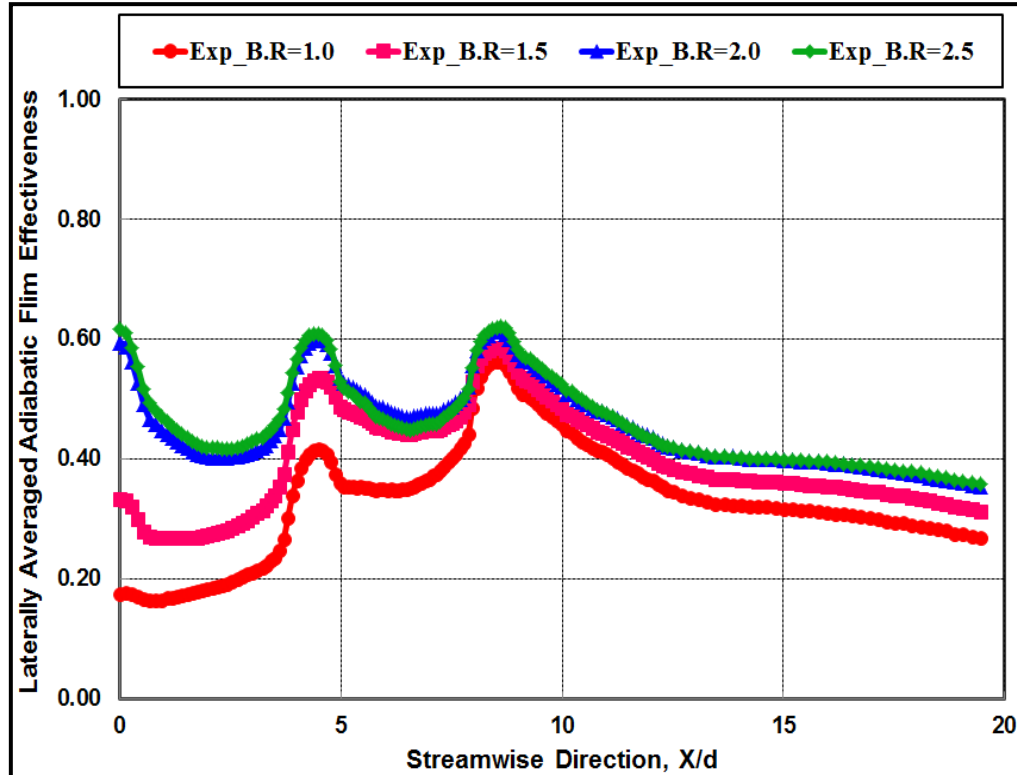


Fig. 5.66 Exp. cooling effectiveness for 22.4 mm pitch model at B.R of 1.0 to 2.5

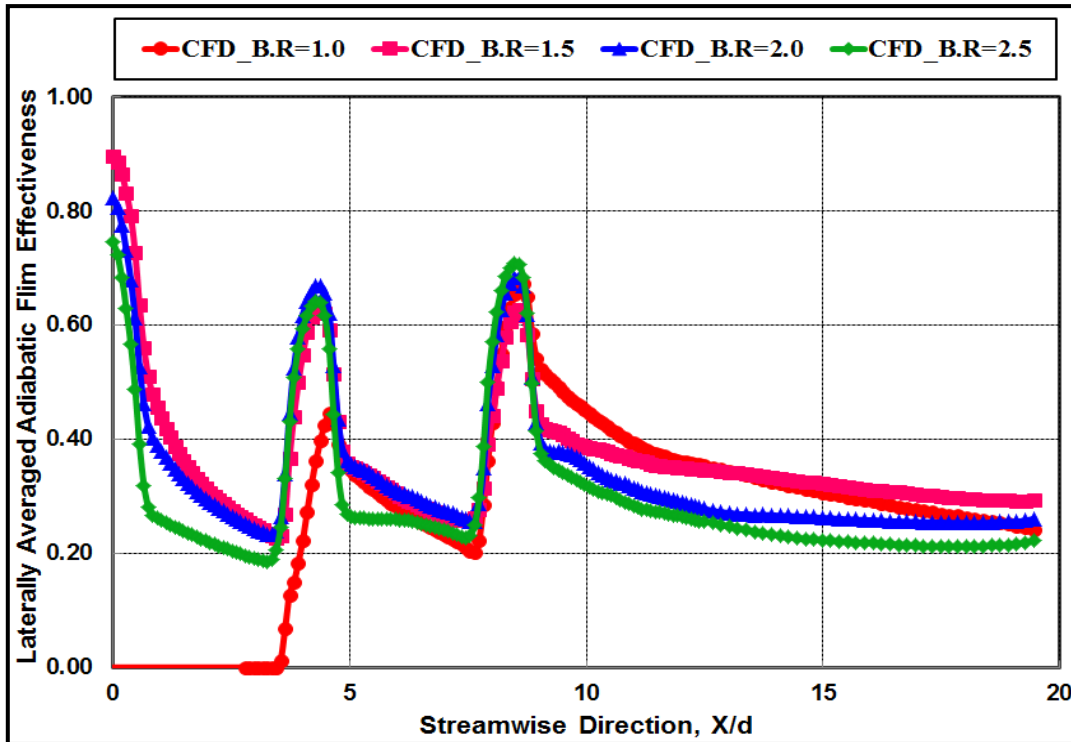


Fig. 5.67 Numerical cooling effectiveness for a 22.4 mm model at B.R of 1.0 to 2.5

Fig. 5.66 and Fig. 5.67 shows experimental and numerical laterally averaged adiabatic film cooling effectiveness results plotted along the streamwise direction for model 8 at blowing ratios of 1.0 to 2.5. Similar to the model 6, the experimental results are showing an increase in effectiveness with an increase in blowing ratio up to blowing ratio of 2.0 considerably. From blowing ratio of 2.0 to 2.5, there is only a marginal increase in averaged effectiveness is observed and this amount of increase is not a consideration with the quantum of increase in coolant mass flow supply. Hence, a blowing ratio of 2.0 is considered as optimized blowing ratio for this geometry. Numerical results are showing similar trends as experimental plots at all the considered blowing ratios. Peaks in the plots are indicating the location of hole rows, and they are in good agreement in both experimental and numerical results.

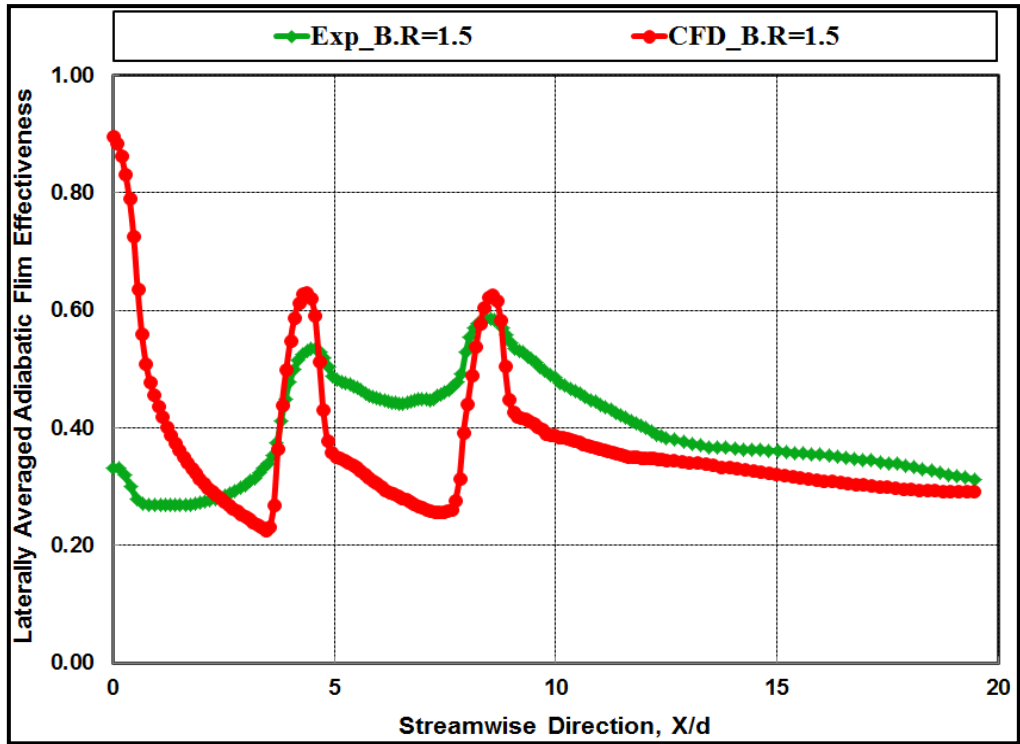


Fig. 5.68 Exp. Vs. Numerical cooling effectiveness for a 22.4 mm hole pitch model at a B.R of 1.5

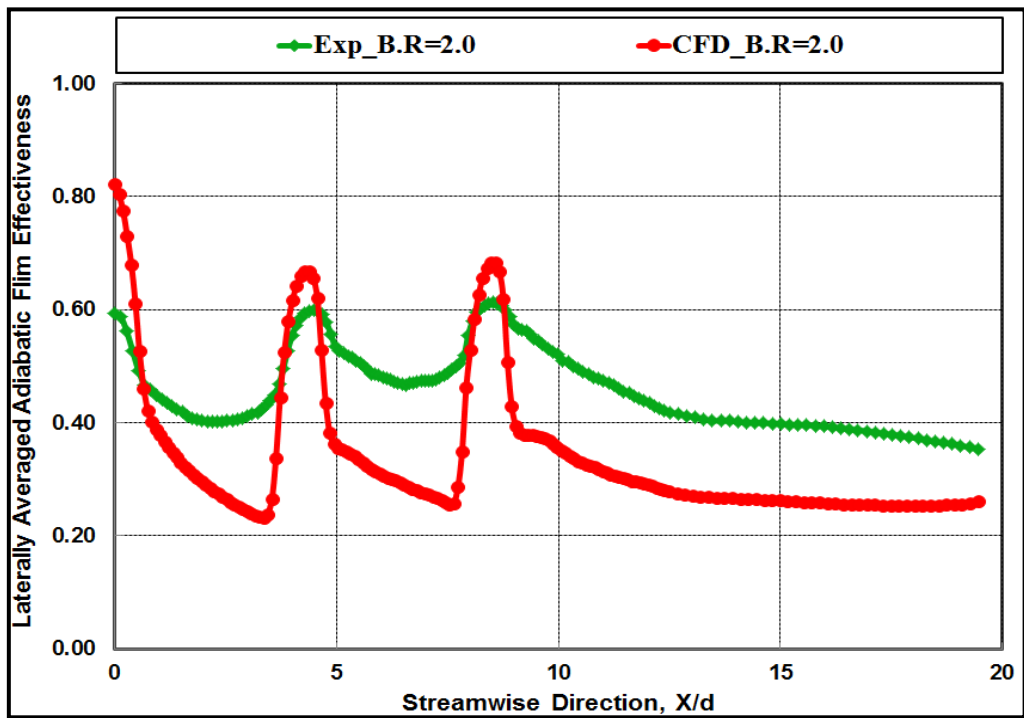


Fig. 5.69 Exp. Vs. Numerical cooling effectiveness at a B.R of 2.0 for a 22.4 mm hole pitch model

Fig. 5.68 and Fig. 5.69 shows the experimental and numerical averaged effectiveness results compared individually for a blowing ratio of 1.5 and 2.0 for a 22.4 mm hole pitch model. In both the blowing ratio cases, the numerical results are showing similar trends as in experimental results. Peaks are indicating the hole row locations and both the experimental and numerical averaged effectiveness results are matching except at stagnation holes. At downstream regions, numerical averaged results are showing lesser values than experimental results because of difference in flow distribution and film coverage over the surface. Similar trends and peak matchings are observed at other considered blowing ratios. Numerical averaged effectiveness results are showing 0.1 to 0.22 lesser averaged effectiveness values at downstream holes region than in experiments at all considered blowing ratios.

Here, the CFD extracted results have shown the little less predicted cooling effectiveness results by 5% than that of experimental. The frictional and mixing phenomenon losses are unable to consider by the CFD. Hence the CFD has shown the variation of the results than the experiments.

5.3.2 Heat Transfer Coefficient Measurements

Heat transfer coefficient measurements are carried out both experimentally and numerically over the leading edge test surfaces at different flow conditions, by varying the blowing ratios in the range of 1.0 to 2.5 with the constant heat flux over the test surface. In this case, the mainstream is allowed to flow over the test surface, and the coolant is allowed through the coolant holes with the respective blowing ratio mass flow conditions. Here both the mainstream and coolant air are at the ambient temperature. The mixed mainstream and coolant air will carry away the test model heat at the varied blowing ratio conditions. Temperature distribution over test surfaces under these flow conditions is obtained and used for heat transfer coefficient calculations. Results are plotted regarding laterally averaged heat transfer coefficients along the streamwise direction.

5.3.2.1 18 mm Spanwise Hole Pitch Model (M6) HTC Results

Fig. 5.70 shows the typical experimental thermal images and numerically obtained temperature contours of heat transfer coefficient measurements at a blowing ratio of 2.5 for an 18 mm hole pitch model. These images are processed to find temperature values and used in the heat transfer coefficient calculations. From Fig. 5.70, it can be seen that flow patterns are almost the same in both experiments and numerical simulations. Due to heat supply to the test surface as heat flux, the test surface temperatures are more than mainstream temperature. From thermal images and temperature contours, hot spots can be seen in between the holes region and in the downstream regions. The units of scale on a thermal image of Fig. 5.70 are the thermal radiation count captured by the infra-red camera and the units of scale on the numerical thermal image of Fig. 5.70 are the temperature values in Kelvin extracted from CFD analysis.

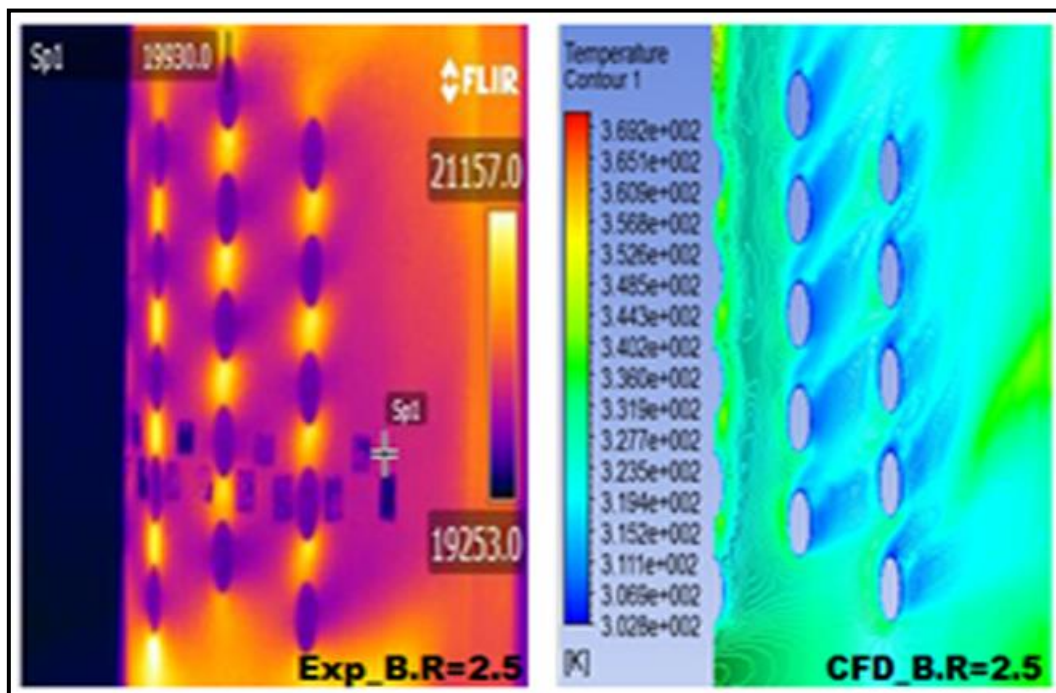


Fig. 5.70 Exp. and CFD temperature contours of HTC for an 18 mm hole pitch model at a B.R of 2.5

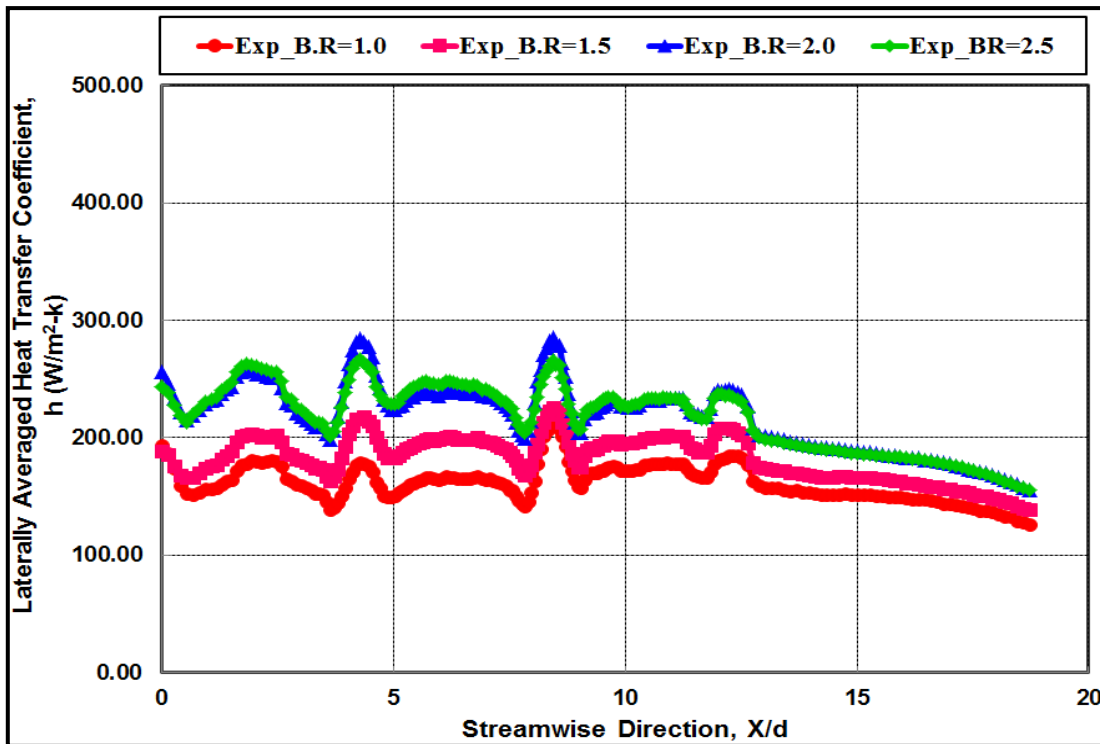


Fig. 5.71 Exp. HTC results for an 18.4 mm hole pitch model at B.R.s of 1.0 to 2.5

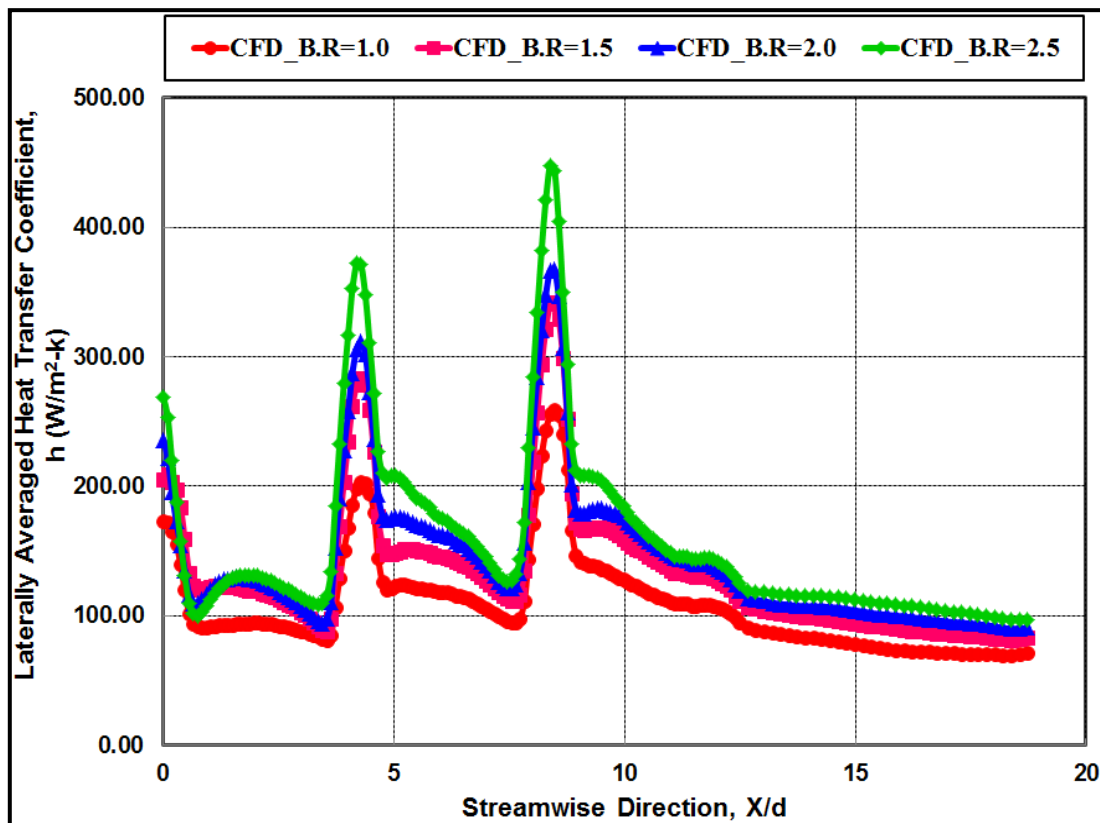


Fig. 5.72 Numerical HTC results for an 18.4 mm pitch model at B.R.s of 1.0 to 2.5

Fig. 5.71 and Fig. 5.72 shows experimental and numerical laterally averaged heat transfer coefficient results plotted along the streamwise direction for model 6 at blowing ratios of 1.0 to 2.5. Experimental results are showing increased heat transfer coefficients with an increase in blowing ratio and maximum averaged heat transfer coefficients are observed at blowing ratio of 2.5. Numerical results are showing similar trends as experimental results for all considered blowing ratios. Peaks are indicating the hole row locations where heat transfer coefficients will be more than at downstream regions in both experiments and numerical simulations. Immediately next to the hole location, there are lesser heat transfer coefficient values due to flow detachments, and after that, it is observed higher heat transfer coefficient values because of flow attachments to the test surface.

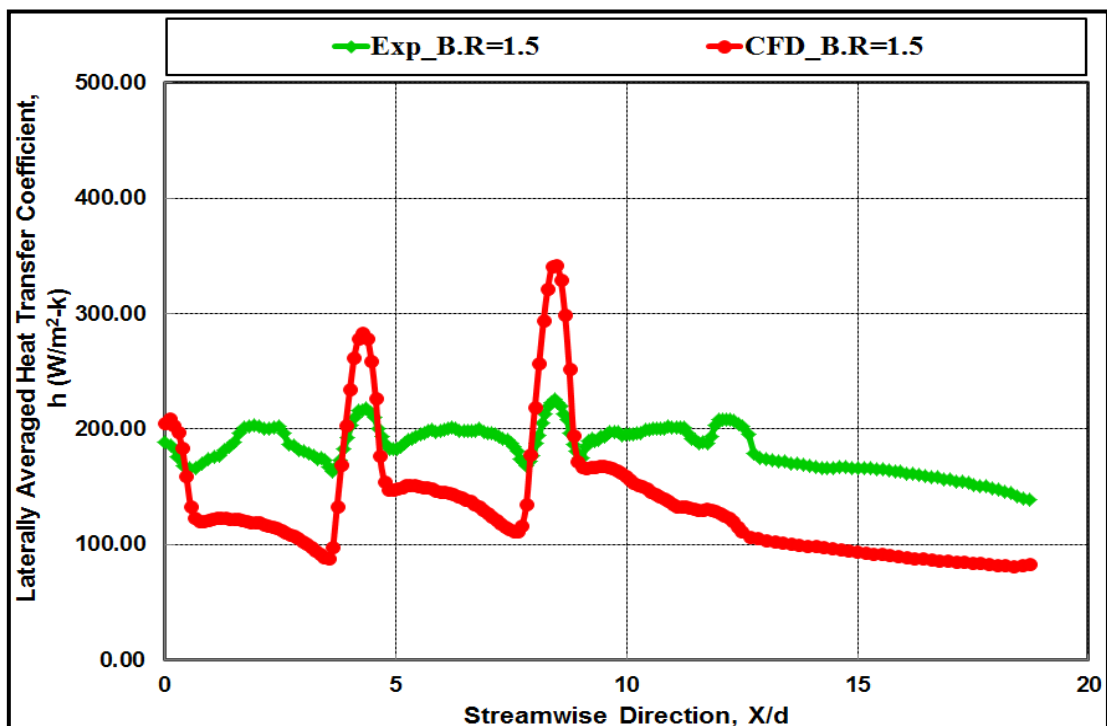


Fig. 5.73 Exp. Vs. Numerical HTC for an 18.4 mm hole pitch model at a B.R of 1.5

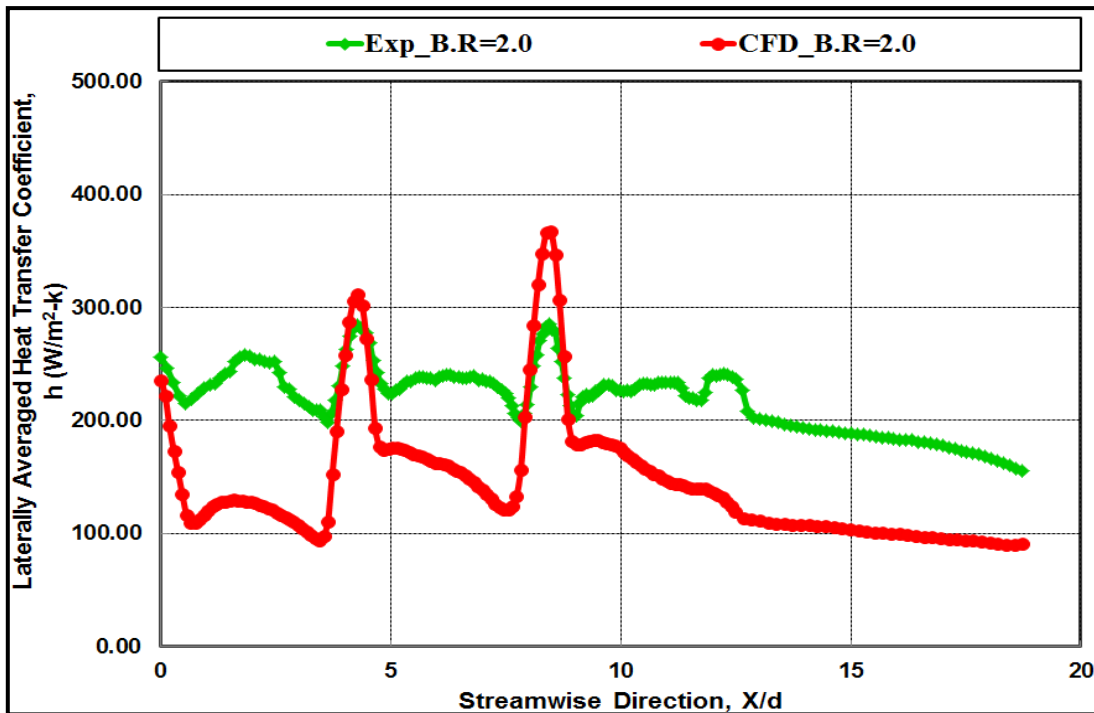


Fig. 5.74 Exp. Vs. Numerical HTC for an 18.4 mm hole pitch model at a B.R of 2.0

Fig. 5.73 and Fig. 5.74 shows the experimental and numerical laterally averaged heat transfer coefficient results compared individually for blowing ratios of 1.5 and 2.0. Numerical results are showing similar trends as in experimental results. Peaks in the plots are indicating hole locations where numerical averaged heat transfer coefficient values are more than experimental results by 10 to 80 W/m²K because during the experiments using IR camera, inside inclined hole test surface radiations are captured, whereas in CFD while extracting results at hole regions, fluid temperature at the hole exit is extracted. At downstream regions, numerical results are showing lesser values than experimental results by 5 to 90 W/m²K due to the difference in flow distributions and film coverage over the surface.

The CFD extracted heat transfer coefficient results have shown the similar trends as that of the experimental values with the little lower prediction than the experimental values. The CFD results are useful for finalizing the geometry based on the trends and comparison of results among the geometries even though the results are not very accurate.

5.3.2.2 22.4 mm Spanwise Hole Pitch Model (M8) HTC Results

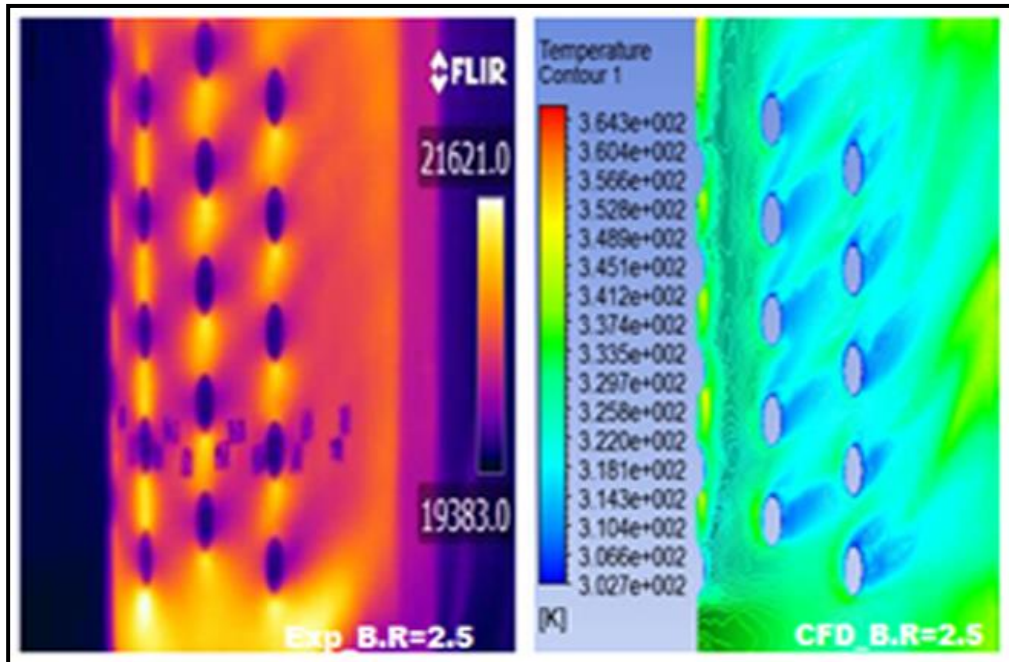


Fig. 5.75 Exp. and CFD temperature contours of HTC for a 22.4 mm hole pitch model at a B.R of 2.5

Fig. 5.75 shows the typical experimental thermal images and numerically obtained temperature contours of heat transfer coefficient measurements at a blowing ratio of 2.5 for a 22.4 mm hole pitch model. These images are processed to find temperature values and used in the heat transfer coefficient calculations. From Fig. 5.75, it can be seen that flow patterns are almost the same in both experiments and numerical simulations. Due to heat supply to the test surface as heat flux, the test surface temperatures are more than mainstream and are in the range of 300 to 350 K. From thermal images and temperature contours; hot spots can be seen in between the holes region and in the downstream regions.

The units of scale on a thermal image of Fig. 5.75 are the thermal radiation count captured by the infra-red camera and the units of scale on the numerical thermal image of Fig. 5.75 are the temperature values in Kelvin extracted from CFD analysis.

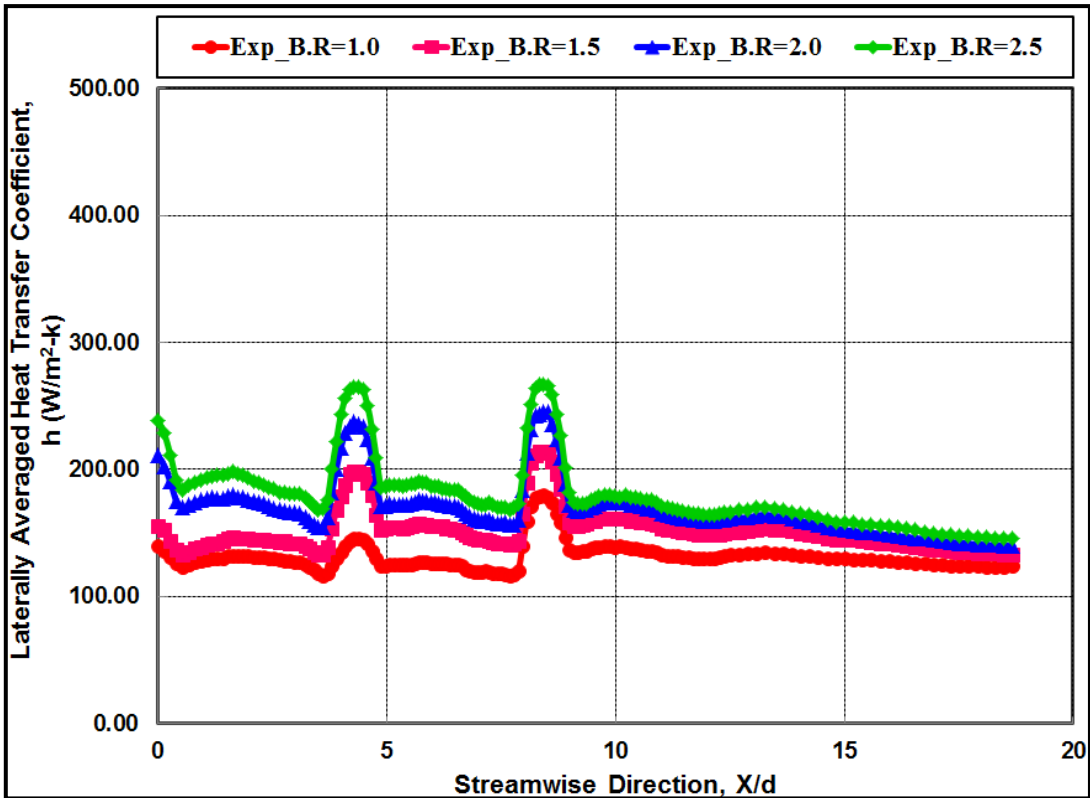


Fig. 5.76 Exp. HTC results for 22.4 mm hole pitch model at B.R of 1.0 to 2.5

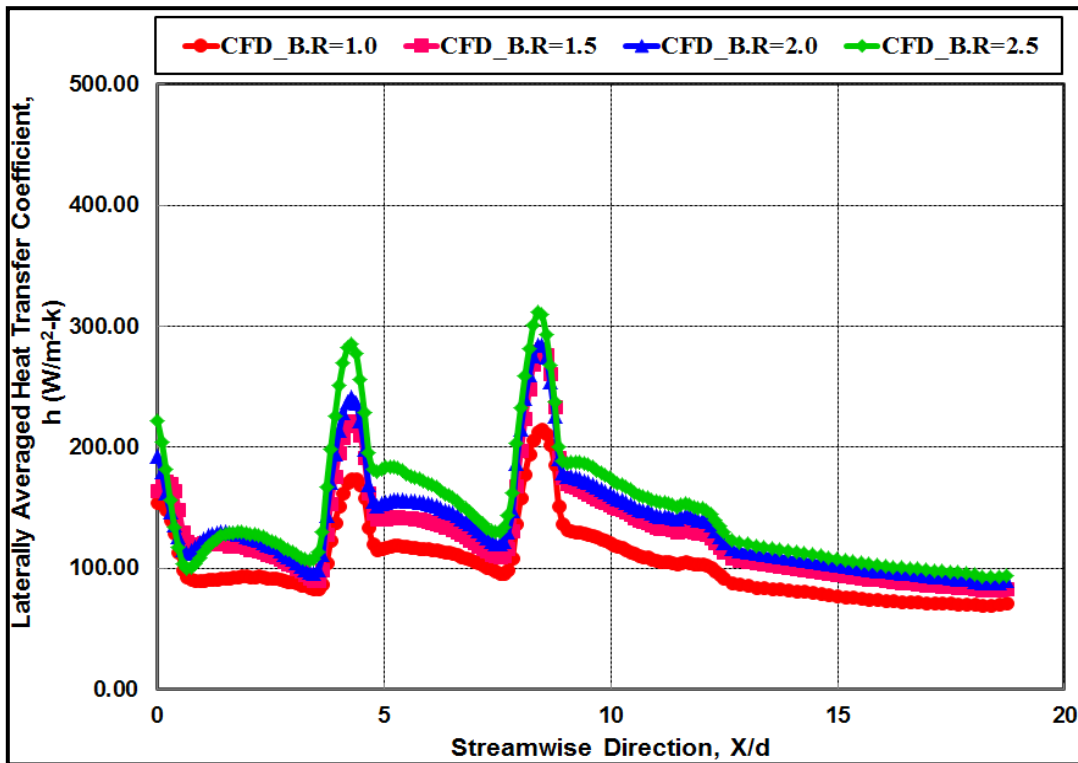


Fig. 5.77 Numerical HTC results for a 22.4 mm hole pitch model at B.R of 1.0 to 2.5

Fig. 5.76 and Fig. 5.77 shows experimental and numerical laterally averaged heat transfer coefficient results plotted along a streamwise direction at blowing ratios of 1.0 to 2.5. Experimental results are showing increased heat transfer coefficients with an increase in blowing ratio and maximum averaged heat transfer coefficients are observed at blowing ratio of 2.5. Numerical results are showing similar trends as experimental results for all considered blowing ratios. Peaks are indicating the hole row locations where heat transfer coefficients will be higher than at downstream regions in both experimental and numerical simulation results. Immediately next to the hole location, there are lesser heat transfer coefficient values due to flow detachments, and after that, it is observed higher heat transfer coefficient values because of flow attachments to the test surface.

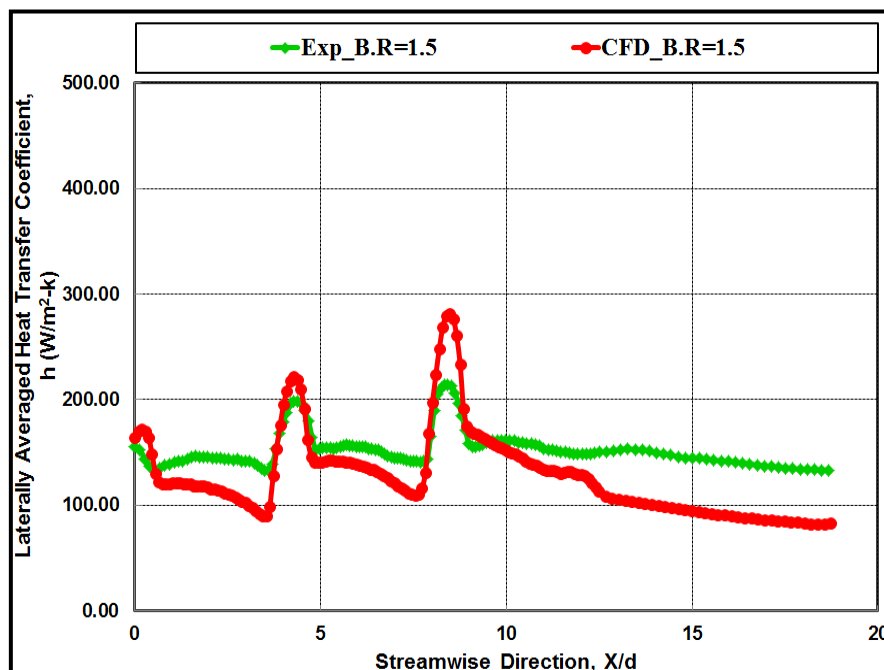


Fig. 5.78 Exp. Vs. Numerical HTC for a 22.4 mm hole pitch model at a B.R of 1.5

Fig. 5.78 and Fig. 5.79 shows the experimental and numerical laterally averaged heat transfer coefficient results compared individually for blowing ratios of 1.5 and 2.0 for a 22.4 mm hole pitch model. Numerical results are showing similar trends as in experimental results. Peaks in the plots are indicating hole locations where numerical averaged heat transfer coefficient values are more than experimental results by 5 to 40 W/m²K because during the experiments using IR camera, inside inclined hole test

surface radiations are captured, whereas in CFD while extracting results at hole regions, fluid temperature at the hole exit is extracted. At downstream regions, numerical results are showing lesser values than experimental results by 5 to 30 W/m²K, due to the difference in flow distributions and film coverage over the test surface.

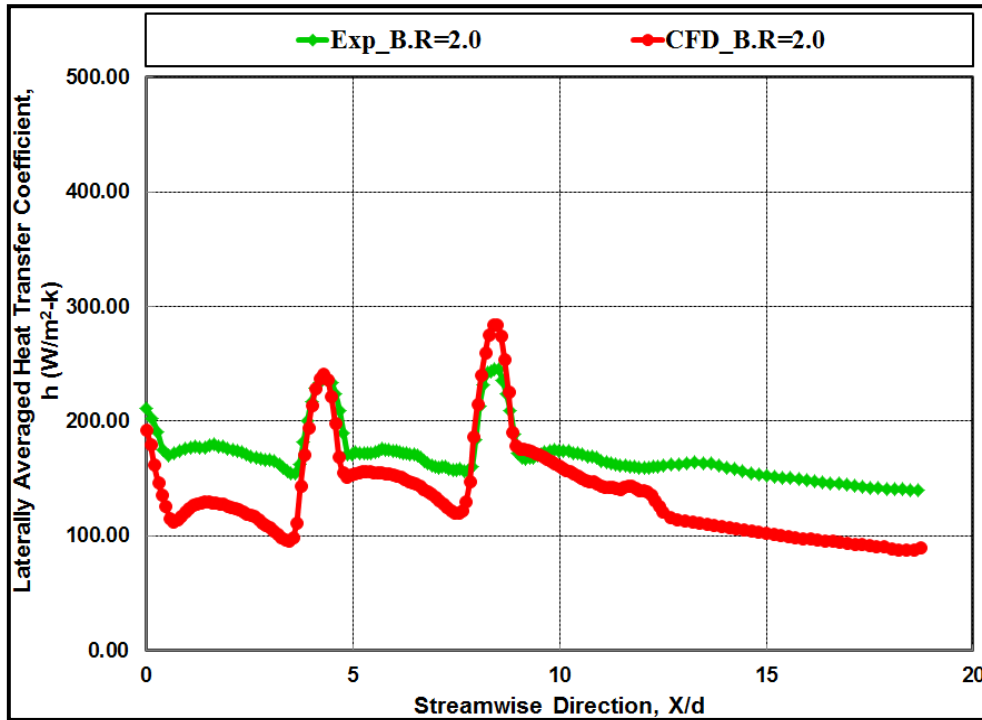


Fig. 5.79 Exp. Vs. Numerical HTC for a 22.4 mm hole pitch model at a B.R of 2.0

Here, the CFD extracted results have shown the little less predicted heat transfer coefficient values by 5% than that of experimental. The frictional and mixing phenomenon losses are unable to consider by the CFD. Hence the CFD has shown the variation of the results than the experiments.

5.3.3 Comparative Study of 18 mm and 22.4 mm Hole Pitch Models

From experimental and numerical results obtained, a comparative study between 18 mm and 22.4 mm hole pitch models are carried out. Comparisons show that the blowing ratios of 1.5 and 2.0 for both the experimental and numerical results separately regarding averaged adiabatic film cooling effectiveness and averaged heat transfer coefficients along the streamwise direction.

5.3.3.1 Adiabatic Film Cooling Effectiveness Results Comparison

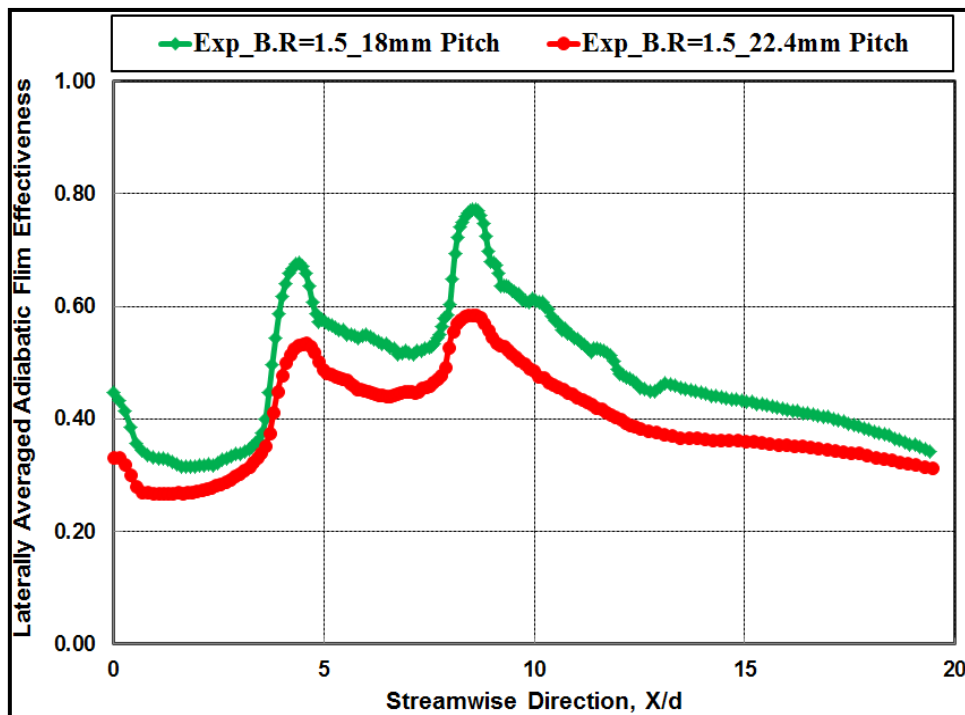


Fig. 5.80 Exp. cooling effectiveness comparison for 18 and 22.4 mm hole pitch models at a B.R of 1.5

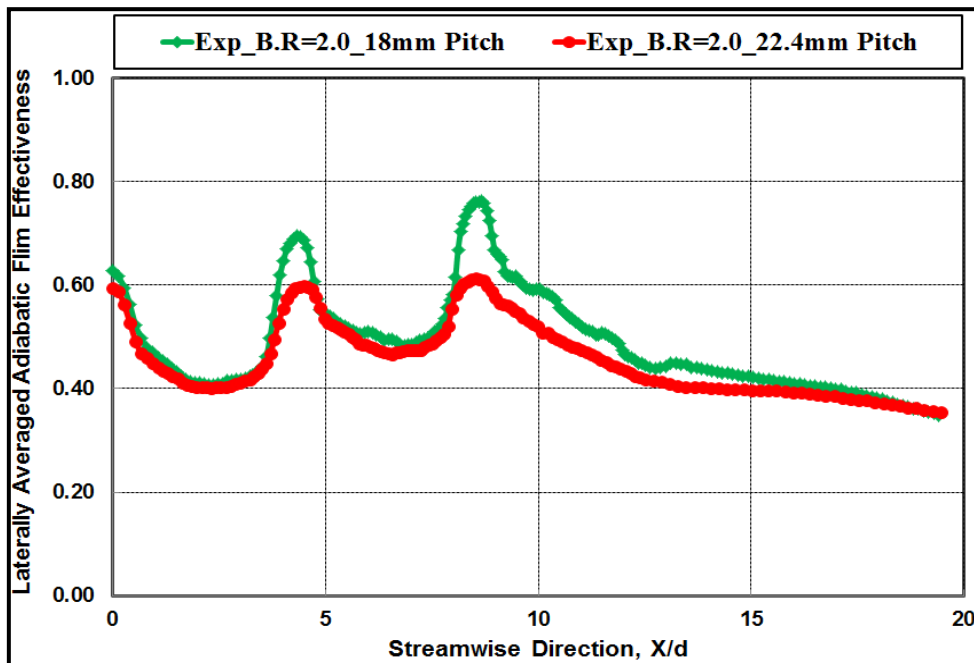


Fig. 5.81 Exp. cooling effectiveness comparison for 18 and 22.4 mm hole pitch models at a B.R of 2.0

Fig. 5.80 and Fig. 5.81 shows the experimental laterally averaged adiabatic film cooling effectiveness results along the streamwise direction for model 6 and model 8 at blowing ratios of 1.5 and 2.0 respectively. Model 6 with 18 mm spanwise hole pitch shows the comparatively higher averaged cooling effectiveness of about 20 % than model 8 at both the blowing ratios. Similarly, the higher averaged cooling effectiveness is observed for model 6 than the model 8 at all the other considered blowing ratios.

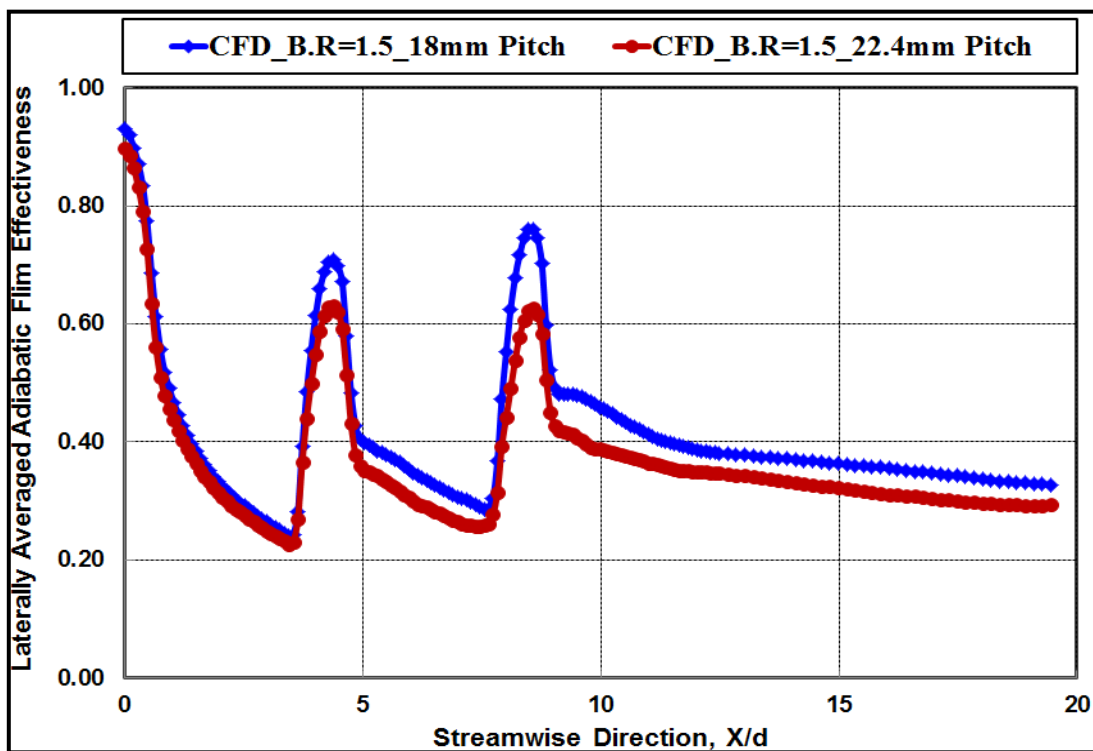


Fig. 5.82 Numerical cooling effectiveness comparison for 18 and 22.4 mm Hole pitch models at a B.R of 1.5

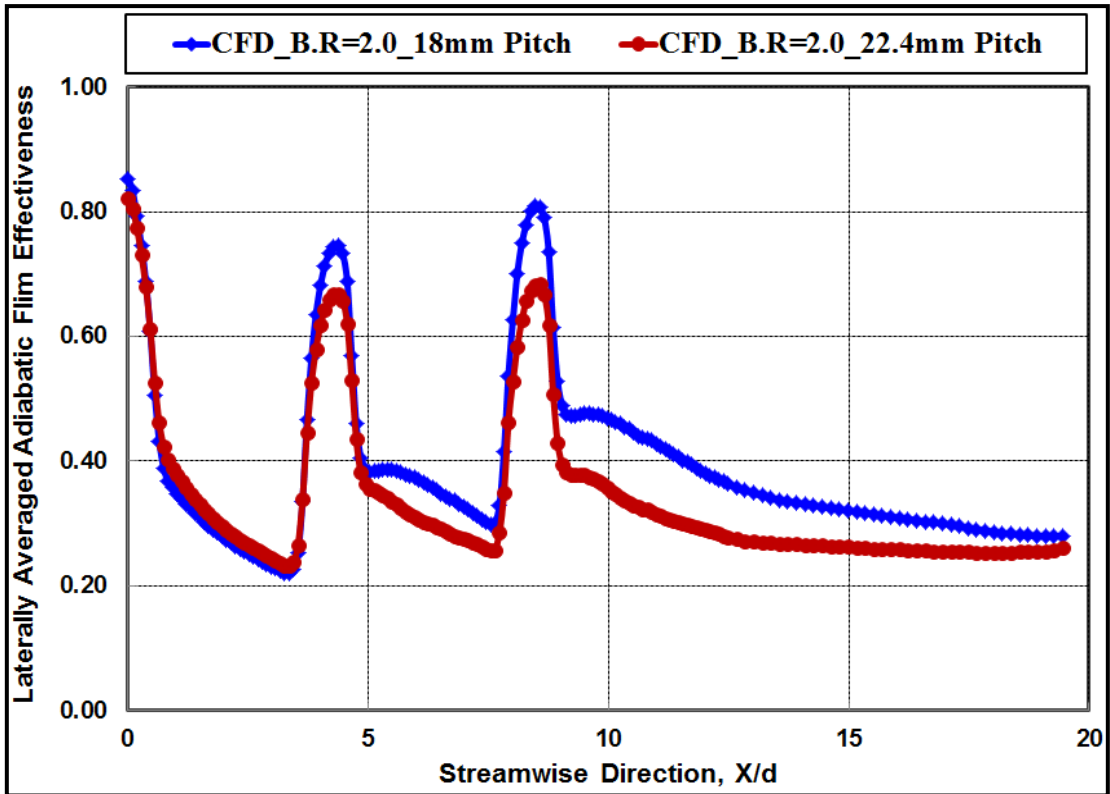


Fig. 5.83 Numerical cooling effectiveness comparison for 18 and 22.4 mm Hole pitch models at a B.R of 2.0

Numerically averaged adiabatic effectiveness results are compared between model 6 and model 8 at blowing ratios of 1.5 and 2.0, are shown in Fig. 5.82 and Fig. 5.83. From the numerical results, 18 mm hole pitch model is showing the slightly higher adiabatic film cooling effectiveness than the model with 22.4 mm hole pitch at both the blowing ratios of 1.5 and 2.0. The same effect is observed at the other considered blowing ratios too; the numerically averaged effectiveness results show higher values for model 6 than model 8.

5.3.3.2 Heat Transfer Coefficients Comparative Results

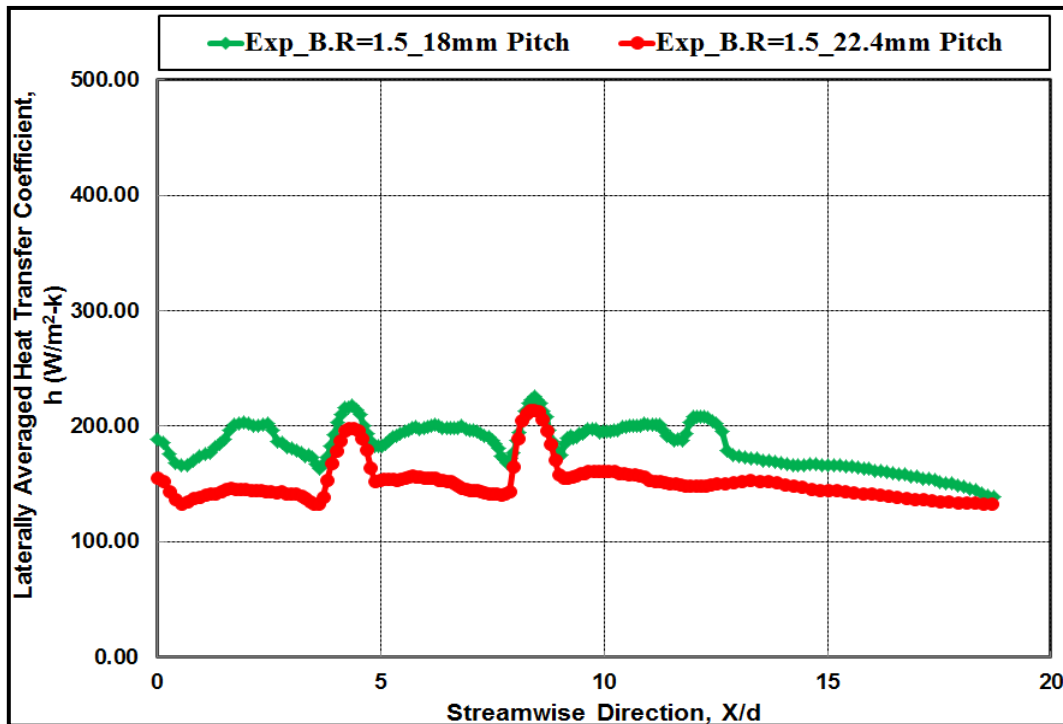


Fig. 5.84 Exp. HTC comparison of 18 and 22.4 mm pitch models at a B.R of 1.5

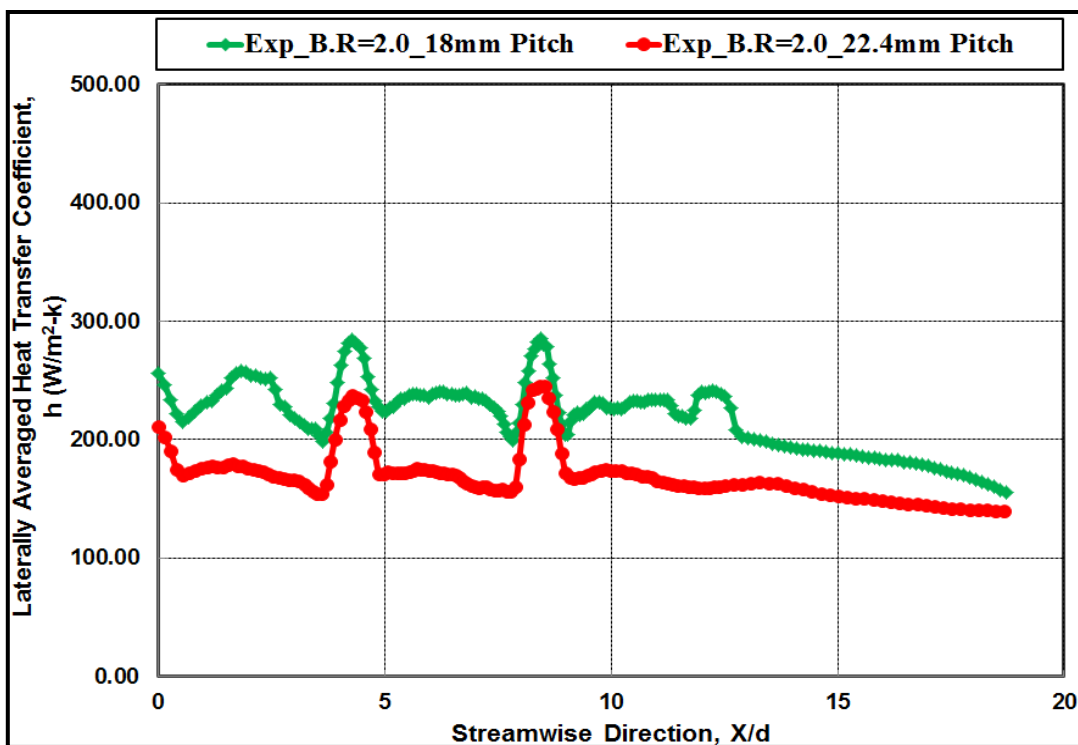


Fig. 5.85 Exp. HTC comparison of 18 and 22.4 mm pitch models at a B.R of 2.0

Fig. 5.84 and Fig. 5.85 shows the experimentally averaged heat transfer coefficient results along the streamwise direction for model 6 and model 8 at blowing ratios of 1.5 and 2.0 respectively. Model 6 with 18 mm spanwise hole pitch is giving comparatively higher averaged heat transfer coefficients of about 10 to 60 W/m^2K than the model 8 with 22.4 mm hole pitch. A similar trend of higher averaged heat transfer coefficients is observed for model 6 than model 8 at all other considered blowing ratios.

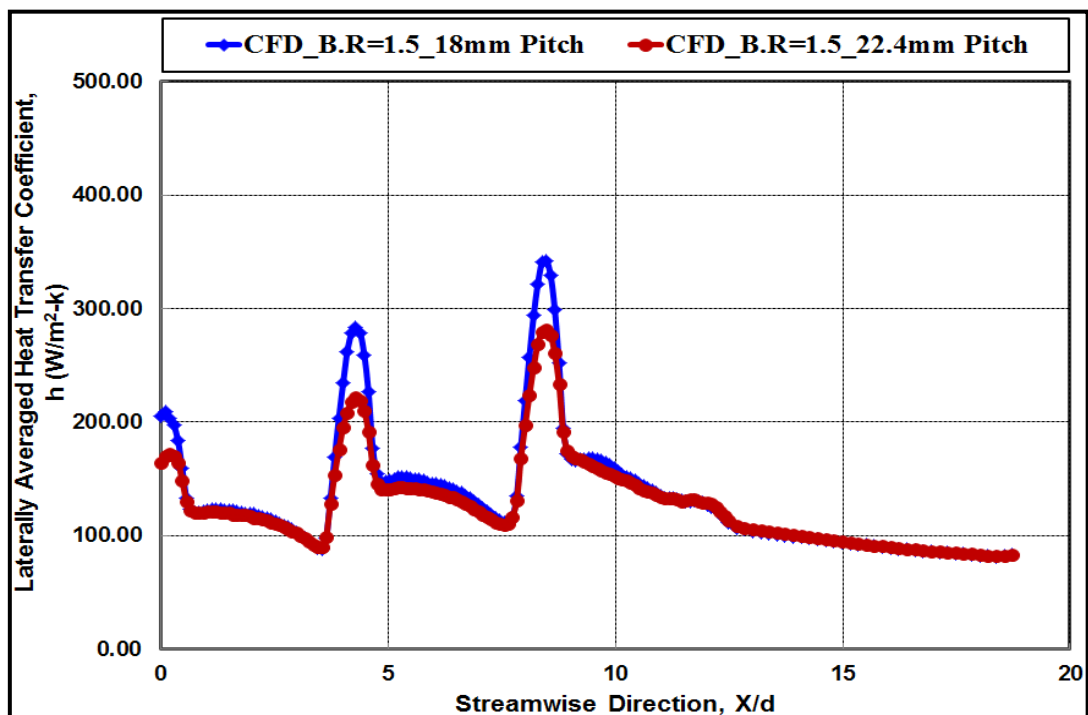


Fig. 5.86 Numerical HTC comparison of 18 mm and 22.4 mm hole pitch models at a B.R of 1.5

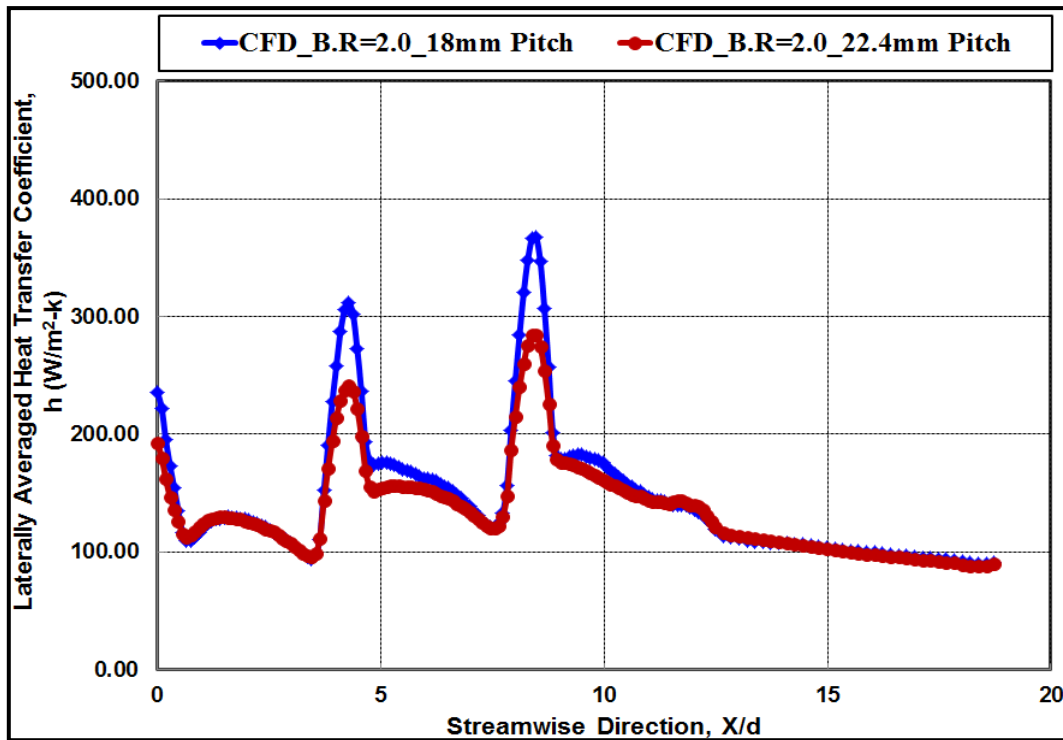


Fig. 5.87 Numerical HTC comparison of 18 mm and 22.4 mm hole pitch models at a B.R of 2.0

Numerically averaged heat transfer coefficient results compared between model 6 and model 8 at blowing ratios of 1.5 and 2.0, are shown in Fig. 5.86 and Fig. 5.87. Numerical results are also showing comparatively higher averaged heat transfer coefficients for model 6 than model 8 at blowing ratios of 1.5 and 2.0, and the same trend is observed at the other considered blowing ratios.

Among the two considered hole pitch test models, the hole geometry with the lower pitch of 18 mm with the p/d of 3.2 has shown the higher cooling effectiveness and heat transfer coefficient values than the model with the higher pitch of 22.4 mm with the p/d of 4. Hence, the geometry with the p/d of 3.2 is suggested for the better performance among the considered realistic p/d test models.

5.4 Effect of Hole Shape

To bring out the effect of hole shape (HS), three test models are considered (M9, M10, and M11) This study aims at investigating the effect of diffused hole shapes on both the average adiabatic film cooling effectiveness and average heat transfer coefficients, experimentally and numerically over the gas turbine blade leading edge model. For this study, three scaled up gas turbine blade leading edge models are taken up with circular, fan shape, and laidback fan exit shaped holes, having five rows of film cooling holes oriented at 0° , 30° and 60° angles respectively on both sides from stagnation line. Each row has the five holes with a hole diameter of 4 mm, the pitch of 21 mm arranged in a staggered manner and had the hole inclination angle of 30° in the spanwise direction.

The mass flow measurements and coefficient of discharge values are found for all the shaped hole test models individually by varying the coolant chamber pressure. The average coefficient of discharge for the circular shape hole model is found as 0.68, for the fan shape hole model is found as 0.83, and for the laid back fan shape, hole model is found as 0.85. The average coefficient of discharge values is found to be increasing with the increase in hole exit area. The detailed mass flow and Cd calculations and values are given in an appendix-I.

5.4.1 Experimental and Numerical Adiabatic Film Cooling Effectiveness Results

5.4.1.1 Circular Hole Model (M9-CHM)

The adiabatic film cooling effectiveness is plotted along the streamline direction from stagnation line to downstream of the coolant holes for the circular hole shape models. The typical experimental temperature contours obtained using IR camera and the numerical temperature contours extracted from CFD for a circularly shaped model at a blowing ratio of 2.0 are as shown in Fig. 5.88. From the experiments, it is found that at a B.R of 1.0 the coolant flow was not established and hence, the coolant films were not found near stagnation line due to low pressure, by visualization from thermal images. Further with the increase in B.R, the coolant flow was fully established, and coolant film was found over the stagnation hole region and at downstream of holes.

The units of scale on a thermal image of Fig. 5.88 are the temperature values in Kelvin captured by the infra-red camera and the units of scale on the numerical thermal image of Fig. 5.88 are the temperature values in Kelvin extracted from CFD analysis.

The experimentally averaged film cooling effectiveness plots in streamwise direction for all the four planned blowing ratios are shown in Fig. 5.89. From the Fig. 5.89 it is found that with the increase in blowing ratio the film cooling effectiveness value increased up to B.R 2.0. Only at the downstream of coolant holes, the film cooling effectiveness is higher at B.R 1.5. Further increase in blowing ratio did not show much improvement in film cooling effectiveness value. Thus overall experimentally it is found for circular hole shape model B.R 2.0 is optimized blowing ratio to have higher average film cooling effectiveness.

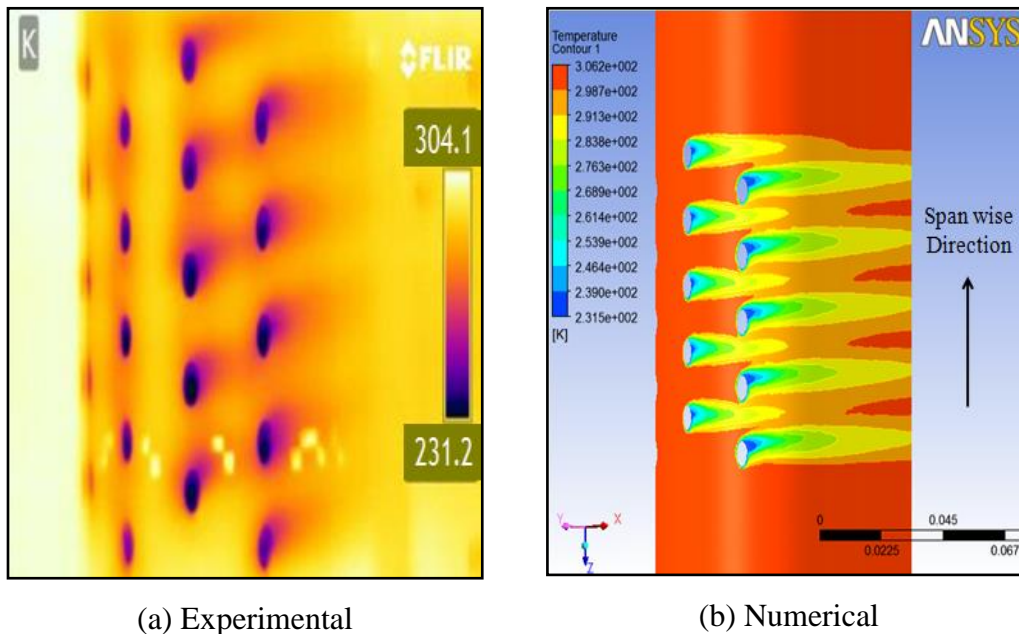


Fig. 5.88 Exp. and Numerical temperature contours of effectiveness for CHM at a typical B.R of 2.0

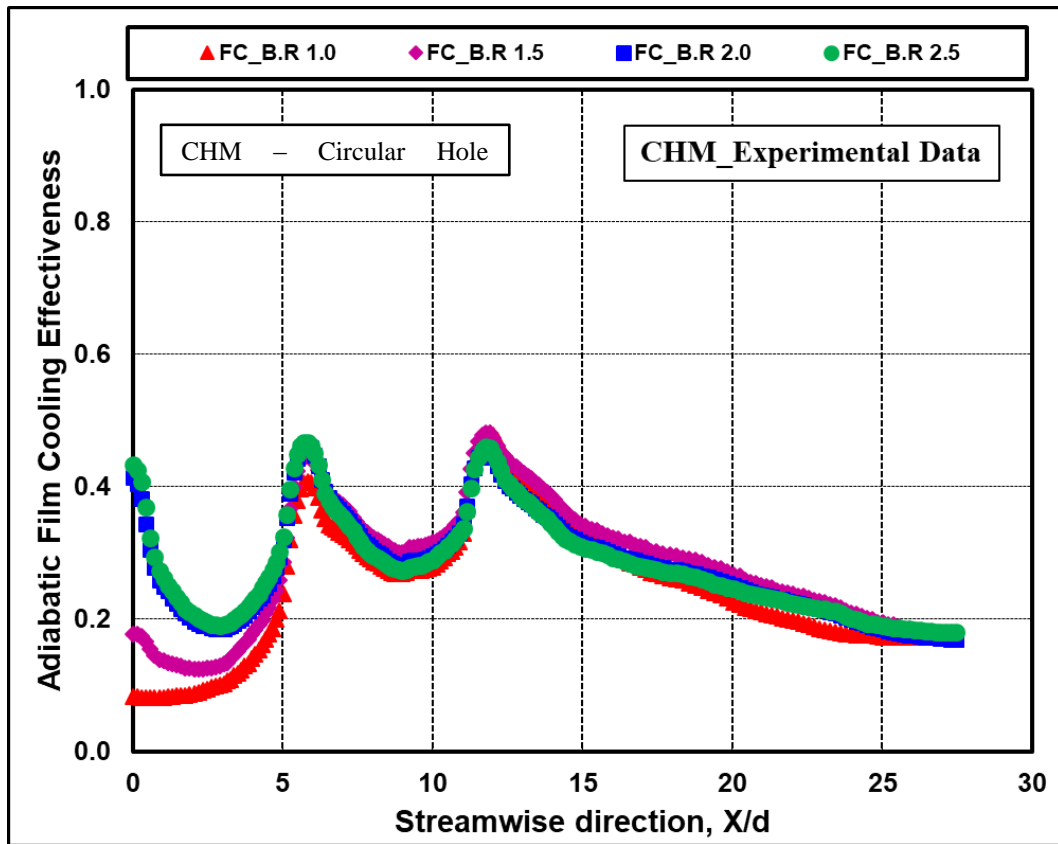


Fig. 5.89 Exp. cooling effectiveness for CHM at the B.Rs of 1.0 to 2.5

The averaged film cooling effectiveness plots in streamwise direction for all the four planned blowing ratios obtained from CFD simulation are shown in Fig. 5.90. From the plots, it can be observed that similar to experimental results the average film cooling effectiveness value is higher at B.R 2.0 and a further increase in blowing ratio showed a decrease in film cooling effectiveness. Thus overall by CFD estimation, it is found for circular hole shape model B.R 2.0 is optimized blowing ratio to have higher average film cooling effectiveness.

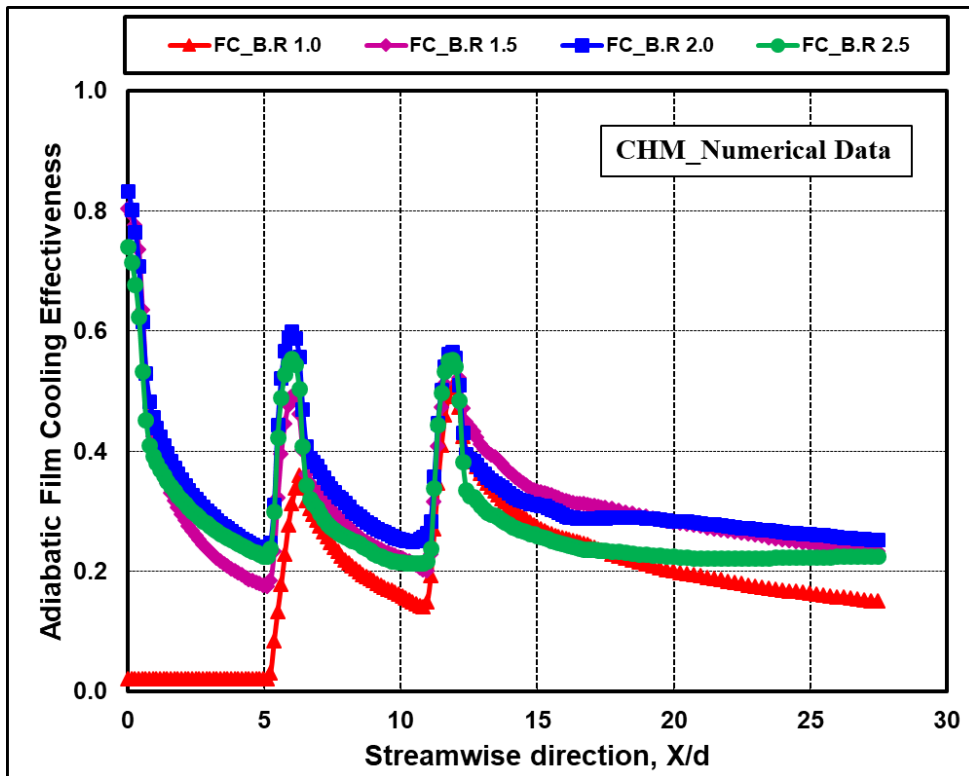


Fig. 5.90 Numerical cooling effectiveness for CHM at the B.Rs of 1.0 to 2.5

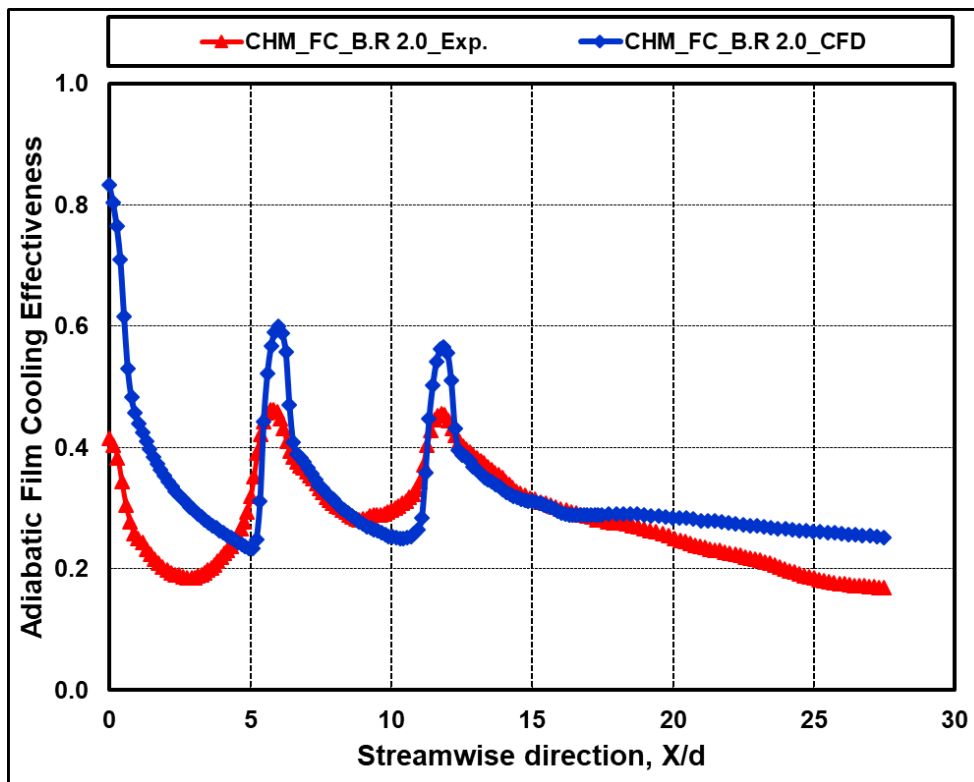


Fig. 5.91 Exp. Vs. CFD cooling effectiveness comparison for CHM at the B.R of 2.0

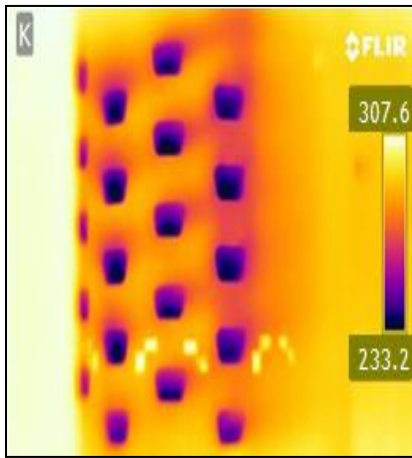
Thus on average, for circular hole shape model with considered hole geometry and configurations over the gas turbine blade leading edge, from both experimental and CFD estimations the B.R 2.0 can be considered as optimized blowing ratio. The Fig. 5.91 shows a comparative plot between experimental and numerical results of film cooling effectiveness in the streamwise direction from stagnation line to downstream of coolant holes at B.R 2.0. From the plot, it can be observed that both the results are in the same trend and gives meaningful validation for CFD results.

5.4.1.2 Fan Shape Hole Model (M10-FSHM)

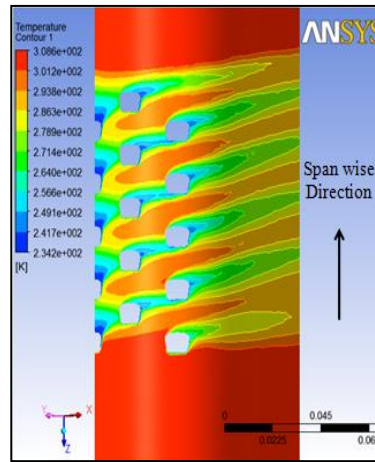
The adiabatic film cooling effectiveness is plotted along the streamline direction from stagnation line to downstream of the coolant holes for the fan shape hole configuration model. The typical experimental temperature contours obtained using an IR camera and the numerical temperature contours extracted from CFD for a fan shaped model at a blowing ratio of 2.0 are as shown in Fig. 5.92. From the experiments, it is found that up to B.R of 2.0 the coolant flow was not established and hence coolant films were not found near stagnation line due to low pressure and increased hole inlet to outlet area ratios. Further, with the increase in blowing ratio, the coolant flow was fully established, and coolant film was found over the stagnation hole region and at downstream of holes.

The units of scale on a thermal image of Fig. 5.92 are the temperature values in Kelvin captured by the infra-red camera and the units of scale on the numerical thermal image of Fig. 5.92 are the temperature values in Kelvin extracted from CFD analysis.

The experimentally obtained averaged film cooling effectiveness plots in streamwise direction for all the four planned blowing ratios are shown in Fig. 5.93. From the Fig. 5.93, it is found that with the increase in blowing ratio the film cooling effectiveness value increased up to a B.R of 2.0. Further increase in blowing ratio showed a decrease in film cooling effectiveness value. This is due to detachment of the cooling films from the surface and mixing with the mainstream flow at higher blowing ratios.



(a) Experimental



(b) Numerical

Fig. 5.92 Exp. and Numerical temperature contours of effectiveness for FSHM at a typical B.R of 2.0

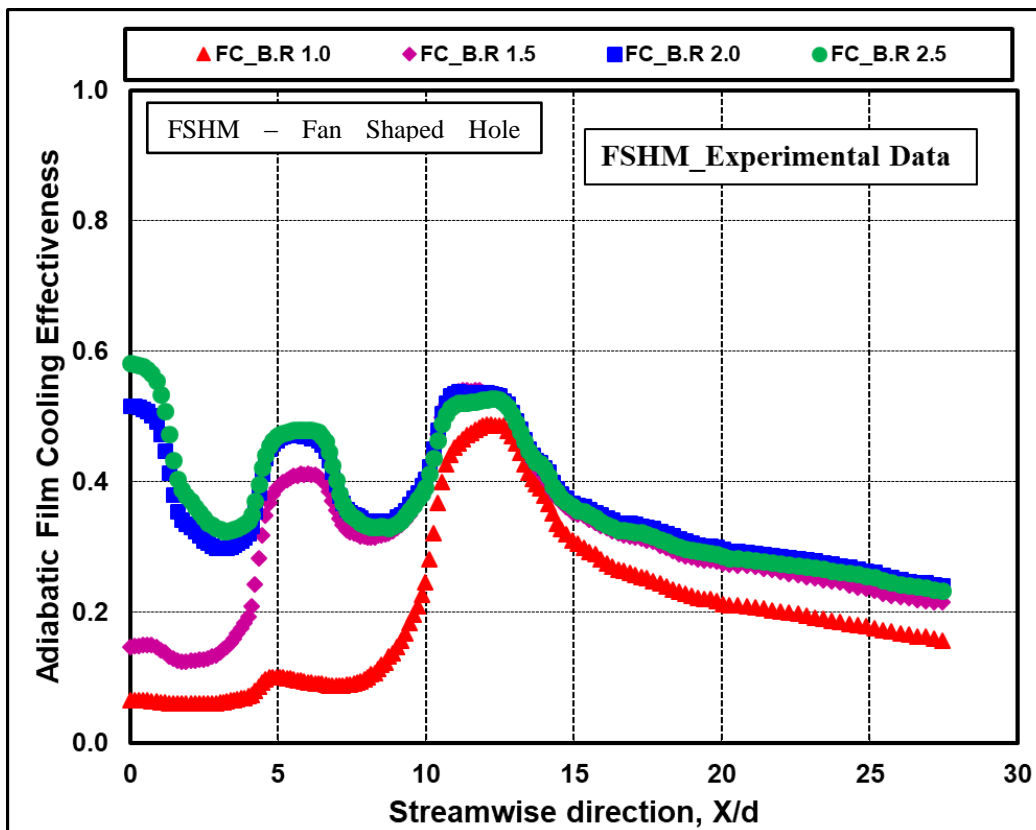


Fig. 5.93 Exp. cooling effectiveness for FSHM at the B.Rs of 1.0 to 2.5

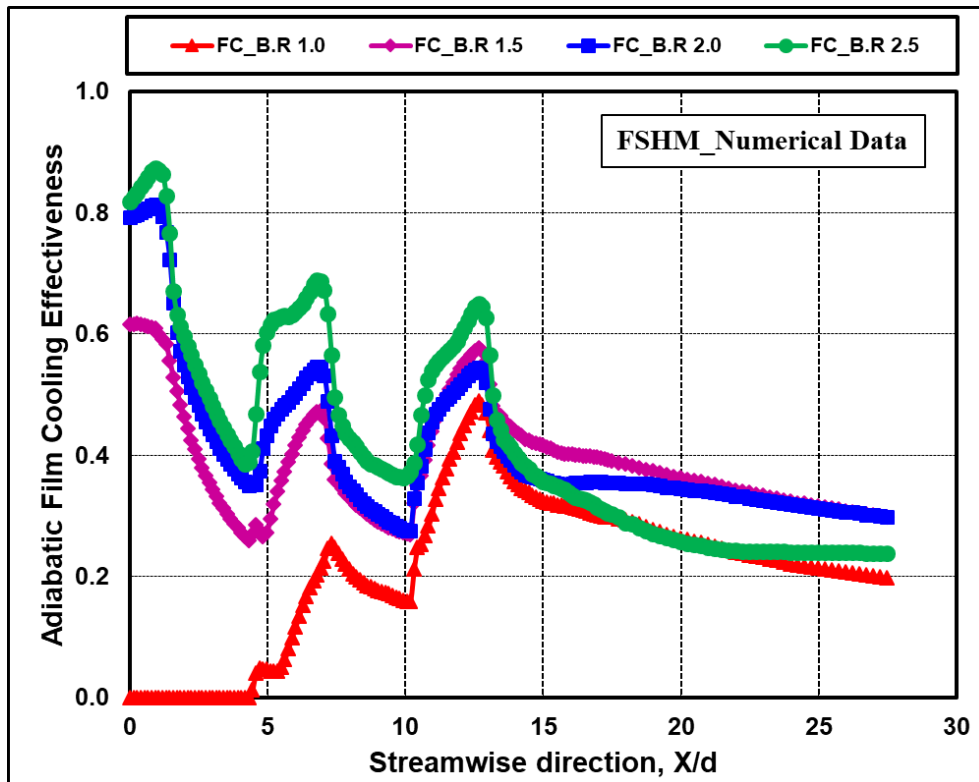


Fig. 5.94 Numerical cooling effectiveness for FSHM at the B.Rs of 1.0 to 2.5

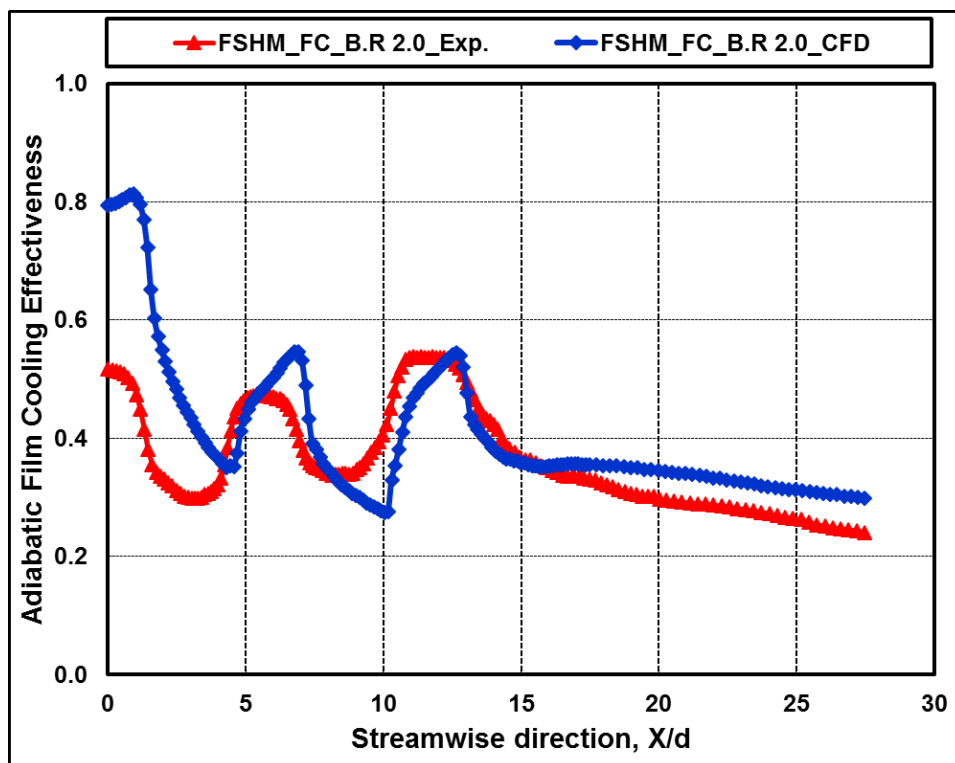


Fig. 5.95 Exp. Vs. Numerical effectiveness comparison for FSHM at the B.R of 2.0

The averaged film cooling effectiveness plots in streamwise direction for all the four planned blowing ratios obtained from CFD simulation are shown in Fig. 5.94. From the plots, it can be observed that similar to experimental results the average film cooling effectiveness value is higher at B.R 2.0 and a further increase in blowing ratio showed a decrease in film cooling effectiveness. Only at downstream of the coolant holes, the film cooling effectiveness is higher at B.R 1.5. This may be due to more attachment of coolant films at lower blowing ratio.

Thus on average, for a fan shape hole model of leading edge of a gas turbine blade with considered hole geometry, from both experimental and CFD estimations the B.R of 2.0 can be considered as optimized blowing ratio. The Fig. 5.95 shows a comparative plot between experimental and numerical results of film cooling effectiveness in the streamwise direction from stagnation line to downstream of coolant holes at a B.R of 2.0. From the plot, it can be observed that both the results are in the same trend and gives meaningful validation.

5.4.1.3 Laid Back Fan Shape Hole Model (M11-LFSHM)

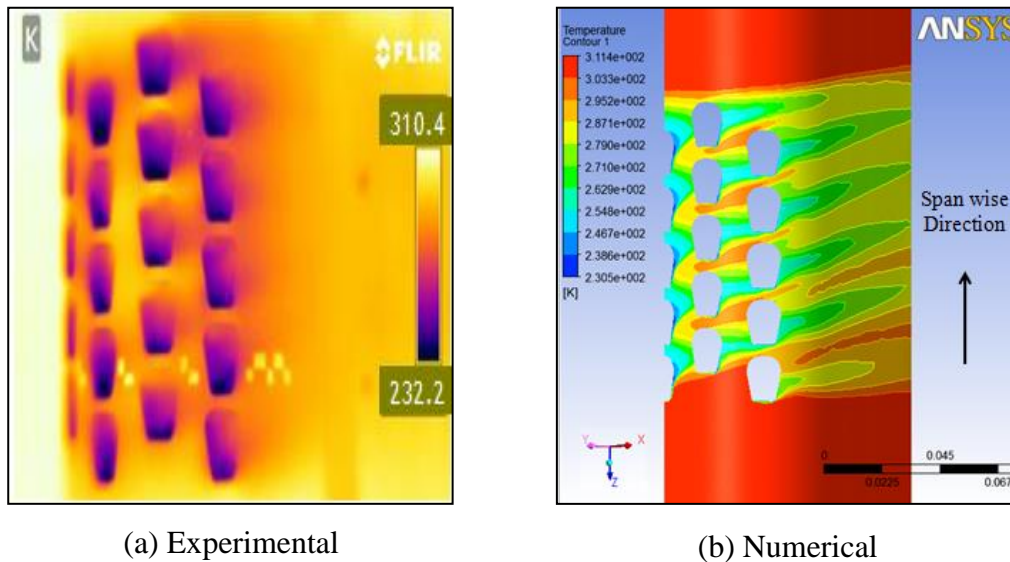


Fig. 5.96 Exp. and Numerical temperature contours of effectiveness for LFSHM at a typical B.R of 2.0

The adiabatic film cooling effectiveness values are plotted along the streamline direction from stagnation line to downstream of the coolant holes for the laidback fan shape hole configuration models. The typical experimental temperature contours obtained using IR camera and the numerical temperature contours extracted from CFD for a laidback fan shaped model at a blowing ratio of 2.0 are as shown in Fig. 5.96. From the experiments, it is found that up to B.R of 1.5 the coolant flow was not established and hence coolant films were not found near stagnation line due to low pressure and increased hole inlet to outlet area ratios, by visualization from the Fig. 5.96. Further, with the increase in blowing ratio, the coolant flow is fully established, and coolant film was found over the stagnation hole region and at downstream of holes. The units of scale on a thermal image of Fig. 5.96 are the temperature values in Kelvin captured by the infra-red camera and the units of scale on the numerical thermal image of Fig. 5.96 are the temperature values in Kelvin extracted from CFD analysis.

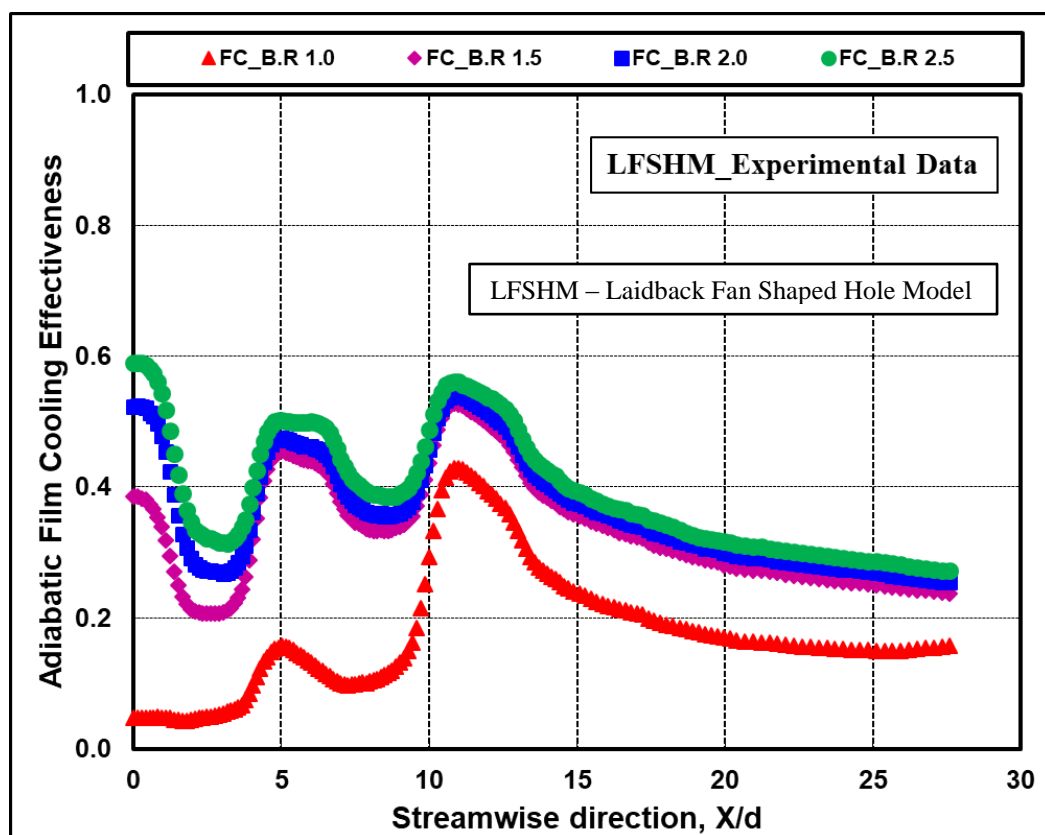


Fig. 5.97 Exp. cooling effectiveness for LFSHM at the B.Rs of 1.0 to 2.5

The experimentally obtained averaged film cooling effectiveness plots in streamwise direction for all the four planned blowing ratios are shown in Fig. 5.97. From the Fig. 5.97, it is found that with the increase in blowing ratio the film cooling effectiveness value increased up to B.R 2.5. This is due to more inlet to outlet hole exit area ratio and hence more area for the cooling films to spread over the surface.

The temperature contours from both experimental and CFD simulation are found to be similar to the same trend.

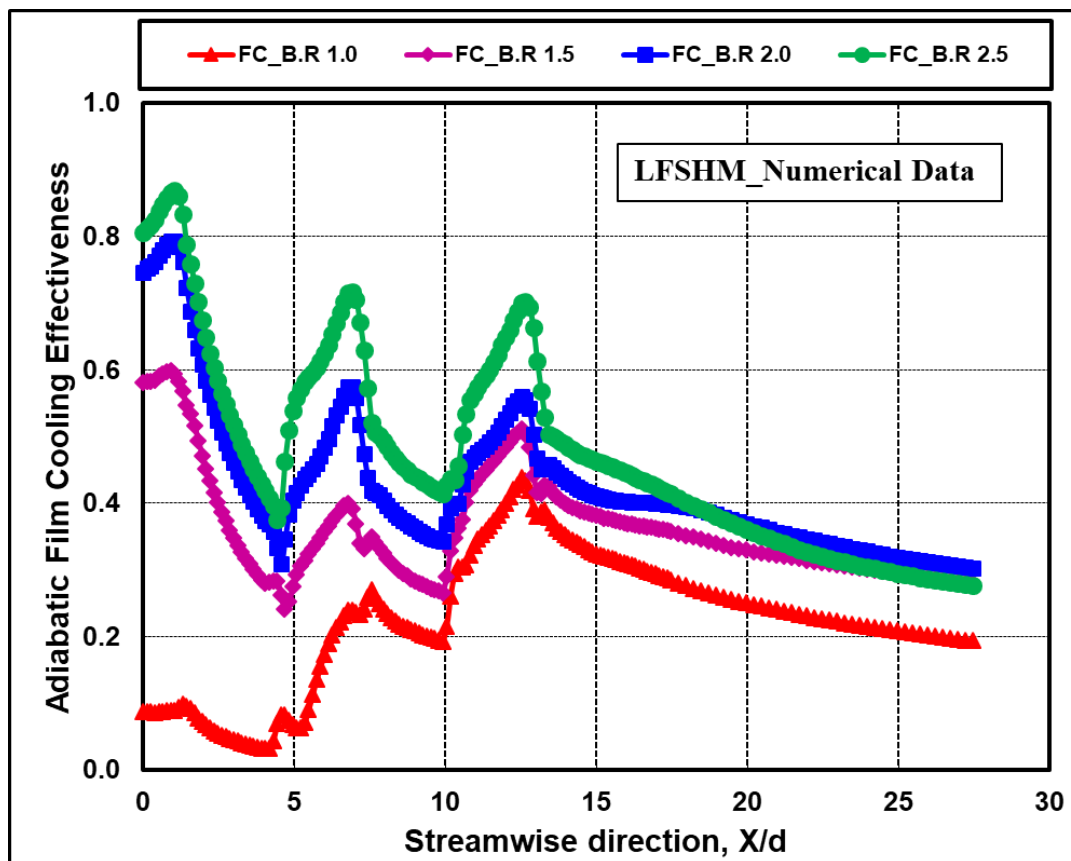


Fig. 5.98 Numerical cooling effectiveness for LFSHM at the B.Rs of 1.0 to 2.5

The averaged film cooling effectiveness plots in streamwise direction for all the four planned blowing ratios obtained from CFD simulation for laidback fan shape hole model are shown in Fig. 5.98. From the plots, it can be observed that similar to experimental results the average film cooling effectiveness value is higher at B.R 2.5. Only at downstream of the coolant holes, the film cooling effectiveness is higher at B.R 2.0. This may be due to more attachment of coolant films at lower blowing ratio.

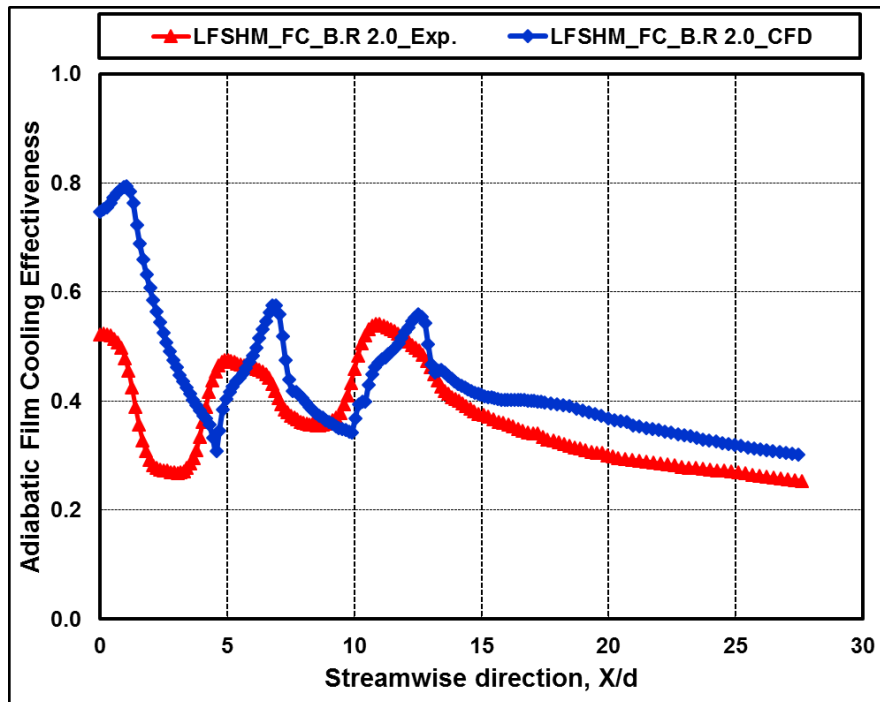


Fig. 5.99 Exp. Vs. Numerical cooling effectiveness for LFSHM at a B.R of 2.0

Thus on average, for laidback fan shape hole exit configuration planned over the leading edge of a gas turbine blade with considered hole geometry, from both experimental and CFD estimations the B.R 2.5 can be considered as optimized blowing ratio. The Fig. 5.99 shows a comparative plot between experimental and numerical results of film cooling effectiveness in streamwise direction from stagnation line to downstream of coolant holes at B.R 2.0. From the plot, it can be observed that both the results are in the same trend and gives meaningful validation. To have a comparative result between the considered hole shapes, B.R 2.0 is considered as optimized blowing ratio for the laidback fan shape model in our further studies.

5.4.2 Experimental and Numerical Heat Transfer Coefficient Results

Heat transfer coefficient value distribution is calculated both experimentally and numerically for all the three considered gas turbine blade leading edge models. The cooling hole configurations and shapes are the same as the leading edge models considered for film cooling effectiveness experiments. During the CFD prediction of heat transfer coefficient experiments, the constant heat flux is given on the leading

edge wall to heat the wall surface whereas in the case of experiments constant heat flux is supplied by the aid of bus bars attached the edges of SS sheet. Similar to film cooling effectiveness measurements the results are extracted for different blowing ratios in the streamwise direction from the stagnation line to downstream of the coolant holes. The experimentally and numerically evaluated temperature contours are taken, and the average heat transfer coefficients at different blowing ratios along the streamwise directions are plotted.

5.4.2.1 Circular Hole Exit Shape Model HTC Results (M9-CHM)

The average heat transfer coefficient values are plotted along the streamwise direction from stagnation line to downstream of the coolant holes for the circular hole shape models. The temperature profile obtained during both the experiments with the aid of FLIR make IR camera, and CFD simulation for B.R 2.0 is as shown in Fig. 5.100. The bus bars can be easily identified from IR thermal image, which is much cooler than the leading edge surface. In the case of numerical simulation, the edges of the leading edge are at a higher temperature than the other parts of the surface. These arrangements cannot be avoided, but this will lead to deviations in the comparative results of experiments with numerical simulation.

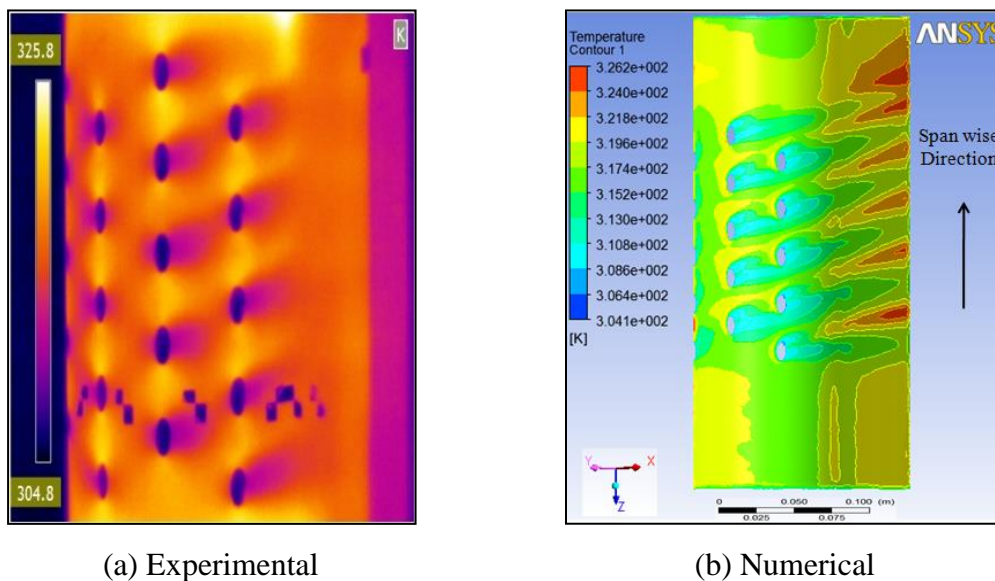


Fig. 5.100 Exp. and Numerical temperature contours of HTC for CHM at a B.R of 2.0

The units of scale on a thermal image of Fig. 5.100 are the temperature values in Kelvin captured by the infra-red camera and the units of scale on the numerical thermal image of Fig. 5.100 are the temperature values in Kelvin extracted from CFD analysis.

The experimentally averaged heat transfer coefficient plots in streamwise direction for all the four planned blowing ratios are shown in Fig. 5.101. From the Fig. 5.101, it is found that for circular hole configuration with the increase in blowing ratio the heat transfer coefficient value increased.

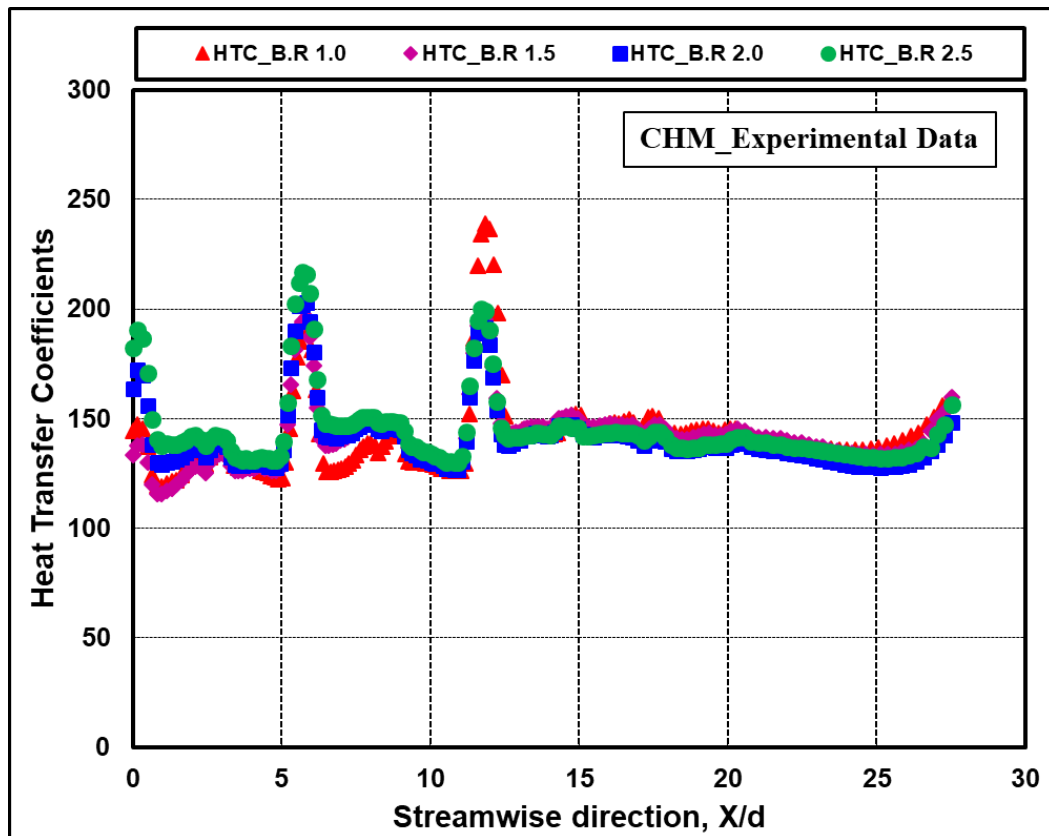


Fig. 5.101 Exp. HTC values for a CHM model at the B.Rs of 1.0 to 2.5

The numerically averaged heat transfer coefficient plots in streamwise direction for all the four planned blowing ratios are shown in Fig. 5.102. From the Fig. 5.102, it is found that same as that of experimental results for circular hole configuration with the increase in blowing ratio the heat transfer coefficient value increased.

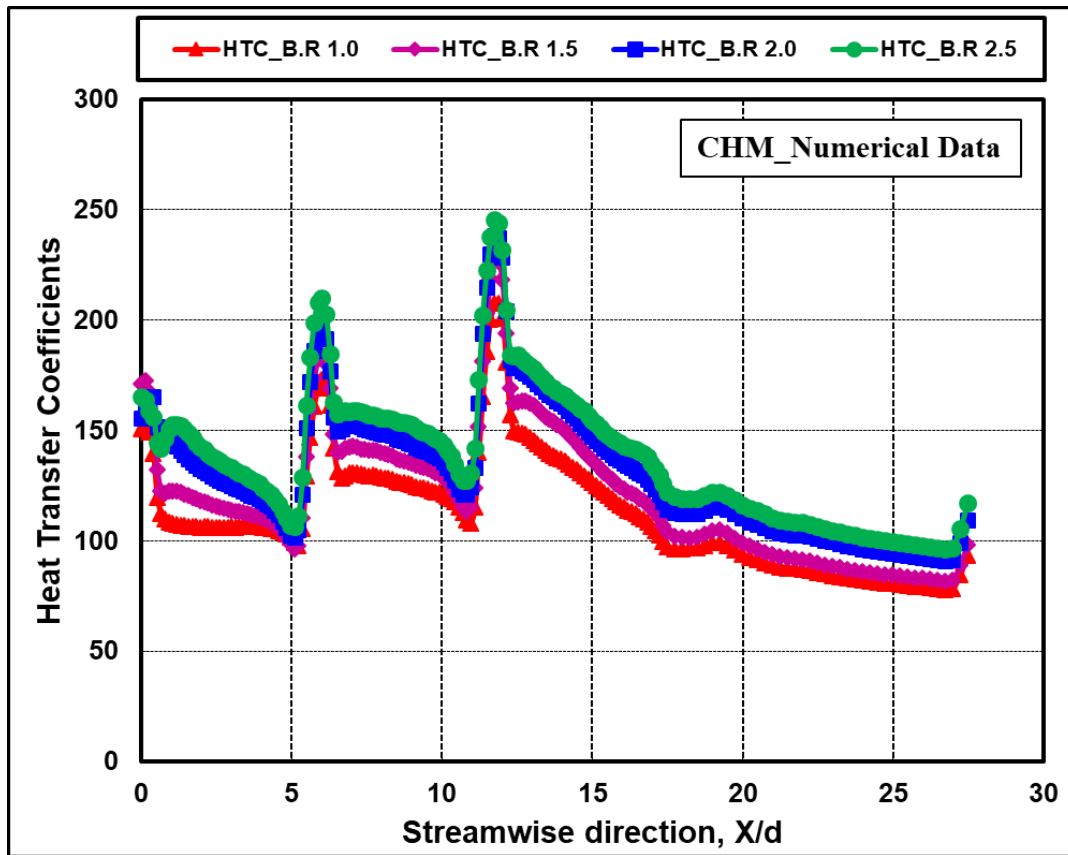


Fig. 5.102 Numerical HTC values for a CHM model at the B.Rs of 1.0 to 2.5

Fig. 5.103 shows a comparative plot between experimental and numerical results of averaged heat transfer coefficient value in the streamwise direction from stagnation line to downstream of coolant holes at B.R 2.0. The CFD results predict low heat transfer coefficients value than the experimental value this is due to the location of the bus bar in experimental case. From the plot, it can be observed that both the results are in the same trend and gives meaningful validation.

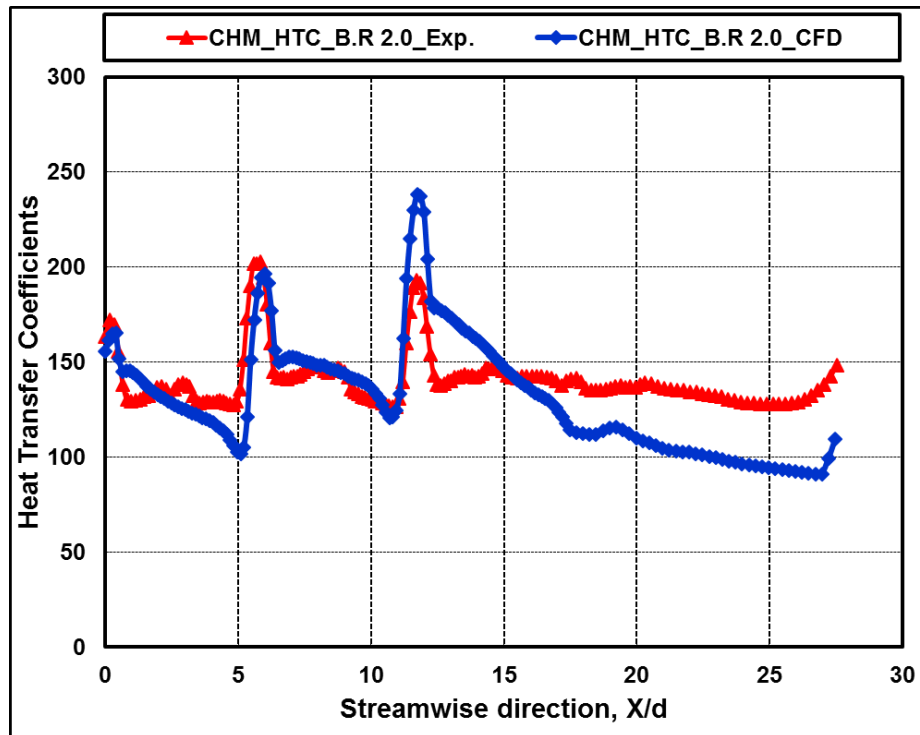


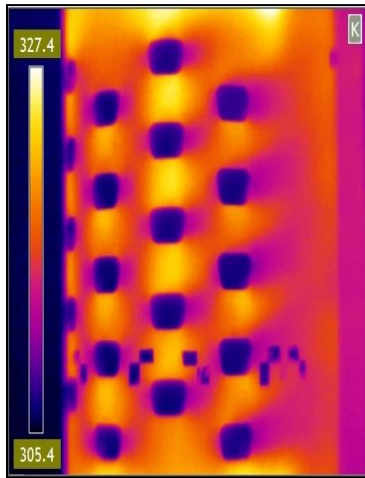
Fig. 5.103 Exp. Vs. Numerical HTC Values for a CHM model at the B.R of 2.0

5.4.2.2 Fan Shape Hole Model HTC Results (M10-FSHM)

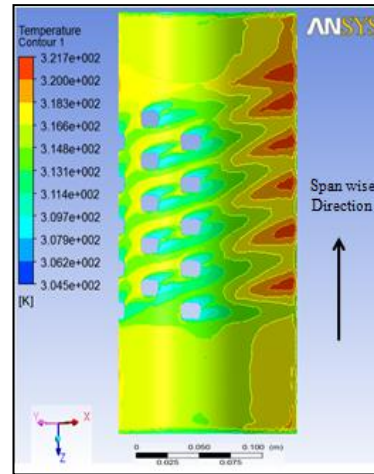
The experimentally averaged heat transfer coefficient plots in streamwise direction for all the four planned blowing ratios are shown in Fig. 5.105. From the Fig. 5.105, it is found that for fan shape hole configuration with the increase in blowing ratio the heat transfer coefficient value increased.

The average heat transfer coefficient value is obtained and is plotted along the streamline direction from stagnation line to downstream of the coolant holes for the fan shape hole configuration Leading edge model. The temperature contours obtained during the experiments with the aid of FLIR make IR camera, and CFD simulation for B.R 2.0 is shown in Fig. 5.104. The temperature contours obtained by experimental and CFD simulation are in the same pattern and give meaningful comparisons.

The units of scale on a thermal image of Fig. 5.104 are the temperature values in Kelvin captured by the infra-red camera and the units of scale on the numerical thermal image of Fig. 5.104 are the temperature values in Kelvin extracted from CFD analysis.



(a) Experimental



(b) Numerical

Fig. 5.104 Exp. and Numerical temperature contours of HTC for FSHM models at a B.R. of 2.0

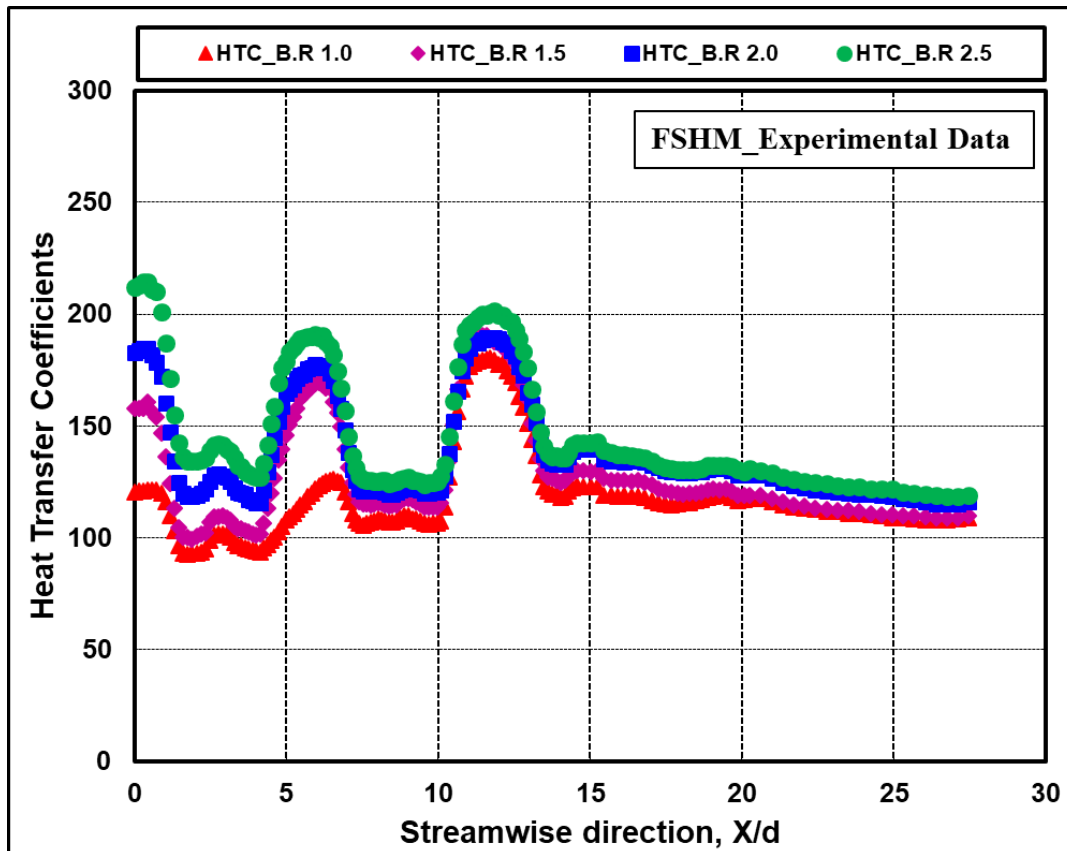


Fig. 5.105 Exp. HTC values for an FSHM at the B.R.s of 1.0 to 2.5

The numerically averaged heat transfer coefficient plots in streamwise direction for all the four planned blowing ratios are shown in Fig. 5.106. From the Fig. 5.106, it is found that same as that of experimental results for fan shape hole configuration with the increase in blowing ratio the heat transfer coefficient value increased.

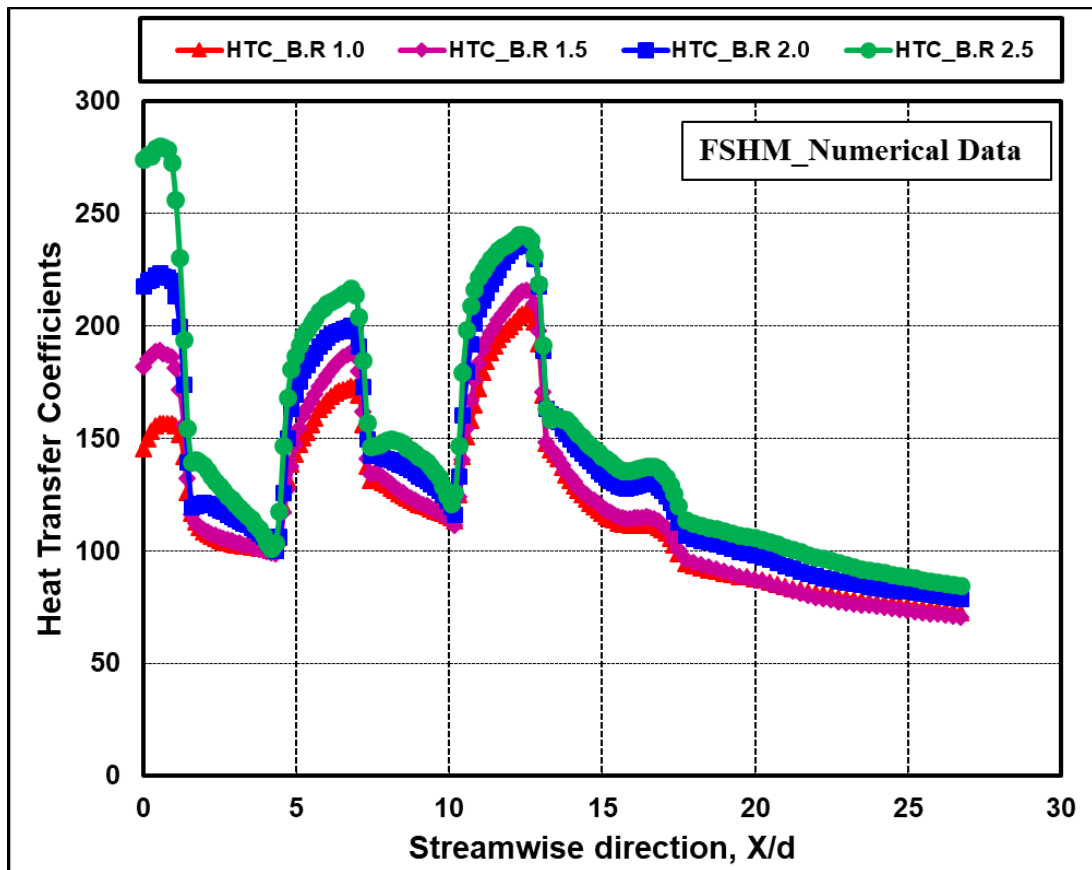


Fig. 5.106 Numerical HTC values for an FSHM at the B.R.s of 1.0 to 2.5

The Fig. 5.107 shows a comparative plot between experimental and numerical results of averaged heat transfer coefficient value in the streamwise direction from stagnation line to downstream of coolant holes at B.R 2.0. From the plot, it can be observed that both the results are in the same trend and gives meaningful validation. The CFD results predict low heat transfer coefficients value than the experimental value this is due to the location of the bus bar in experimental case.

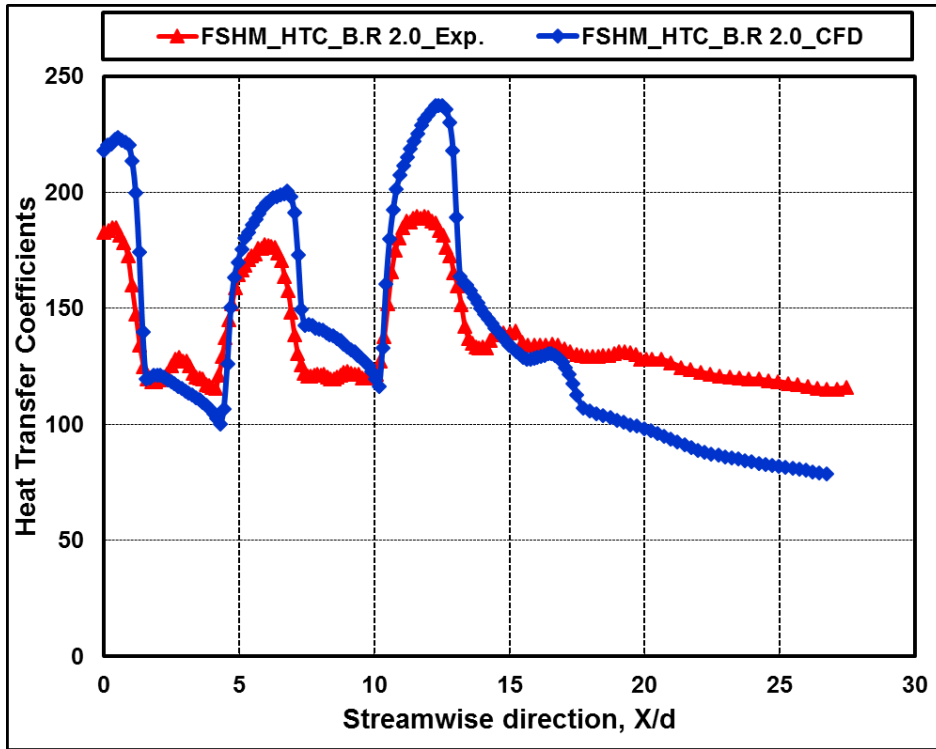
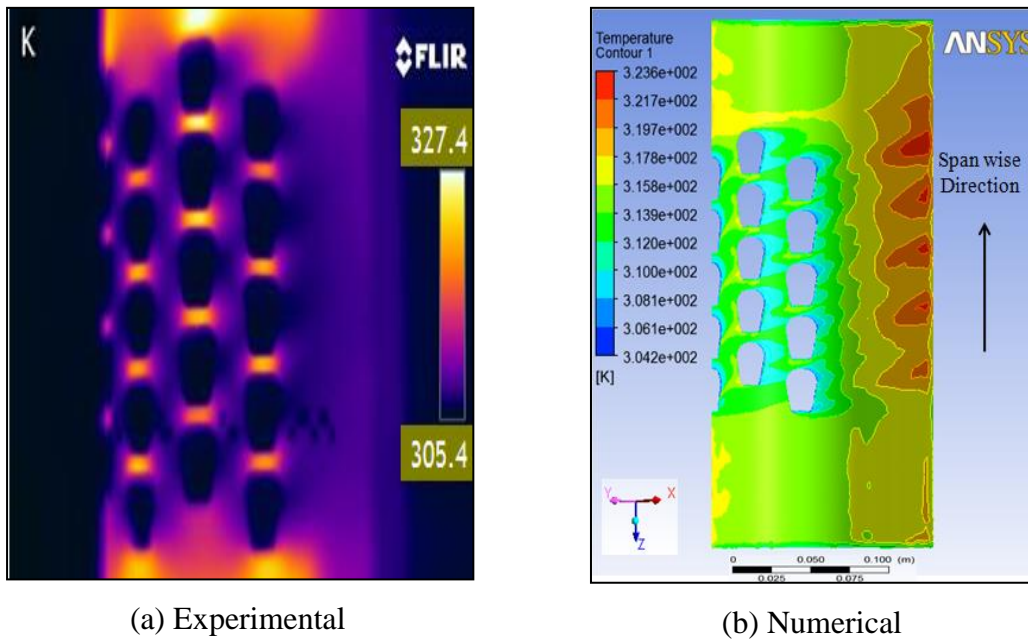


Fig. 5.107 Exp. Vs. numerical HTC for FSHM at the B.R of 2.0

5.4.2.3 Laidback Fan Shape Hole Model HTC Results (M11-LFSHM)



(a) Experimental

(b) Numerical

Fig. 5.108 Exp. and Numerical temperature contours of HTC for LFSHM at a B.R of 2.0

The average heat transfer coefficient values in W/m^2K are obtained and are plotted along the streamwise direction from stagnation line to downstream of the coolant holes for the fan shape hole configuration leading edge models. The temperature contours obtained during the experiments with the aid of FLIR make IR camera, and CFD simulation for B.R 2.0 is shown in Fig. 5.108. The temperature contours obtained by experimental and CFD simulation are in the same pattern and give meaningful comparisons. The units of scale on a thermal image of Fig. 5.108 are the temperature values in Kelvin captured by the infra-red camera and the units of scale on the numerical thermal image of Fig. 5.108 are the temperature values in Kelvin extracted from CFD analysis.

The experimentally averaged heat transfer coefficient plots in streamwise direction for all the four planned blowing ratios are shown in Fig. 5.109. From the Fig. 5.109, it is found that for laidback fan shape hole configuration with the increase in blowing ratio the heat transfer coefficient value increased.

The numerically averaged heat transfer coefficient plots in streamwise direction for all the four planned blowing ratios are shown in Fig. 5.110. From the Fig. 5.110, it is found that same as that of experimental results for laidback fan shape hole configuration with the increase in blowing ratio the heat transfer coefficient value increased.

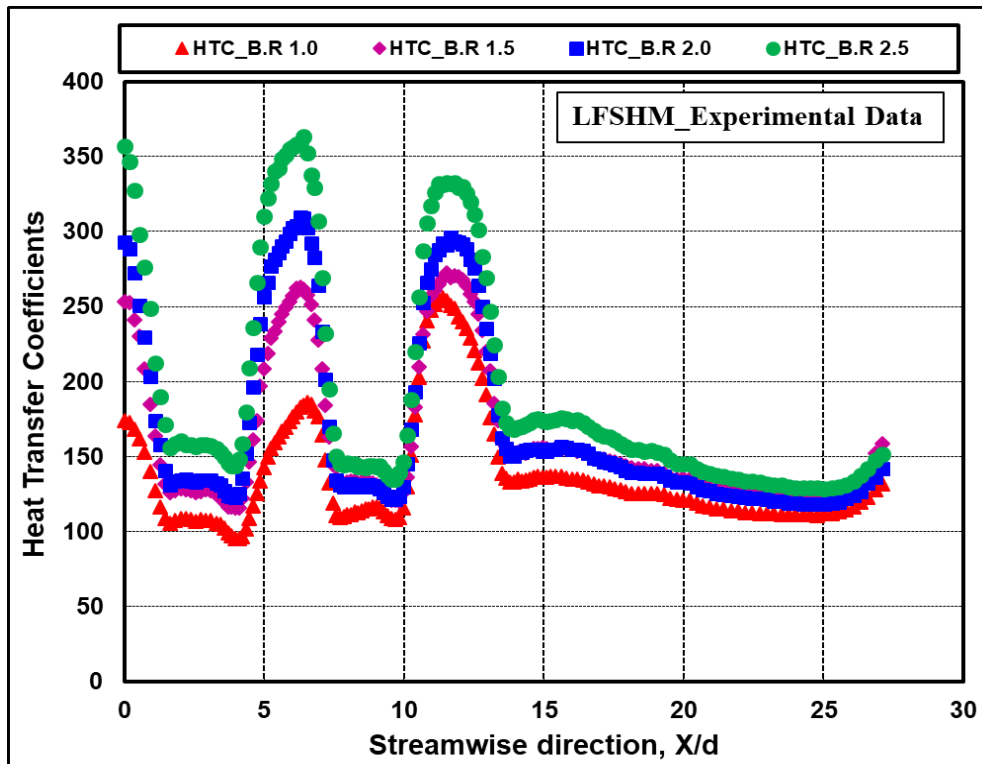


Fig. 5.109 Exp. HTC values for an LFSHM at the B.R.s of 1.0 to 2.5

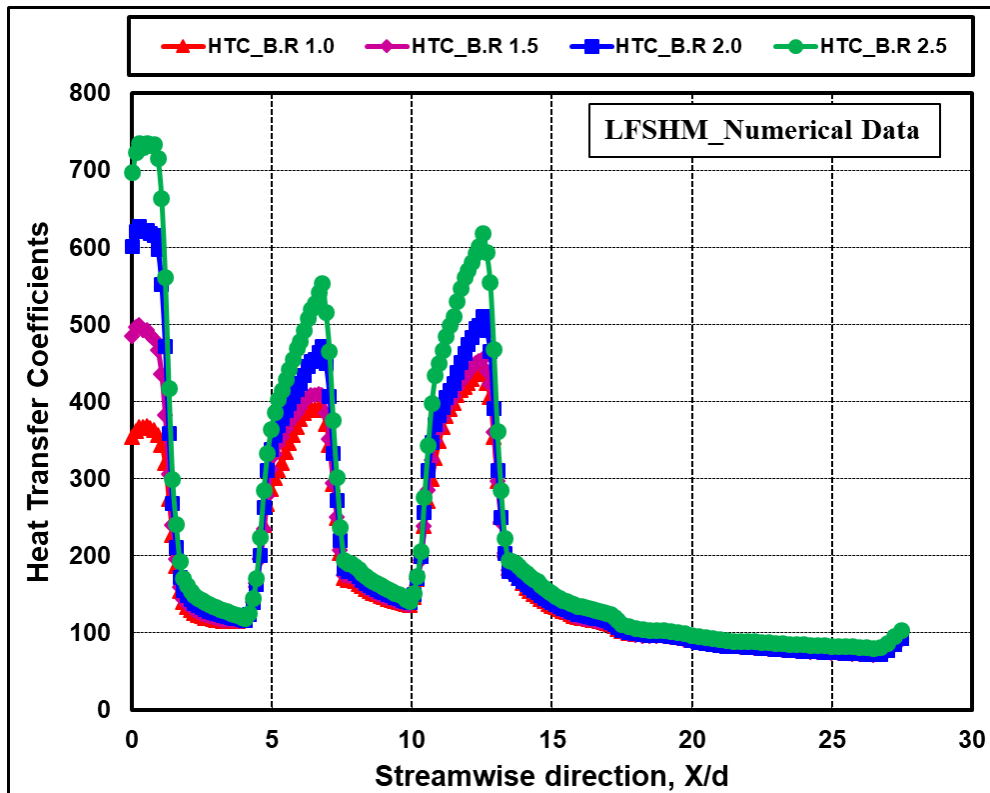


Fig. 5.110 Numerical HTC values for an LFSHM at the B.R.s of 1.0 to 2.5

The Fig. 5.111 shows a comparative plot between experimental and numerical results of averaged heat transfer coefficient value in the streamwise direction from stagnation line to downstream of coolant holes at a B.R of 2.0. From the plot, it can be observed that both the results are in the same trend and gives meaningful validation. The CFD results predict low heat transfer coefficients value than the experimental value this is due to the location of the bus bar in experimental case.

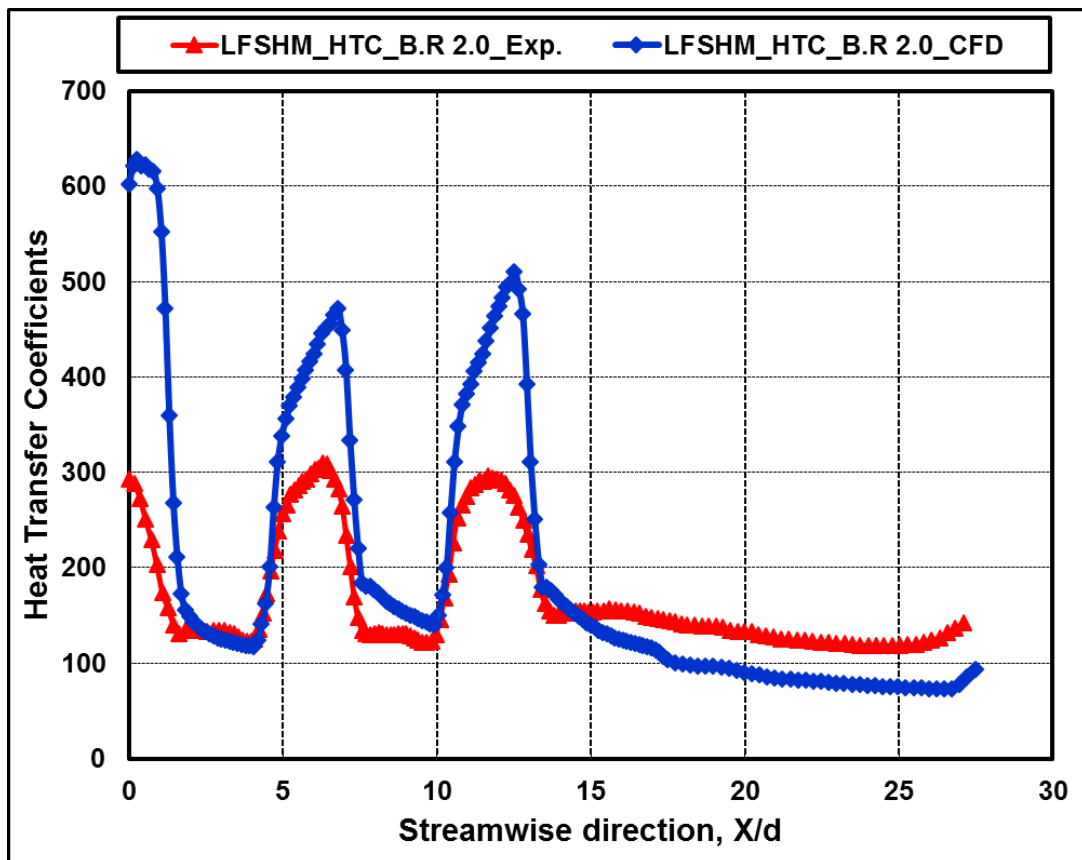


Fig. 5.111 Exp. Vs. Numerical HTC values for an LFSHM at the B.R of 2.0

Here in the case of shaped hole studies, the numerically extracted results have shown the very good comparison of cooling effectiveness and heat transfer coefficient values almost within 5% than that of experimental results. The frictional and mixing phenomenon losses are unable to consider by the CFD. Hence the CFD has shown the minor variation of the results than the experiments.

5.4.3 Experimental and Numerical Comparative Study of shaped holes

The influence of diffused hole shape over film cooling on gas turbine leading edge surface is accomplished by having a comparative study between the considered cooling hole shapes. All the considered three models are compared for average film cooling effectiveness values, which are plotted in the streamwise direction.

5.4.3.1 Experimental Comparative Study of Shaped hole models

All the three considered hole shapes over gas turbine blade leading edge surface film cooling are compared for experimental adiabatic film cooling effectiveness measurements. The experimentally obtained film cooling effectiveness results in the streamwise direction, from the stagnation line to downstream of the holes for all the planned blowing ratios are shown in Fig. 5.112 to Fig. 5.115.

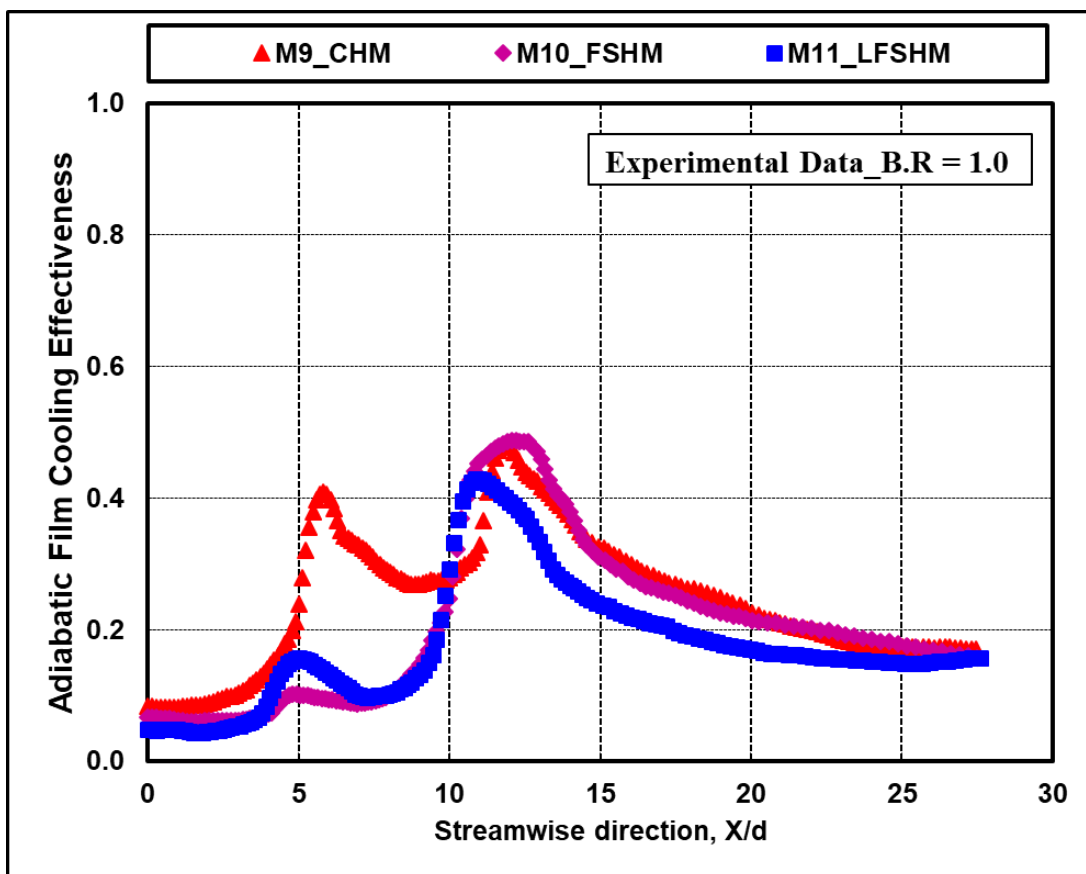


Fig. 5.112 Exp. cooling effectiveness comparison of CHM, FSHM and LFSHM models at a B.R of 1.0

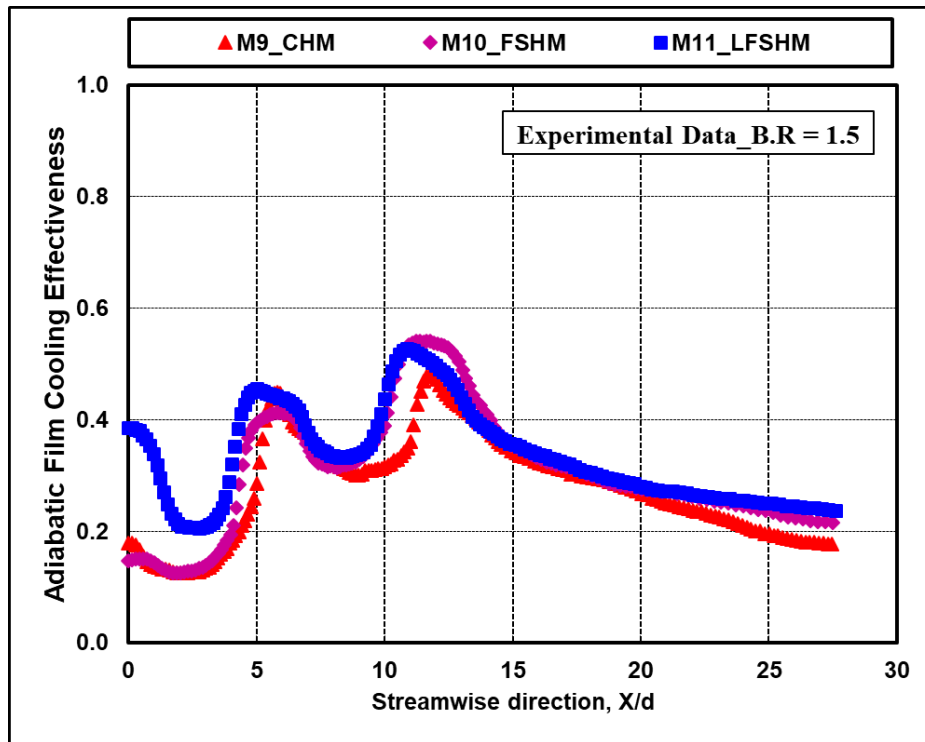


Fig. 5.113 Exp. cooling effectiveness comparison of CHM, FSHM and LFSHM models at a B.R of 1.5

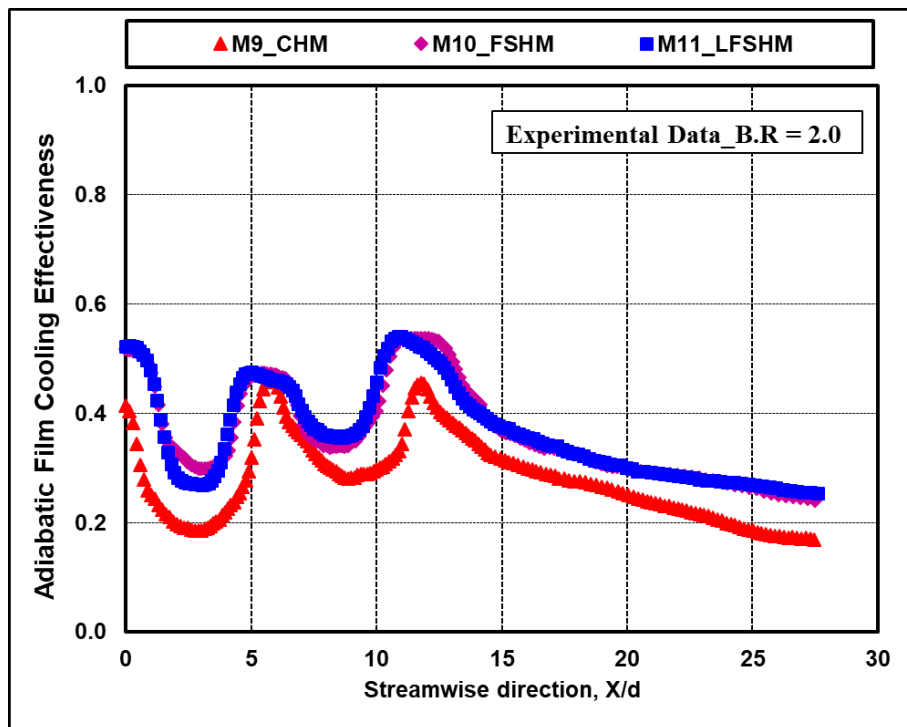


Fig. 5.114 Exp. cooling effectiveness comparison of CHM, FSHM and LFSHM models at a B.R of 2.0

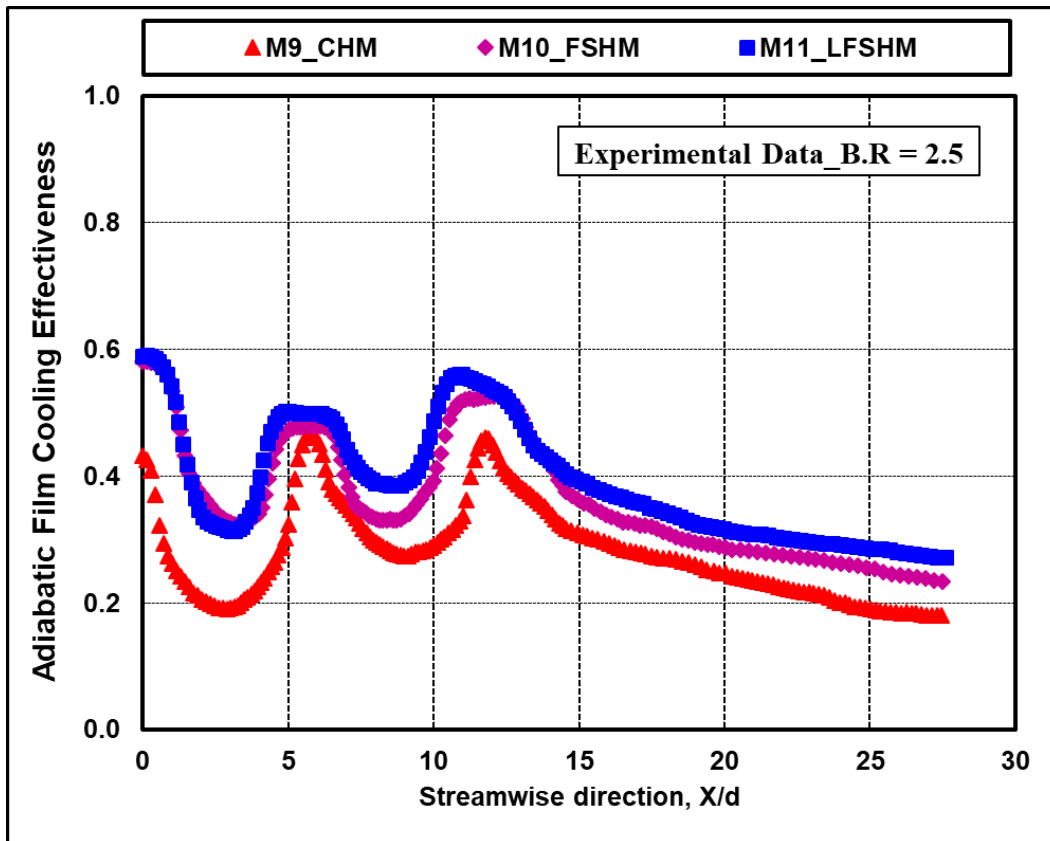


Fig. 5.115 Exp. cooling effectiveness comparison of CHM, FSHM and LFSHM models at a B.R of 2.5

From all the figures it is found that with the increase in blowing ratios the coolant films over the gas turbine blade is well established. The film cooling effectiveness value obtained experimentally increased with the increase in blowing ratio up to B.R 2.0 for all the considered models and a further increase in blowing ratio did not show much improvement. Also experimentally it is found that for the same blowing ratio the film cooling effectiveness value obtained is highest for laidback fan shape hole model and is lowest for circular hole model.

It can be concluded from the experiments that diffused cooling hole shapes gives higher film cooling effectiveness value over a gas turbine blade leading edge compared to circular hole exit shapes. Also experimentally it can be concluded that B.R 2.0 is optimized blowing ratio and laidback fan shape is optimized diffused cooling hole shape for these type of studies.

5.4.3.2 Numerical Comparative Study of All Exit Hole Shapes

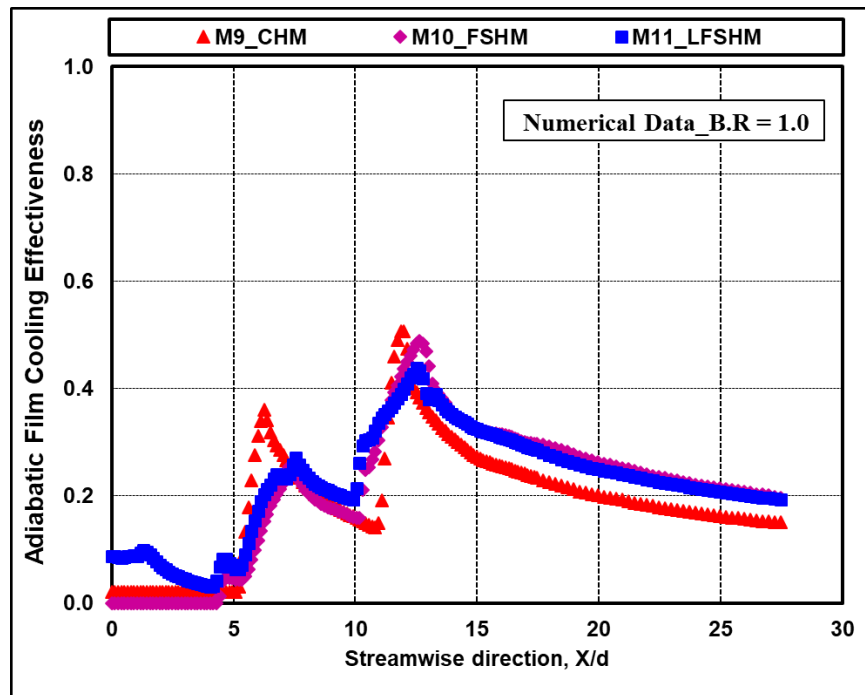


Fig. 5.116 Numerical cooling effectiveness comparison of CHM, FSHM and LFSHM models at a B.R of 1.0

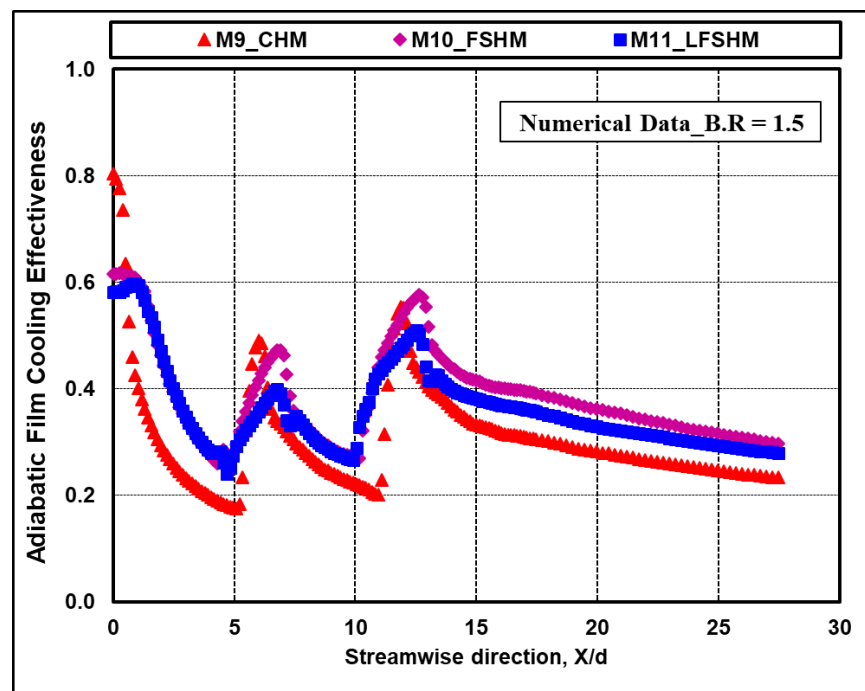


Fig. 5.117 Numerical cooling effectiveness comparison of CHM, FSHM and LFSHM models at a B.R of 1.5

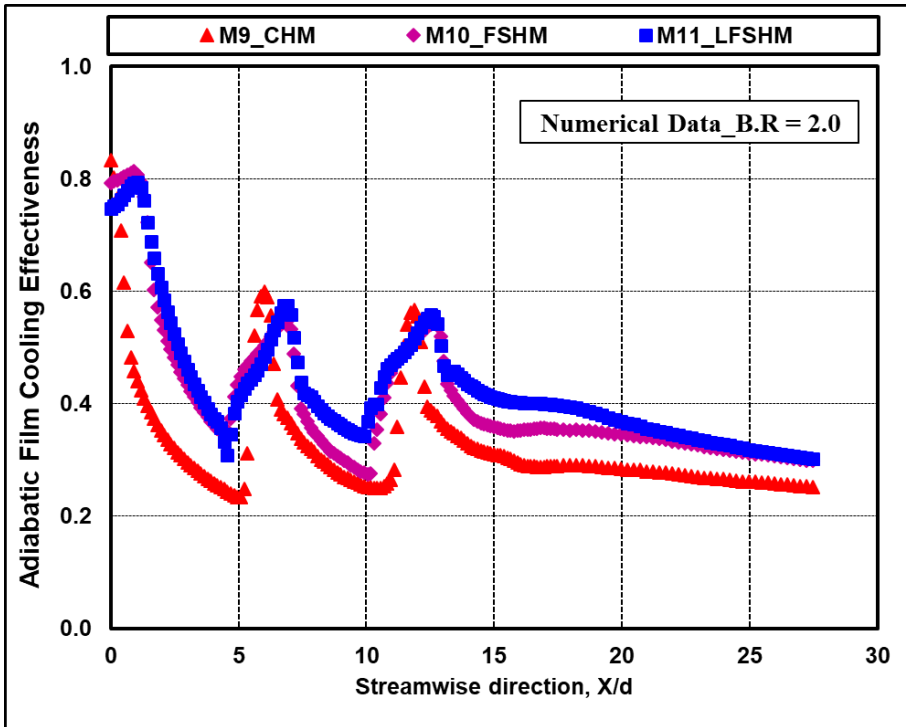


Fig. 5.118 Numerical cooling effectiveness comparison of CHM, FSHM and LFSHM models at a B.R of 2.0

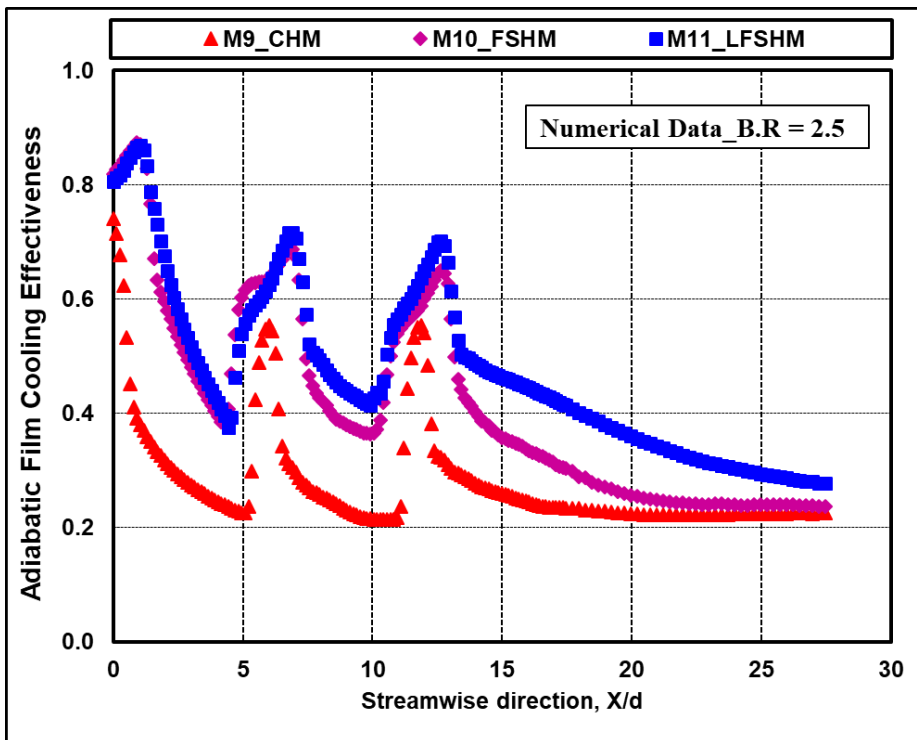


Fig. 5.119 Numerical cooling effectiveness comparison of CHM, FSHM and LFSHM models at a B.R of 2.5

All the three considered hole exit shapes for gas turbine blade leading edge film cooling are compared for adiabatic film cooling effective measurements obtained through CFD simulation. The numerically obtained film cooling effectiveness results in the streamwise direction, from the stagnation line to downstream of the holes for all the planned blowing ratios are shown in Fig. 5.116 to Fig. 5.119.

From all the figures similar to experimental results it is found that with the increase in blowing ratios the coolant films over the gas turbine blade is well established. The film cooling effectiveness value obtained numerically increased with the increase in blowing ratio up to B.R 2.0 for all the considered models and a further increase in blowing ratio did not show much improvement similar to experimental results. Also numerically it is found that for the same blowing ratio the film cooling effectiveness value obtained is highest for laidback fan shape hole model and is lowest for circular hole model.

It can be concluded from the numerical study that diffused cooling hole exit gives higher film cooling effectiveness value over a gas turbine blade leading edge compared to circular cooling hole shapes. Also same as that of the experimental study it can be concluded numerically that B.R 2.0 is optimized blowing ratio and laidback fan shape is optimized diffused hole exit shape for these type of studies.

In the case of shaped hole studies, the numerically extracted results have shown the very good comparison of cooling effectiveness and heat transfer coefficient values almost within 10 % than that of experimental results except at the hole locations. The deviation of CFD values is mainly due to the non-consideration of mixing phenomenon and frictional losses, lateral conduction of the test model. However, the CFD results are very useful for finding the trends of results and for the optimization of flow and geometrical parameters.

CHAPTER 6

CONCLUSIONS AND FUTURE SCOPE OF WORK

6 CONCLUSIONS

This study shows the effect of film cooling hole geometrical and flow parameters on adiabatic film cooling effectiveness and heat transfer coefficients over the gas turbine blade leading edge surfaces by both the experimental and numerical methods.

➤ Effect of hole orientation angle study

- ❑ 45° hole orientation angle model has shown a 20% higher adiabatic film cooling effectiveness than the 30°, and 30° model has shown 10% higher than the 15° hole orientation angle model.
- ❑ 45° hole orientation angle model has shown higher cooling effectiveness at a blowing ratio of 2.0
- ❑ 15° and 30° hole orientation angle models have shown higher cooling effectiveness at the blowing ratio of 1.5.

➤ Effect of hole inclination angle study

- ❑ The film cooling effectiveness has shown the increase with a decrease in hole inclination angle. Among the considered four models of 20°, 25°, 30° and 35° hole inclination angle, the 20° inclination hole angle model has shown the higher cooling effectiveness for the gas turbine blade leading edge configuration.
- ❑ 20° hole inclination angle model has shown a 20 % higher adiabatic film cooling effectiveness than the 25° and 30° hole inclination angle models.
- ❑ 25° and 30° hole inclination angle models have not shown the much difference in the cooling effectiveness.
- ❑ 30° hole inclination angle model has shown 5% higher adiabatic film cooling effectiveness than the 35° hole inclination angle model.
- ❑ All the hole inclination angle models have shown the higher cooling effectiveness at a blowing ratio of 1.5
- ❑ All the hole inclination angle models have shown the increase in heat transfer coefficient values with the increase in blowing ratio.
- ❑ At a lower B.R of 1.0, the 30° HIA has shown the higher cooling effectiveness. Whereas, at the higher B.Rs above 1.0, 20° HIA has shown higher effectiveness.

➤ **Effect of hole pitch study**

- ❑ 18 mm hole pitch model has shown the higher effectiveness of about 10 to 20% more than the 22.4 mm hole pitch model at all the considered blowing ratios.
- ❑ 18 mm hole pitch model has shown higher averaged heat transfer coefficients of about 10 to 60 W/m²K more than that of 22.4 mm hole pitch model at all considered blowing ratios.

➤ **Effect of hole shape study**

- ❑ Among the considered three hole exit shapes of Circular, Fan and Laidback Fan Shapes, Laidback fan shaped hole model has shown the higher cooling effectiveness and heat transfer coefficient values at all the blowing ratios. Both the Laidback Fan Shape and the Fan Shape have shown around the 10% increase in cooling effectiveness than the Circular Shape whereas the Laidback Fan Shape has shown around 1 to 2% increase than the Fan shape geometry.
- ❑ Among the considered three-hole exit shapes, film cooling effectiveness and heat transfer coefficient value shown the highest at a blowing ratio of 2.0. Further increase in blowing ratio did not show much improvement.

➤ **CFD analysis study**

- ❑ From CFD analysis, among the considered turbulence models, k-ε realizable turbulence model gives the better solution for these film cooling studies, nearer to the experimental values. Hence, the k-ε realizable turbulence model can be used for these type of film cooling CFD simulations.
- ❑ CFD results have shown similar trends as that of the experimental values. The CFD results showed the five peaks, which indicate the adiabatic film cooling effectiveness values at the five-hole locations. The CFD trends are useful in deciding the better geometry even though the results have the deviations from the experimental values.
- ❑ The CFD extracted results have shown the little over predicted cooling effectiveness results than that of experimental results, and in the case of heat transfer coefficients, lesser predicted results than the experimental values. The numerical deviations are occurred mainly due to the non-consideration of near

stagnant conditions of mainstream flow at the leading edge region, complex mixing phenomenon and frictional losses, and the presence of lateral conduction in the experiments.

Table 6.1 Brief conclusions

Blade Leading Edge Hole Geometry	Adiabatic Cooling effectiveness	Heat Transfer Coefficient	Optimized Blowing Ratios	
			Models	B.R
Increase in hole orientation angle	Increases	Increases	For 15° and 30°	1.5
			For 45°	2.0
Increase in hole inclination angle	Decreases	Decreases	For 20°, 25°, 30° and 35°	1.5
Increase in hole pitch	Decreases	Decreases	For 18 mm and 22.4 mm	2.0
Increase in hole exit area (CHM, FSHM, LFSHM)	Increases	Increases	For all CHM, FSHM, and LFSHM	2.0

Table 6.1 shows the optimized values of flow and geometrical parameters for the better adiabatic film cooling effectiveness and heat transfer coefficient values over the gas turbine nozzle guide vane leading edge surface. The effect of hole orientation angles, hole inclination angles, hole pitches and hole shapes over the gas turbine blade leading edge surface are considered in this study. Based on the results, the test model with the Laidback Fan Shape exit (higher exit area), with a pitch of 18 mm (lower pitch), with a hole inclination angle of 20° (lower inclination angle) and with the orientation angle of 45° (higher orientation angle) can be considered as the best film cooling hole configuration. These inputs are useful for the design of gas turbine blades for the better film cooling effectiveness in the thermal point of view. The combined effect of adiabatic cooling effectiveness and heat transfer coefficient values are useful for the designers in the optimization of cooling hole geometrical parameters accurately to implement in the engine programs.

6.1 Future Scope of Work

- Net heat flux ratio (NHFR) values can be calculated for the local heat flux values with the combined effects of heat transfer coefficients and the cooling effectiveness values. The heat loads for the base profiles without holes are needed to measure for finding the NHFR values. This needs to be carried out for the accurate optimization film cooling hole geometries.
- New cooling hole shapes on turbine blades can be modeled and experimented for the enhanced cooling effectiveness, engine power, and efficiency.
- CFD evaluation can be done for the various shapes of holes as the CFD evaluation is showing the considerable validation with the similar trends as that of experimental results. With the CFD estimation, any other flow and geometrical parameters other than the considered can be studied. CFD analysis needs to be improved for considering the two streams mixing phenomenon and lateral conduction values.
- Effect of different turbulent intensity levels of mainstream flow near the leading edge surface can be studied.

REFERENCES

Journal References

Ali Rozati and Danesh K. Tafti (2008). "Effect of Coolant-Mainstream Blowing Ratio on Leading Edge Film Cooling Flow and Heat Transfer-Les Investigation." *International Journal of Heat and Fluid Flow*, 29, 857-873.

Baldauf, S., Schulz, A. and Witting, S. (2001). "High-Resolution Measurements of Local Effectiveness from Discrete Hole Film Cooling.", *Journal of Turbomachinery*, 123, 758-765.

Bogard, D.G., and Thole, K.A. (2006). "Gas Turbine Film Cooling." *Journal of Propulsion and Power*, 22(2), 249-270.

Brittingham, R.A. and Leylek, J.H. (2000). "A Detailed Analysis of Film Cooling Physics: Part IV - Compound-Angle Injection with Shaped Holes." *Journal of Turbomachinery*, 122, 133-145.

Dileep Chandran and Bhamidi Prasad (2015). "Conjugate Heat Transfer Study of a Combined Impingement and Showerhead Film Cooling Near NGV Leading Edge." *International Journal of Rotating Machinery*, 2015, 315036/1-13.

Diganta, P.N, Kuo, C.N, Akhilesh, P.R and Je, C.N. (2012). "Influence of coolant density on turbine blade film cooling using pressure sensitive paint Technique." *Journal of Turbomachinery*, 134, 031006/1-10

Ekkad, S.V, Han, J.C. and Du, H. (1998). "Detailed Film Cooling Measurements on a Cylindrical Leading Edge Model; Effect of Free-Stream Turbulence and Coolant Density." *Journal of Turbomachinery*, 120, 799-807.

Florschuetz, L.W., Metzger, D.E., and Su, C.C. (1984). "Heat Transfer Characteristics for Jet Array Impingement with initial Crossflow." *ASME Journal of Heat Transfer*, 106, 34-41.

Frederic C. Yeb, Herbert J. Gladden, James W. Gauntner and Daniel J. Gauntner (1974). "Comparison of Cooling Effectiveness of Turbine Vanes with and Without Film Cooling." *NASA Technical Memorandum*, NASA TM X-3022.

Giovanna Barigozzi, Giuseppe Franchini, Antonio Perdichizzi and Silvia Ravelli (2010). "Film cooling of a contoured end wall nozzle vane through fan shaped holes." *International Journal of Heat and Fluid Flow*, 31, 576-585.

Goldstein, R. J. and Eckert, E. R. G. (1974). "Effects of hole geometry and density on three-dimensional film cooling." *International Journal of Heat and Mass Transfer*, 17, 595-607.

Goldstein, R.J., Jin, P. and Olson, R.L. (1999). "Film Cooling Effectiveness and Mass/Heat Transfer Coefficient Downstream of One Row of Discrete Holes" *Journal of Turbomachinery*, 121, 225-232.

Gritsch, M. and Schulz S. Witting. (1998). "Adiabatic Wall Effectiveness Measurements of Film Cooling Holes with Expanded Exits." *Journal of Turbomachinery*, 120, 549-556.

Gritsch, M. and Schulz S. Witting. (2000). "Film-cooling holes with expanded exits: near hole heat transfer coefficients." *International Journal of Heat and Fluid Flow*, 21, 146-155.

Gritsch, M., Saumweber, C., Schulz, A., Witting, S. and Sharp, E. (2000). "Effect of Internal Coolant Crossflow Orientation on the Discharge Coefficient of Shaped Film-Cooling Holes." *Journal of Turbomachinery*, 122, 146-152.

Hams, D.G. and Leylek, J.H. (2000). "A Detailed Analysis of Film Cooling Physics: Part III-Streamwise Injection with Shaped Holes." *Journal of Turbomachinery*, 122, 122-132.

In Sung Jung and Joon Sik Lee (2000). "Effects of Orientation Angles on Film Cooling Over a Flat Plate: Boundary Layer Temperature Distributions and Adiabatic Film Cooling Effectiveness." *Journal of Turbomachinery*, 122, 153-160.

Jae Su Kwak and Je-Chin Han. (2003). "Heat Transfer Coefficients and Film Cooling Effectiveness on the Squealer Tip of a Gas Turbine Blade." *Journal of Turbomachinery*, 125, 648-657.

James E. Mathew, James W. Baughn and Aaron R. Byerley (2003). "The Effect of Freestream Turbulence on Film Cooling Adiabatic Effectiveness." *International Journal of Heat and Fluid Flow*, 24, 669-679.

Jason E. Dees, David G. Bogard, Gustavo A. Ledezma and Gregory M. Laskowski (2013). "Overall and Adiabatic Effectiveness Values on a Scaled-Up, Simulated Gas Turbine Vane." *Journal of Turbomachinery*, 135, 051017/1-10.

Jason K. Ostanek (2014). "Improving Pin-Fin Heat Transfer Predictions Using Artificial Neural Networks." *Journal of Turbomachinery*, 136, 051010/1-9.

Je Chin Han and Srinath Ekkad (2001). "Recent Development in Turbine Blade Film Cooling." *International Journal of Rotating Machinery*, 7(1), 21-40.

Je-Chin Han (2004). "Recent Studies in Turbine Blade Cooling." *International Journal of Rotating Machinery*, 10(6), 443-457.

Jun Yu Liang and Shun Kang (2012). "Experimental and numerical investigation of cooling effectiveness and heat transfer coefficient for straight and curved holes." *International Journal of Heat and Mass Transfer*, 56, 158-171.

Ken-ichi Funazaki, Hirokazu Kawabata and Okita Yoji (2012). "Free-Stream Turbulence Effects on Leading Edge Film Cooling." *International Journal of Gas Turbine, Propulsion and Power System*, 4(1).

Ki Don Lee and Kwang Yong Kim (2010). "Shape optimization of a fan shaped hole to enhance film cooling effectiveness." *International Journal of Heat and Mass Transfer*, 53, 2996-3005.

Kline, S. J., and Mc Clintock, F. A. (1953). "Describing Uncertainties in Single Sample Experiments." *Mechanical Engineering*, 75, 3-8.

LI Shaohua Tao Peng, Li- Xian Liu, Ting-ting GUO and Bin Yuan (2007). "Numerical Simulation of Turbine Blade Film cooling with Different Blowing Ratio and Hole to hole space." *International Conference on Power Engineering*.

LI Xu, Sun Bo, You Hongde and Wang Lei (2014). "Evolution of Rolls Royce air-cooled turbine blades and feature analysis." *Procedia Engineering*, 00(2014) 000-000, 1-10.

Li, X. C., Subbuswamy, G. and Zhou, J. (2013). "Performance of Gas Turbine Film Cooling with Backward Injection." *Energy and Power Engineering*, 5, 132-137.

Marc L. Nathan, Thomas E. Dyson, David G. Bogard, Sean D. Bradshaw (2014). "Adiabatic and overall effectiveness for the showerhead film cooling of a turbine vane." *ASME Journal of Turbomachinery*, 136, 031005/1-9.

May Kyu Kyu Soe, Ding Shui Ting and Wu Hong (2011). "Analysis of Film Cooling Effectiveness on Antivortex Hole." *IEEE Conference Publications*, 4763 - 4766.

McGovern, K.T., and Leylek, J.H. (2000). "A Detailed Analysis of Film Cooling Physics: Part II-Compound-Angle Injection with Cylindrical Holes." *Journal of Turbomachinery*, Vol. 122, 113-121.

Michael Gritsch, Achmed Schulz and Sigmar Witting (2003). "Effect of Internal Coolant Crossflow on the Effectiveness of Shaped Film Cooling Holes." *Journal of Turbomachinery*, 125, 547-554.

Michael Gritsch, Will Colban, Heinz Schar, Klaus Dobbeling (2005). "Effect of Hole Geometry on the Thermal Performance of Fan Shaped Film Cooling Holes." *Journal of Turbomachinery*, 127, 718-725.

Pedersen, D.K., Eckert, E.R.G. and Goldstein, R.J. (1977). "Film cooling with large density difference between mainstream and secondary fluid measured by heat-mass transfer analogy." *ASME Journal of Heat Transfer*, 99, 621-627.

Pedersen, D.R. (1977). "Film cooling with large density differences b/w mainstream and secondary fluid measured by the heat transfer analogy." *ASME Journal of Heat transfer*.

- Prasad Kalghatgi and Sumanta Acharya (2015). "Improved Film Cooling Effectiveness with a Round Film Cooling Hole Embedded in a Contoured Crater." *Journal of Turbomachinery*, 137, 101006/1-10.
- Rajesh Kumar Panda and Prasad, B. V. S. S. S. (2014). "Conjugate heat transfer from impingement and film-cooled flat plate." *ASME Journal of Thermo physics and Heat Transfer*, 28(4), 647-678.
- Reiss, H. and Bolcs, A. (2000). "Experimental Study of Showerhead Cooling on a Cylinder Comparing Several Configurations Using Cylindrical and Shaped Holes." *Journal of Turbomachinery*, 122 / 163.
- Robert Kiml, Sadanari Mochizuki and Akira Murata (2001), "Effects of Rib arrangements on heat transfer and flow behavior in a rectangular rib –roughened passage: Application to cooling of gas turbine blade trailing edge." *Journal of Heat Transfer*, 123, 675-681.
- Ronald S. Bunker (2005). "A Review of Shaped Hole Turbine Film Cooling Technology." *Journal of Heat Transfer*, 127, 441-453.
- Sang Woo Lee, Yong Beom and Joon Sik Lee (1997). "Flow Characteristics and Aerodynamic Losses of Film Cooling Jets with Compound Angle Orientations." *Journal of Turbomachinery*, 119, 310–319.
- Sangkwon Na and Tom I-P. Shih (2007). "Increasing Adiabatic Film Cooling Effectiveness by using an Upstream Ramp." *Journal of Heat Transfer*, 129, 464-471.
- Shaker, S. F., Abdullah, M.Z., Mujeebu, M. A., Ahmad, K.A. and Abdullah, M.K. (2012). "Study on the Effect of Number of Film Cooling Rows on The Thermal Performance of Gas Turbine Blade." *Journal of Thermal Science and Technology*, 32(2), 89-98.
- Shuye Teng and Je-Chin Han (2000). "Effect of Film-Hole shape on Turbine Blade Heat Transfer Coefficient Distribution." *Journal of Thermophysics and Heat Transfer*, 15(3), 249-256.

Siddarth Thakur, Jeffry wright and Wei Shyy (1999). "Convective film cooling over a representative turbine blade." *International Journal of Heat and Mass Transfer*, 42/2269-2285.

Sinha, A.K., Bogard, D.G. and Crawford, M.E. (1991). "Film-cooling effectiveness downstream of a single row of holes with variable density ratio." *Journal of Turbomachinery*, 113, 442-449.

Srinath V. Ekkad, Shichuan Ou and Richard B. Rivir (2004). "A transient infrared thermography method for simultaneous film cooling and heat transfer coefficient measurements from a single test." *Journal of Turbomachinery*, 126, 597-603.

Suryanarayanan, A., Mhetras, S.P., Schobeiri, M.T. and Han, J.C. (2009). "Film Cooling Effectiveness on a Rotating Blade Platform." *Journal of Turbomachinery*, 131, 011014/1-11.

Sweeney, P.C., and Rhodes, J.F. (2000). "An Infrared Technique for Evaluating Turbine Airfoil Cooling Designs." *Journal of Turbomachinery*, 122, 170-177.

Tarek Elnady, Ibrahim Hassan, Lyse Kadem and Terry Lucas (2013). "Cooling effectiveness of shaped film holes for leading edge." *Experimental Thermal and Fluid Science*, 44, 649-661.

Vijay K. Garg and David L. Rigby (1999). "Heat transfer on a film-cooled blade - the effect of hole physics." *International Journal of Heat and Fluid Flow*, 20, 10-25.

Vijay K. Garg, Reza S. Abhari (1997). "Comparison of predicted and experimental Nusselt number for a film cooled rotating blade." *International Journal of Heat and Fluid Flow*, 18, 452- 460.

Walters, D.K., and Leylek, J.H. (2000). "A Detailed Analysis of Film-Cooling Physics: Part I - Streamwise Injection with Cylindrical Holes." *Journal of Turbomachinery*, 122, 102-112.

William D. York and James H. Leylek (2003). "Leading Edge Film Cooling Physics-part III: Diffused Hole Effectiveness." *Journal of Turbomachinery*, 125, 252-259.

Xue, S., Newman, A., Ng, W., Moon, H.K. and Zhang. L. (2013). "Heat Transfer Performance of a Showerhead and Shaped Hole Film Cooled vane at Transonic Conditions" *Journal of Turbomachinery*, 135, 031007/1-8.

Yiping Lu, David Allison and Srinath V. Ekkad. (2007). "Turbine blade showerhead film cooling: influence of hole angle and shaping." *International Journal of Heat and Fluid Flow*, 28, 922–931.

Youn J. Kim and Kim, S. M. (2004). "Influence of Shaped Injection Holes on Turbine Blade Leading Edge Film Cooling." *International Journal of Heat and Mass Transfer, Elsevier*, 47, 245-256.

Yusop, N.M., Ali., A.H. and Abdullah M.Z. (2013). "Conjugate film cooling of a new multi-layer convex surface of turbine blades." *International Communication of Heat and Mass Transfer*, 45, 86-94.

Zhihong Gao and Je Chin Han (2009). "Influence of Film Hole Shape and Angle on Showerhead Film Cooling Using PSP Technique." *Journal of Heat Transfer*, 131, 06170/1-11.

Books

Bruce R. Munson, Donald F. Young, and Theodore H. Okiishi (2009). "Fundamentals of Fluid Mechanics, Fourth Edition." John Wiley and Sons Publications, India.

Holman, J.P. (2012). "Experimental Methods for Engineers, Eighth Edition." McGraw-Hill Publication, New York.

Je-Chin Han, Sandip Dutta and Srinath Ekkad (2012). "Gas Turbine Heat Transfer and Cooling Technology, Second Edition." CRC Press, Boca Raton.

John H. Leinhard IV and John H. Leinhard V. (2011). "A Heat Transfer Text Book, Fourth Edition." Dover Publications, New York.

Lakshminarayana B. (1996). "Fluid Dynamics and Heat Transfer of Turbomachinery" Wiley, New York.

Robert W. Fox and Alan T. McDonald (2009). "Introduction to Fluid Mechanics, Seventh Edition." Wiley India Private Limited, India

Versteeg, H.K. and Malalasekera, W. “An Introduction to Computational Fluid Dynamics, Second Edition.” Dorling Kindersley India Pvt. Ltd., India, 1-23.

William W. Bathie. (1996). “Fundamentals of Gas Turbine Second Edition.” Wiley Publishers.

Yunus A. Cengel and Afshin J. Ghajar (2012). “Heat and Mass Transfer Fourth Edition” McGraw-Hill Publication.

Yunus A. Cengel and John M. Cimbala (2012). “Fluid Mechanics, Second Edition” McGraw-Hill Publication.

Yunus A. Cengel and Michael Boles (2008). “Thermodynamics an Engineering Approach, The Sixth Edition.” McGraw-Hill Publication.

Thesis and Dissertations

Gwennael Beirnaert Chartrel (2011). “CFD Predictions of Heat Transfer Coefficient Augmentation on a Simulated Film Cooled Turbine Blade Leading Edge.” *M.S Thesis, The University of Texas at Austin.*

Shakeel Nasir (2008). “Showerhead Film Cooling Performance of a Turbine Vane at High Freestream Turbulence in a Transonic Cascade.” *Virginia Polytechnic Institute and State University, Blacksburg, Virginia Tech.*

Yiping Lu (2007). “Effect of Hole Configurations on Film Cooling from Cylindrical Inclined Holes for The Application to The Gas Turbine Blades.” *Louisiana State University and Agricultural and Mechanical College, China.*

Conference Proceedings

James L. Rutledge, Paul L. King and Richard Rivir (2008). “CFD Predictions of Pulsed Film Cooling Heat Flux on A Turbine Blade Leading Edge.” Proceedings of IMECE2008, ASME International Mechanical Engineering Congress and Exposition, Boston, Massachusetts, USA, 1-11.

Funazaki Ken-inchi, Kawabata Hirokazu, Takahashi Daichi and Okita Yoji (2012). “Experimental and Numerical Investigation on Leading Edge Film Cooling Performance: Effects of Hole Exit Shape and Free Stream Turbulence.” Proceedings of ASME Turbo Expo, Copenhagen, Denmark.

Francis S. Stepka and Raymond E. Gaugler (1983). "Comparison of Predicted and Experimental External Heat Transfer Around a Film Cooled Cylinder in Crossflow." NASA Technical Memorandum, International Gas Turbine Conference, NASA TM 83017.

Vijay K. Garg (1999). "Heat transfer on a Film-cooled Rotating Blade" NASA/CR-1/1999-20930, Turbo Expo 99, ASME, Indianapolis, Indiana.

Web Pages

Harlan, H.B. (2015). "Convection heat transfer coefficient estimation." http://s3.amazonaws.com/suncam/pdocs/119_La3w.pdf (Apr. 15, 2013).

Sounak, B. (2012). "Gas Power Cycles." <http://sounak4u.weebly.com/gas-power-cycle.html> (Apr. 8, 2013).

https://en.wikipedia.org/wiki/Brayton_cycle (Feb. 2, 2013).

<https://www.quora.com/Aerospace-and-Aeronautical-Engineering> (Mar. 5, 2013).

<http://www.infrared-thermography.com/glossary2.htm> (Mar. 10, 2013).

<http://www.me.umn.edu/labs/tcht/measurements/what.html> (Oct. 18, 2013).

http://d2n4wb9orp1vta.cloudfront.net/resources/images/cdn/cms/MMS_0313_RT_turbine-blade.jpg (Nov. 20, 2013).

Appendix-I

I MEASUREMENT OF MASS FLOW AND COEFFICIENT OF DISCHARGE

I.1 Coolant mass flow and Cd values

The coolant mass flow and the hole coefficient of discharge (C_d) values for the film cooling holes were found before carrying out the cooling effectiveness and heat transfer coefficient experiments. Mass flow measurements are done by supplying the secondary coolant air to the NGV model through the coolant chamber by varying the coolant chamber pressures. The coolant holes area is much smaller compared to the coolant chamber area. Hence, the measured chamber pressure will be equal to total coolant pressure. The coolant chamber pressure was varied by using pressure regulator over a pressure range up to 400 mm of H₂O for the different coolant mass flow rates through the cooling holes with coolant ejection through the holes at atmospheric pressure. The actual mass flow (W_{actual}) through the film cooling holes for the respective hole geometries is measured using the orifice meter based on the upstream and downstream pressures of the coolant line orifice meters. The orifice diameter of 20.13 mm is used in the coolant flow line. The upstream and downstream static pressure ports to the orifice plate are made at D and $D/2$ locations as per the BIS standards of mass flow measurements. The orifice flow measurement formula is made using the BIS standards reference of IS15675:2006. The theoretical mass flow ($W_{\text{theoretical}}$) is calculated based on the coolant density; coolant holes flow area and coolant flow velocity through the film cooling holes. The theoretical flow velocity through the film holes is calculated based on the pressure difference across the film holes using Bernoulli's equation. Using this theoretical velocity, the theoretical mass flow rate is calculated. The ratio of actual to theoretical coolant mass flow provides the cooling hole flow coefficient of discharge (C_d).

The coefficient of discharge is found using the relation:

$$C_d = \frac{W_{actual}}{W_{theoretical}}$$

The coolant flow orifice equation is arrived based on the BIS standards reference IS15675:2006 and is,

$$\text{Mass flow in Kg/hr, } m_o = 0.121198 * \sqrt{\Delta P * (P_{up} + 680)}$$

Here, the coolant line Orifice diameter is 20.13 mm, and the 2-inch diameter pipe is used for the coolant line flow.

Where, ΔP = Differential Pressure across the orifice plate in mm of H₂O

P_{up} = Orifice upstream pressure in mm of Hg

Some of the typical coolant flow hole discharge coefficient measurements are mentioned below.

Table I.1 shows the coolant mass flow data measured for the 20° hole inclination angle test model using the orifice flow meter. Fig. I.1 shows the variation of mass flow through the film cooling holes as a function of coolant plenum pressure and Fig. I.2 shows the variation of C_d with the coolant flow Reynolds number for a 20° hole inclination angle test model. The average C_d value for this model is found as 0.61.

Table I.1 Coolant flow hole Cd for a 20° hole Inclination angle model

LE Model_20Deg Hole inclination Angle											
04th Nov 2013	Pcha (mm of H ₂ O)	Delta P (mm of H ₂ O)	Pup (mm of Hg)	Wactual (kg/hr)	PCha (N/m ²)	Vcalc (m/s)	Wtheory (kg/hr)	Cd	Mass flow/unit area (Kg/m ² s)	Re	Vact (m/s)
	25.60	121.44	26.79	35.51	251.12	21.86	56.87	0.62	16.02	3203.64	13.65
	50.20	210.20	46.60	47.37	492.43	30.61	79.64	0.59	21.37	4273.48	18.21
	75.20	316.87	69.58	59.07	737.66	37.47	97.47	0.61	26.65	5329.27	22.70
	100.40	411.49	91.20	68.27	984.85	43.29	112.63	0.61	30.80	6159.97	26.24
	125.40	504.47	112.47	76.63	1230.09	48.38	125.87	0.61	34.57	6913.96	29.46
	150.70	594.80	132.50	84.25	1478.26	53.04	137.98	0.61	38.01	7601.78	32.39
	175.30	680.23	152.40	91.20	1719.57	57.20	148.82	0.61	41.14	8228.30	35.06
	200.20	752.00	171.20	96.97	1963.82	61.13	159.04	0.61	43.74	8748.68	37.27
	225.20	835.60	189.16	103.29	2209.05	64.84	168.68	0.61	46.59	9318.95	39.70
	250.40	925.59	213.66	110.23	2456.25	68.37	177.86	0.62	49.73	9945.20	42.37
	275.17	984.00	230.90	114.74	2699.23	71.67	186.45	0.62	51.76	10352.63	44.11
	300.00	1043.50	243.50	118.98	2942.79	74.83	194.68	0.61	53.67	10734.52	45.73
	325.00	1131.04	265.40	125.33	3188.02	77.89	202.63	0.62	56.54	11307.45	48.17
	350.40	1214.50	285.13	131.22	3437.18	80.88	210.40	0.62	59.19	11838.85	50.44
	375.60	1271.60	302.48	135.47	3684.37	83.73	217.84	0.62	61.11	12222.36	52.07
	401.00	1342.90	321.50	140.55	3933.53	86.52	225.08	0.62	63.41	12681.34	54.03
Average Cd Value:								0.614			

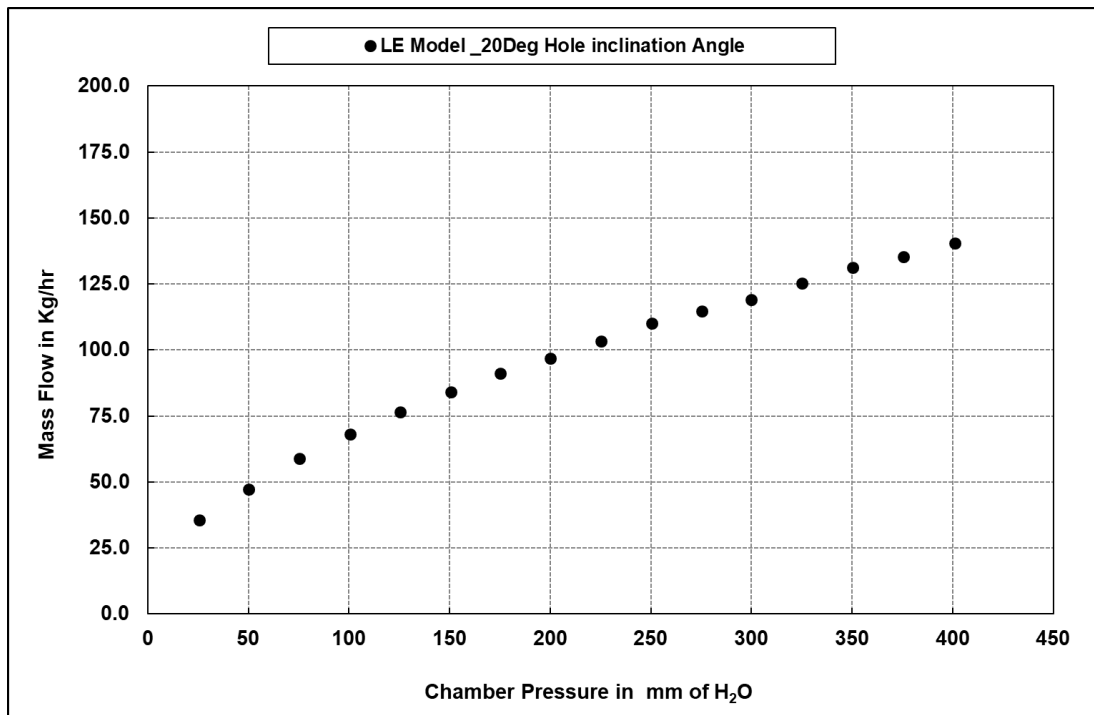


Fig. I.1 Mass flow Vs. Coolant chamber pressure for a 20° hole Inclination angle model.

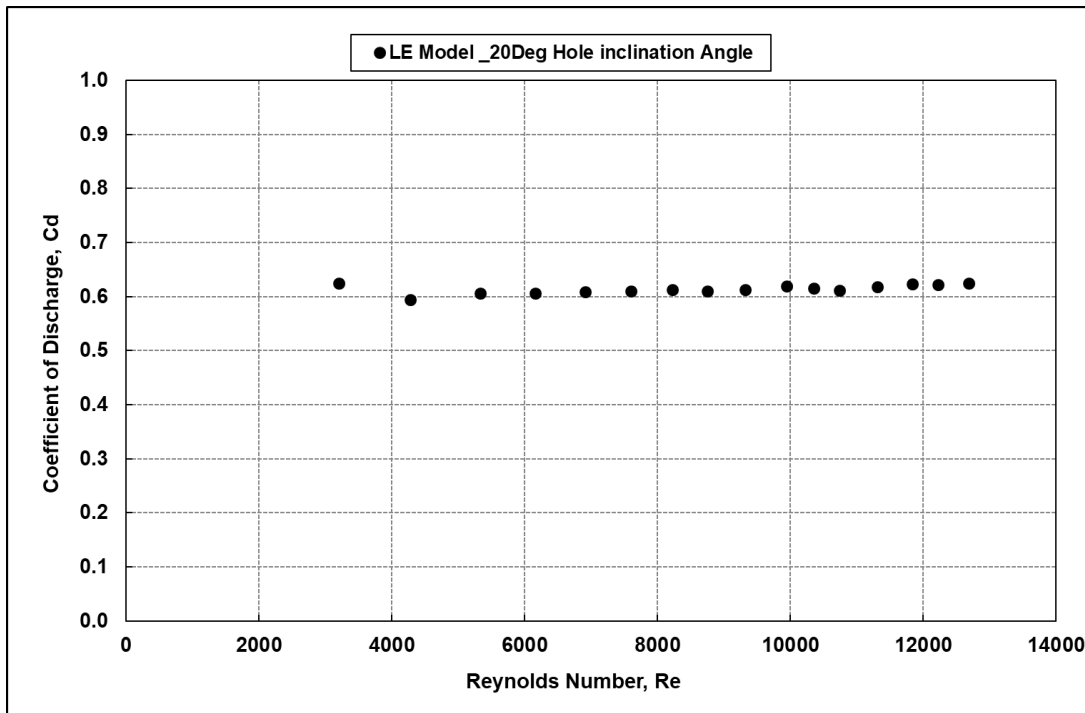


Fig. I.2 Coolant Cd Vs. Coolant Reynolds number for a 20° hole Inclination angle model

Table I.2 shows the coolant mass flow data measured for a 25° hole inclination angle test model using the orifice flow meter. Fig. I.3 shows the variation of mass flow through the film cooling holes as a function of coolant plenum pressure and Fig. I.4 shows the variation of Cd with the coolant flow Reynolds number. The average Cd value for this model is found as 0.63.

Table I.2 Coolant flow hole Cd for a 25° hole Inclination angle model

LE Model _25Deg Hole Inclination Angle											
12th Nov 2013	Pcha (mm of H ₂ O)	Delta P (mm of H ₂ O)	Pup (mm of Hg)	Wactual (kg/hr)	PCha (N/m ²)	Vcalc (m/s)	Wtheory (kg/hr)	Cd	Mass flow/unit area (Kg/m ² s)	Re	Vact (m/s)
	25.41	118.79	30.59	35.21	249.25	21.78	56.66	0.62	15.89	3177.00	13.54
	50.36	216.25	58.40	48.43	494.00	30.66	79.76	0.61	21.85	4369.55	18.62
	75.40	318.53	80.33	59.64	739.57	37.52	97.60	0.61	26.91	5381.34	22.93
	100.28	412.03	108.37	69.08	983.68	43.27	112.56	0.61	31.16	6232.25	26.55
	125.51	508.17	129.11	77.71	1231.17	48.40	125.92	0.62	35.06	7011.75	29.87
	150.84	594.25	155.92	85.42	1479.63	53.06	138.05	0.62	38.53	7706.96	32.83
	175.27	678.45	171.49	92.12	1719.23	57.20	148.80	0.62	41.56	8311.27	35.41
	200.39	753.91	199.15	98.67	1965.69	61.16	159.11	0.62	44.51	8902.44	37.93
	225.14	837.76	212.49	104.80	2208.47	64.83	168.65	0.62	47.28	9455.36	40.28
	250.24	919.15	239.92	111.45	2454.68	68.35	177.81	0.63	50.28	10055.09	42.84
	274.61	979.71	253.98	115.93	2693.68	71.60	186.26	0.62	52.30	10460.06	44.56
	300.09	1044.81	276.32	121.15	2943.62	74.85	194.71	0.62	54.65	10930.40	46.57
	325.02	1130.28	293.91	127.16	3188.22	77.89	202.64	0.63	57.36	11472.79	48.88
	350.23	1197.40	315.50	132.32	3435.46	80.86	210.35	0.63	59.69	11938.67	50.86
	375.59	1264.37	332.25	137.11	3684.23	83.73	217.83	0.63	61.85	12370.83	52.70
	400.60	1323.50	347.32	141.32	3929.61	86.48	224.97	0.63	63.75	12750.63	54.32
Average Cd Value:								0.621			

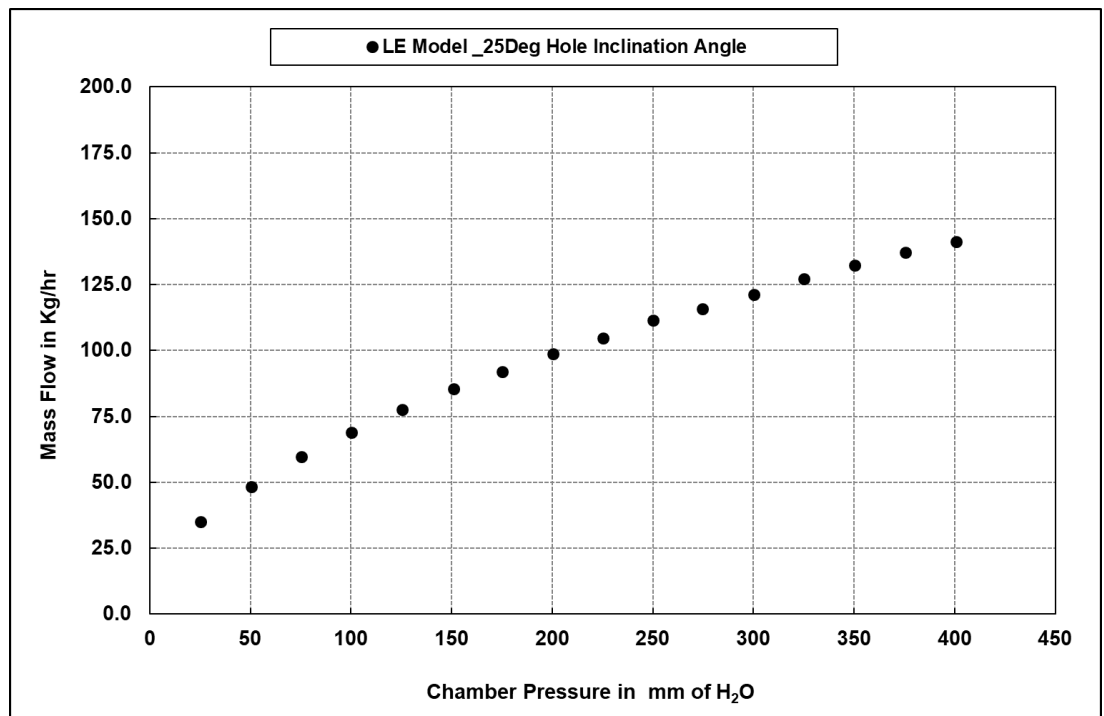


Fig. I.3 Mass flow Vs. Coolant chamber pressure for a 25° hole Inclination angle model.

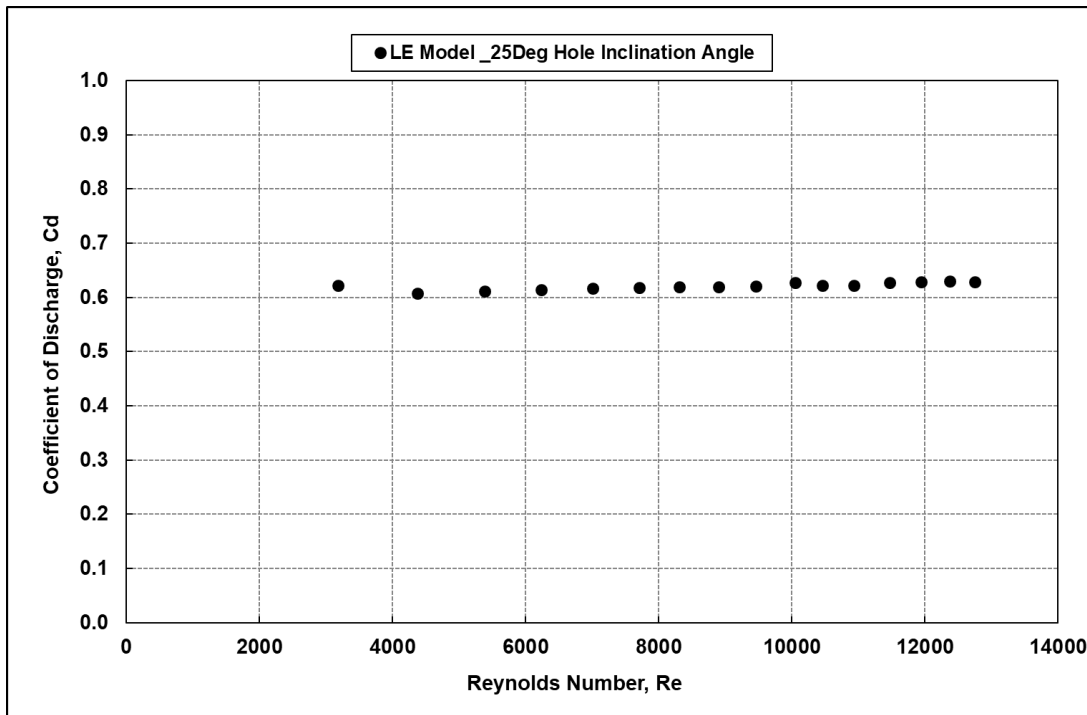


Fig. I.4 Coolant Cd Vs. Coolant Reynolds number for a 20° hole Inclination angle model

Table I.3 shows the coolant mass flow data measured for a 30° hole inclination angle test model using the orifice flow meter. Fig. I.5 shows the variation of mass flow through the film cooling holes as a function of coolant plenum pressure and Fig. I.6 shows the variation of Cd with the coolant flow Reynolds number. The average Cd value for this model is found as 0.63.

Table I.3 Coolant flow hole Cd for a 30° hole Inclination angle model

LE MODEL_30Deg Hole Inclination Angle											
29-11-13	Pcha (mm of H ₂ O)	Delta P (mm of H ₂ O)	Pup (mm of Hg)	W actual (kg/hr)	PCha (N/m ²)	Vcalc (m/s)	Wtheory (kg/hr)	Cd	Mass flow/unit area (Kg/m ² s)	Re	Vact (m/s)
	25.22	116.14	34.39	34.91	247.39	21.70	56.45	0.62	91.46	18291.90	13.42
	50.52	222.29	70.20	49.49	495.57	30.71	79.89	0.62	129.66	25932.75	19.02
	75.59	320.18	91.08	60.22	741.48	37.56	97.72	0.62	157.77	31553.46	23.15
	100.16	412.57	125.53	69.87	982.50	43.24	112.49	0.62	183.05	36609.17	26.86
	125.62	511.87	145.75	78.80	1232.24	48.43	125.98	0.63	206.43	41286.14	30.29
	150.98	593.69	179.34	86.57	1481.01	53.09	138.11	0.63	226.79	45358.90	33.28
	175.23	676.68	190.58	93.02	1718.88	57.19	148.79	0.63	243.71	48741.19	35.76
	200.58	755.82	227.10	100.35	1967.55	61.19	159.19	0.63	262.91	52581.98	38.57
	225.08	839.91	235.82	106.30	2207.88	64.82	168.63	0.63	278.48	55695.69	40.86
	250.08	912.71	266.18	112.63	2453.11	68.33	177.75	0.63	295.07	59013.78	43.29
	274.04	975.41	277.06	117.10	2688.14	71.52	186.07	0.63	306.78	61356.89	45.01
	300.17	1046.11	309.13	123.29	2944.46	74.86	194.74	0.63	322.99	64597.47	47.39
	325.04	1129.52	322.41	128.96	3188.41	77.89	202.65	0.64	337.86	67572.47	49.57
	350.05	1180.29	345.86	133.36	3433.75	80.84	210.30	0.63	349.39	69877.69	51.26
	375.57	1257.14	362.02	138.72	3684.08	83.73	217.83	0.64	363.41	72682.52	53.32
	400.20	1304.10	373.13	142.03	3925.68	86.43	224.86	0.63	372.11	74421.19	54.60
Average Cd Value:								0.628			

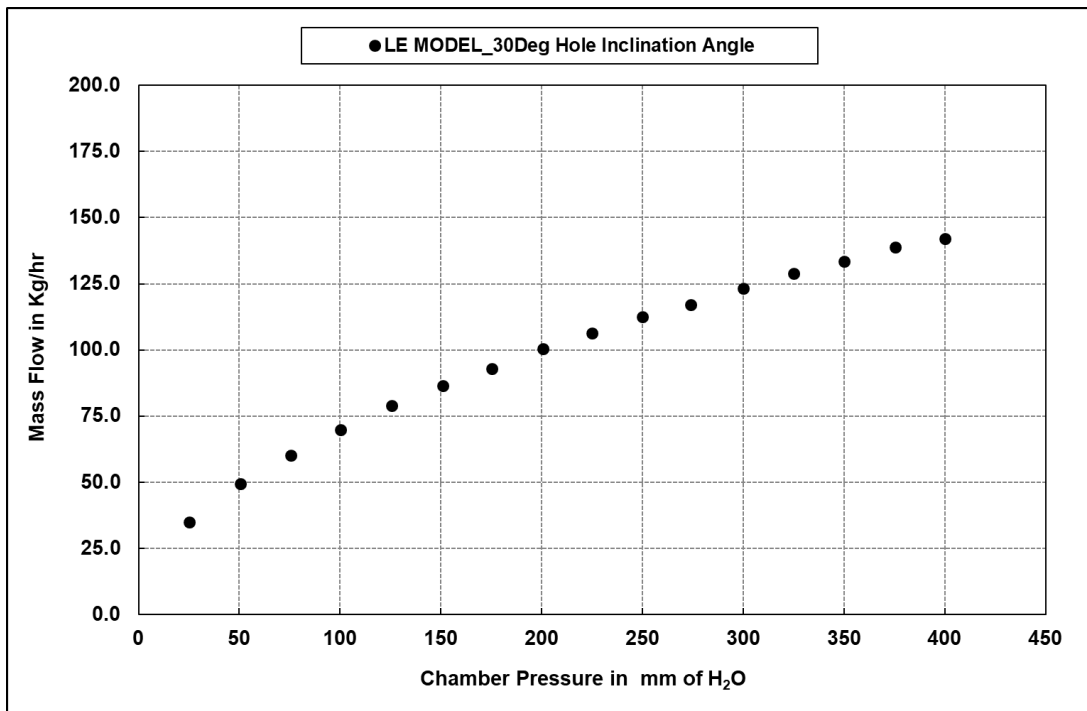


Fig. I.5 Mass flow Vs. Coolant chamber pressure for a 30° hole Inclination angle model

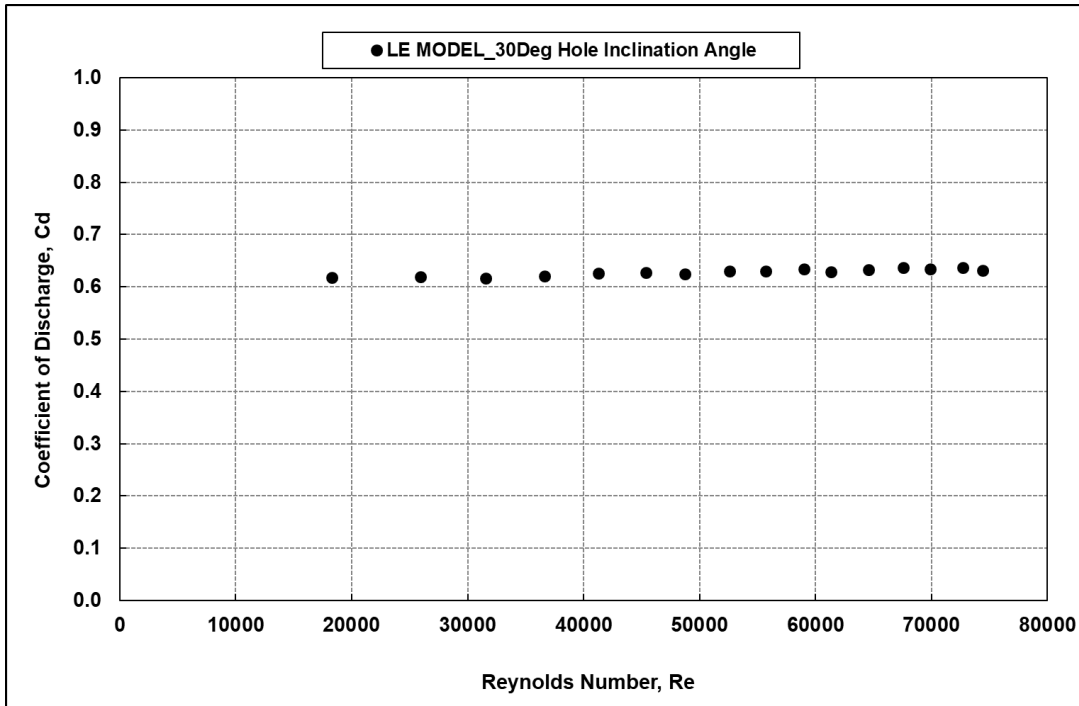


Fig. I.6 Coolant Cd Vs. Coolant Reynolds number for a 30° hole Inclination angle model

Table I.4 shows the coolant mass flow data measured for a 30° hole inclination angle test model using the orifice flow meter. Fig. I.7 shows the variation of mass flow through the film cooling holes as a function of coolant plenum pressure and Fig. I.8 shows the variation of Cd with the coolant flow Reynolds number. The average Cd value for this model is found as 0.63.

Table I.4 Coolant flow hole Cd for a 35° hole Inclination angle model

LE MODEL_35Deg Hole Inclination Angle											
04-12-13	Pcha (mm of H ₂ O)	Delta P (mm of H ₂ O)	Pup (mm of Hg)	W actual (kg/hr)	PCha (N/m ²)	Vcalc (m/s)	Wtheory (kg/hr)	Cd	Mass flow/unit area (Kg/m ² s)	Re	Vact (m/s)
	25.03	113.49	38.19	34.60	245.53	21.62	56.23	0.62	90.65	18130.03	13.30
	50.68	228.34	82.00	50.55	497.14	30.76	80.02	0.63	132.44	26488.90	19.43
	75.79	321.84	101.83	60.80	743.40	37.61	97.85	0.62	159.27	31854.66	23.37
	100.04	413.11	142.70	70.66	981.32	43.21	112.42	0.63	185.11	37021.45	27.16
	125.73	515.57	162.39	79.87	1233.32	48.45	126.03	0.63	209.25	41850.49	30.70
	151.12	593.14	202.76	87.70	1482.38	53.11	138.18	0.63	229.76	45951.35	33.71
	175.20	674.91	209.67	93.91	1718.54	57.19	148.77	0.63	246.04	49208.12	36.10
	200.77	757.73	255.05	102.02	1969.41	61.22	159.26	0.64	267.27	53453.34	39.21
	225.02	842.07	259.15	107.78	2207.29	64.81	168.61	0.64	282.36	56472.95	41.43
	249.92	906.27	292.44	113.78	2451.54	68.30	177.69	0.64	298.08	59615.66	43.73
	273.48	971.12	300.14	118.24	2682.60	71.45	185.88	0.64	309.78	61955.45	45.45
	300.26	1047.42	341.95	125.39	2945.29	74.87	194.77	0.64	328.51	65701.20	48.20
	325.06	1128.76	350.92	130.74	3188.61	77.90	202.65	0.65	342.52	68503.44	50.26
	349.88	1163.19	376.23	134.34	3432.03	80.82	210.24	0.64	351.94	70388.67	51.64
	375.56	1249.91	391.79	140.28	3683.93	83.73	217.82	0.64	367.51	73501.19	53.92
	399.80	1284.70	398.95	142.69	3921.76	86.39	224.75	0.63	373.83	74765.40	54.85
Average Cd Value:								0.635			

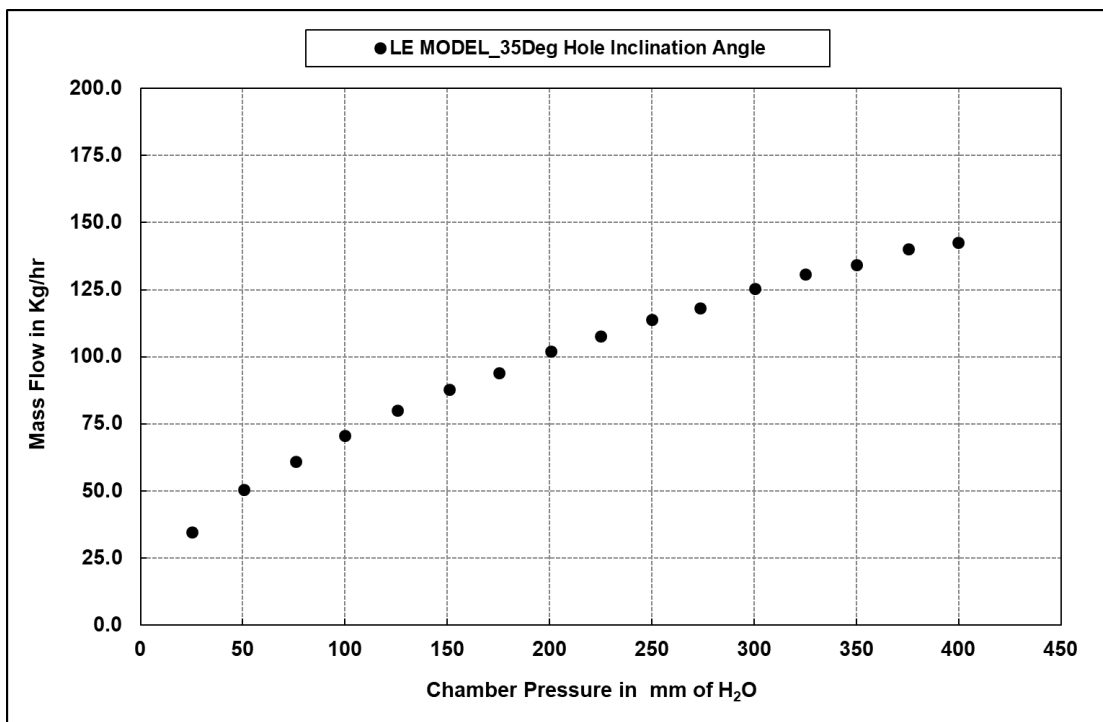


Fig. I.7 Mass flow Vs. Coolant chamber pressure for a 35° hole Inclination angle model.

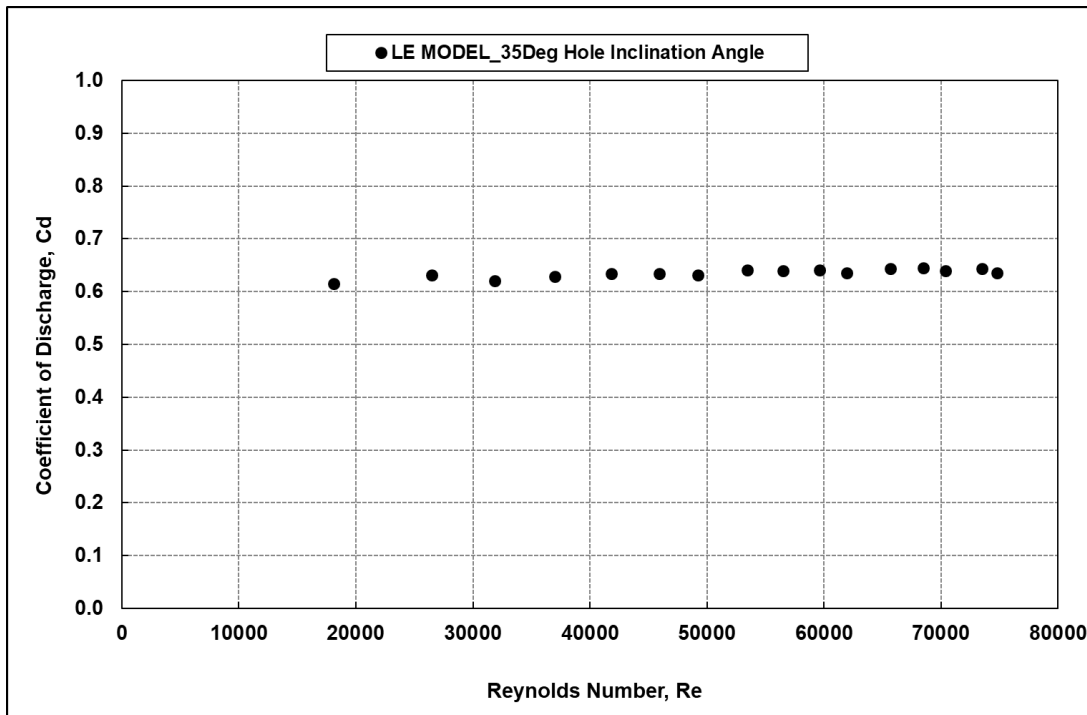


Fig. I.8 Coolant Cd Vs. Coolant Reynolds number for a 35° hole Inclination angle model

Table I.5 shows the coolant mass flow data measured for Circular Holes test model using the orifice flow meter. Fig. I.9 shows the variation of mass flow through the film cooling holes as a function of coolant plenum pressure and Fig. I.10 shows the variation of Cd with the coolant flow Reynolds number. The average Cd value for this model is found as 0.68.

Table I.5 Coolant flow hole Cd for Circular Holes Model

CHM_4mmHD, 21mmPitch_30HA											
08-04-14	Pcha (mm of H ₂ O)	Delta P (mm of H ₂ O)	Pup (mm of Hg)	W actual (kg/hr)	PCha (N/m ²)	Vcalc (m/s)	Wtheory (kg/hr)	Cd	Mass flow/unit area (Kg/m ² s)	Re	Vact (m/s)
	25.00	31.02	40.00	18.11	245.23	20.44	27.13	0.67	16.02	2562.42	13.65
	50.60	59.17	81.00	25.72	496.35	29.07	38.59	0.67	22.74	3638.37	19.38
	75.00	84.20	116.60	31.39	735.70	35.40	46.98	0.67	27.75	4440.58	23.65
	100.02	108.21	154.20	36.41	981.13	40.88	54.26	0.67	32.20	5151.54	27.43
	125.00	132.19	187.32	41.04	1226.16	45.70	60.65	0.68	36.29	5805.66	30.92
	150.06	153.65	220.73	45.09	1471.98	50.07	66.46	0.68	39.87	6378.61	33.97
	175.00	170.90	249.20	48.30	1716.63	54.07	71.77	0.67	42.70	6832.66	36.39
	200.49	192.57	282.73	52.18	1966.67	57.87	76.82	0.68	46.14	7382.66	39.32
	225.00	200.36	313.50	54.07	2207.09	61.31	81.38	0.66	47.81	7649.86	40.74
	250.85	230.42	343.72	58.86	2460.66	64.73	85.92	0.69	52.05	8327.52	44.35
	275.03	249.55	372.50	62.11	2697.85	67.78	89.97	0.69	54.92	8787.27	46.80
	300.08	259.55	401.27	64.21	2943.60	70.80	93.98	0.68	56.77	9083.25	48.37
Average Cd Value:								0.68			

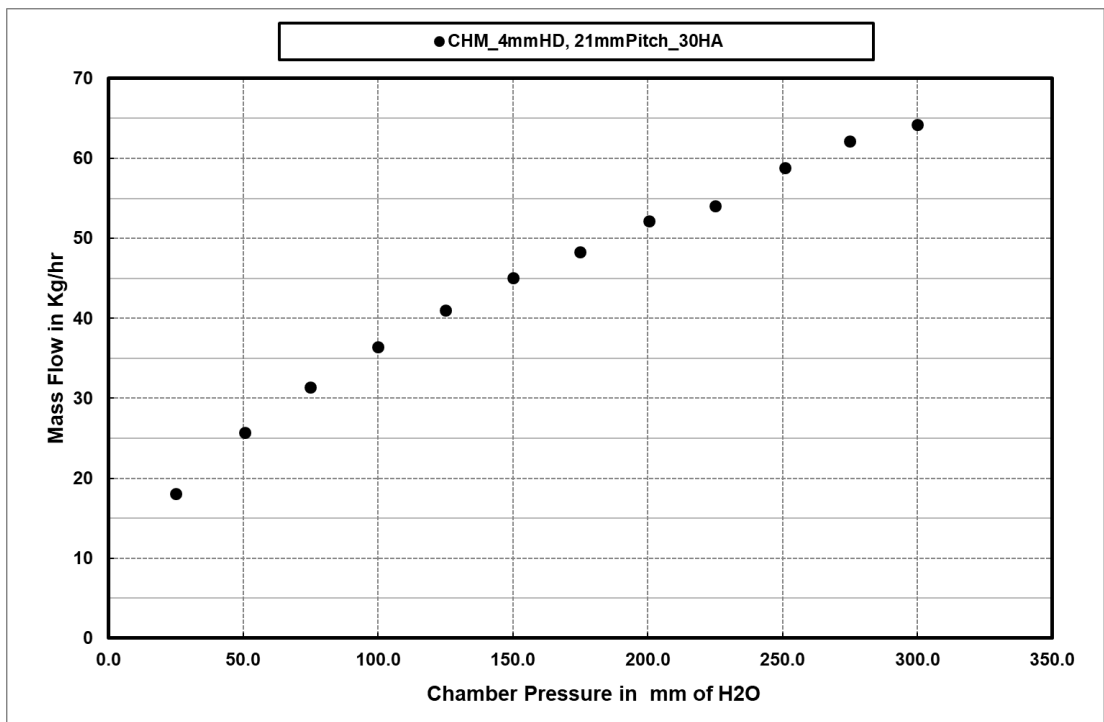


Fig. I.9 Mass flow Vs. Coolant chamber pressure for Circular Hole model

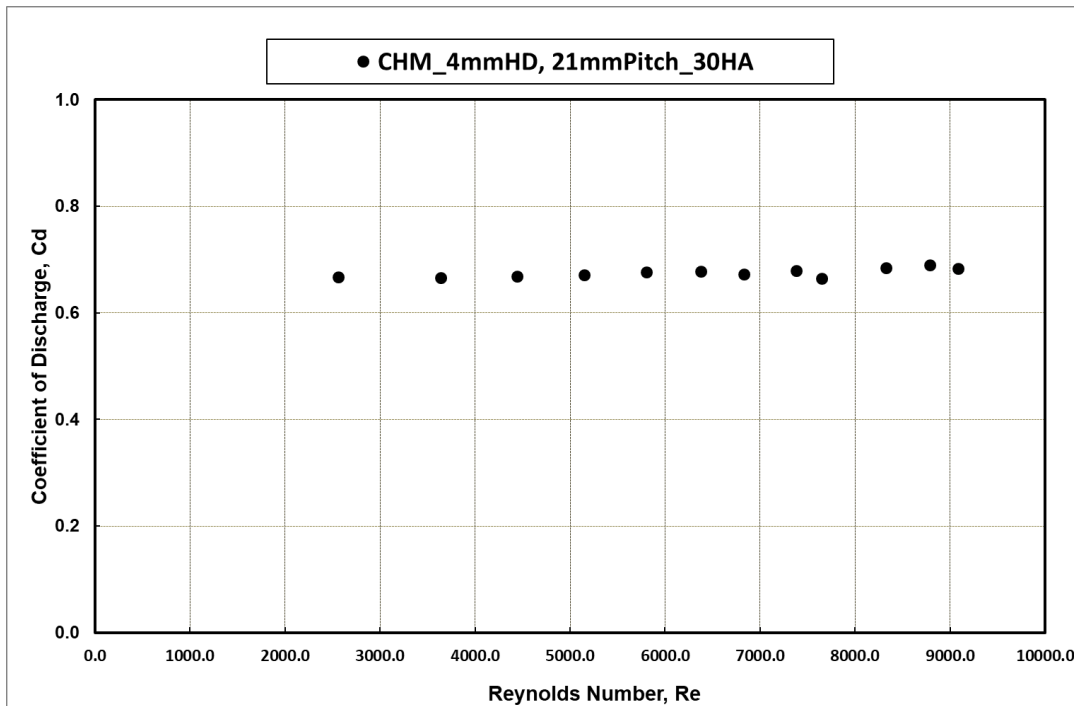


Fig. I.10 Coolant Cd Vs. Coolant Reynolds number for Circular Hole Model

Table I.6 shows the coolant mass flow data measured for Fan Shaped Holes test model using the orifice flow meter. Fig. I.11 shows the variation of mass flow through the film cooling holes as a function of coolant plenum pressure and Fig. I.12 shows the variation of Cd with the coolant flow Reynolds number. The average Cd value for this model is found as 0.83.

Table I.6 Coolant flow hole Cd for Fan Shaped Holes Model

Fan Shaped Hole Model_4mmHD, 21mmPitch_30HA											
27-05-14	Pcha (mm of H ₂ O)	Delta P (mm of H ₂ O)	Pup (mm of Hg)	W actual (kg/hr)	PCha (N/m ²)	Vcalc (m/s)	Wtheory (kg/hr)	Cd	Mass flow/unit area (Kg/m ² s)	Re	Vact (m/s)
	25.030	47.685	12.570	22.025	245.527	20.448	27.141	0.811	19.475	3115.922	16.594
	50.780	93.540	24.050	31.103	498.116	29.126	38.659	0.805	27.501	4400.118	23.433
	75.120	145.684	36.740	39.164	736.875	35.425	47.020	0.833	34.628	5540.522	29.506
	100.530	188.176	47.610	44.846	986.129	40.981	54.394	0.824	39.653	6344.470	33.787
	125.850	226.607	56.720	49.520	1234.500	45.852	60.859	0.814	43.786	7005.704	37.309
	150.280	273.328	69.130	54.842	1474.142	50.105	66.505	0.825	48.491	7758.622	41.318
	175.210	312.120	78.320	58.963	1718.687	54.101	71.809	0.821	52.135	8341.631	44.423
	200.770	359.280	90.390	63.763	1969.413	57.913	76.869	0.830	56.379	9020.607	48.039
	226.030	401.637	100.750	67.869	2217.196	61.449	81.561	0.832	60.009	9601.449	51.132
	250.410	437.140	109.770	71.213	2456.347	64.678	85.847	0.830	62.966	10074.523	53.652
	275.560	473.333	119.120	74.539	2703.051	67.848	90.055	0.828	65.907	10545.163	56.158
	300.230	524.180	132.700	79.105	2945.046	70.820	94.000	0.842	69.944	11191.010	59.598
	325.490	555.210	139.750	81.765	3192.829	73.739	97.875	0.835	72.296	11567.334	61.602
	350.520	596.488	150.030	85.279	3438.356	76.522	101.568	0.840	75.404	12064.565	64.250
	375.840	631.404	159.710	88.250	3686.727	79.238	105.173	0.839	78.030	12484.819	66.488
	400.430	681.310	171.900	92.334	3927.938	81.789	108.559	0.851	81.641	13062.629	69.565
Average Cd Value:								0.829			

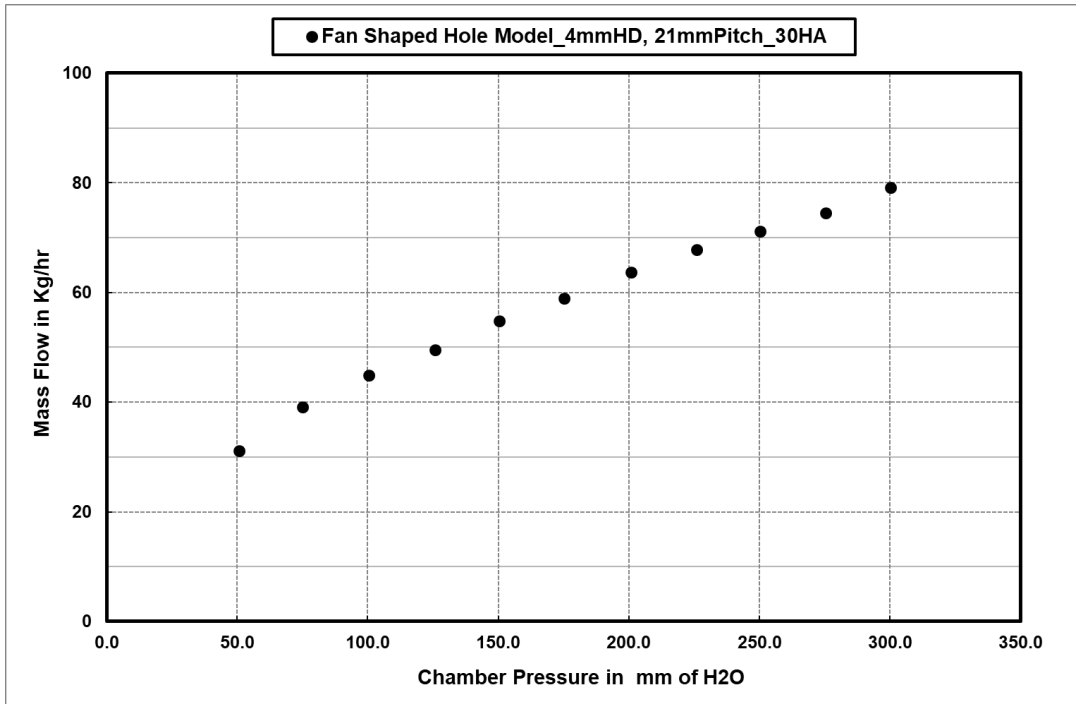


Fig. I.11 Mass flow Vs. Coolant chamber pressure for Fan Shaped Hole Model

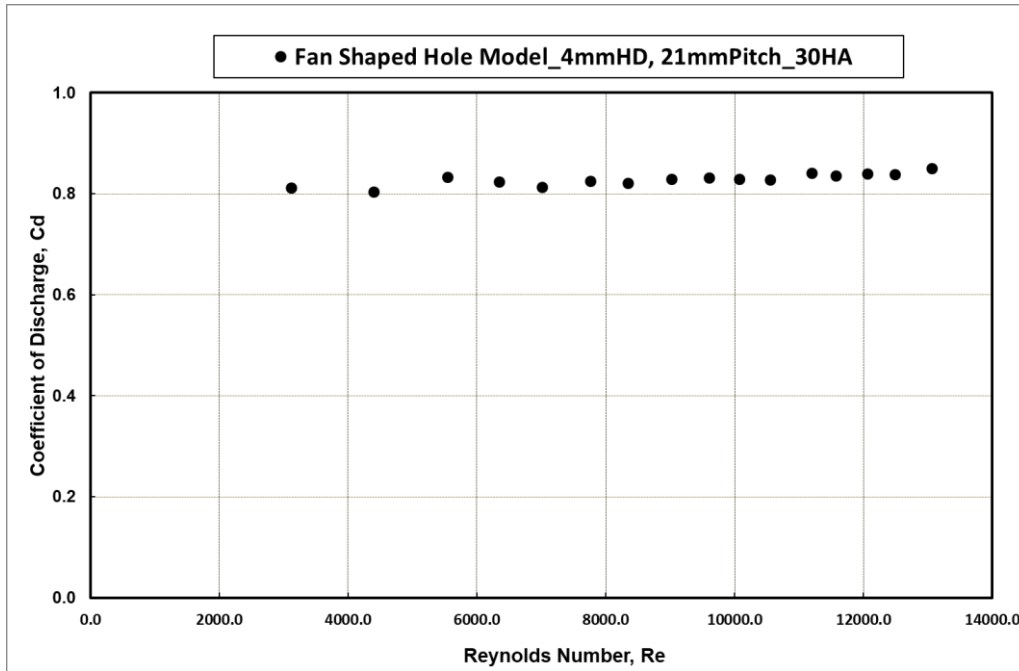


Fig. I.12 Coolant Cd Vs. Coolant Reynolds number for Fan Shaped Hole Model

Table I.7 shows the coolant mass flow data measured for 0 and 45° hole orientation angle test model using the orifice flow meter. Fig. I.13 shows the variation of mass flow through the film cooling holes as a function of coolant plenum pressure and Fig. I.14 shows the variation of Cd with the coolant flow Reynolds number. The average Cd value for this model is found as 0.57.

Table I.7 Coolant flow hole Cd for 0 and 45° Hole Orientation Angle Model

LE Model 1_0 & 45 Deg Hole Orientation Angle											
04-04-13	Pcha (mm of H ₂ O)	Delta P (mm of H ₂ O)	Pup (mm of Hg)	W actual (kg/hr)	PCha (N/m ²)	Vcalc (m/s)	Wtheory (kg/hr)	Cd	Mass flow/unit area (Kg/m ² s)	Re	Vact (m/s)
	27.500	44.700	9.500	5.189	269.756	21.434	9.602	0.540	13.596	2719.127	11.585
	49.700	83.000	17.100	7.110	487.522	28.814	12.908	0.551	18.628	3725.591	15.872
	74.400	126.000	25.800	8.815	729.812	35.255	15.793	0.558	23.094	4618.859	19.678
	102.700	174.300	34.800	10.434	1007.415	41.420	18.555	0.562	27.335	5467.007	23.292
	126.400	213.600	42.300	11.611	1239.896	45.952	20.585	0.564	30.419	6083.704	25.919
	151.700	255.700	50.500	12.776	1488.071	50.341	22.551	0.567	33.470	6693.975	28.519
	174.300	290.000	57.500	13.671	1709.761	53.961	24.173	0.566	35.814	7162.896	30.517
	201.400	336.700	66.100	14.816	1975.593	58.004	25.984	0.570	38.815	7762.985	33.073
	226.000	375.300	73.600	15.720	2216.902	61.445	27.525	0.571	41.185	8236.987	35.093
	251.900	417.500	82.000	16.673	2470.963	64.870	29.060	0.574	43.680	8736.035	37.219
	274.700	447.900	88.100	17.338	2694.615	67.742	30.346	0.571	45.423	9084.647	38.704
	299.100	487.500	95.900	18.180	2933.962	70.687	31.665	0.574	47.629	9525.742	40.583
	323.000	521.000	102.100	18.869	3168.404	73.457	32.906	0.573	49.434	9886.866	42.122
	350.900	561.500	111.000	19.700	3442.083	76.563	34.298	0.574	51.611	10322.188	43.977
	375.600	599.100	118.100	20.440	3684.373	79.212	35.484	0.576	53.550	10709.938	45.629
	401.900	639.700	126.100	21.227	3942.358	81.939	36.706	0.578	55.611	11122.215	47.385
Average Cd Value:								0.567			

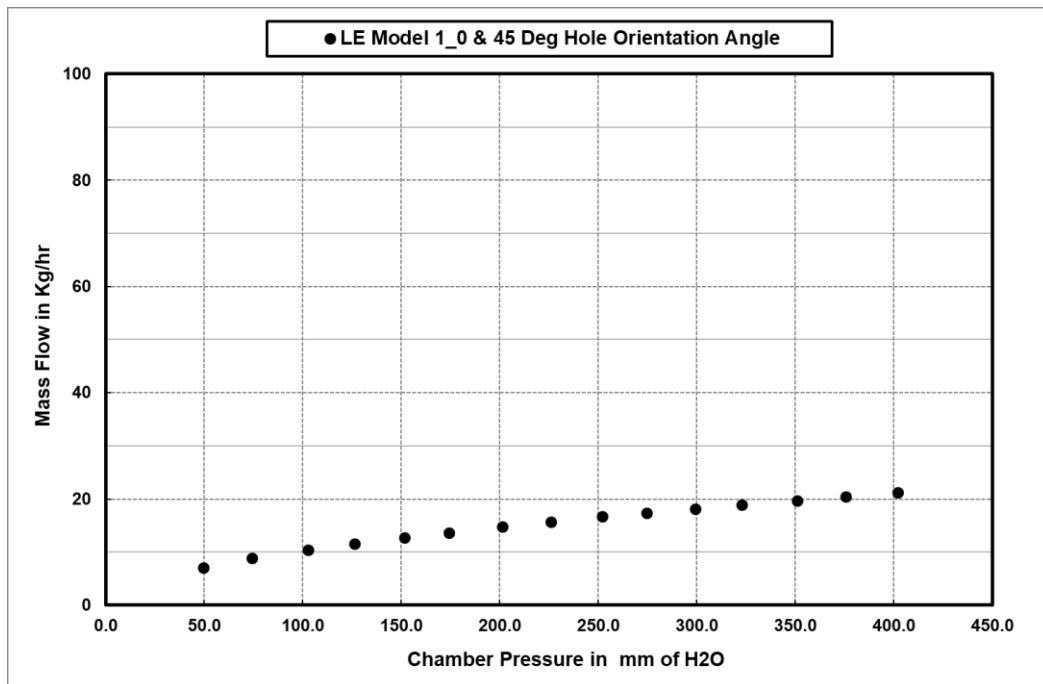


Fig. I.13 Mass flow Vs. Coolant chamber pressure for 0 and 45° Hole Orientation Angle model

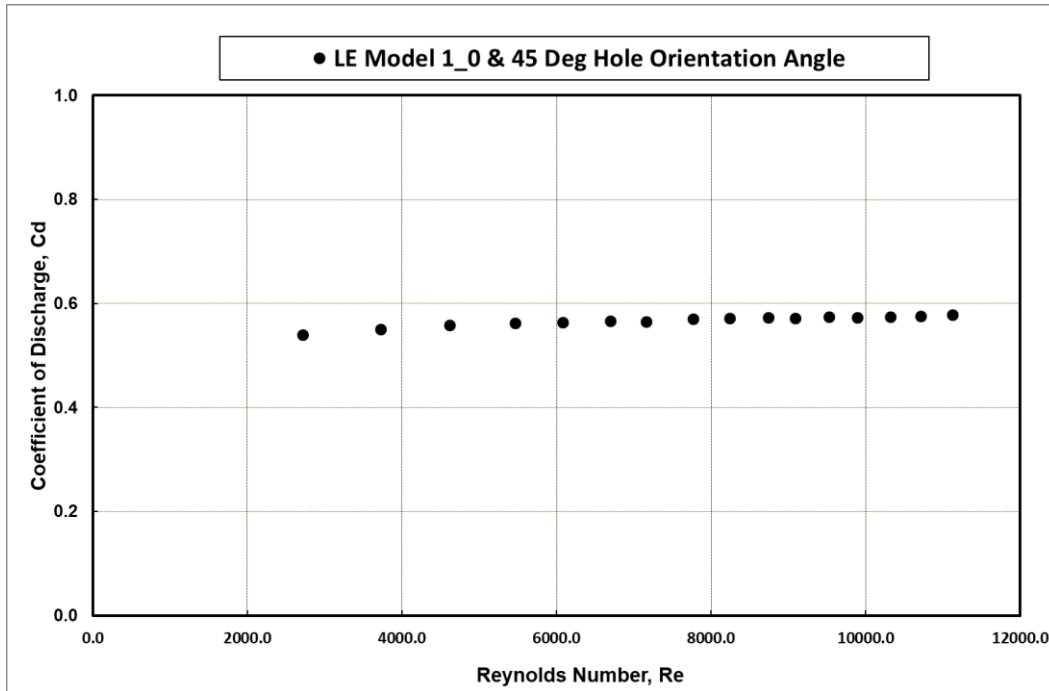


Fig. I.14 Coolant Cd Vs. Coolant Reynolds number for 0 and 45° Hole Orientation Angle model

Table I.8 shows the coolant mass flow data measured for 15 and 30° hole orientation angle test model using the orifice flow meter. Fig. I.15 shows the variation of mass flow through the film cooling holes as a function of coolant plenum pressure and Fig. I.16 shows the variation of Cd with the coolant flow Reynolds number. The average Cd value for this model is found as 0.86.

Table I.8 Coolant flow hole Cd for 15 and 30° Hole Orientation Angle Model

LE Model 2_15 & 30 Deg Hole Orientaion Angle											
15-03-13	Pcha (mm of H ₂ O)	Delta P (mm of H ₂ O)	Pup (mm of Hg)	W actual (kg/hr)	PCha (N/m ²)	Vcalc (m/s)	Wtheory (kg/hr)	Cd	Mass flow/unit area (Kg/m ² s)	Re	Vact (m/s)
	25.600	21.500	5.600	3.589	251.118	20.680	4.323	0.830	7.253	2417.730	17.167
	51.400	43.600	11.100	5.131	504.198	29.303	6.126	0.838	10.370	3456.741	24.545
	75.900	65.400	16.300	6.308	744.526	35.608	7.444	0.847	12.749	4249.523	30.174
	101.900	87.200	21.700	7.312	999.568	41.259	8.625	0.848	14.778	4925.917	34.977
	126.500	111.700	27.100	8.308	1240.876	45.970	9.610	0.864	16.790	5596.546	39.739
	149.300	130.200	31.500	8.997	1464.528	49.941	10.440	0.862	18.183	6061.025	43.037
	176.600	155.500	37.200	9.872	1732.322	54.316	11.355	0.869	19.951	6650.257	47.221
	201.400	176.500	42.300	10.554	1975.593	58.004	12.126	0.870	21.331	7110.240	50.487
	224.800	196.900	47.100	11.185	2205.131	61.281	12.811	0.873	22.604	7534.823	53.502
	248.900	214.300	51.400	11.703	2441.535	64.483	13.480	0.868	23.652	7883.910	55.981
	276.400	238.100	57.400	12.386	2711.291	67.951	14.205	0.872	25.033	8344.194	59.249
	299.200	257.900	61.500	12.927	2934.943	70.699	14.780	0.875	26.125	8708.320	61.835
	326.800	282.600	67.200	13.583	3205.679	73.887	15.446	0.879	27.452	9150.770	64.976
	351.100	299.200	71.600	14.018	3444.045	76.585	16.010	0.876	28.330	9443.376	67.054
	374.800	320.200	77.200	14.555	3676.526	79.128	16.542	0.880	29.416	9805.485	69.625
	403.800	344.100	82.100	15.137	3960.995	82.132	17.170	0.882	30.593	10197.681	72.410
Average Cd Value:								0.865			

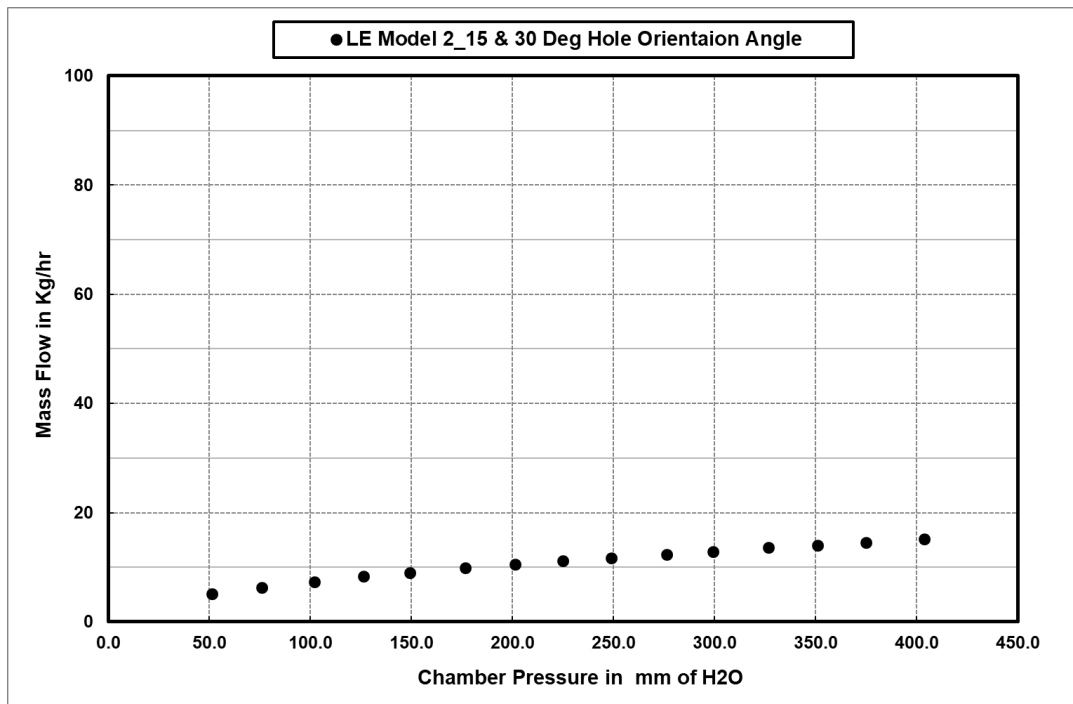


Fig. I.15 Mass flow Vs. Coolant chamber pressure for 15 and 30° hole Orientation angle model

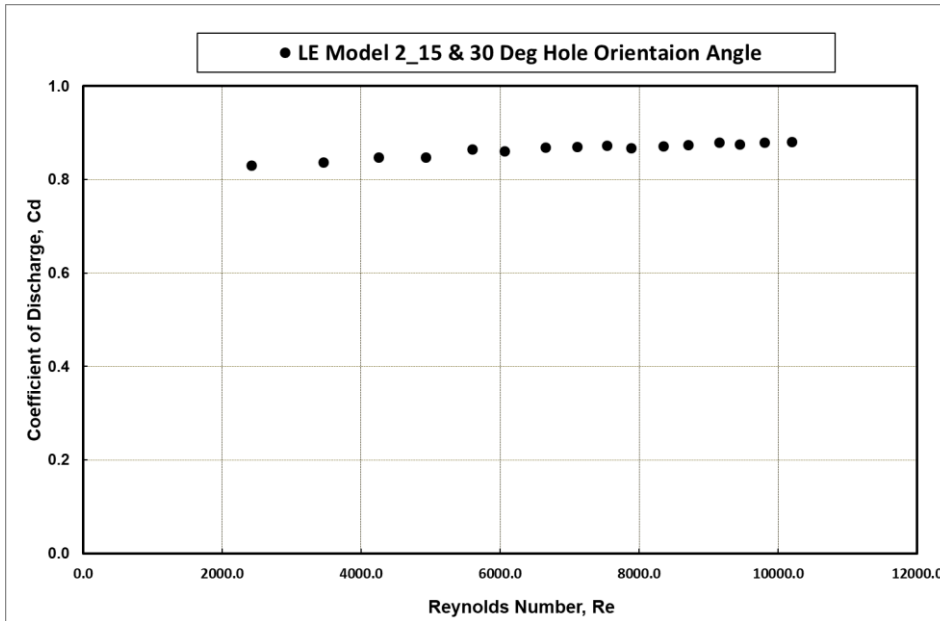


Fig. I.16 Coolant Cd Vs. Coolant Reynolds number for 15 and 30° hole Orientation angle model

The hole coefficient of discharge values was found for all the considered models. The Cd values were found to be marginal increase with the increase in hole inclination angle and with the increase in hole locational orientation and hole exit shape area the cd values were found increasing at a greater value.

I.2 Mainstream mass flow measurements

The main flow orifice equation is arrived based on the BIS standards reference IS15675:2006 is,

$$\dot{m} = 5.472964717 * \sqrt{(P_{up1} - P_{down}) * (P_{up2} + 680)}$$

Where,

Mainstream flow orifice diameter = 119.78 mm.

P_{up1} = Upstream pressure in mm of H₂O = 680 mm of H₂O

P_{up2} = Upstream pressure in mm of Hg = 50 mm of Hg

P_{down} = Downstream pressure in mm of H₂O = -408 mm of H₂O

Mainstream mass flow, $\dot{m} = 4877.514$ kg/hr i.e. 1.35 Kg/s

Appendix – II

II CONDUCTION LOSS MEASUREMENTS

The conduction loss data of the non-contact side of test models is found separately for all the considered models, and these loss values are accounted for the accurate heat transfer coefficient calculations. For the generation of conduction loss, the leading edge models are insulated with glass wool material to avoid the heat loss from the model. Experiments are carried out by supplying the electric current to test model through a copper bus bars, and copper bus bars are attached to the S.S sheet wound on the leading edge model. The thin stainless steel sheet with the hole geometries wound on the test model surface is heated with the constant heat flux conditions by connecting the brass bus bars in series to supply the high current at a low voltage over the model.

From the Fig. II.1 and Fig. II.2, it shows that when the voltage increases the heat loss in plate also increases for the considered two models. And this linear conduction loss is accounted in the heat transfer coefficient distribution calculations.

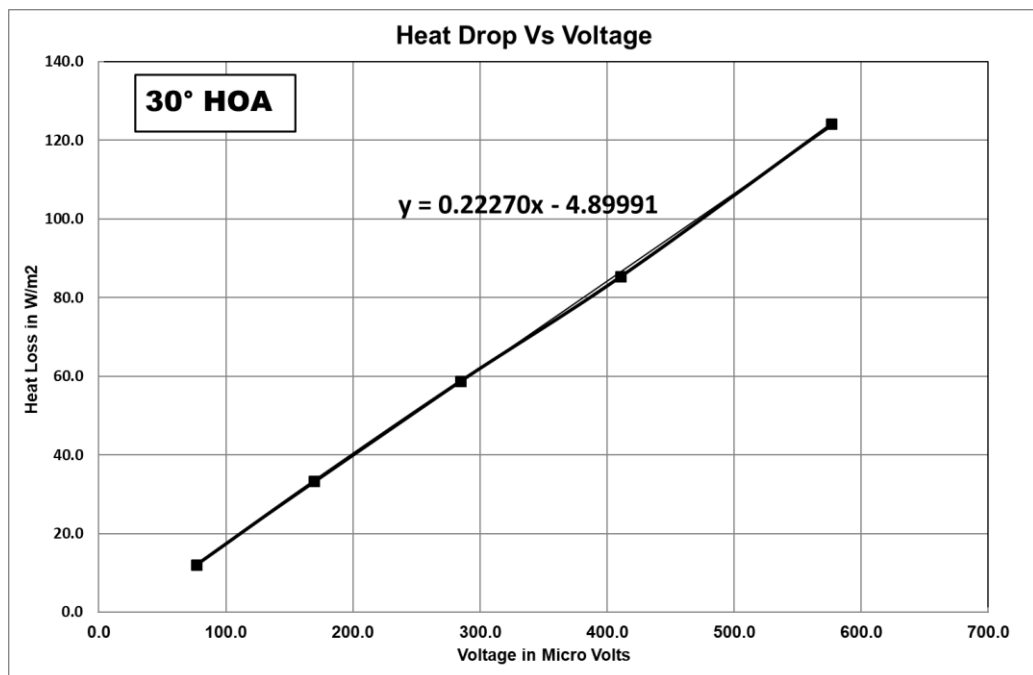


Fig. II.1 Heat Loss vs. Voltage for 30° HOA Model

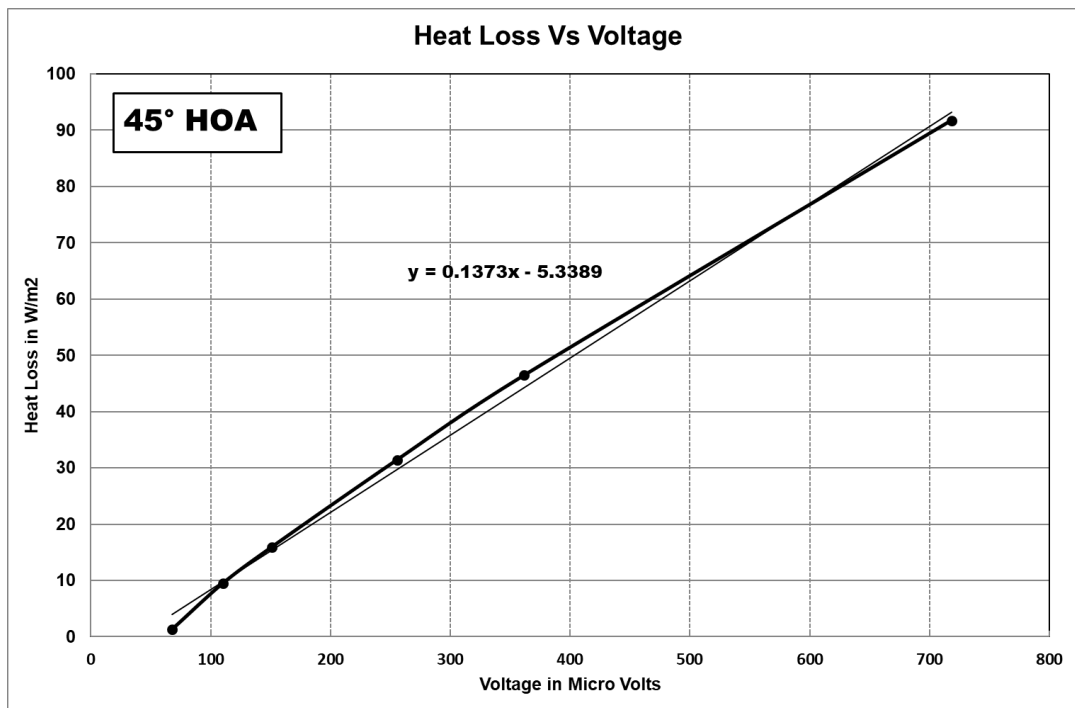


Fig. II.2 Heat Loss Vs. Voltage for 45° HOA Model

II.1 Voltage Versus Current Measurements

Voltage versus current experiments is carried out for both models. Electric wires are soldered between holes at the known distances. From Fig. II.3 and Fig. II.4 it is found current is increased with supplying voltage, and the linear equation is found to calculate the current from the applied voltage. This product of voltage and current is used to find the gross heat input to the test surface during the heat transfer coefficient experiments.

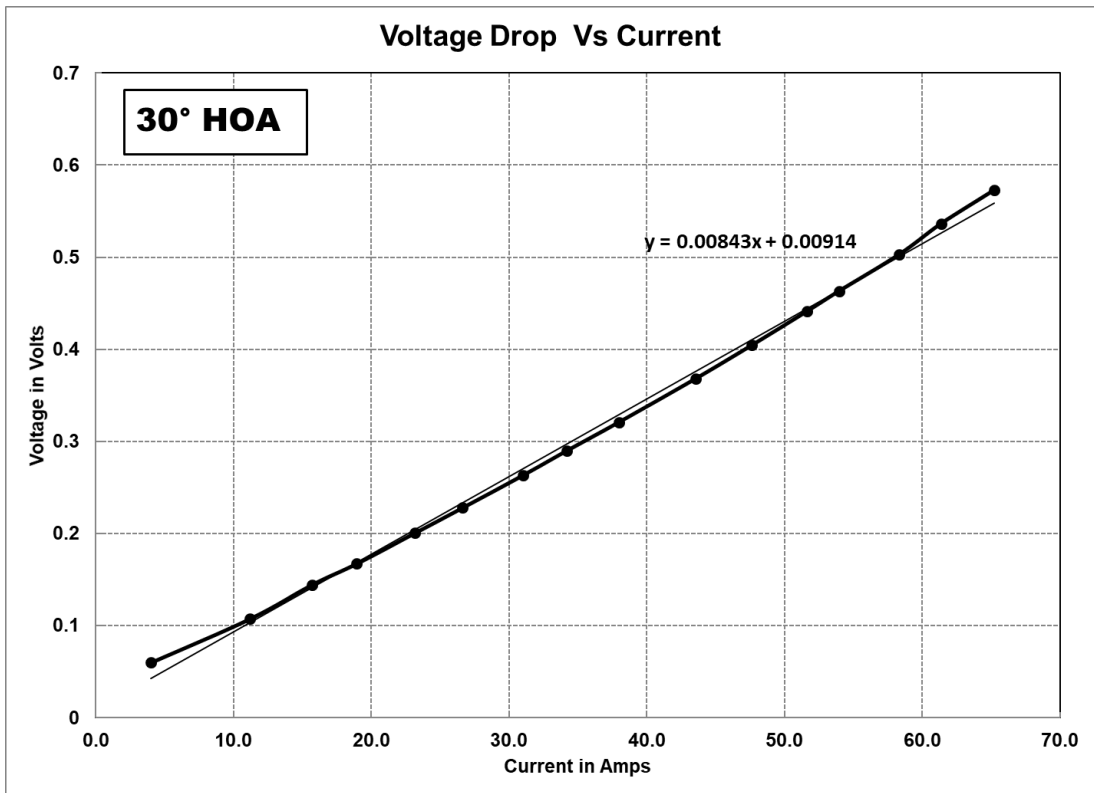


Fig. II.3 Voltage Drop Vs. Current for 30° HOA Model

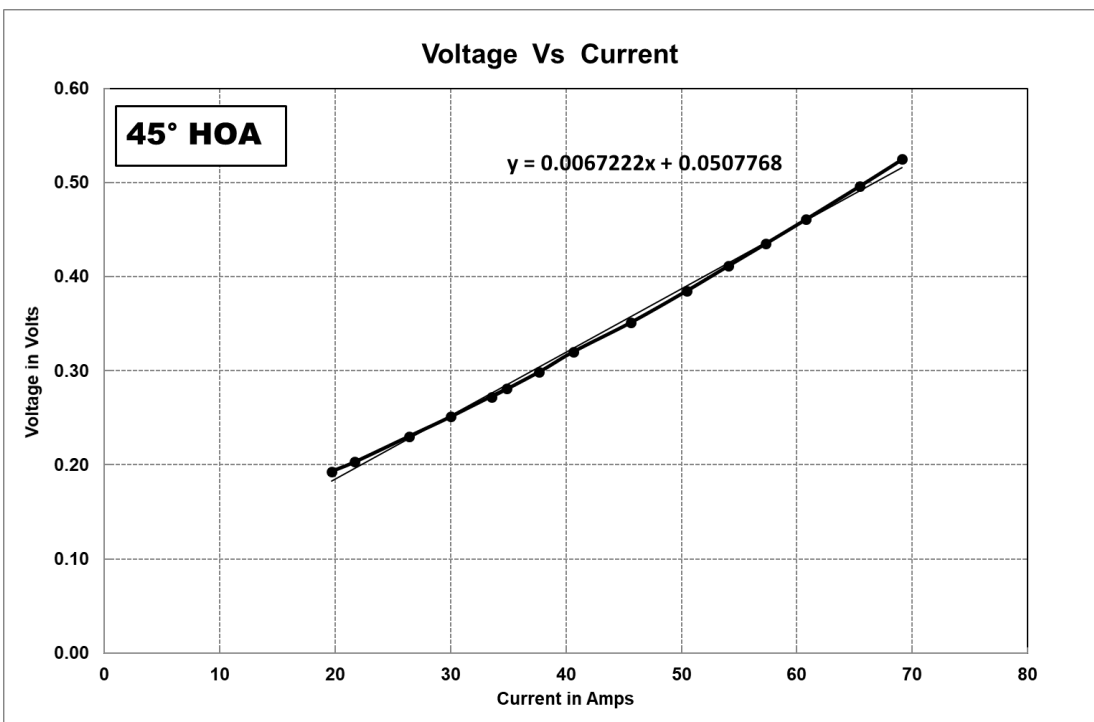


Fig. II.4 Voltage Drop Vs. Current for 45° HOA Model

Appendix-III

III INFRA-RED THERMAL CAMERA CALIBRATION

A long wavelength Infrared thermographic system (M/s Flir make A655sc) is used for the non-contact type surface temperature measurements of the test surfaces. The photographic view of the Infrared camera is shown in the Fig. III.1. The A655sc thermal camera is equipped with an uncooled, maintenance free, Vanadium Oxide (VoX) microbolometer detector that produces thermal images of 640 x 480 Pixels. These pixels generate crisp and clear detailed images that are easy to interpret with high accuracy. The FLIR A655sc will make temperature differences as small as 50 mK visible. This infrared thermography system is a high-resolution science grade LWIR camera, has the spectral range of 7.5 to 14.0 μm . The camera has several temperatures ranges between -40 °C and up to 2000 °C. The camera has set at a range 1 of -40° C to 150 °C with the accuracy of ± 2 °C over the full-scale measurement. The accuracy of the camera measurement temperature is ± 2 °C over the full-scale measurement. This camera helps to see and accurately quantify heat patterns, leakage, dissipation, and other heat-related factors in equipment, products, and processes in real time. The images captured by IR camera are recorded and saved to a computer using FLIR Research IR software. The transparent window was so selected that it allows the infrared radiation in the spectral band of the IR camera. The test surface is viewed using an IR camera, through this transparent window of thin polyurethane sheet of thickness at five μm and it has a very little effect on IR transmissivity.



Fig. III.1 Infra Red Thermal Camera A 655sc

During the experiments, the test model was viewed through a window of a thin polyurethane sheet. The test model has a curved surface. One of the important parameters, which influences the radiation measurement is the emissivity of the surface. To ensure that the surface has a uniform emissivity, the surface was painted with black paint. However, because of the surface curvature, the viewing angle varies for a fixed camera position. As this can result in emissivity variation (specular emissivity), it was necessary to evaluate its effect on the thermographic system calibration. Also, the presence of the window with specific transmission characteristics and the re-radiation from the tunnel walls need the calibration of the infrared thermographic system in the presence of the viewing window in the tunnel. For this purpose, a hollow cylindrical test piece with small wall thickness was fabricated. Thermocouples were fixed at 4 locations 0° , 30° , 60° and 90° from the stagnation line to measure the local surface temperature. The thermocouple output was connected to a data logger for recording. The model was cooled to different temperatures by supplying cold air to the cylinder. To prevent ice formation on the outer surface, the mainstream flow was established with low velocity. The test model was viewed by the thermographic system through the window. The thermographic system was so oriented that all the four thermocouples were visible in the thermogram. The surface temperature was set at various levels, and the thermogram and surface thermocouple temperatures were recorded. From the analysis of the thermogram, the thermographic system output at the pixels corresponding to the

location of the thermocouples was extracted and are plotted against the temperature measured by the thermocouples to identify the variation in thermographic system output due to the specular emissivity effect. The results indicated that for the selected camera viewing angle the effect of the surface radius of curvature on the system output is small. The data suggest that a single calibration curve can be fit through the measurement point which can be used for evaluating the surface temperature over the entire surface.

A number of factors influence the radiation intensity reaching the IR camera. The major parameters are the transmissivity of the window material, window temperature, the reflected radiation from the tunnel wall. Hence, the thermographic system output can be considered as the sum of actual radiation from the viewed source and background radiation. The thermographic system needs to be calibrated for the required temperature range of measurement with the similar geometrical model. Accordingly, the calibration of the system is carried out, and the calibration curves are generated for the maintained known temperature values. The temperature of the test plate is maintained at the range of requirement by electrical heating. The calibrated thermocouples having an accuracy of ± 0.36 °C are used for maintaining the temperature over the test surface. Aluminum stickers are used for identifying the thermocouples over the acquired thermal images. The system raw count output versus temperature curves are generated as a calibration equation. These equations are used for correcting the images in the actual run cases.

The estimated values from the in-situ calibration are used to correct the measured values in the test runs to estimate temperature from the system output. The in-situ calibration is carried out for all the test models by incorporating the calibrated thermocouples over the test surface. These thermocouple values are used for correcting the images for the actual values. A similar procedure is adopted in both the cooling effectiveness and heat transfer coefficient experiments to evaluate the local temperature. The temperature recorded by the thermocouples attached to the model was used as a reference to estimate the background radiation correction to be applied

to the thermogram pixel data to estimate the corrected system output for estimating the surface temperature from the calibration curve. From the thermogram, the pixels corresponding to the location of the thermocouples were identified, and the system output for those pixels was extracted. Based on the measured thermocouple temperatures, the system output was estimated from the calibration data. The difference between the measured and estimated value gives the background correction required. The average value of correction was estimated and the thermogram pixel data were corrected using that before estimating the temperature using the calibration curve.

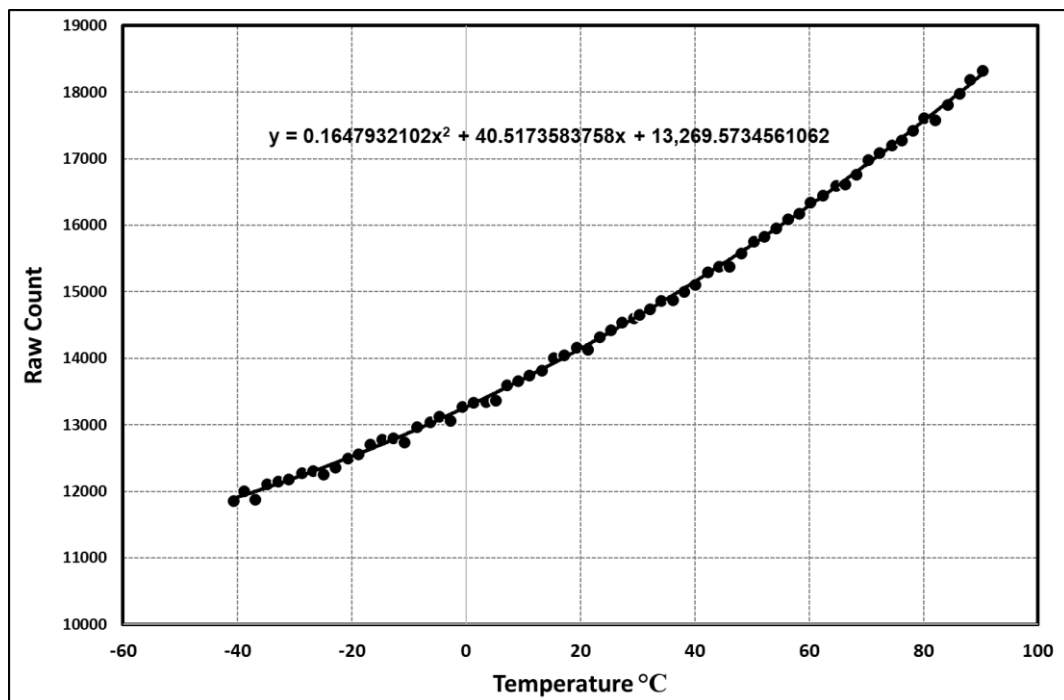


Fig. III.2 Calibration curve to convert temperature to raw counts

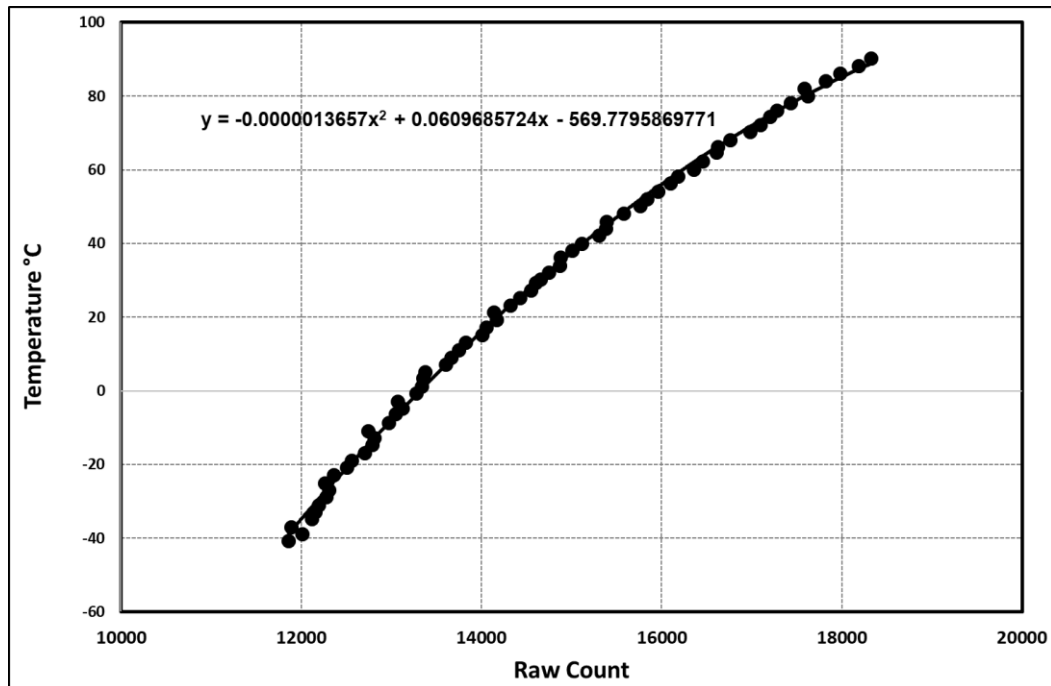


Fig. III.3 Calibration curve to convert raw counts to temperature

Fig. III.2 shows the calibration curve for estimating the thermographic system output in raw count as a function of temperature. In this, the measured data from all the thermocouples is used. This curve was used for estimating the system output corresponding to the temperature measured by the thermocouples and was used to calculate the background radiation correction. Fig. III.3 shows the best fit relation for the temperature range of $-40\text{ }^{\circ}\text{C}$ to $90\text{ }^{\circ}\text{C}$ as a function of thermographic system output. Using this calibration curve, the corrected thermogram pixel data is converted to temperature for finding out the correct surface temperature over the test model. These surface temperature values are used for finding out the cooling effectiveness and heat transfer coefficient values

Appendix IV

IV UNCERTAINTY MEASUREMENTS

The instruments used in the experiments for the data acquisition and monitoring of the flow parameters are shown in the Table IV.1. The details of specifications, range, accuracy, and resolution values are shown in the table for all the instruments. All the instruments are calibrated using the standard calibrating of primary and secondary sources before using in the experiments.

Table IV.1 Range, Resolution and Accuracy of the Instruments

Sl. No.	Name of Instrument	Specifications & Range	Accuracy & Resolution	Nos. Used
1	Intelligent Pressure Scanner (Model: 9116, Pressure System)	Measurement Range: 10 Inches of Water Column to 10 PSID. No. of Channels: 16 Operating temperature: 0 to 50 °C	Accuracy: $\pm 0.05\%$ of FS Resolution: 0.01 Inch of water column	01 No.
2	Fluke Temp. Data Acquisition System (Model: 2680 A)	No. of Channels: 80 Channels	Accuracy: ± 0.75 °C Resolution: 0.01 °C	01 No.
3	FLIR Make A655sc InfraRed Camera	Measurement Temperature range: -40 to 2000 °C (In Four Ranges)	Accuracy: ± 2 °C Resolution: 0.001 °C	01 No.
4	K – Type Thermocouples	Omega make, -200 to 1260 °C	Accuracy: ± 0.36 °C Resolution: 0.01 °C	12 Nos.
5	Pressure Gauges	Omega make, 0-14 Bar	Accuracy: ± 0.2 Bar Resolution: 0.02 Bar	04 Nos.

The uncertainty estimates are determined using the methodology proposed by J. P. Holman (2012). Uncertainty in the calculation comes from the measurement of

mainstream and coolant pressures, temperatures, and test surface infra-red wall temperatures measurements. The calibrated pressure sensors and thermocouples are used for maintaining the flow parameters as per the requirement. The temperatures are measured using type K thermocouples with the uncertainty of ± 0.36 °C. The measurement system (FLUKE 2680A data acquisition system temperature scanner) has an overall absolute accuracy of ± 0.75 °C. Hence, the overall uncertainty on the temperature measurement is approximately 1.1 °C. This uncertainty is dependent upon the thermocouple calibration procedure. Uncertainty in the test surface wall temperature measured by the IR camera is ± 2 °C. Some uncertainty also gets involved during calibration of thermal images. This happens due to uncertainty in determining the exact locations of thermocouples concerning pixel values used for calibration. Pressure Net scanner uncertainty is $\pm 0.05\%$ of the measured pressure, and this uncertainty is dependent upon the pressure transducer calibration procedure. All the instruments used in the experiments are calibrated with the standard calibrating of primary and secondary sources. Orifice mass flow meters are used for coolant and mainstream mass flow data acquisition.

Cooling effectiveness is found for the effusion cooled test plates by varying the flow parameters at different geometrical parameters of cooling holes. The flow parameters varied are density ratio (Coolant and mainstream temperatures variation), blowing ratio (coolant and mainstream pressures variation) and Reynolds number (coolant and mainstream pressures variation). Hence, the uncertainty in the pressure and the temperature measurements has a strong impact on the cooling effectiveness accuracy. The uncertainties in the blowing ratios, density ratios, Reynolds numbers and thereby the uncertainty of cooling effectiveness and heat transfer coefficients are calculated. The typically calculated uncertainties of measured and calculated parameters are shown below.

IV.1 Uncertainty in Mass flow rate

Coolant mass flow rate based on coolant line orifice diameter of 20.13 mm,

At a coolant mass flow rate of 35.50 kg/hr,

$$\dot{m} = 0.121198 * \sqrt{(P_{up1} - P_{down}) * (P_{up2} + 680)}$$

Where,

P_{up1} = upstream pressure in mm of H₂O, 364.344 mm of H₂O

P_{up2} = upstream pressure in mm of Hg, 26.79 mm of Hg

P_{down} = downstream pressure in mm of H₂O, 242.904 mm of H₂O

Uncertainty in pressure measurements are,

$\omega P_{up1} = \pm 0.101972$ mm of H₂O

$\omega P_{up2} = \pm 0.007501$ mm of Hg

$\omega P_{down} = \pm 0.101972$ mm of H₂O

$$\dot{m} = 0.121198 * \sqrt{(P_{up1} - P_{down}) * (P_{up2} + 680)}$$

$$\frac{\partial \dot{m}}{\partial P_{up1}} = \frac{0.121198 * (P_{up2} + 680)}{2 * \sqrt{(P_{up1} - P_{down}) * (P_{up2} + 680)}}$$

$$\frac{\partial \dot{m}}{\partial P_{down}} = \frac{-0.121198 * P_{up2} + 680}{2 * \sqrt{(P_{up1} - P_{down}) * (P_{up2} + 680)}}$$

$$\frac{\partial \dot{m}}{\partial P_{up2}} = \frac{0.121198 * (P_{up1} - P_{down})}{2 * \sqrt{(P_{up1} - P_{down}) * (P_{up2} + 680)}}$$

The uncertainty in the mass flow,

$$\omega \dot{m} = \left[\left(\frac{\partial \dot{m}}{\partial P_{up1}} * \omega P_{up1} \right)^2 + \left(\frac{\partial \dot{m}}{\partial P_{down}} * \omega P_{down} \right)^2 + \left(\frac{\partial \dot{m}}{\partial P_{up2}} * \omega P_{up2} \right)^2 \right]^{\frac{1}{2}}$$

$$\omega\dot{m} = \left[\left(\frac{0.121198 * (P_{up2} + 680)}{2 * \sqrt{(P_{up1} - P_{down}) * (P_{up2} + 680)}} * \omega Pt \right)^2 \right. \\ \left. + \left(\frac{-0.121198 * (P_{up2} + 680)}{2 * \sqrt{(P_{up1} - P_{down}) * (P_{up2} + 680)}} * \omega Ps \right)^2 \right. \\ \left. + \left(\frac{0.121198 * (P_{up1} - P_{down})}{2 * \sqrt{(P_{up1} - P_{down}) * (P_{up2} + 680)}} * \omega Tms \right)^2 \right]^{\frac{1}{2}}$$

$$\omega\dot{m} = \pm 0.021083443 \text{ kg/hr}$$

$$\dot{m} = 35.50761732 \text{ kg/hr}$$

$$\frac{\omega\dot{m}}{\dot{m}} = \frac{0.021083443}{35.50761732} \\ = 0.000593772$$

Percentage uncertainty = 0.06% i.e. $35.50761732 \pm 0.021083443$

At mass flow rate of 35.50 kg/hr, the uncertainty is 0.06% i.e. 35.5 ± 0.021

At a coolant mass flow rate of 140.44 kg/hr,

P_{up1} = upstream pressure in mm of H₂O, 4372.4 mm of H₂O

P_{up2} = upstream pressure in mm of Hg, 321.5 mm of Hg

P_{down} = downstream pressure in mm of H₂O, 3029.5 mm of H₂O

The uncertainty in the mass flow, $\omega\dot{m} = \pm 0.007565143 \text{ kg/hr}$

$$\dot{m} = 140.553857 \text{ kg/hr}$$

$$\frac{\omega\dot{m}}{\dot{m}} = \frac{0.007565143}{140.553857} \\ = 5.38238E-05$$

Percentage uncertainty = 0.0054% i.e. 140.55 ± 0.00756

At mass flow rate of 140.44 kg/hr, the uncertainty is 0.0054% i.e. 140.55 ± 0.0076

Mainstream mass flow rate based on the orifice diameter of 119.78 mm,

$$\dot{m} = 5.472964717 * \sqrt{(P_{up1} - P_{down}) * (P_{up2} + 680)}$$

Where,

P_{up1} = upstream pressure in mm of H₂O, 680 mm of H₂O

P_{up2} = upstream pressure in mm of Hg, 50 mm of Hg

P_{down} = downstream pressure in mm of H₂O, -408 mm of H₂O

The uncertainty of pressure measurement is approximately

$\omega P_{up1} = \pm 0.101972$ mm of H₂O

$\omega P_{up2} = \pm 0.007501$ mm of Hg

$\omega P_{down} = \pm 0.101972$ mm of H₂O

The uncertainty in the mass flow, $\omega \dot{m} = \pm 0.324216435$ kg/hr

$$\dot{m} = 4877.514 \text{ kg/hr}$$

$$\begin{aligned} \frac{\omega \dot{m}}{\dot{m}} &= \frac{0.324216435}{4877.514} \\ &= 6.64717E-05 \end{aligned}$$

Percentage uncertainty = 0.007% i.e. 4877.514 ± 0.3242164

At mass flow rate of 4877.514 kg/hr, the uncertainty is 0.007% i.e. 4877.514 ± 0.324

IV.2 Uncertainty in Mainstream Reynolds Number

Mainstream Reynolds Number,

$$Re_{ms} = \frac{\rho V D}{\mu}$$

Where,

The density of the mainstream, $\rho = \frac{Pt}{R.Tms}$

The velocity of the mainstream, $V = \sqrt{\frac{2(Pt - Ps)}{\rho}}$

Here,

ρ is the mainstream density in kg/m^3

V is the mainstream velocity in meter/sec

D is the hydraulic diameter of the duct which is 0.1142 m

P_t = total mainstream pressure, 92486.0744 Pa

P_s = mainstream static pressure, 92332.0744 Pa

R = characteristic gas constant, 287 J/KgK

T_{ms} = mainstream temperature, 300 K

μ = dynamic viscosity, 1.6×10^{-5} Kg/ms

Uncertainty in temperature and pressure measurements are,

The temperatures are measured using type K thermocouples with the uncertainty of ± 0.36 °C or K

The measurement system (PCI 6280 DAQ card with SCXI 1102) has an overall absolute accuracy of ± 0.75 °C or K

Hence the overall uncertainty on the temperature measurement is approximately 1.1 °C or K

$$\omega_{T_{ms}} = \pm 1.1 \text{ K}$$

$$\omega_{P_t} = \pm 1 \text{ Pa}$$

$$\omega_{P_s} = \pm 1 \text{ Pa}$$

$$\omega_{P_c} = \pm 1 \text{ Pa}$$

$$Re = \left(\sqrt{\frac{2(P_t - P_s) \cdot P_{ms}}{T_{ms} \cdot R}} \right) \cdot \left(\frac{D}{\mu} \right)$$

$$\frac{\partial Re}{\partial P_t} = \left(\frac{2P_t - P_s}{\mu} \right) \left(\sqrt{\frac{2(P_t - P_s) \cdot P_t}{T_{ms} \cdot R}} \right)$$

$$\frac{\partial Re}{\partial P_s} = \left(\frac{D}{\mu} \right) \left(\sqrt{\frac{P_t}{2T_{ms} \cdot R(P_t - P_s)}} \right)$$

$$\frac{\partial Re}{\partial T_{ms}} = \left(\frac{D}{\mu} \right) \left(\sqrt{\frac{P_t}{2T_{ms} \cdot R(P_t - P_s)}} \right)$$

$$\omega Re = \left[\left(\frac{\partial Re}{\partial Pt} \omega Pt \right)^2 + \left(\frac{\partial Re}{\partial Ps} \omega Ps \right)^2 + \left(\frac{\partial Re}{\partial Tms} \omega Tms \right)^2 \right]^{\frac{1}{2}}$$

1. $\omega Re =$

$$\left[\left(\left(\frac{2Pt - Ps}{\mu} \right) \cdot \left(\sqrt{\frac{2(Pt - Ps) \cdot Pt}{Tms \cdot R}} \right) \omega Pt \right)^2 + \left(\left(\frac{D}{\mu} \right) \cdot \left(\sqrt{\frac{Pt}{2Tms \cdot R(Pt - Ps)}} \right) \omega Ps \right)^2 + \left(\left(\frac{D}{\mu} \right) \cdot \left(\sqrt{\frac{Pt}{2Tms \cdot R(Pt - Ps)}} \right) \omega Tms \right)^2 \right]^{\frac{1}{2}}$$

Reynolds Number Based on the Hydraulic Diameter of Mainstream Duct:

$$\omega Re = 1505.134952$$

$$Re = 304213.2193$$

$$\frac{\omega Re}{Re} = \frac{1505.134952}{304213.2193}$$

$$= 0.004947632$$

Percentage uncertainty = 0.49% i.e 304213.22 ± 1505

At Reynolds number of 3×10^5 , the uncertainty is 0.49% i.e 304213.22 ± 1505

Reynolds Number Based on the Leading Edge Diameter:

D is the diameter of the blade leading edge which is 0.089 m

$$\omega Re = 500.5867367$$

$$Re = 101177.0423$$

$$\frac{\omega Re}{Re} = \frac{500.5867367}{101177.0423}$$

$$= 0.004947632$$

Percentage uncertainty = 0.49% i.e 101177.04 ± 500.59

At Reynolds number of 1×10^5 , the uncertainty is 0.49% i.e 101177.04 ± 500.59

IV.3 Uncertainty in the Density ratio

Density Ratio (DR),

$$d = \frac{(\rho_c)}{(\rho_m)}$$

$$d = \frac{(P_c \cdot T_m)}{(T_c \cdot p_t)}$$

Let, d= density ratio

Pt = mainstream pressure, 92486.07437 Pa

Pc = chamber pressure, 93086.41437 Pa

Tc= chamber temperature, 243 K

Tm= mainstream temperature, 300 K

Uncertainty in temperature and pressure measurements are,

The temperatures are measured using type K thermocouples with the uncertainty of ± 0.36 °C or K

The measurement system (PCI 6280 DAQ card with SCXI 1102 has an overall absolute accuracy of ± 0.75 °C or K

Hence the overall uncertainty on the temperature measurement is approximately 1.1 °C or K

$$\omega_{T_{ms}} = \pm 1.1 \text{ K}$$

$$\omega_{T_c} = \pm 1.1 \text{ K}$$

$$\omega_{P_t} = \pm 1 \text{ Pa}$$

$$\omega_{P_c} = \pm 1 \text{ Pa}$$

$$\frac{\partial d}{\partial P_c} = \frac{(T_m)}{(T_c \cdot P_t)}$$

$$\frac{\partial d}{\partial T_c} = \frac{(-P_c \cdot T_m)}{(P_t) \cdot (T_c)^2}$$

$$\frac{\partial d}{\partial T_{ms}} = \frac{(P_c)}{(T_c \cdot P_t)}$$

$$\frac{\partial d}{\partial p_t} = \frac{(-P_c \cdot T_m)}{(T_c) \cdot (P_t)^2}$$

$$\omega d = \left[\left(\frac{\partial d}{\partial P_c} \omega P_c \right)^2 + \left(\frac{\partial d}{\partial T_c} \omega T_c \right)^2 + \left(\frac{\partial d}{\partial T_{ms}} \omega T_{ms} \right)^2 + \left(\frac{\partial d}{\partial p_t} \omega p_t \right)^2 \right]^{\frac{1}{2}}$$

$$\omega d = \left[\left(\frac{(T_m)}{(T_c \cdot P_t)} \cdot \omega P_c \right)^2 + \left(\frac{(-P_c \cdot T_m)}{(P_t) \cdot (T_c)^2} \cdot \omega T_c \right)^2 + \left(\frac{(P_c)}{(T_c \cdot P_t)} \cdot \omega T_{ms} \right)^2 + \left(\frac{(-P_c \cdot T_m)}{(T_c) \cdot (P_t)^2} \cdot \omega p_t \right)^2 \right]^{\frac{1}{2}}$$

$$\omega d = 0.007238626$$

$$d = 1.242582$$

$$\frac{\omega d}{d} = \frac{0.007238626}{1.242582}$$

$$= 0.005825473$$

At the Density Ratio of 1.242, the uncertainty is 0.58% i.e 1.242 ± 0.0072

IV.4 Uncertainty in the Blowing ratio

Blowing Ratio (BR),

$$b = \frac{\rho_c \cdot V_c}{\rho_m \cdot V_m}$$

Let,

b = blowing ratio

P_t = mainstream pressure, 92486.07437 Pa

P_s = static pressure, 92332.07437 Pa

P_c = chamber pressure, 92486.07437 Pa

T_c = chamber temperature, 243 K

T_m = main stream temp, 300 K

Uncertainty in temperature and pressure measurements are,

The temperatures are measured using type K thermocouples with the uncertainty of ± 0.36 °C or K

The measurement system (PCI 6280 DAQ card with SCXI 1102) has an overall absolute accuracy of ± 0.75 °C or K

Hence the overall uncertainty on the temperature measurement is approximately 1.1 °C or K

$$\omega T_{ms} = \pm 1.1 \text{ K}$$

$$\omega T_c = \pm 1.1 \text{ K}$$

$$\omega P_t = \pm 1 \text{ Pa}$$

$$\omega P_s = \pm 1 \text{ Pa}$$

$$\omega P_c = \pm 1 \text{ Pa}$$

$$b = \left(\sqrt{\frac{P_c \cdot T_m \cdot (P_c - P_s)}{P_t \cdot T_c \cdot (P_t - P_s)}} \right)$$

$$\frac{\partial b}{\partial P_c} = \left(\sqrt{\frac{T_m \cdot (2P_c - P_s)^2}{4(P_c^2 - P_c \cdot P_s)(P_t \cdot T_c \cdot (P_t - P_s))}} \right)$$

$$\frac{\partial b}{\partial T_m} = \left(\sqrt{\frac{P_c(P_c - P_s)}{4T_m P_t \cdot T_c(P_t - P_s)}} \right)$$

$$\frac{\partial b}{\partial P_s} = \sqrt{\frac{P_c \cdot T_m \cdot (P_c - P_t)^2}{4 \cdot P_t \cdot T_c \cdot (P_t - P_s)^3 \cdot (P_c - P_s)}}$$

$$\frac{\partial b}{\partial P_t} = \sqrt{\frac{P_c \cdot T_m \cdot (-2P_t + P_s)^2 \cdot (P_c - P_s)}{4 \cdot P_t^3 \cdot T_c \cdot (P_t - P_s)^3}}$$

$$\frac{\partial b}{\partial T_c} = \sqrt{\frac{P_c \cdot T_m \cdot (P_c - P_s)}{P_t \cdot T_c^3 \cdot (P_t - P_s)}}$$

$$\omega b = \left[\left(\frac{\partial b}{\partial T_c} \omega T_c \right)^2 + \left(\frac{\partial b}{\partial p_t} \omega p_t \right)^2 + \left(\frac{\partial b}{\partial P_s} \omega p_s \right)^2 + \left(\frac{\partial b}{\partial T_{ms}} \omega T_{ms} \right)^2 + \left(\frac{\partial b}{\partial p_c} \omega p_c \right)^2 \right]^{\frac{1}{2}}$$

$$\omega b$$

$$= \left[\left(\sqrt{\frac{P_c \cdot T_m \cdot (P_c - P_s)}{P_t \cdot T_c^3 \cdot (P_t - P_s)}} \cdot \omega T_c \right)^2 + \left(\sqrt{\frac{P_c \cdot T_m \cdot (-2P_t + P_s)^2 \cdot (P_c - P_s)}{4 \cdot P_t^3 \cdot T_c \cdot (P_t - P_s)^3}} \cdot \omega p_t \right)^2 \right]$$

$$+ \left(\sqrt{\frac{P_c \cdot T_m \cdot (P_c - P_t)^2}{4 \cdot P_t \cdot T_c \cdot (P_t - P_s)^3 \cdot (P_c - P_s)}} \cdot \omega p_s \right)^2 \left(\left(\sqrt{\frac{P_c(P_c - P_s)}{4T_m P_t \cdot T_c(P_t - P_s)}} \right) \omega T_{ms} \right)^2$$

$$+ \left(\sqrt{\frac{T_m \cdot (2P_c - P_s)^2}{4(P_c^2 - P_c \cdot P_s)(P_t \cdot T_c \cdot (P_t - P_s))}} \cdot \omega p_c \right)^2 \right]^{\frac{1}{2}}$$

$$\begin{aligned}\omega b &= 0.01293802 \\ b &= 2.466533327 \\ \frac{\omega b}{b} &= \frac{0.01293802}{2.466533327} \\ &= 0.005245427\end{aligned}$$

At the **Blowing Ratio of 2.47**, the uncertainty is 0.52% i.e. 2.47 ± 0.013 .

Similarly, for the **Blowing Ratio of 1.14**,

$$\begin{aligned}\omega b &= 0.005780758 \\ b &= 1.14198918 \\ \frac{\omega b}{b} &= \frac{0.005780758}{1.14198918} \\ &= 0.005062008\end{aligned}$$

At the Blowing Ratio of 1.14, the uncertainty is 0.51% i.e. 1.14 ± 0.006 .

IV.5 Uncertainty in the Cooling Effectiveness

Adiabatic Cooling Effectiveness,

$$\eta = \frac{T_{ms} - T_w}{T_{ms} - T_c}$$

For $\eta = 0.85$,

T_{ms} = mainstream temperature, 300 K

T_w = wall temperature, 251.55 K

T_c = coolant temperature, 243 K

The temperatures are measured using type K thermocouples with the uncertainty of ± 0.36 °C or K

The measurement system (PCI 6280 DAQ card with SCXI 1102) has an overall absolute accuracy of ± 0.75 °C or K

Hence the overall uncertainty on the temperature measurement is approximately 1.1 °C or K

i.e., $\omega T_{ms} = \pm 1.1$ K

$$\omega T_w = \pm 1.1 \text{ K}$$

$$\omega T_c = \pm 1.1 \text{ K}$$

$$\frac{\partial \eta}{\partial T_{ms}} = \frac{T_w - T_c}{(T_{ms} - T_c)^2}$$

$$\frac{\partial \eta}{\partial T_w} = \frac{-1}{(T_{ms} - T_c)}$$

$$\frac{\partial \eta}{\partial T_c} = \frac{T_{ms} - T_w}{(T_{ms} - T_c)^2}$$

$$\omega \eta = \left\{ \left(\frac{\partial \eta}{\partial T_{ms}} * \omega T_{ms} \right)^2 + \left(\frac{\partial \eta}{\partial T_w} * \omega T_w \right)^2 + \left(\frac{\partial \eta}{\partial T_c} * \omega T_c \right)^2 \right\}^{0.5}$$

$$\omega \eta = \left\{ \left(\frac{T_w - T_c}{(T_{ms} - T_c)^2} * \omega T_{ms} \right)^2 + \left(\frac{-1}{(T_{ms} - T_c)} * \omega T_w \right)^2 + \left(\frac{T_{ms} - T_w}{(T_{ms} - T_c)^2} * \omega T_c \right)^2 \right\}^{0.5}$$

$$\omega \eta = 0.025493$$

$$\frac{\omega \eta}{\eta} = \frac{0.025493}{0.85}$$

$$= 0.02999$$

Uncertainty in Cooling effectiveness is 3%

Error in Cooling Effectiveness, η at 0.85 = 0.85 ± 0.0255

Similarly, for $\eta = 0.3$,

T_{ms} = mainstream temperature, 300 K

T_w = wall temperature, 282.9 K

T_c = coolant temperature, 243 K

$$\omega \eta = 0.024258$$

$$\frac{\omega \eta}{\eta} = \frac{0.024258}{0.3}$$

$$= 0.080858$$

Uncertainty in Cooling effectiveness is 8.09%

Error in Cooling Effectiveness, η at 0.3 = 0.3 ± 0.02427

IV.6 Uncertainty in Heat transfer coefficient

Heat transfer coefficient,

$$h = \frac{(K_1 * I^2 + K_2 * I)}{A(T_w - T_{ms})}$$

Where,

K_1, K_2 are constants (0.003, 0.06158)

I is the current in Ampere, 140 A

T_w is the wall temperature, 323 K

T_{ms} is the mainstream temperature, 300 K

A is the area of the test surface, 0.041075 m²

$\omega T_{ms} = \pm 1.1$ K

$\omega T_w = \pm 1.1$ K

$\omega I = \pm 2$ A

$$h = \frac{(K_1 * I^2 + K_2 * I)}{A(T_w - T_{ms})}$$

$$\frac{\partial h}{\partial I} = \frac{(2K_1 * I + K_2)}{A(T_w - T_{ms})}$$

$$\frac{\partial h}{\partial T_w} = \frac{(K_1 * I^2 + K_2 * I)}{A(T_w - T_{ms})^2}$$

$$\frac{\partial h}{\partial T_{ms}} = \frac{(K_1 * I^2 + K_2 * I)}{A(T_w - T_{ms})^2}$$

$$\omega h = \left[\left(\frac{\partial h}{\partial I} \omega I \right)^2 + \left(\frac{\partial h}{\partial T_w} \omega T_w \right)^2 + \left(\frac{\partial h}{\partial T_{ms}} \omega T_{ms} \right)^2 \right]^{\frac{1}{2}}$$

$$\omega h = \left[\left(\frac{(2K_1 * I + K_2)}{A(T_w - T_{ms})} \cdot \omega I \right)^2 + \left(\frac{(K_1 * I^2 + K_2 * I)}{A(T_w - T_{ms})^2} \cdot \omega T_w \right)^2 \right.$$

$$\left. + \left(\frac{(K_1 * I^2 + K_2 * I)}{A(T_w - T_{ms})^2} \cdot \omega T_{ms} \right)^2 \right]^{\frac{1}{2}}$$

$$\omega h = 4.992033$$

$$h = 71.36595$$

$$\frac{\omega h}{h} = \frac{4.992033}{71.36595}$$

$$= 0.06995$$

Uncertainty in Heat transfer coefficient is 6.99%

Error in Heat transfer coefficient, h at 71.37 = 71.37 ± 4.99 W/m²k

IV.7 Uncertainty Summary

The error estimate is carried out based on the accuracy deviations in the measurements of pressure, temperature and mass flows. By using these deviations, an error estimate is made for the Reynolds number; mass flows, density ratio, blowing ratio, cooling effectiveness and heat transfer coefficient values for the accuracy of results. Based on the calculations, the % error in the flow parameters and the derived results are found as follows. These values are to be taken into consideration for the accuracy of results.

- Reynolds numbers are 0.49% (at a Reynolds number of 3,00,000 based on the hydraulic diameter of the duct, the uncertainty is ± 1505, and at a Reynolds number of 1,00,000 based on the test model leading edge diameter, the uncertainty is ± 500).
- Coolant mass flow is 0.06% (at a mass flow of 35.5 Kg/hr, the uncertainty is ±0.021 Kg/hr) and 0.005% (at a mass flow of 140.6 Kg/hr, the uncertainty is ±0.0076 Kg/hr).
- Mainstream mass flow is 0.007% (at a mass flow of 4877.5 Kg/hr, the uncertainty is ±0.3242 Kg/hr).
- Density ratio of 1.24 is 0.58% (± 0.072).
- Blowing ratios is 0.51% (at a blowing ratio of 2.5, the uncertainty is ± 0.013, and at a blowing ratio of 1.1, the uncertainty is ± 0.006).
- Cooling effectiveness at 0.85 is 3% (the uncertainty is ± 0.025) and 0.3 is 8.09% (the uncertainty is ± 0.024).
- Heat transfer coefficient at 71 W/m²K is 6.99% (the uncertainty is ± 5 W/m²K)

BIODATA

NAME: GIRIDHARA BABU YEPURI

Designation: Sr. Scientist

Organisation: Propulsion Division,
CSIR-National Aerospace laboratories,
Bangalore, India- 560017

Date of Birth: 05-02-1972

Mobile No.: +91 9480267609

Email: giridhar.nal@gmail.com



ADDRESS:

Res: Flat No.: 311, Ds Max Seasons Apartment, Annasandara Palya, Bangalore - 560017.

Off: Propulsion Division, CSIR-National Aerospace Laboratories, Kodihalli, Bangalore -560017.

QUALIFICATION:

B.E (Mechanical Engineering)– M.S University of Baroda, Gujarat - 1999

M.E (Mechanical Engineering) – M.S University of Baroda, Gujarat – 2001

EXPERIENCE:

1. 01 Year as Assistant Professor at Ananda Engineering College, Agra, U.P
2. 05 Years as Assistant Engineer at Thermal Power Station, Jhansi, U.P Govt.
3. 11 Years as a Scientist at CSIR-National Aerospace Laboratories, Bangalore.

PUBLICATIONS:

International Journal Papers	:07
International Conference Papers	:25
M. Tech Projects Guided	:12

MEMBERSHIP OF PROFESSIONAL BODIES:

1. ISHMT Lifetime member

PUBLICATIONS

International Journal Publications: 03

1. Giridhara Babu Yepuri, T.P. Ashok Babu, Kolke Deepak Kumar, Felix Jesuraj (2016). "Effect of RANS-type Turbulence Models on Adiabatic Film Cooling Effectiveness on a Scaled up Gas Turbine Blade Leading Edge Surface" in Journal of the Institution of Engineers (India): Series C published by Springer. pp. 1-8, First online: 23 June 2016, DOI: 10.1007/S40032-016-0302-5.
2. Giridhara Babu Y., Ashok Babu T.P., Anbalagan M., Meena R. (2014). "Experimental and Numerical Investigation of Adiabatic Film Cooling Effectiveness over the Compound Angled Gas Turbine Blade Leading Edge Model." International Journal of Mechanical Engineering and Technology (IJMET), Volume 5, Issue 9, September (2014), pp. 91-100. ISSN 0976-6340.
3. Giridhara Babu Y., Ashok Babu T.P., Raghavan Rajendran, Anbalagan M. and Felix J. (2014). "Influence of Hole Diameter on Film Cooling Effectiveness over a Compound Angled Gas Turbine Blade Leading Edge Surfaces." International Journal of Scientific & Engineering Research (IJSER), Volume 5, Issue 7, July 2014, pp. 919-928, ISSN 2229-5518.

Journals Communicated: 01

1. Giridhara Babu Yepuri, Ashok Babu Talanki Puttarangasetty, Shiva Raju and Felix J. "Experimental and Numerical Investigation of Influence of Injection Hole Angle on Film Cooling Over Gas Turbine Blade Leading Edge" International Journal of Aerospace Engineering, Hindawi Publications.

International Conference Papers: 07

1. Yepuri Giridhara Babu, Gururaj Lalg, Ashok Babu Talanki Puttarangasetty, Jesuraj Felix, Sreenivas Rao V. Kenkere and Nanjundaiah Vinod Kumar: "Experimental and Numerical Investigation of Effect of Blowing Ratio on Film Cooling Effectiveness and Heat Transfer Coefficient over a Gas

- Turbine Blade Leading Edge Film Cooling Configurations.” Proceedings of the ASME 2013 Gas Turbine India Conference, GTINDIA2013, December 5-6, 2013, Bangalore, Karnataka, India. Paper No. GTINDIA2013-3552, pp. V001T04A002; 10 pages, Doi: 10.1115/GTINDIA2013-3552.
2. Giridhara Babu Yepuri, Ashok Babu Talanki Puttarangasetty, Raghavan Rajendran, Felix Jesuraj: “Experimental Investigation of Adiabatic Film Cooling Effectiveness and Heat Transfer Coefficients over a Gas Turbine Blade Leading Edge Configuration” Paper No.: MSME435, International Conference on Material Science and Material Engineering [MSME2014] March, 15-16, 2014, Chicago, Illinois, USA.
 3. Giridhara Babu Y., Anbalagan M, Meena R and Ashok Babu TP “Experimental and numerical investigation of adiabatic film cooling effectiveness and heat transfer coefficients over the compound angled gas turbine blade leading edge model.” Paper No.: T43, Proceedings of International Conference on Innovations and Emerging Trends in Mechanical Engineering, 13th June 2014, Nagarjuna College of Engg. & Tech, Bangalore, India.
 4. Giridhara Babu Y., Anbalagan M., Meena R. and Ashok Babu T.P. “Experimental and Numerical Investigation of Adiabatic Film Cooling Effectiveness over the Compound Angled Gas Turbine Blade Leading Edge Model.” Paper No.: ME226, Proceedings of the 2nd International Conference on Current Trends in Engineering and Management, ICCTEM-2014, 17– 19, July 2014, Mysore, Karnataka, India.
 5. Giridhara Babu Yepuri, Ashok Babu Talanki Puttarangasetty, Raghavan Rajendran, Felix Jesuraj, Anbalagan M. “Influence of Hole Diameter on Film Cooling Effectiveness over a Compound Angled Gas Turbine Blade Leading Edge Surfaces.” Paper No.: IMMM2014-TSPE-24, Proceedings of the 2nd International Conference on Materials, Mechanics and Management, IMMM2014, 17– 19, Dec 2014, College of Engineering and Technology, Trivandrum, Kerala, India.
 6. Giridhara Babu Yepuri, Kolke Deepak Kumar, Ramesha D K, Felix J and Ashok Babu T.P.: “Effect of RANS-type Turbulence Models on Adiabatic Film Cooling Effectiveness on a Scaled up Gas Turbine Blade Leading Edge Surface.” Paper No.: NPC2015-71, Proceedings of the National Propulsion Conference, NPC2015, 23rd - 24th Feb 2015, IITB, Mumbai, India.

7. Giridhara Babu Yepuri, Felix J. Bharath Kumar S.B., D. K. Ramesha, Anbalagan M., Ashok Babu T. P.: “CFD Validation of adiabatic film cooling effectiveness over gas turbine blade leading edge surfaces.” Paper No.: IHMTC2015-1057, presented at the proceedings of the 23rd National & 1st ISHMT- ASTFE Heat and Mass Transfer Conference, IHMTC2015, during December 17-20, 2015, at VSSC, ISRO, Thiruvananthapuram, Kerala, India.